NEXAFS Spectroscopy of Condensed *N*-alkanes

A Thesis Submitted to the

College of Graduate and Postdoctoral Studies

In Partial Fulfilment of the Requirements

For the Degree of Doctor of Philosophy

In the Department of Chemistry

University of Saskatchewan

Saskatoon

By

Sadegh Shokatian

October 2020

PERMISSION TO USE

In presenting this dissertation in partial fulfillment of the requirements for a postgraduate degree from the University of Saskatchewan, I agree that the Libraries of this University may make it freely available for inspection. I further agree that permission for copying of this thesis in any manner, in whole or in part, for scholarly purposes may be granted by Professor S. G. Urquhart who supervised my thesis work or, in his absence, by the Head of the Department of Chemistry or the Dean of the College of Graduate Studies and Research. It is understood that any copying or publication or use of this thesis or parts thereof for financial gain shall not be allowed without my written permission. It is also understood that due recognition shall be given to me and to the University of Saskatchewan in any scholarly use that may be made of any material in my dissertation.

DISCLAIMER

This dissertation is exclusively created to meet the thesis requirements for the degree of Ph.D. at the University of Saskatchewan. Reference in this dissertation to any specific commercial products, process, or service by trade name, trademark, manufacturer, or otherwise, does not constitute or imply its endorsement, recommendation, or favoring by the University of Saskatchewan. The views and opinions of the author expressed herein do not state or reflect those of the University of Saskatchewan and shall not be used for advertising or product endorsement purposes.

Requests for permission to copy or to make other uses of materials in this dissertation in whole or part should be addressed to:

Head of the Department of Chemistry
110 Science Place
University of Saskatchewan
Saskatoon, Saskatchewan, S7N 5C9, Canada

OR

Dean
College of Graduate and Postdoctoral Studies
University of Saskatchewan
116 Thorvaldson Building, 110 Science Place
Saskatoon, Saskatchewan, S7N 5C9, Canada

Abstract

The carbon 1s Near-Edge X-ray Absorption Fine Structure (NEXAFS) spectra of alkanes vary with chain length, substitution, and phase change. For short gaseous alkanes, the carbon 1s NEXAFS spectra of alkanes are dominated by Rydberg transitions with distinctive vibronic features. In the case of condensed alkanes, the characteristic C-H feature appears at 287-288 eV.

Computational models can effectively reproduce and interpret NEXAFS spectra of simple gaseous alkanes, provided that vibronic transitions are neglected. However, computational methods have been ineffective in reproducing and interpreting the NEXAFS spectra of condensed alkanes. We hypothesize that this shortcoming is due to computational limitations in modeling effect such as structural variations and disorder.

An objective of this thesis is to study the effect of structural changes such as chain length on the NEXAFS spectra of *n*-alkanes. This objective involves computational modelling as well as experimental studies of the spectra of liquid *n*-alkanes. It should be noted that the NEXAFS spectra of liquid *n*-alkanes are entirely unexplored.

The second objective of this thesis is to study the role of disorder caused by nuclear motion on the NEXAFS spectra of n-alkanes. The effect of nuclear motion refers to the contribution of the range of thermally accessible structures to the average NEXAFS spectrum of a material. In liquids, this effect can give a distribution of molecular structures rather than the single lowest energy structure. These thermally accessible structures include geometry defects such as gauche defects, thermally populated vibrational states, as well as zero-point motion. This thesis will characterize the role of disorder such geometry defects and nuclear motion on the NEXAFS spectra of *n*-alkanes using a Density Functional Theory approach. As part of this objective, the effect of temperature change on the NEXAFS spectra of *n*-alkanes will be studied.

Acknowledgements

I would like to thank my supervisor, Professor Stephen G. Urquhart for all his support and guidance throughout my PhD program. I certainly learned more than I could imagine in various fields of research.

I would also like to thank the members of my committee: Professor Matthew Paige, Professor Richard Bowles, and, Dr Yongfeng Hu for their valuable advice and discussions throughout my program.

I am thankful to the members of Urquhart group, Dr Sahan Perera, Amara Zuhaib, and Curtis Senger for all their help and support.

I am grateful to the members of the Physics Machine Shop, the department of Chemistry staff members, and the Saskatchewan Structural Science Centre of the University of Saskatchewan.

Special thanks go to my undergraduate teaching laboratory managers, Dr Valerie Mackenzie and Dr Alexandra Bartole-Scott for their endless support and faith in me throughout the program.

Further, I would like to thank Soft X-ray Microscopy (SM) beamline scientist at the Canadian Light Source, Dr Jian Wang, for his endless support even during long midnight shifts.

Dedication

I dedicate my dissertation work to my wonderful wife, Yasaman Hosseini whom I would not be able to finish this study without her encouragements and support since the starting point. I would also dedicate my thesis to my lovely parents, Ghodratollah Shokatian and Zeinab Ahangari for their support.

Table of Contents

List of Tables

List of Figures

List of Abbreviations

ΔKS	ΔKohn-Sham	97
AEY	Auger Electron Yield	61
BE	Binding Energy	2
BM	Bending Magnets	51
BO	Born-Oppenheimer	13
CCD	Charged Coupled Device	76
CLS	Canadian Light Source	42
DFT	Density Functional Theory	iii
ECP	Effective Core Potential	105
EICVOM	Equivalent Ionic Core Virtual Orbital Model	95
EMR	Electromagnetic Radiation	2
EPU	Elliptically Polarized Undulator	56
EXAFS	Extended X-ray Absorption Fine Structure	4
FC	Franck-Condon	14
FCH	Full Core-Hole	97
FEL	Free Electron Lasers	52
FY	Fluorescence Yield	61
GGA	Generalized Gradient Approximation	94

HCH	Half-Core Hole	97
HF	Hartree-Fock	82
ID	Insertion Devices	52
IP	Ionization Potential	2
KS	Kohn-Sham	90
LCAO	Linear Combination of Atomic Orbitals	84
LCGTO	Linear Combination of Gaussian Type Orbitals	104
LD	Linear Dichroism	17
LDA	Local-Density Approximation	92
LINAC	Linear Accelerator	51
LJ	Lennard-Jones	101
LSDA	Local Spin Density Approximation	93
MD-DFT	Molecular Dynamics-Density Functional Theory	81
MM	Molecular Mechanics	82
MO	Molecular Orbital	98
NEXAFS	Near-Edge X-ray Absorption Fine Structure	iii
OM	Optical Microscopy	76
OSA	Order Sorting Aperture	73
PBC	Periodic boundary conditions	102

PBE	Perdew-Burke-Ernzerhof	95
PCB	Printed Circuit Board	72
PEY	Partial Electron Yield	61
PGM	Plane Grating Monochromator	63
PIMD	Path Integral Molecular Dynamics Simulations	34
PMT	Photomultiplier	60
QM	Quantum Mechanics	36
RF	Radio Frequency	52
SCF	Self-Consistent Field	87
SD	Standard Deviation	112
SDD	Silicon Drift Detector	73
SE	Schrödinger’s Equation	81
SM	Spectromicroscopy	62
STO	Slater Type Orbitals	92
STXM	Scanning Transmission X-ray Microscope	42
TDM	Transition Dipole Moment	6
TEY	Total Electron Yield	61
TP-DFT	Transition Potential Density Functional Theory	7
XAS	X-ray Absorption Spectroscopy	1

X-PEEM	X-ray Photoemission Electron Microscope	63
ZP	Zone Plate	64

List of Symbols and Nomenclature

c	Speed of Light ($2.99782 \times 10^{8} ms^{-1}$)
e	Electron Charge ($1.602 \times 10^{-19} C$)
$\boldsymbol{E}$	Electric Field Vector of Polarized X-rays
h	Planck Constant ($6.62607 \times 10^{-34} m^2\ kgs^{-1}$)
$\hbar$	$h/2\pi$
m_e	Mass of Electron ($9.11 \times 10^{-31} kg$)
N_A	Avogadro Number (6.023×10^{23})
λ	Wavelength
μ	Dipole Operator
ψ	Wavefunction / Eigenfunction
π	3.14
ρ	Density
Z	Nuclear Charge

Chapter 1 – Introduction

NEXAFS spectroscopy is a unique tool for studying the electronic and geometric structure,[1-3] elemental and chemical composition,[4-7] molecular orientation,[8-9] and magnetism of organic materials.[7, 10] In this thesis, NEXAFS spectroscopy is used along with computational models to study the effect of structural variations on the NEXAFS spectra of liquid phase *n*-alkanes as a means to understand the spectra of the liquid phase of larger molecules. The principles of NEXAFS spectroscopy and the carbon 1s NEXAFS spectra of *n*-alkanes are presented in this chapter.

1.1 X-ray Absorption Spectroscopy (XAS)

XAS has made a major contribution to a wide variety of material chemistry research topics over the past 30 years. The XAS technique is defined as the absorption of the X-rays by a substance leading to the excitation or ionization of core electrons.[3] Figure 1.1 shows a schematic of the transmission of X-rays through a sample.

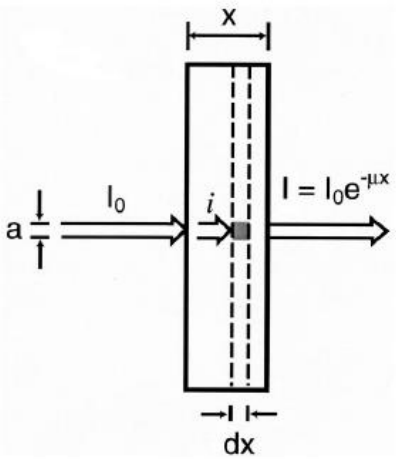

Figure 1.1 - Schematic of transmission of the X-ray through the sample. Figure is reprinted with permission[11]

In this figure, I_0 is the intensity of the incident beam. For monochromatic photons, the intensity changes of the X-ray beam passing through a material can be obtained using the following equation:

$$dI(x) = -I(x).n.\sigma.dx \qquad \textit{Equation 1.1}$$

In this equation, dI is the change in the intensity (*I*) at position x, n is the number density of atoms (number per cm^3), and σ is a constant that reflects the total probability of a photon being absorbed or scattered. Equation 1.1 can be written as the following equation, which is known as the Lambert-Beer's law. When X-rays are passing through a sample of thickness x, some X-rays will be absorbed. The intensity of the transmitted beam, (*I)* can be obtained using the Lambert-Beer's law.[3, 11]

$$I = I_0 e^{-\mu_l x} \qquad \textit{Equation 1.2}$$

In this equation, μ_l is defined as the linear absorption coefficient. The mass absorption coefficient μ (cm^2/g) is defined as the transmitted intensity through a material with the density of ρ (g/cm^3) and thickness of *d* as follows:

$$I = I_0 e^{-\mu\rho d} \qquad \textit{Equation 1.3}$$

And, the linear absorption coefficient μ_l (cm^{-1}) is defined as follows:

$$\mu_l = \mu\rho = \frac{1}{d} ln\left(\frac{I_0}{I}\right) \qquad \textit{Equation 1.4}$$

The photon transmission can be converted to optical density using the following equations:

$$OD = -ln(\frac{I}{I_0}) = \mu\rho d = \mu_l d \qquad \textit{Equation 1.5}$$

When an X-ray interacts with an atom or molecule, the oscillating electric field of the electromagnetic radiation (EMR) interacts with the electrons in the atom or molecule. This X-ray can be scattered or absorbed. The absorption of an X-ray can lead to the excitation of core electrons to the unoccupied levels (photoabsorption) or the ionization of these electrons (photoionization). Photoionization can occur when the X-ray energy exceeds the Binding Energy (BE) of the electron. This is also known as the Ionization Potential (IP) and is defined as the energy required to remove an electron from an atom/molecule to form a cation. The background in a photoabsorption spectrum before the core edge is from valence (or shallower core) electron photoionization, while the core edge represents the onset of photoionization from that core level. Figure 1.2 presents a schematic of XAS with its corresponding energies.

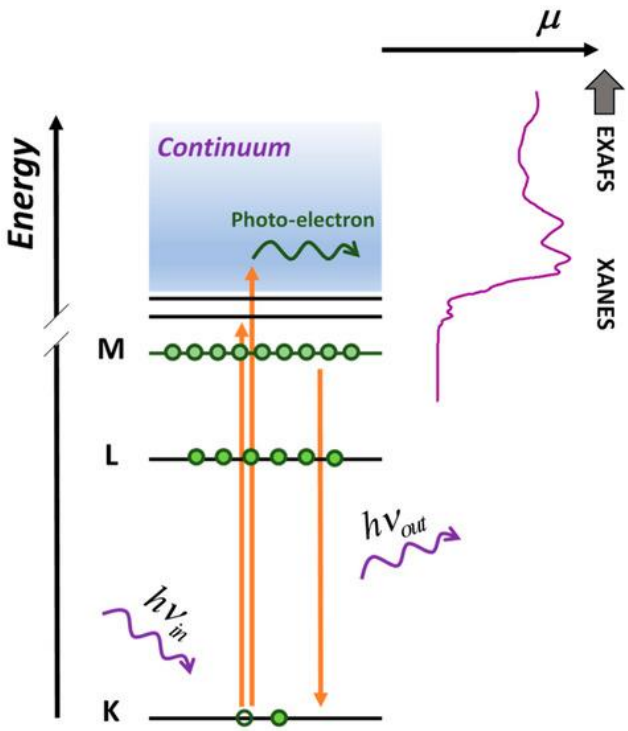

Figure 1.2 - Schematic of the soft X-ray XAS process with its corresponding energies. Figure is reprinted with permission.[12]

A plot of the absorption coefficient, μ, as a function of the photon energy, can show discontinuities known as absorption edges. A plot of μ versus photon energy for a hypothetical element is presented in figure 1.3.

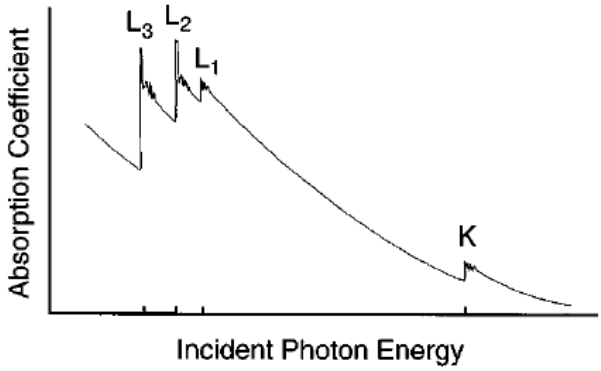

Figure 1.3 - X-ray absorption coefficient as a function of incident photon energy. Figure is reprinted with permission.[11]

The BE of the electron is a function of the atomic number (Z) and the electronic shell from which the electrons are ionized from (e.g., 1s, 2s, 2p, etc.) These electron shells are labelled as K (1s level), L (second electron shell; 2s and 2p), M (third electron shell, 3s, 3p, and 3d), etc. XAS is therefore sensitive to elemental composition and the electronic configuration of the sample. Depending on the origin of the excited electron, X-ray absorption spectra are labeled as K-edge (excitation from the first shell of electrons, 1s), L-edge (excitation from the second shell of electrons, 2s, 2p), etc.

The X-ray absorption probability is described by the X-ray absorption cross-section or the optical oscillator strength. The X-ray absorption cross-section is the number of excited electrons per unit time divided by the number of incident photons per unit time per unit area of the sample. This cross-section can be calculated as follows:[3]

$$\sigma_x = \frac{4\pi^2 h}{m^2}\frac{e^2}{\hbar c}\frac{1}{\hbar\omega}|\langle f|E.\mu|i\rangle|^2\rho_f(E) \qquad \textit{Equation 1.6}$$

where σ_x is the X-ray absorption cross-section (cm^2 or $barn$=10^{-24} cm^2), *e* is the electron charge, c is the speed of light, E is the electric field vector of X-ray photons, *m* is the mass of the electron, $\hbar = \frac{h}{2\pi}$, *h* is the Planck constant, $\hbar\omega$ is the photon energy, μ is the dipole operator, *f* is the wavefunction of the final state, *i* is the wavefunction of the initial state, and $\rho_f(E)$ is the energy density of the final state.[3]

The optical oscillator strength, *f*, is another way of expressing the probability of absorption. This dimensionless quantity is related to the X-ray absorption cross-section by:[3]

$$\sigma_x = C\frac{df}{dE} \qquad \textit{Equation 1.7}$$

where $C = \frac{2\pi^2 e^2 \hbar}{mc} = 1.1 \times 10^2 Mb\ \ eV$($1Mb$= $1\ mega\ \ barn$). The variable *f* is the energy integral of the cross-section and is a measure of the intensity of a resonance, which often is referred to as the "*f* number".[3]

$$f = \frac{2}{m\hbar\omega}|\langle f|\varepsilon.\mu|i\rangle|^2 \qquad \textit{Equation 1.8}$$

XAS is described as the Near Edge X-ray Absorption Fine Structure (NEXAFS) and Extended X-ray Absorption Fine Structure (EXAFS). NEXAFS studies features near the absorption edge while EXAFS studies the scattering of the ionized electron by its neighboring atoms, which is generally observed more than 50 eV above the edge.[3] Since EXAFS spectroscopy was not used for this thesis, no further information on this topic will be presented.

The research described in this thesis contributes to an improved understanding of the effect of structural diversity and nuclear motion on the carbon 1s NEXAFS spectra of linear *n*-alkanes. Further information on NEXAFS spectroscopy will be presented in the following section.

1.2 NEXAFS Spectroscopy

NEXAFS spectroscopy was used extensively in the early 1980s to study low-Z molecules adsorbed to surfaces.[3] Several different acronyms have been used to refer to this spectroscopy in the literature (e.g., XANES, XAS, etc.). For reasons of consistency with our published works, NEXAFS will be used throughout this thesis. NEXAFS is capable of detecting specific types of bonds (single, double, etc.), oxidation states, and the orientation of molecules and functional groups for species on surfaces as well as in bulk.[3] In NEXAFS spectroscopy, electronic transitions occur when the energy of the incoming photon matches the energy required to create the core excited state. When a system (atom or molecule) absorbs photons with the appropriate energy ($h\upsilon$), the system will be excited from the ground state (ψ_i) to an excited state (ψ_f). These transitions are often discussed as one electron transitions from core levels to unoccupied molecular orbitals (labeled as π^* or σ^* orbitals) or to atomic-like orbitals known as Rydberg orbitals.[1, 3, 13]

The removal of an electron from a core orbital creates a core hole, causing the deshielding of the nucleus. This process will increase the Coulombic attraction between the remaining electrons and the deshielded nucleus, which will generally shift occupied and unoccupied molecular orbitals to lower energy. Because of this Coulombic core hole effect, transitions to lower energy unoccupied orbitals shift to below the IP, leading to fine

structures observed below the absorption edge in the NEXAFS spectrum. Figure 1.4 presents a schematic molecular potential and corresponding NEXAFS 1s edge spectrum of a hypothetical diatomic molecule.

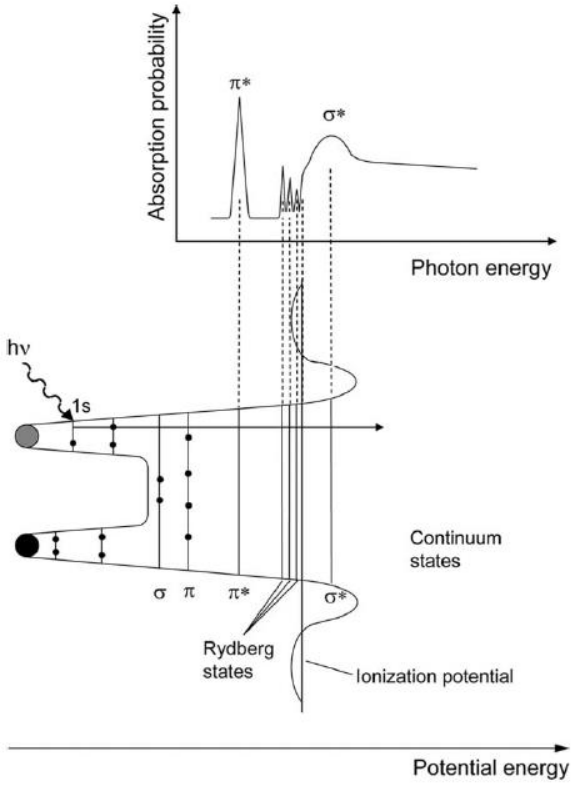

Figure 1.4 - Schematic NEXAFS spectrum corresponding to the potential of a diatomic molecule. Figure is reprinted with permission[1]

NEXAFS spectroscopy is the probe of the unoccupied valence and Rydberg orbitals, localized at the site of the core excited atom. This localization is a function of the overlap between the 1s orbital and the unoccupied molecular orbital in the Transition Dipole Moment (TDM) integral (§1.2.3.1), which is strongest for unoccupied molecular orbital density at the site of the core excited atom. In calculations, it is possible to localize the core hole on a selected atom and then calculate the NEXAFS spectrum for that atom.[14]

State and orbital language can be used to describe features in NEXAFS spectroscopy. A state contains information about the location and motion of all atoms and electrons in the molecule, described in the form of a wavefunction. Since the primary

change in an X-ray absorption process occurs for the electron that is being excited, the simpler one-electron picture is often used. This model treats the absorption process in terms of one electron that is excited from an initial 1s orbital to a final unoccupied molecular orbital. An orbital level diagram shows the occupancy of specific MOs before or after X-ray absorption. Figure 1.5 presents a schematic of the differences between the orbital, transition, configuration and state descriptions for the lowest energy N $1s \rightarrow \pi^*$ transition observed in the nitrogen 1s NEXAFS spectrum of N_2.[13]

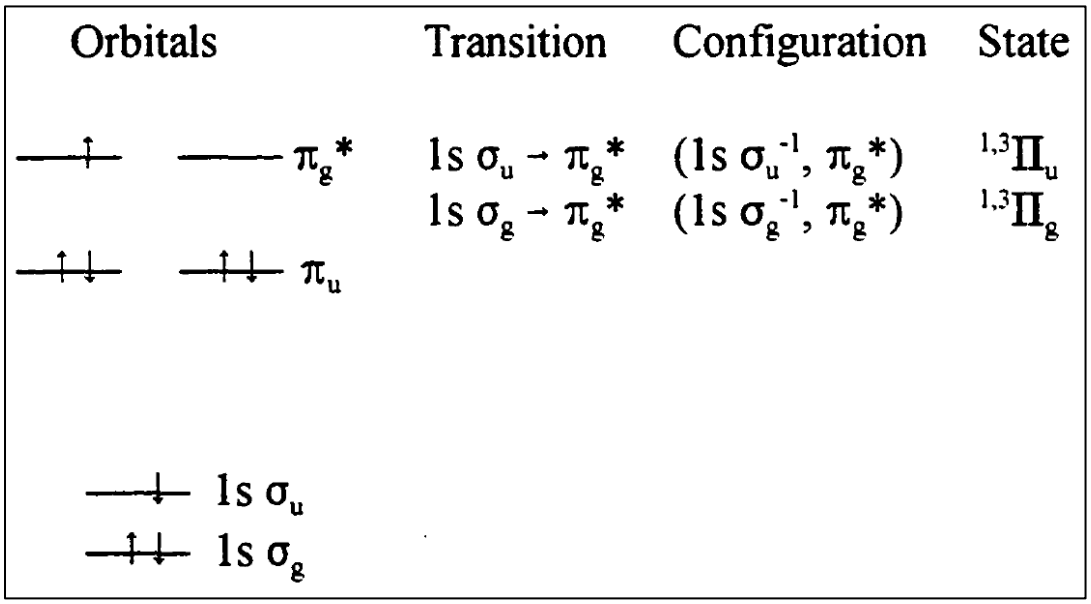

Figure 1.5 - Orbital, transition, configuration, and state description of N $1s \rightarrow \pi^*$ feature in the N 1s core excitation spectrum of N_2. Figure is reprinted with permission.[13]

In this figure, a one-electron picture is used to describe the transition from the nitrogen core level (1s σ_u and σ_g) to the π_g^* (LUMO) molecular orbital, as well as the core excited state configuration. These core excited states are described by the term symbols ($^{1,3}\Pi_g$ and $^{1,3}\Pi_u$), which represents the spin-allowed singlet core excited state ($^1\Pi$) and the spin-forbidden triplet core excited state ($^3\Pi$). Note that this diagram assumes that only the $g \rightarrow u$ transition is allowed based on selection rules.[13]

Figure 1.6 presents the simulated carbon 1s NEXAFS spectra of but-1-ene (1-butene), highlighting contributions from individual carbons atoms as well as the total spectrum. This simulation is obtained using Transition Potential Density Functional

Theory (TP-DFT) with the half-core hole approach in the deMon2k program. This approach is explained in detail in Chapter 3 – Computational methodology.

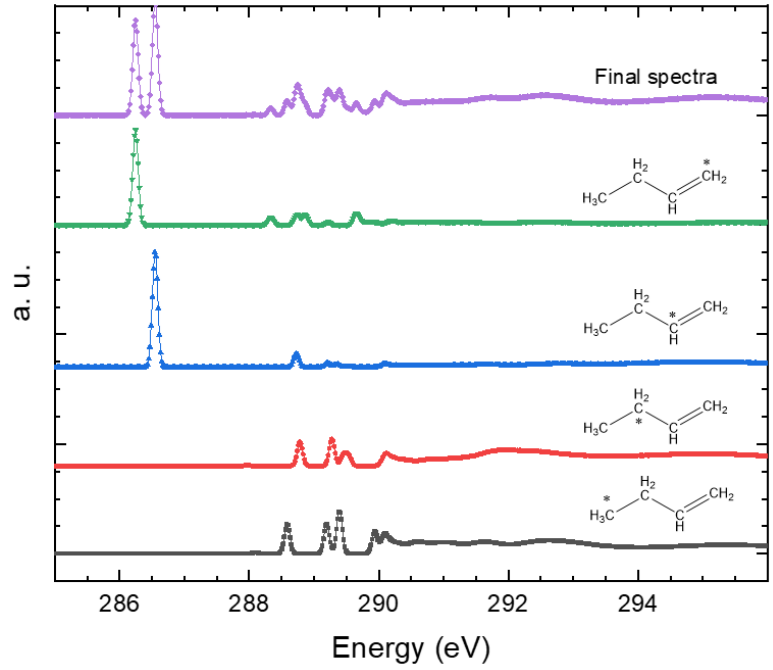

Figure 1.6 - Simulated carbon 1s NEXAFS spectrum of 1-butene. The position of the core hole is indicated by the asterisk on the carbon in the molecular structure. Final spectrum is the sum of individual spectrum of each of the carbons.

The carbon $1s \rightarrow \pi^*$ peak is only observed when the core hole is localized on one of the sp^2 carbons involved in the double bond, e.g., this carbon $1s \rightarrow \pi^*$ excitation occurs from one of the two carbon atoms bonded by the C=C double bond. The carbon 1s NEXAFS spectrum of the sp^3 carbon atoms will not show the carbon $1s \rightarrow \pi^*$ peak as there is no unsaturated character at these atoms. Since NEXAFS probes the local electronic structure at the site of the core hole, it is highly sensitive to the chemistry of the sample. This includes the oxidation state, the electronic and geometric structure, the functional group that the excited atom belongs to, molecular orientation, and magnetism.[1, 3, 15-17] Figure 1.7. shows the sensitivity of NEXAFS to the functional group and the chemical environment.[18]

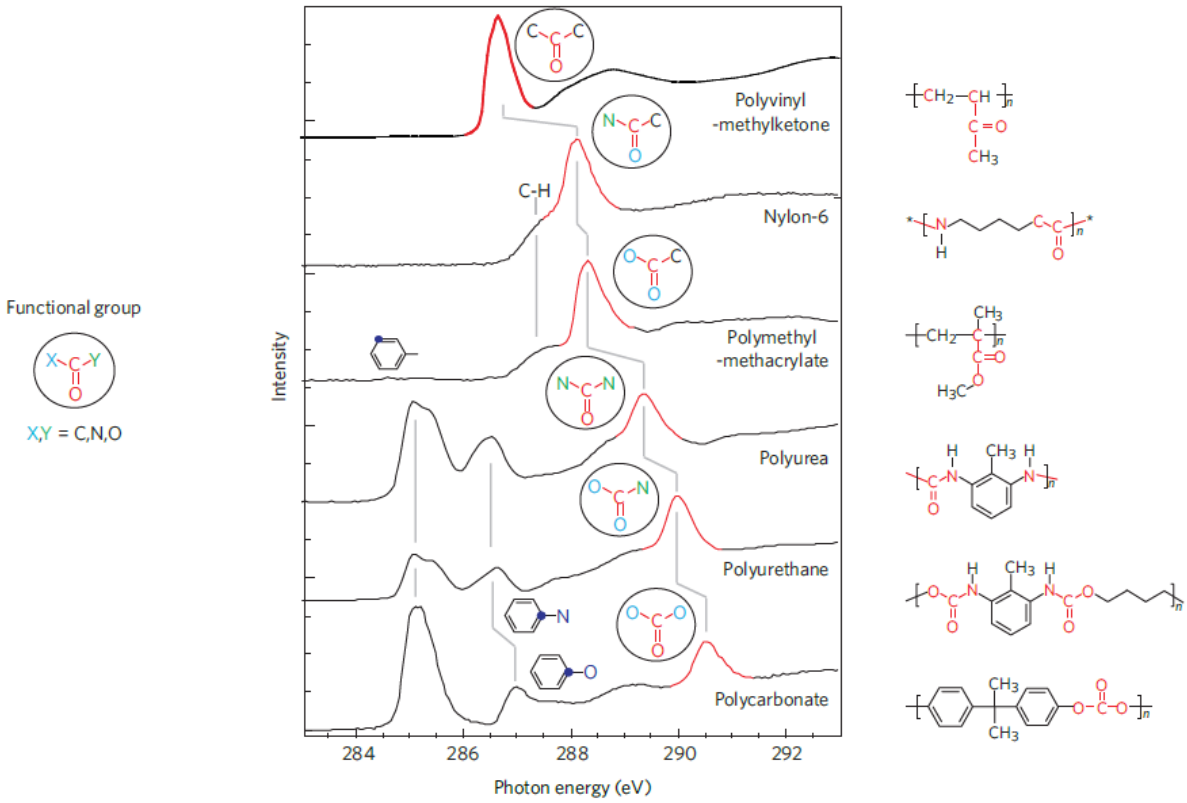

Figure 1.7 - Carbon 1s NEXAFS spectra of various polymers. Figure is reprinted with permission[18]

Since these transitions are governed by the dipole selection rules, it is possible to study molecular orientation through Linear Dichroism measurements, as described in section 1.2.3.

1.2.1 Electronic Transitions in Molecular NEXAFS Spectra

NEXAFS refers to the X-ray absorption spectra that includes features a few eV below the IP to ~50 eV above the IP. The absorption of the EMR will excite core electrons to bound orbitals or into the continuum. The width of specific transitions in a NEXAFS spectrum is affected by the energy resolution of the monochromator being used and the lifetime of the core excited states. For practical spectroscopy of molecules, the broadness of observed features will also depend on the overlap of closely separated features, including vibronic transitions, disorder, and nuclear motion broadening.

Using the Heisenberg time-energy uncertainty principle ($\Delta E \Delta t \geq \frac{\hbar}{2}$),[19] it is possible to obtain the lifetime broadening from the lifetime of the core excited state. In this equation

ΔE is the uncertainty in the energy measurement which gives the width of a transition, Δt is the uncertainty in the lifetime of the core excited state and h is the Planck constant ($4.136 \times 10^{-15}\ eV.s$ or $6.626 \times 10^{-34}\ J.s$). Short lifetimes give a smaller uncertainty, and thus an increased lifetime broadening. The core excited state lifetime can be expressed in terms of separate contributions from the excited electron configuration lifetime and the core-hole lifetime according to the following equation.[3, 19-20]

$$\frac{1}{\tau} = \frac{1}{\tau_e} + \frac{1}{\tau_h} \qquad \textit{Equation 1.9}^{3}$$

In this equation, τ is the overall lifetime, and τ_e and τ_h are the lifetimes of excited state and the core hole, respectively. Generally, transitions to the bound orbitals will have a longer lifetime and smaller broadening than transitions to unbound orbitals that have a much shorter lifetime. Therefore, using the following equation, the core-hole lifetime can be obtained from the energy broadening:

$$\tau_e \Delta E \simeq \hbar = 6.6 \times 10^{-16}\ eV.s \qquad \textit{Equation 1.10}^{3}$$

As an example, assuming that the lifetime of the excited electron configuration is long relative to the core hole, the energy width for the carbon 1s → π^* transition in CO is obtained to be $\Delta E \sim 80\ meV$, which leads to the core-hole lifetime of $\tau_h \sim 8.25 \times 10^{-15}\ s$. For these transitions, if the energy of a vibration in a core excited molecule is larger than the energy width of the transition, it may be possible to resolve vibronic peaks. Vibronic features are transitions from a molecule's electronic and vibrational ground state to an electronically and vibrationally excited state. Linear diatomic molecules such as CO and N_2 only have one vibrational mode, which has greater energy than the lifetime broadening. This means that vibronic peaks are resolved and observable. Methane, on the other hand, has 3N-6=9 (N=5 atoms) vibrational modes, for which only the higher energy vibrational modes can be resolved.[3]

In the NEXAFS spectra of unsaturated molecules, $\text{core} \rightarrow \pi^*$ transitions appear at the lowest energy, below the IP. Depending on the sample, the π^* orbital could be empty (e.g., CO) or partially filled (e.g., NO, O_2). In core excited molecules, these π^* orbitals are pulled down in energy below IP because of the increased Coulombic interaction caused

by the core hole. Since the π^* transitions are longer lived and therefore narrow, vibronic features (see 1.2.2) can be more easily resolved for these transitions (figure 1.8). [3, 13]

Carbon $1s \rightarrow \sigma^*$ transitions are broad and usually appear above the IP. However, it is possible to observe $1s \rightarrow \sigma^*$ transitions below the IP in case of molecules with weak σ bonds.[3, 21] Continuum σ^* transitions are generally broad on account of the large overlap of the σ^* orbitals with the continuum, which leads to a shorter lifetime.[17, 22-23]

In an atom, a Rydberg orbital has a principal quantum number greater than that of the highest occupied orbital in the ground state.[24] Transitions to these Rydberg orbitals are known as the Rydberg transitions, e.g., 1s → 3s, 1s → 3p, etc. Similar atomic-like Rydberg transitions also appear in the NEXAFS spectra of small molecules. Rydberg transitions appear as a series of sharp but weak peaks below the IP in NEXAFS spectra of atoms and small molecules.[3] Figure 1.8 shows a series of Rydberg transitions of the gas phase NEXAFS spectra of CO and N_2, plotted as a function of the term value.[25]

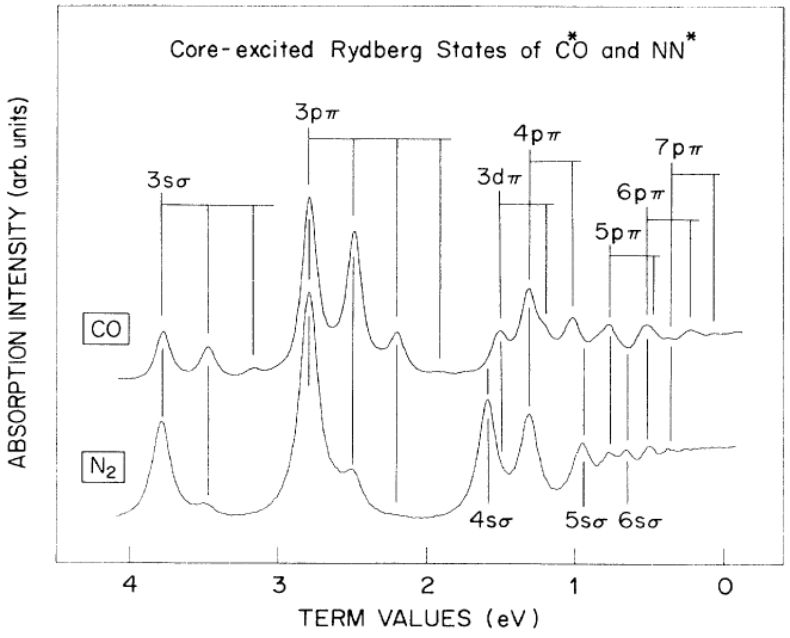

Figure 1.8 - Absorption intensity of the Rydberg transitions with the vibronic features of CO and N_2 plotted as a function of their term values. Figure is reprinted with permission.[25]

The term value expresses the transition energy relative to the IP, and is defined as the difference between the transition energy and the IP:

$$Term\,Value = IP - E_n = \frac{R}{(n-\delta_l)^2}$$ *Equation 1.11*[3]

In this equation, E_n is the energy of a Rydberg transition, *R* is the Rydberg constant (13.6 eV), and δ_1 is the quantum defect associated with the angular momentum number *l*. As the value of the angular momentum quantum number *l* increases (e.g., s → p → d), the quantum defect decreases as penetration decreases. For example, the quantum defect value for a carbon atom (Z = 6) is 0.9784, 0.5801, 0.0080, and 0.0001 for the *s*, *p*, *d*, and *f* Rydberg transitions, respectively.[26] An increase in the atomic number, Z, leads to the attenuation of the Rydberg transition intensity as the size of 1s orbital decreases and with that the spatial overlap with the Rydberg orbitals.[3]

In some molecules, Rydberg orbitals can have the same energy and symmetry as the hydrogen-derived antibonding molecular orbitals, e.g. σ^*_{C-H} MOs. This leads to the mixing of Rydberg and valence character in the core excited state.

1.2.2 Molecular Vibrations and Vibronic Features

Molecular motion will affect the NEXAFS spectra of molecules. This can be manifested in two ways: as molecular vibrations that are populated in the ground and electronically excited states, or as vibronic transitions in the NEXAFS spectra. Vibronic transitions occur when X-ray absorption induces an electronic transition from a molecule's electronic and vibrational ground state to an electronically and vibrationally excited state, e.g., a carbon $1s(v = 0) \rightarrow \pi^*(v = 1)$ transition. Examples of vibronic features can be observed in figures 1.8 and 1.9.[27]

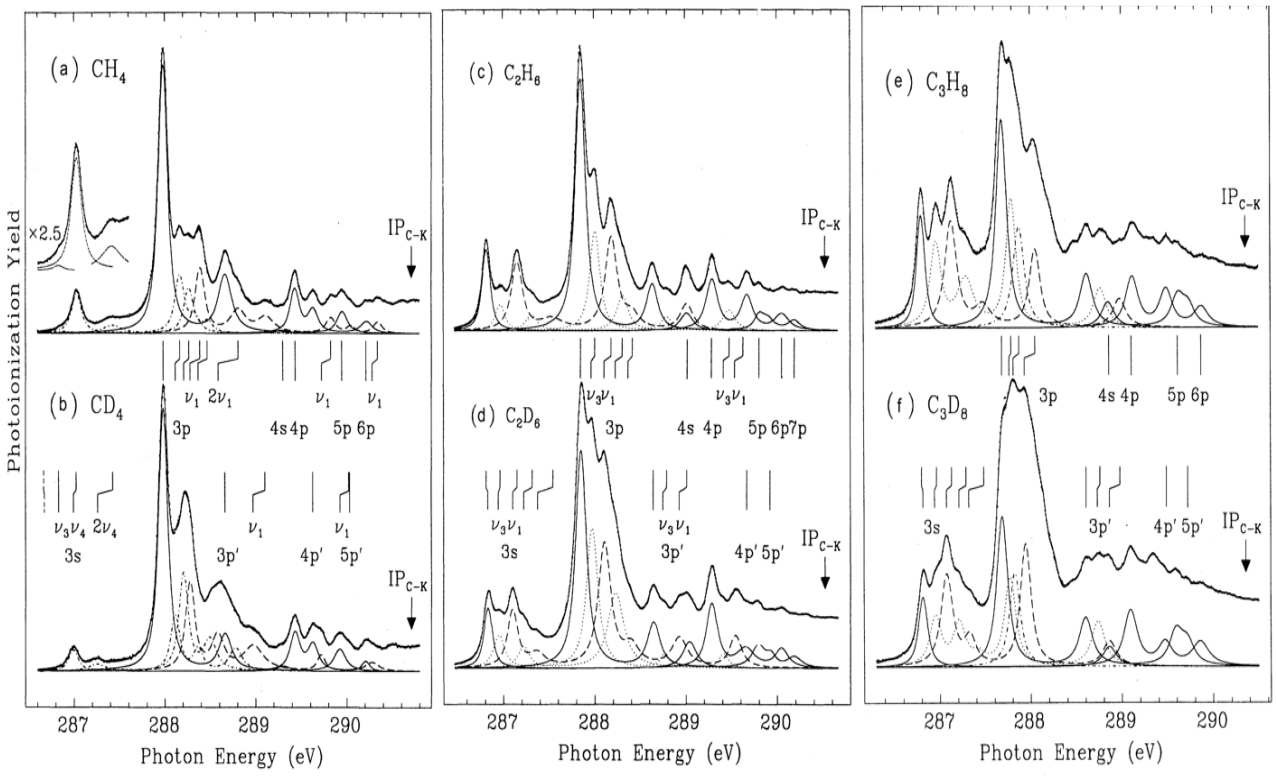

Figure 1.9 - Carbon 1s NEXAFS spectra of (a) CH_4, (b) CD_4,(c) C_2H_6,(d) C_2D_6, (e) C_3H_8,(f) C_3D_8. Figure is regenerated with permission.[27]

Multiple vibronic peaks can be observed for each Rydberg band (3s, 3p, etc.) in figure 1.9. As can be observed, an increase in the complexity of the molecule will increase the number and complexity of vibronic features. The vibronic features are usually only resolved in small, simple molecules (Figure 1.8) as complex molecules will have overlap between many closely separated vibronic transitions.[27]

The vibrational motion of a molecule is slower than the electronic excitation process. This is the basis of the Born-Oppenheimer (BO) approximation[20], which treats nuclear motion as a parameter in the electronic wavefunction rather than as a variable. This separation allows simpler calculations of electronic energy, based on frozen molecular geometries.

Nuclear motion can be treated with the harmonic approximation, which gives vibrational eigenfunctions (ψ_{vib}) and vibrational energies (E_{vib}). For a diatomic molecule,

for example, the vibrational energy of the system as a function of the internuclear distance ($E_0(R)$) is obtained from the harmonic oscillator using the following equation:

$$E_{vib}(v) = hv_e(v + \frac{1}{2}) \qquad \textit{Equation 1.12}$$

In this equation $v = 0, 1, 2, \ldots$ is the vibrational quantum number and v_e is the vibrational frequency. The vibrational frequency can be obtained by calculating the following equation.[3]

$$v_e = \frac{1}{2\pi}\sqrt{\frac{k}{\mu}} \qquad \textit{Equation 1.13}^{3}$$

In this equation, $\mu = \frac{m_1 m_2}{m_1 + m_2}$ is the reduced mass (obtained from the mass of the two atoms, m_1 and m_2) and k is the force constant, which depends directly on the nature of the bond between the two atoms. Rotational features are ignored because the energy separation is too small to be resolved in NEXAFS spectra.[3]

The relative intensity of vibronic transitions is given by their Franck-Condon (FC) overlap.[3] The FC principle (Figure 1.10) treats internuclear distance as a constant during the electronic excitation process. According to the FC principle, in a vertical transition, only those vibrational levels of the excited electronic state (v_f) can be reached if their wavefunctions have a constructive overlap with the lowest vibrational states of the electronic ground state ($v_i = 0$). The FC diagram is presented in the figure 1.10.[3]

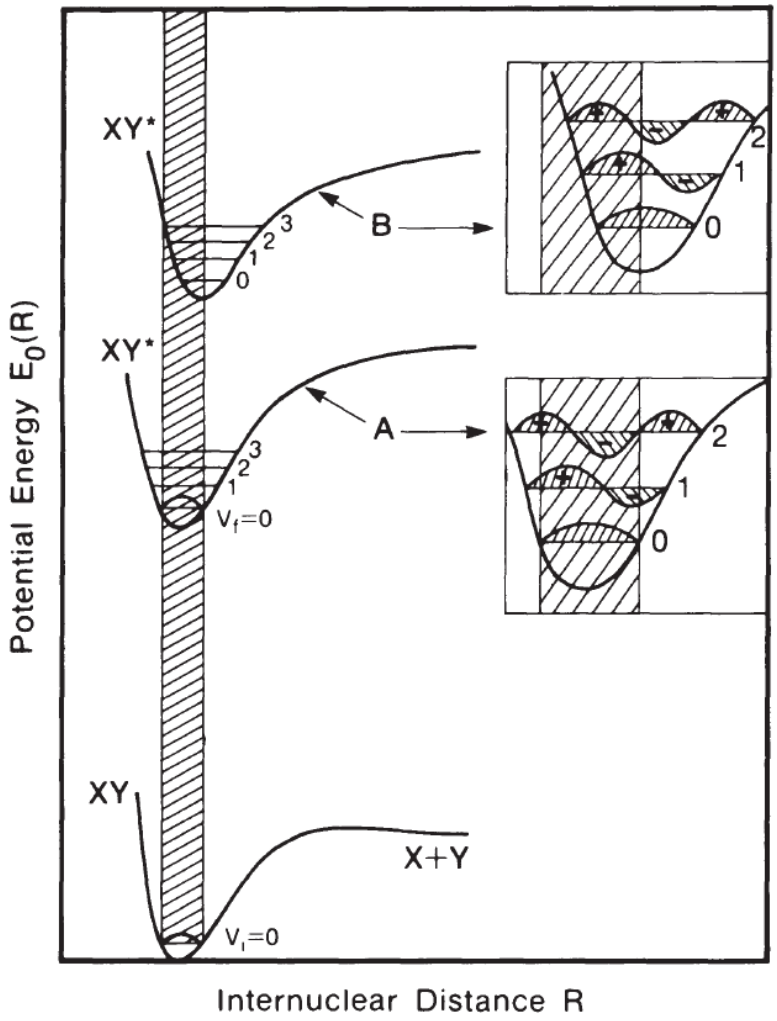

Figure 1.10 - The schematic of the FC principle. Figure is reprinted with permission[3]

In this figure, *XY* represents a hypothetical diatomic molecule in its ground state, and *XY** represents this molecule in various electronically excited states. Potential energy surfaces are presented for the ground state and several hypothetical excited states.[3] The FC overlap with various vibronic states is illustrated.

Figure 1.11 presents an example of vibronic features for the C_2H_6 in comparison with the C_2D_6 from Y. Ma *et al.* [25] The only difference between C_2H_6 and C_2D_6 in the mass of deuterium versus hydrogen. This increased mass of deuterium leads to an increase in the reduced mass of the molecule (Equation 1.13), but there is no change in the force constant of the bond. The mass change affects the vibronic energies.[25] The isotope effect

in vibronic transitions is observed for transitions with a long lifetime and minimal broadening, which includes both Rydberg and low-energy valence transitions.[3]

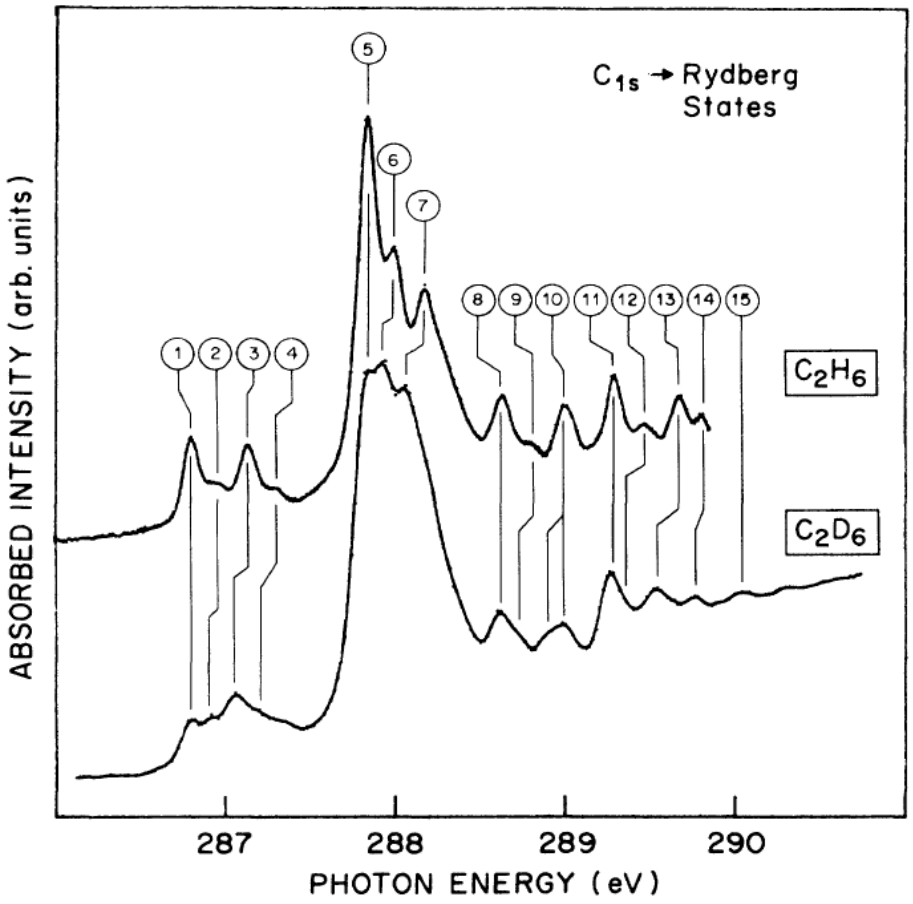

Figure 1.11 - Carbon 1s NEXAFS spectra of C_2H_6 and C_2D_6. Figure is reprinted with permission.[25]

The population of vibrational modes in the electronic ground state is one of the contributors toward nuclear motion and will influence the energy and shape of the NEXAFS spectra of *n*-alkanes. As the temperature increases, the fraction of molecules in a vibrationally excited state will increase. This can change the shape and energy of the peaks in the NEXAFS spectrum, as slightly different molecular geometries are sampled. The effect of the vibrational population in the ground state on the NEXAFS spectra will be discussed in Chapter 6 in detail.

1.2.3 Orientation Sensitivity of NEXAFS Spectroscopy

1.2.3.1 Transition Dipole Moment (TDM)

The TDM is defined as the net linear displacement of charge during any transition and can be calculated using the following equation.[3]

$$\mu_{if} = \langle \psi_i | \mu | \psi_f \rangle \qquad \textit{Equation 1.14}$$

In this equation, μ_{if} is the TDM, ψ_i and ψ_f are the initial and final states, and μ is the electric dipole moment operator, which defines the polarization of the transition according to the following equation.

$$\mu = \mu_x + \mu_y + \mu_z = \sum_i e_i x_i + \sum_i e_i y_i + \sum_i e_i z_i \qquad \textit{Equation 1.15}$$

Where μ_x, μ_y, and μ_z are electric dipole moment operators along the x, y, and z directions, respectively. Also, e_i is the charge on the i^{th} particle and x_i, y_i, z_i are the Cartesian coordinates of the molecule.[3, 22]

1.2.3.2 Intensity of Transitions

The intensity of a specific transition in the NEXAFS spectrum depends on the orientation of the TDM associated with a transition relative to the electric field polarization vector of the X-ray beam. This expression is given by Equation 1.16.

$$I \propto \left| E \cdot \mu_{if} \right|^2 = |E|^2 \left| \mu_{if} \right|^2 cos^2\,\theta \qquad \textit{Equation 1.16}^{3}$$

In this equation, ***E*** is the polarization of the electric field vector of the linearly polarized X-ray beam, and θ is the angle between the ***E*** and μ_{if}. This shows that the intensity of the transition directly depends on the orientation of the TDM, which is a molecular property.[3, 28-29] This relationship is presented in Figure 1.12 for a hypothetical molecule. In this figure, the ***E*** vector of the X-ray beam is in the plane of the paper. The molecule has two electric dipole allowed transitions with TDM of μ_{if1} and μ_{if2} parallel and perpendicular to the ***E***, respectively. As can be observed, when the TDM (μ_{if1}) and ***E*** are parallel ($\theta = 0 \rightarrow \cos^2\theta = 1$), the absorption spectrum has maximum probability of absorption and when the TDM (μ_{if2}) and ***E*** are perpendicular ($\theta = {}^{\pi}/_{2} \rightarrow \cos^2\theta = 0$), no absorption is observed. [29] This effect is called Linear Dichroism (LD).[8, 29]

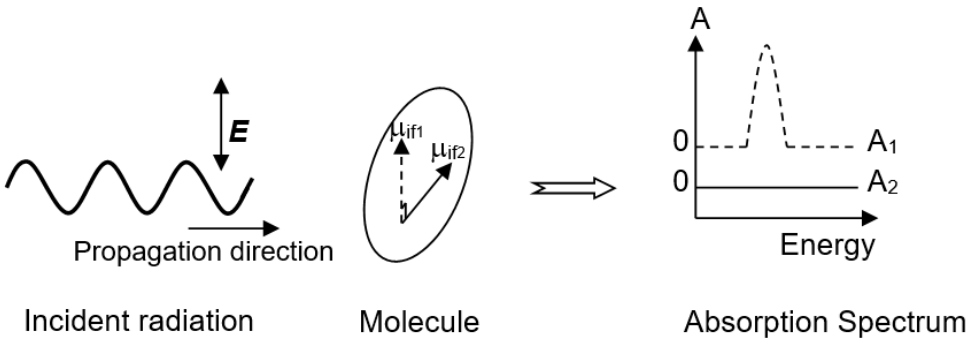

Figure 1.12 - The LD of absorption. Figure is reprinted with permission[29]

Therefore, NEXAFS spectroscopy is sensitive to the orientation of the TDM, which can be mapped onto the molecular geometry. Figure 1.13 presents a schematic of the maximum observable intensity (I_{max}) as a function of the TDM for a linear molecule.[1]

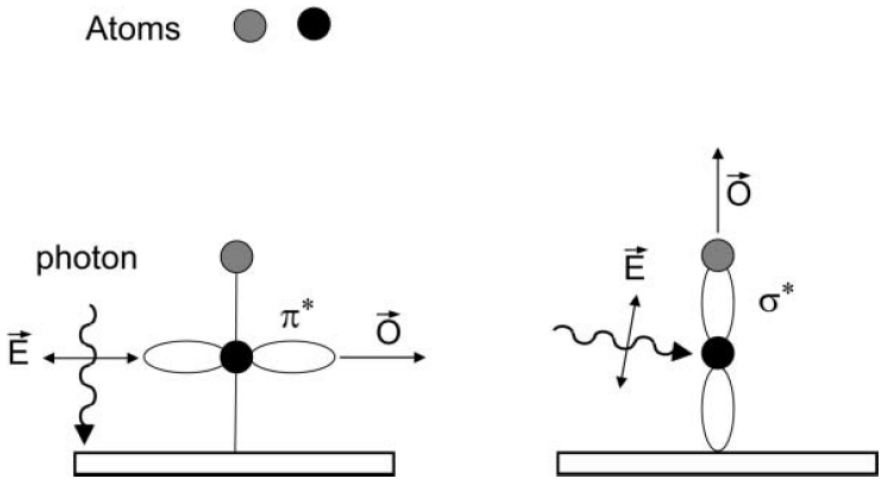

Figure 1.13 - The maximum intensity of the π^* and the σ^* resonances at the normal incident angle(left) and the glancing incidence (right), respectively. Figure is reprinted with permission.[1]

1.2.3.3 Angular Dependence of the Transition Matrix Element

As shown above, the intensity in NEXAFS spectroscopy is related to the angle between the electric field vector and the direction of the molecular orbital (Equation 1.16). The transition intensities depend on the angle of the electric field vector relative to the TDM. This angle can be changed by either rotating the sample or changing the polarization of the X-ray beam.

This sensitivity of NEXAFS spectroscopy to the orientation of *n*-alkanes was examined by J. Fu and S. Urquhart in a study of the LD of linear *n*-alkanes. Figure 1.14 presents the carbon 1s NEXAFS spectra of a well-oriented *n*-hexacontane (*n*-$C_{60}H_{122}$) thin film at two different angles of the X-ray electric field vector with respect to the chain axis.[8]

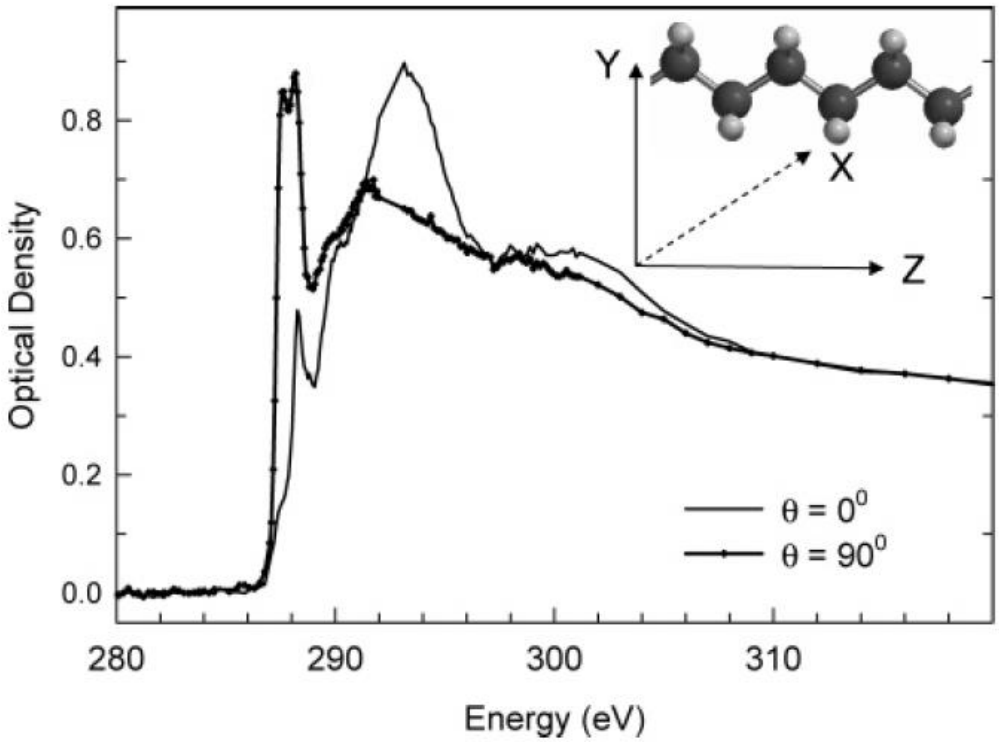

Figure 1.14 - Carbon 1s NEXAFS spectra of n-hexacontane (n-$C_{60}H_{122}$) for the electric field oriented along (solid line) and perpendicular (÷ line) to the macromolecular backbone. Figure is reprinted with permission.[8]

In this figure, the carbon $1s \rightarrow \sigma^*_{C-H}$ transition (~288 eV) has the highest intensity when the electric field vector is perpendicular to the *n*-alkane backbone (e.g., when ***E*** is in the C-H bond plane), The intensity of this transition decreases as the sample is rotated to place ***E*** perpendicular to the C-H bond plane. This is an outcome of the relation shown in equation 1.16. In this case, the carbon $1s \rightarrow \sigma^*_{C-C}$ (~293 eV) transition has the highest intensity, as ***E*** is parallel to the *n*-alkane backbone. The reason for this is because of the TDM for the $1s \rightarrow \sigma^*_{C-C}$ transition is oriented along the backbone of the molecule. This

finding is closely corresponding to the MO model and rejects the building block model for the σ^* TDM in n-alkane molecules.[8]

1.3 Carbon 1s NEXAFS Spectroscopy of *N*-alkanes

Hydrocarbons are among some of the important molecules in chemistry as their chains are common components in many modern materials and as side chains in the polymer P3HT,[5] as well as refractory carbon in soil with relevance to global carbon cycles.[30] Monolayer and multilayer alkanes deposited on various substrates have been studied extensively from the point of the orientation of the deposited alkane,[31-36] the effect of functional groups,[37-38] chain length,[39-40] and crystal structure[33, 41-43] on the properties of thin films. The previous approaches to the experimental and computational carbon 1s NEXAFS spectroscopy of *n*-alkanes will be discussed in this section.

1.3.1 Experimental Carbon 1s NEXAFS Spectroscopy of *N*-alkanes

- **Gas Phase**

The carbon 1s NEXAFS spectra of *n*-alkanes have a surprising complexity, particularly given their chemical simplicity. High-resolution carbon 1s NEXAFS spectra of simple gaseous alkanes such as methane, ethane, and propane are dominated by carbon $1s \rightarrow$ Rydberg transitions with a series of vibronic features.[25, 44] An example of the vibronic features would be the study conducted by Ueda *et al*.[45] on the vibronic features in the carbon 1s excited states of methane (CH_4). The following figure presents the high-resolution carbon 1s NEXAFS spectrum studied by the Ueda *et al*.[45]

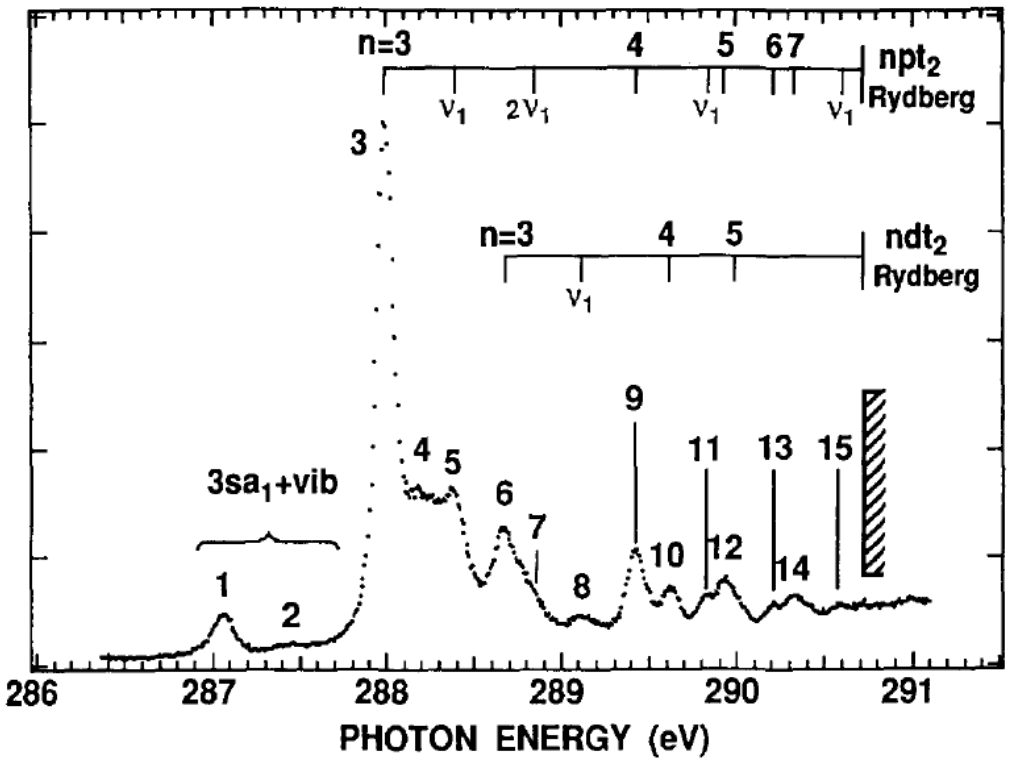

Figure 1.15 - High-resolution carbon 1s electron yield NEXAFS spectrum of methane. Figure is reprinted with permission.[45]

As can be observed, each of the Rydberg transitions in the spectrum of methane shows a few peaks attributed to various vibronic transitions of this molecule. Figure 1.16 presents the carbon 1s NEXAFS spectra of short gaseous alkanes obtained by Urquhart and Gillies.[44]

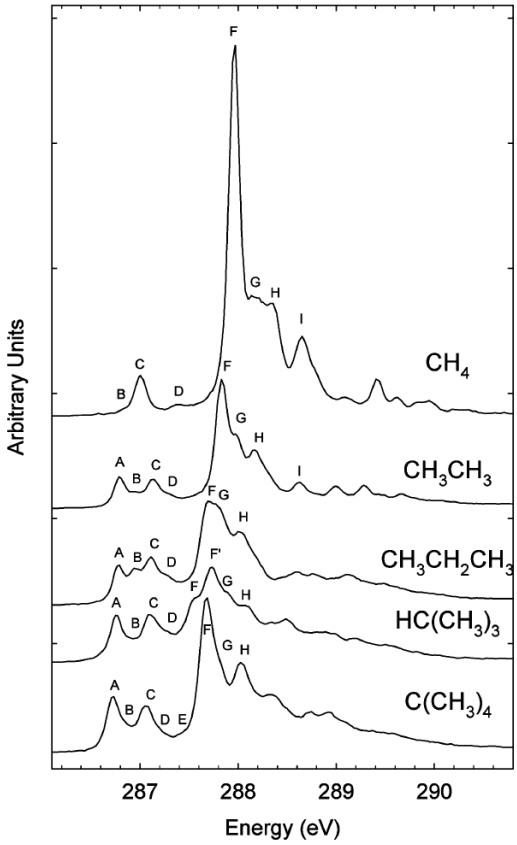

Figure 1.16 - Carbon 1s NEXAFS spectra of methane, ethane, propane, 2-methylpropane, and 2,2-dimethylpropane. Figure is reprinted with permission[44]

Similarly, all of these spectra are dominated by Rydberg peaks with rich vibronic features. As an example, peak A is attributed to the carbon $1s(v=0) \rightarrow 3s(v=0)$ transition (absent by selection rules in methane), and B, C, and D are assigned as vibronic transitions ($1s(v=0) \rightarrow 3s(v=1,2,3)$). Therefore, these features in the carbon 1s NEXAFS spectra of gas phase *n*-alkanes are predominantly Rydberg features.[44] Some Rydberg-valence mixing is observed in the gas phase NEXAFS spectra of alkanes when the energy and symmetry of the Rydberg and σ^*_{C-H} valence orbitals are matched.[44]

Urquhart *et al.*[44] have examined the degree of Rydberg-valence mixing for methane, ethane, propane, butane, 2-methylpropane, and 2,2-dimethylpropane. The authors have observed a larger valence character for the 3s states relative to the 3p states since the energy and symmetry of the 3s and σ^*_{C-H} orbitals are more similar. The authors have shown that in the case of hydrocarbons, the degree of Rydberg / σ^*_{C-H} mixing is

proportional to the number of C-H bonds to the core excited carbon atom.[44] The energy difference between the calculated singlet and triplet excited state, ΔE(S-T), is a useful proxy for the Rydberg character in the computational studies. In the Improved Virtual Orbital (IVO) calculations (Section 3.5.7.1) a singlet-triplet energy difference of less than 0.05 eV indicates 'pure' Rydberg character as the electron excited into the Rydberg orbitals will have less interaction with the rest of electrons, in comparison with an electron that is excited into a valence orbital which is closer to the rest of the molecule.[8, 45]

- **Condensed Phase**

Carbon 1s NEXAFS spectra of the solid phase *n*-alkanes show a double peak in the pre-edge region (~288 eV) that is called the C-H band and is the characteristic feature of these spectra. The interpretation of this characteristic feature in the carbon 1s NEXAFS spectra of the solid phase alkanes is a point of discussion among researchers.[22, 46-49] The double peak (carbon $1s \rightarrow \sigma^*_{C-H}$) is presented at Figure 1.17-(b).[22]

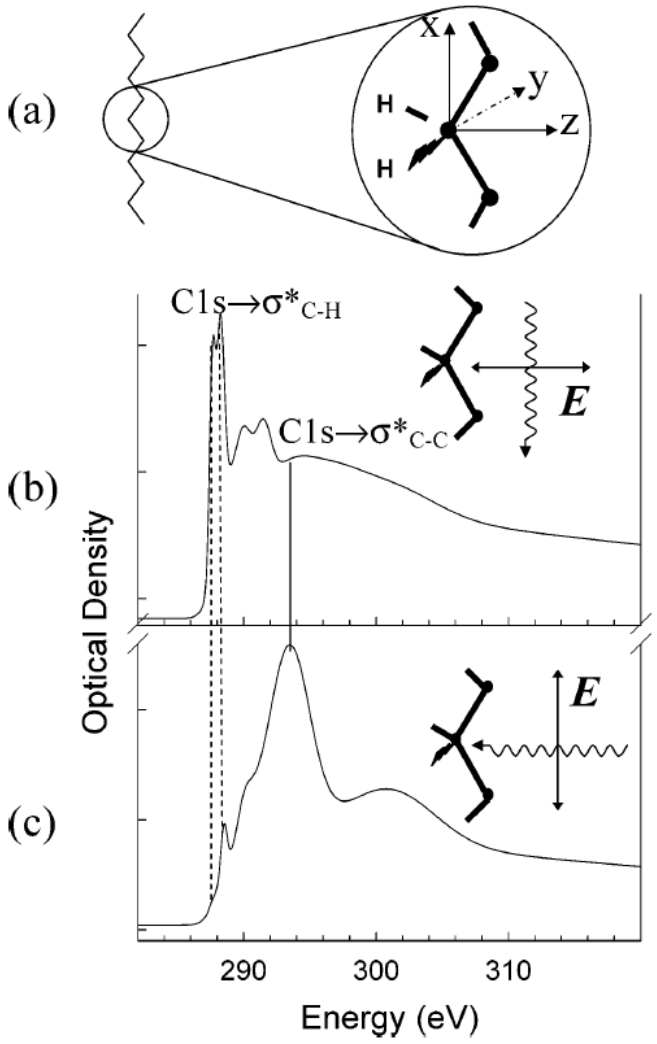

Figure 1.17 - (a) Schematic of the geometry of a carbon atom in a linear alkane, carbon 1s NEXAFS spectrum of n-$C_{60}H_{122}$ when the electric field vector is (b) perpendicular and (c) parallel to the backbone of the molecule. Figure is reprinted with permission.[22]

As can be observed, when the electric field vector (***E***) is parallel to the backbone of the molecule, the maximum intensity occurs for the carbon 1s→ σ^*_{C-C}. For the ***E*** perpendicular to the backbone of the molecule, the maximum intensity occurs for the carbon 1s→ σ^*_{C-H} forming the characteristic double peak in the carbon 1s NEXAFS spectra of alkanes, also known as the C-H band.[22, 50] Endo *et al.*[42] have studied the orientation of *n*-alkanes deposited on graphite and characterized the two components in the C-H band region. These low energy and high energy components in the C-H band are assigned as carbon 1s à $\sigma^*_{CH}/R_{\parallel}$ and carbon 1s à $\sigma^*_{CH}/R_{\perp}$ transitions, respectively.

The *R* in this notation represents the Rydberg character indicating the mixture of Rydberg and valence character at the C-H band. The parallel and perpendicular indices represent the direction of the TDM of the beam against the 'C-C-C' backbone of the molecule.[42]

The nature of NEXAFS transitions in condensed alkanes has been controversial.[47, 50-51] M. Robin[51] proposed that low energy features in the carbon 1s NEXAFS spectra of the condensed alkanes are dominated by Rydberg transitions, which are broadened and shifted to the higher energy compared to the spectra of the gas phase. The overlap of the Rydberg orbitals with the σ^* antibonding valence orbitals is discussed to have an effect on the energy of the spectra as well as the origin of the double peak in the carbon 1s NEXAFS spectra of solid *n*-alkanes.

Stöhr *et al.*[50] have studied the carbon 1s NEXAFS spectra of solid polyethylene and concluded that the double peak in the spectra of alkanes has a valence character and can be described as carbon $1s \rightarrow \sigma^*_{C-H}$ transitions. Figure 1.18 presents the carbon 1s NEXAFS spectra of highly oriented polyethylene for two orientations of the electric field vector against the chain direction.[50]

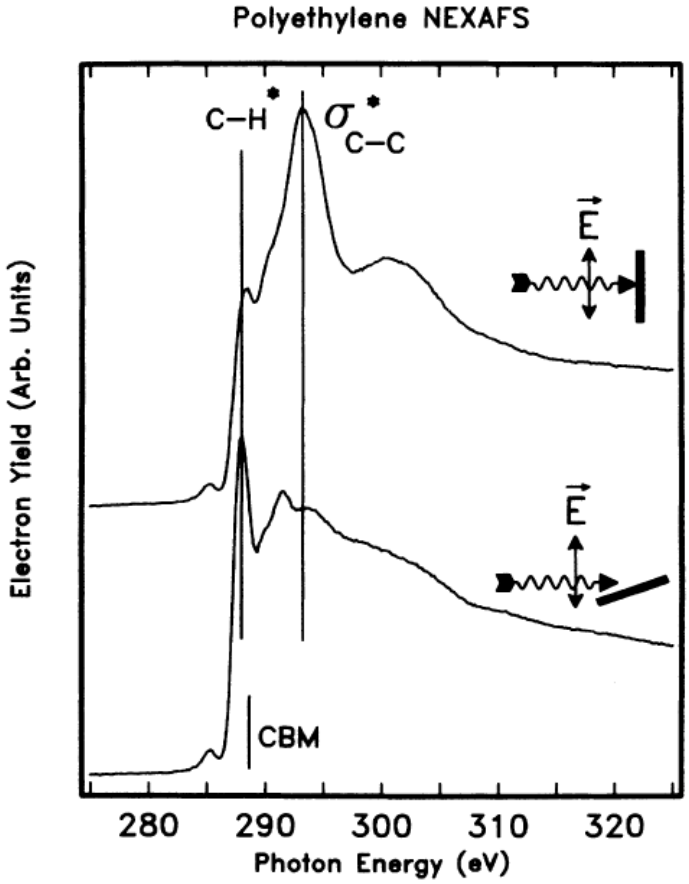

Figure 1.18 - Carbon 1s NEXAFS spectra of polyethylene for the electric field vector parallel and nearly perpendicular to the chain direction. Figure is reprinted with permission.[50]

Schöll *et al.*[49] explored the pre-edge features in the ordered solid alkanes and concluded that there features are dominated by valence character.

Bagus *et al*.[47] used experimental and computational measurements to argue that even though the Rydberg features are partially attenuated in the condensed phase, the transitions that occur at 286-288 eV maintain their predominantly Rydberg character in the solid phase. The authors used *ab initio* calculations of an isolated small molecule (propane) to model solid-state behavior. However, as the isolated propane molecule is not a good representative of the solid-state, it cannot consider intermolecular interactions. Without considering these intermolecular interactions, it is not possible to comment on the changes to the transitions that take place in the condensed phase.[47] Weiss *et al*.[48] have further developed their approach using small clusters of propane. However, as the

size of the cluster is smaller than the radius of the Rydberg orbitals in the condensed phase, some parts of the Rydberg orbitals will still be in the vacuum. This leads to a mixed cluster/vacuum around the Rydberg orbitals and might not properly model the carbon 1s NEXAFS spectra of the condensed phase. The mixed cluster/vacuum environment and its effect on the calculated carbon 1s NEXAFS spectrum was studied for small clusters of propane in neon by Urquhart *et al.*[52] The authors have designed a model comparing the computational spectra of an isolated molecule of propane with a molecule of propane embedded in clusters of neon atoms with various sizes. The authors have concluded that a computational model of the cluster is not useful if it cannot reproduce the Rydberg character for the isolated molecule. Also, Rydberg states are extended into the vacuum for small clusters and, therefore, only clusters larger than the Rydberg orbitals will be able to reproduce the condensed phase spectra. Authors have also concluded that the predominantly Rydberg features in the spectra of gas phase alkanes will change to a mixture of Rydberg and valence character in the spectra of the condensed phase alkanes.[52]

Perera *et al*.[41] have studied LD in the carbon 1s NEXAFS spectra of *n*-$C_{28}H_{58}$, *n*-$C_{32}H_{66}$, and *n*-$C_{40}H_{82}$ for both orthorhombic and monoclinic crystal structures. The authors have observed a high energy shoulder in the C-H band for the monoclinic structure in comparison with the orthorhombic structure; This is also observed in Fu *et al.*,[22] which is presented in Figure 1.17(c). This peak is observed when the polarization component is directed along the molecule's backbone. (Figure 1.19), it shows the effect of crystal structure on the carbon 1s NEXAFS spectra of *n*-alkanes.[41]

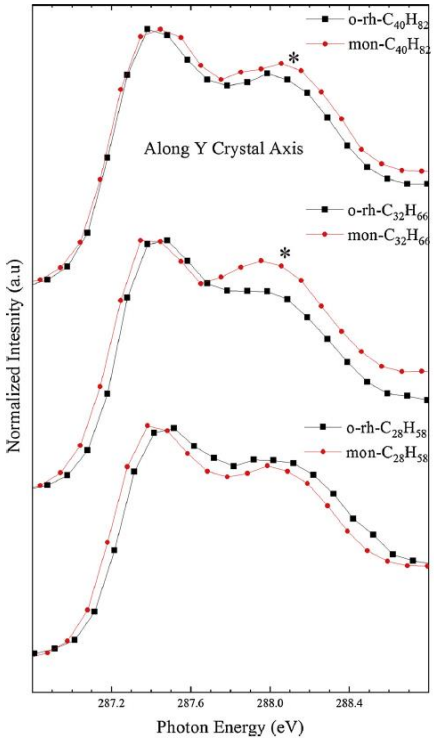

Figure 1.19 - Carbon 1s NEXAFS spectra of the "C-H" band of three n-alkanes with orthorhombic (black) and monoclinic (red) crystal structure. Figure is reprinted with permission.[41]

A phase change will influence the nuclear motion as well as the intermolecular interactions since the order of molecules and their interactions are changing. Other changes such as the degree of crystallinity, branching ratio (in case of polymers), and chain length will also affect the carbon 1s NEXAFS spectra of *n*-alkanes.[41, 49, 53] Schöll *et al*.[49] have studied the effect of chain length, branching ratio, and crystallinity on the carbon 1s NEXAFS spectra of ethylene-1-alkene copolymers. As can be observed in Figure 1.20, melting of solid polyethylene samples will change the NEXAFS spectra significantly.[49]

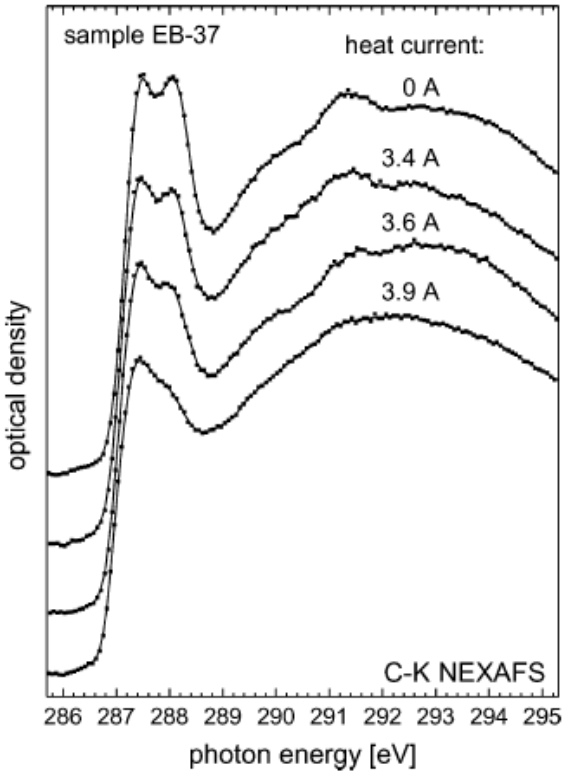

Figure 1.20 - Carbon 1s NEXAFS of heated polybutene. Figure is reprinted with permission[49]

The authors have observed that, as the sample melts, the degree of crystallinity will decrease, and this will change the carbon 1s NEXAFS spectra significantly. This change can be observed in the form of the disappearance of the double peak as the sample melts, as shown in Figure 1.20. Authors have also studied the effect of density on the carbon 1s NEXAFS spectra by varying frequency and length of the crosslinkers in the polymers. This effect is observed in the form of a change from the doublet C-H band to a broad single peak with an increase in the branching ratio and the length of branches. The broadening is observed as for the σ^*_{C-C} region as well.[49] The effect of intermolecular distance on the carbon 1s NEXAFS spectra of two butene dimers in parallel and perpendicular configurations was also studied by the authors using *ab initio* calculations. Figure 1.21 shows the calculated spectra for two butene dimers calculated by Schöll *et al*.[49] The authors have concluded that a decrease in the intermolecular distance will shift the C-H band transitions to higher energy and will have a significant effect on the intensity of various transitions.[49] However, the small butene model does not present all the

transitions in the alkanes as it does not reproduce the transitions coming from the inner CH_2 groups (two carbons into the chain).

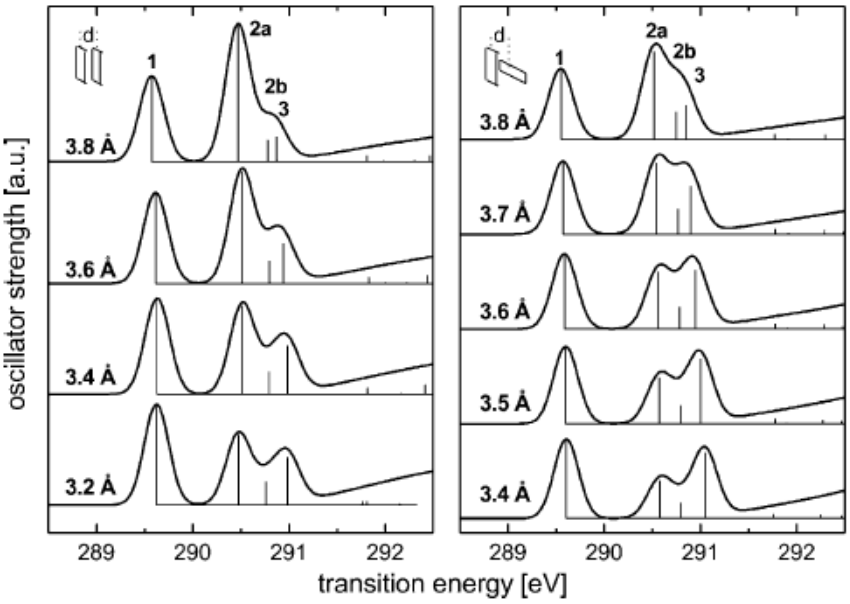

Figure 1.21 - Calculated spectra for two butene dimers (parallel and perpendicular) in various intermolecular distances. Figure is reprinted with permission[49]

The crystal phase, chain length, and parity of alkanes could affect the transitions significantly. Swaraj and Ade[53] studied the carbon 1s NEXAFS spectra of *n*-alkanes as a function of the *n*-alkane chain length and the parity of the carbon backbone. They proposed that while the parity of the carbon backbone changes the carbon 1s NEXAFS spectra of *n*-alkanes, the chain length does not play an important role in the formation of the transitions in the spectra.[53] However, this work did not explicitly consider the crystal polymorphism of the *n*-alkane crystals.

A change from the condensed phase to the gas phase will lead to an increase in the nuclear motion as molecules have more freedom to move. These changes in the nuclear motion and intermolecular interactions will change the spectra significantly. Urquhart *et al*.[52] examined the effect of phase change on the carbon 1s NEXAFS spectra of 2,2-dimethylpropane (neopentane). Figure 1.22 presents the change in the carbon 1s NEXAFS spectra of 2,2-dimethypropane with the change from the gas phase to the solid phase.[52]

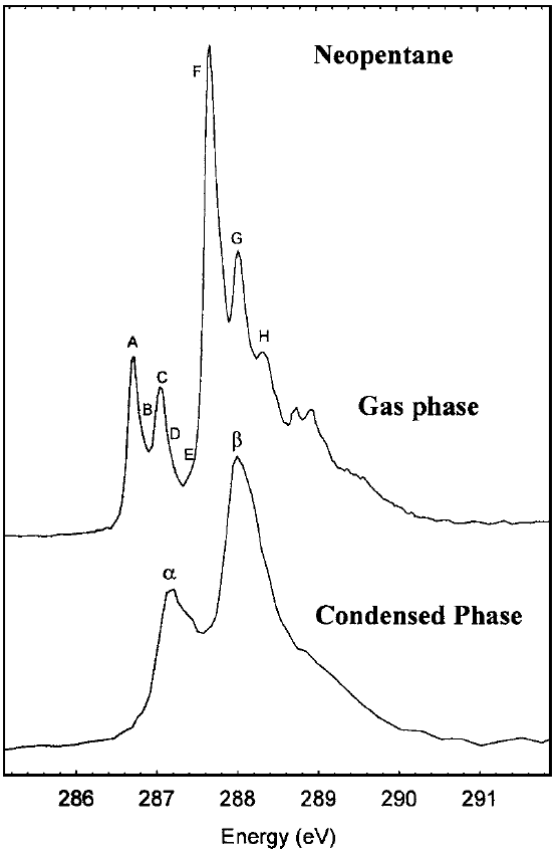

Figure 1.22 - Carbon 1s NEXAFS spectrum of 2,2-dimethylpropane(neopentane) in the gas phase and the condensed phase obtained by Total Electron Yield (TEY) detection. Figure is reprinted with permission[52]

In this study, the carbon 1s NEXAFS spectra of gas-phase and solid-phase 2,2-dimethypropane are obtained at the same time. This measurement shows many sharp features in the 286 - 289 eV region for the gas phase NEXAFS spectrum. These features are shifted to higher energy and reduced to only two broad peaks in the solid 2,2-dimethypropane NEXAFS spectrum. The authors also observed that the phase change from gas to condensed leads to broadening and quenching of the Rydberg features.[52] They have concluded that the intermolecular interactions play an important role in the carbon 1s NEXAFS spectra of the molecule. It is concluded that while the gas phase spectra are predominantly Rydberg, in the condensed phase, the degree of valence character increases substantially.[52] The authors have concluded that condensation in alkanes will change the degree of Rydberg-valence mixing. These authors designed a model of propane molecules in a neon cluster to calculate the carbon 1s NEXAFS spectra

in the condensed phase. Although the experimental shift to the higher energy from the isolated molecule to the cluster is observed for the model of propane in the neon cluster, it does not represent the intermolecular environment provided by neighboring alkanes. However, this model was what was feasible at the time.[52]

Because of the complexity of models vs. computational cost, modeling the Rydberg features vs. Rydberg-valence mixing is a challenge. Most of the computational studies have been focused on isolated molecules in their lowest geometries or used small molecules such as propane in a cluster of neon as a representative of the condensed phase. The issue is that short chains will not reproduce all the effects in the condensed phase. Also, a comprehensive study about the effect of structural variations on the carbon 1s NEXAFS of *n*-alkanes is not yet been done. Therefore, modeling carbon 1s NEXAFS spectra of longer chain *n*-alkanes in the solid phase, to understand the observed variation in the spectra compared to the gas phase is one of the objectives of this study.

1.3.2 Effect of Nuclear Motion on NEXAFS Spectra

The contributions of thermally populated vibrations, zero-point motion, and various conformations to the NEXAFS spectra of molecules in a given temperature[54-55] are known as nuclear motion effects. The final spectrum of a given molecule is an average of the spectra of that molecule in all the modes, including various conformations, vibrations, and other motions. (see chapter 6).

In the discussion of the nuclear motions, it should be noted that only in a perfect crystal at absolute zero (or in a computational study of a static, lowest energy geometry) the molecule will exist in global minimum energy. Various defects and constant motions will exist in any material, and a sample will never be in global minimum energy, but rather in a series of thermally accessible configurations. Depending on the temperature, the population of molecules in the defect states or vibrationally excited states could change, and this contributes to the broadening of the spectra.

An increase in the temperature will increase the kinetic energy of the molecule and, subsequently, the nuclear motion of atoms in the molecule. This will also increase the number of molecules in the thermally populated vibrational states. The effect of

temperature changes on the NEXAFS spectra of water was studied by Pettersson group[56] using MD-DFT spectra calculations. The authors have also compared the computational results with the experimental spectra in various temperatures. Figure 1.23 presents the experimental NEXAFS spectra measurement of liquid water obtained using the transmission detection method.[56]

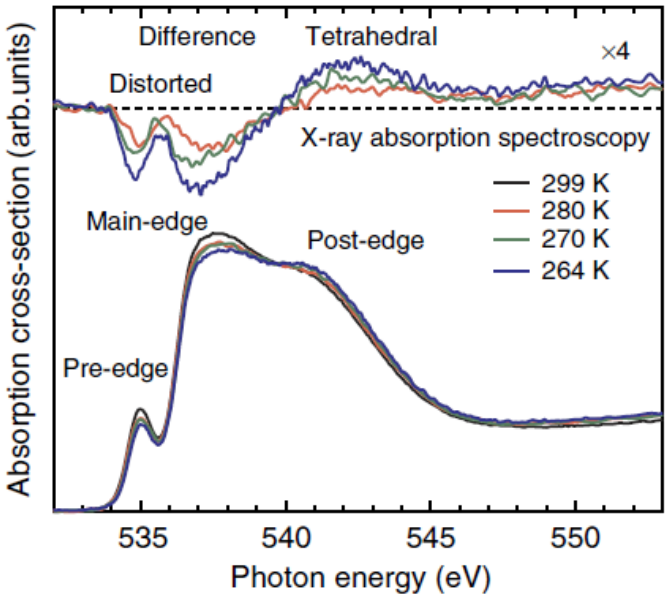

Figure 1.23 – Oxygen 1s NEXAFS spectrum of liquid and supercooled liquid water. Figure is reprinted with permission[56]

As can be observed, an increase in the temperature of the water has changed the intensity of the peaks but not their position. The authors observe that the post-edge peaks (which are associated with strong H-bonds) will lose their intensity relative to the pre-edge peaks (distorted H-bonds) as the temperature increases.[56]

In another study, the same group used the MD-DFT approach to study the oxygen 1s NEXAFS spectra of bulk liquid water considering the nuclear motions.[57] In this approach, these authors have used MD simulations to obtain many snapshots containing various geometries of the cluster in equilibrium. These snapshots are then used to calculate the NEXAFS spectra of water. Figure 1.24 presents the final spectra of 1326 snapshots on a water cluster containing 39 molecules of water. 15 spectra from randomly selected snapshots are also presented in this figure.[57]

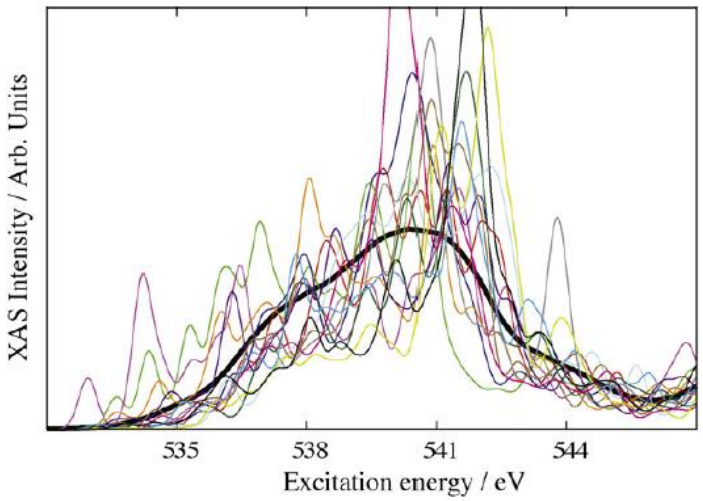

Figure 1.24 - The summed spectrum (black line) of 1326 spectra obtained using the MD-DFT approach. Figure is reprinted with permission[57]

The final spectrum is broad and shows less features compared to the individual computational spectra. This is because the sum spectrum contains many possible geometries that happen experimentally. The selected individual spectrum are a good example of changes in the spectra because of the nuclear motions of the molecules in the liquid.

The effect of nuclear motions on the nitrogen 1s NEXAFS spectra of amino acids and their residue molecules was also explored by the Prendergast research group[54] using MD-DFT calculations. Figure 1.25 presents the experimental nitrogen 1s NEXAFS spectra of *s*-triazine molecule compared with the computational spectra obtained using fixed nuclei, classical MD simulations, and Path Integral Molecular Dynamics Simulations (PIMD) approaches.

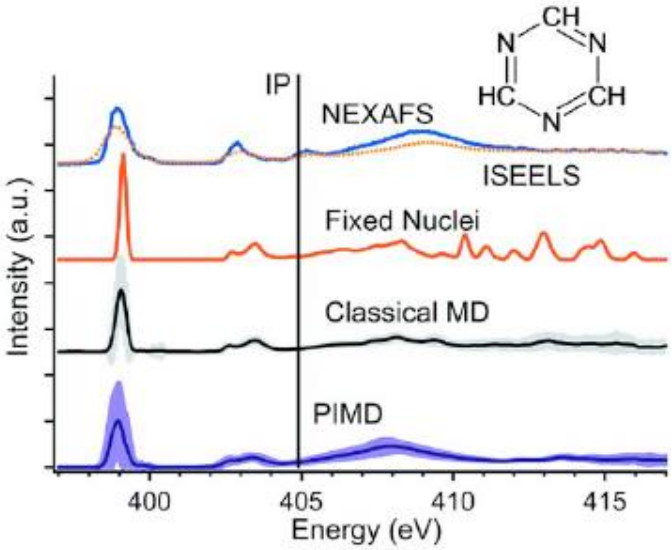

Figure 1.25 - Experimental and computational nitrogen 1s NEXAFS spectra of s-triazine. Figure is reprinted with permission[54]

Both classical MD and PIMD simulations consider nuclear motions, and this leads to a similarity between the calculated spectra and the experimental measurements. The fixed nuclei spectra only show the contributions from electronic transitions without nuclear motion broadening. This is the main reason that the resulted spectra from this method are much narrower than the experimental spectra. The following figure presents the calculated nitrogen 1s NEXAFS spectra of solid glycine at various temperatures using classical MD simulations coupled with the DFT spectra calculations performed by Schwartz *et al.*[58]

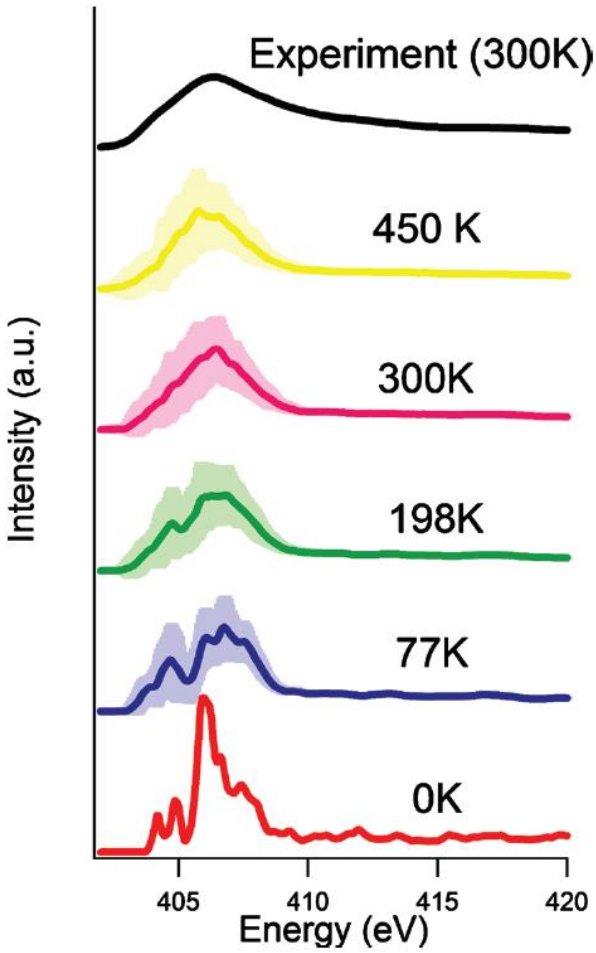

Figure 1.26 - Calculated N 1s edge spectra of solid glycine at various temperatures. Figure is reprinted with permission.[58]

As can be observed, as the temperature increases, the sharp peaks will start to broaden and converge into a single broad peak. This is due to the increase in nuclear motion as the temperature increases. This shows the effect of nuclear motion on the NEXAFS spectra of various molecules.

Effects such as zero-point motion are not calculated in the classical MD simulations. The PIMD simulation[59] is one of the approaches to take these effects into consideration. This approach uses the Feynman Path-Integral formulation of Quantum Mechanics (QM)[55] to incorporate an approximate treatment for the non-electronic part of the problem. This means that PIMD can be used to incorporate the effect of finite temperature and QM properties of the nuclear into the calculation, which means the effect of zero-point motions and quantum tunneling will be included in the calculations.[54, 59]

Using the combination of MD simulations with the DFT based NEXAFS calculation, it will be possible to calculate the effect of nuclear motion on the calculated NEXAFS spectra of *n*-alkanes. This will help replicate the experimental spectra using calculations.

1.4 Research Objectives

An understanding of the spectra of simple species such as *n*-alkanes will allow researchers to examine effects that will be obscured in larger molecules and may help us understand complex spectroscopic phenomena. Therefore, the objective of this research is to understand the effect of structural variations in *n*-alkanes on their carbon 1s NEXAFS spectra. Linear *n*-alkanes are selected as the molecules to be studied in this thesis because of their relatively simple structures. The interpretations of these results can be used to study more complicated molecules and molecules in different physical states.

As explained in the previous sections, the nature of core excited states in the carbon 1s NEXAFS spectra of *n*-alkanes are not well understood. Modeling Rydberg orbitals as well as Rydberg-valence mixing is difficult since there is a trade-off between the size of the model and the computational cost. This means that an increase in the size of the model will improve the calculated spectra but also increase the computational cost significantly. Most of the models in the literature are either focused on the isolated molecules or small molecules such as propane in a cluster. Isolated molecules cannot reproduce the intermolecular interactions and are not a good representative of the solid phase. For a cluster to act as a model of the solid state, the size of the cluster must be large enough to contain the Rydberg orbitals within the cluster. In such a model, the spectra calculation is performed on the central molecule since it has the maximum distance from the borders of the cluster. However, an increase in the size of the cluster will increase the computational cost significantly.

The carbon 1s NEXAFS spectra of *n*-alkanes are well explored for the gas phase[17, 44, 60], and the solid phase.[52-53, 61] The carbon 1s NEXAFS spectra of the liquid phase is entirely unexplored. Molecules are dynamic in the liquid phase, constantly undergoing various structural changes such as reptation. These changes are categorized as various types of nuclear motions. This includes geometry defects (gauche defects), thermally

populated vibrational states, and the zero-point motions. The effects of nuclear motions in liquids can give a distribution of thermally accessible molecular structures rather than a single “lowest energy” structure. Characterizing the effect of nuclear motions on the spectra of *n*-alkanes through experimental measurements, as well as computational modeling, could help understand the complicated NEXAFS spectra of these simple molecules.

Therefore, a comprehensive study to understand how structural variations will affect the carbon 1s NEXAFS spectra of *n*-alkanes helps shed some light on the ambiguous area in the field. This includes obtaining the carbon 1s NEXAFS spectra of liquid *n*-alkanes as well as designing and studying various computational models to characterize the effect of nuclear motions on the NEXAFS spectra of *n*-alkanes. These objectives are explained in detail in the following sections.

1.4.1 Effect of Structural Differences in Solid Phase *N*-alkanes on their NEXAFS Spectra

The first objective of this study is to examine the effect of structural differences in *n*-alkanes on their carbon 1s NEXAFS spectra. This includes taking steps to gain a better understanding of the nature of the core-excited states in *n*-alkanes. The effect of structural variations, such as chain length, on the carbon 1s NEXAFS spectra of *n*-alkanes, is not well explored. This is mainly because the computational models have not been successful in fully reproducing the changes in the carbon 1s NEXAFS spectra as a function of structural changes.[49, 62]

As discussed in the previous section, quenching of Rydberg orbitals, the emergence of valence character, and a shift to the higher energy are observed when the physical phase is changed from the gas phase to the condensed phase.[8, 52] For *n*-alkanes, Rydberg mixing with the C-H character valence orbitals has a direct correlation with the number of hydrogen atoms directly bonded to the core excited carbon atom. The role of chain length on the Rydberg-valence mixing in the carbon 1s NEXAFS spectra of *n*-alkanes has not been well explored. Therefore, the main focus of this objective is to study the effect of chain length on the carbon 1s NEXAFS spectra of *n*-alkanes and also to establish a methodology to study the Rydberg-valence mixing of molecules using DFT.

Chapter 4 discusses the development of various cluster sizes using an orthorhombic structure of *n*-pentane as a model, and the DFT approach to obtain the spectra of these clusters. However, because of various reasons such as computational cost, this work was abandoned, in order to focus on more productive avenues of work.

Studying the effect of chain length on the carbon 1s NEXAFS spectra of *n*-alkanes would fit in the overall goal of understanding how the structural differences could affect the NEXAFS spectra of *n*-alkanes. In the discussion of Rydberg and valence character in the carbon 1s NEXAFS spectra of hydrocarbons, the role of chain length and chain length effects has largely been ignored. The role of chain length – either as an 'averaging' phenomena (of the different atomic sites in an *n*-alkane molecule) or as an electronic change with chain length – has not been explicitly explored. Simple calculations of longer hydrocarbons have often focused on simple molecules (propane,[47] butane,[49, 63] *n*-hexane,[64], etc.), or where a single CH_2 group in the centre of a longer hydrocarbon is used to simulate the average hydrocarbon spectrum.[8]

Using the DFT approach with the high-performance computing resources and scripting, we will be able to explore and study many molecules in a short time. The angle integrated spectra compared with the angle-resolved spectra would also shed light on the effect of structural variations on the NEXAFS spectra, especially if they are studied as a function of the chain length of *n*-alkanes. The results of this part of the research are explained in detail in chapter 5 – The effect of chain length on the NEXAFS spectra of *n*-alkanes.

1.4.2 Understand the Role of Disorder on the NEXAFS Spectra of *N*-alkanes

The second objective of this study is to examine the role of disorder on the NEXAFS spectra of *n*-alkanes. Structural disorder in this context is referred to variations such as gauche defects, thermally populated vibrations, and molecular motions (e.g., in the liquid phase). This objective is studied through experimental NEXAFS spectroscopy of liquids *n*-alkanes as well as various computational models to study the effect of gauche defects, vibrations, and nuclear motions on the NEXAFS spectra. Various approaches to

understand the role of disorder on the NEXAFS spectra of *n*-alkanes are explained in the following sections.

- **Effect of Gauche Defects on the NEXAFS Spectra of Linear *N*-alkanes**

Gauche defects are defined as the rotations about the individual C-C bonds distorting the *n*-alkane from the lowest energy geometry. Basson *et al*.[65] have observed the thermally populated gauche defects below the melting point for solid *n*-alkanes of length 28 (*n*-$C_{28}H_{58}$). This defect was observed well below the characteristic temperature of the solid phase transition. Only a small energy is required to bend an extended chain into a bent chain with single or multiple gauche defects resulting in various defect structures. Some of these structures (particularly the hairpin structure) could be more stable than the all-trans structure in the case of longer chains.[65-66] With increasing the chain length, at some point, the self-solvation between the two aligned chains will win over the defect formation energy. This turning point is experimentally unknown yet, but several computational attempts have been carried out to predict the maximum chain length with the all-trans global minimum. The calculated chain length with the all-trans as the global minimum is different based on the computational approach and varying from *n*-$C_{11}H_{24}$, *n*-$C_{17}H_{36}$, *n*-$C_{21}H_{44}$, *n*-$C_{25}H_{52}$, and *n*-$C_{59}H_{120}$.[67] Figure 1.27 shows some of the possible structures of *n*-alkanes.

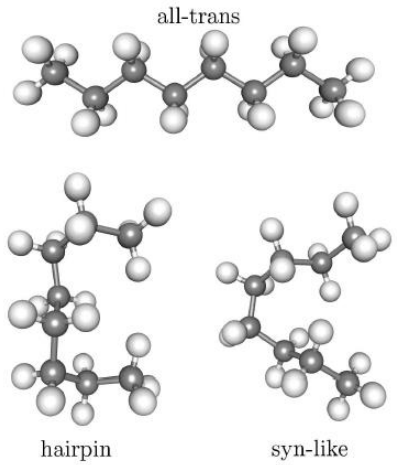

Figure 1.27 - All-trans, hairpin, and syn-like structures of n-alkanes. Figure is reprinted with permission.[66]

Liquid *n*-alkanes are not expected to be all-trans but have a distribution of geometries because of their constant motions and reptation. So, in this study, using the computational measurements, the effect of the gauche defect on the NEXAFS spectra of *n*-alkanes will be explored to find the changes in the energy and shape of various transitions in the spectra. This computational study is performed on selected *n*-alkanes using DFT as well as MD-DFT approaches. The results of this work are explained in detail in Chapter 6 – Temperature dependence in NEXAFS spectra of *n*-alkanes.

- **Effect of Thermally Populated Vibrations on the NEXAFS Spectra of *N*-alkanes**

The Pendergast group[54, 68] have examined the effect of nuclear motions on the NEXAFS spectra of amino acids and predicted that zero-point motion and thermally excited vibrational modes contribute to the shape of NEXAFS spectra. Therefore, as part of the second objective, the effect of thermally populated vibrations on the NEXAFS spectra of *n*-alkanes has been studied using computational modeling. Many forms of motion, including zero-point motion and thermally populated vibrations, contribute to the "nuclear motion effect" in the NEXAFS spectra of *n*-alkanes. Zero-point motions are expected to contribute to all temperatures, while the Boltzmann distribution of molecules in the thermally populated vibrational modes will increase with the increase in the temperature of the sample. Both zero-point motions and thermally populated vibrations contribute to the shape of the NEXAFS spectra. These effects can be simulated using MD simulations. The Pendergast group[54, 68] have studied these effects by comparing the DFT spectra of molecules in their lowest geometry with the snapshots from the MD simulations. The authors have concluded that the zero-point motion and thermally populated vibrational states can contribute to the NEXAFS spectra. The MD-DFT simulation results have shown that the origin of temperature broadening is the vibrational modes.[54, 58, 68] An increase in the chain length is expected to lead to a significant increase in the number of thermally populated vibrations. This will lead to the broadening of the spectra.

Studying the effect of thermally populated vibrations on the NEXAFS spectra of *n*-alkanes helps understand the spectra of *n*-alkanes better. As the nuclear motion leads to

variations in the structures, studying their effect on the NEXAFS spectra fits in the first objective if this research which is to study the effect of structural diversity on the NEXAFS spectra of *n*-alkanes. Using DFT as well as MD-DFT approaches, the effect of thermally populated vibrations on the NEXAFS spectra is studied for several selected *n*-alkanes. These calculations are carried out in various temperatures, so the same effect is also studied as a function of temperature changes. The results of this work are explained in detail in Chapter 6 – Temperature dependence in NEXAFS spectra of *n*-alkanes.

- **NEXAFS Spectroscopy of Liquid *N*-alkanes**

Another part of the second objective of this thesis is to study the effect of nuclear motions on the NEXAFS spectra of *n*-alkanes. NEXAFS is sensitive to features such as atomic number, the orientation of the molecule, and the physical state of the material. In the case of *n*-alkanes, NEXAFS spectra of the gas phase and the solid phase are well explored.[8-9, 22, 44, 52, 69-71] The liquid phase is almost entirely unexplored. In the liquid phase, molecules have some degree of freedom compared to the solid phase and yet limited in movements compared to the gas phase. This leads to multiple bond rotations known as gauche defects and various entanglements, especially in longer chain *n*-alkanes. Because of the sensitivity of NEXAFS to the molecular orientations and molecular interactions, any small change in the environment could lead to a change in the spectra.

Therefore, studying the NEXAFS spectra of *n*-alkanes in the liquid phase could help to fill the gap between the gas phase and the solid phase. These results could be used to obtain a better understanding of the effect of various changes such as chain length, physical phase, nuclear motions, and entanglements on the NEXAFS spectra. The carbon 1s NEXAFS spectra of liquid *n*-C_6H_{14}, *n*-$C_{12}H_{26}$, *n*-$C_{13}H_{28}$, *n*-$C_{14}H_{30}$, *n*-$C_{15}H_{32}$, and *n*-$C_{16}H_{34}$ are obtained using the transmission technique in the Scanning Transmission X-ray Microscope (STXM) end station at Canadian Light Source (CLS). The effect of chain length on the spectra has been investigated. The experimental methods and tools to obtain the carbon 1s NEXAFS spectra of liquid *n*-alkanes are explained in detail in Chapter 7 – NEXAFS spectroscopy of liquid *n*-alkanes.

1.5 Outline of Thesis Chapters

Chapter Two will discuss the experimental approaches used, including the liquid *n*-alkane sample preparation, measurement techniques, and detection modes for the NEXAFS spectroscopy measurements of liquid *n*-alkanes. **Chapter Three** will discuss the computational approaches used in this research. Specifically, DFT, TP-DFT, and MD-DFT approaches will be discussed in detail. The models developed for each computational study will also be discussed in chapter three. This includes the orthorhombic cluster, the chain length model, the gauche defect model, the thermally populated vibrations model, the temperature-dependent model, and the MD-DFT models for the chain length and temperature dependence studies. **Chapter Four** will discuss the model development for the orthorhombic cluster of *n*-pentane and the attempts to obtain the NEXAFS spectra of these clusters to understand the effect of Rydberg-valence mixing and the effect on structural changes on the NEXAFS spectra of solid *n*-alkanes. **Chapter Five** will review the effect of chain length on the NEXAFS spectra of *n*-alkanes using a computational approach. The effect of chain length on the spectra is studied for *n*-alkanes from C_3H_8 to *n*-$C_{40}H_{82}$. The angle-dependent and angle-resolved spectra are also studied for the same set of molecules. In **Chapter Six**, the temperature dependence NEXAFS spectra of *n*-alkanes will be discussed. Both experimental and computational results will be provided to gain a better understanding of the effect of change in the temperature on the NEXAFS spectra of *n*-alkanes. This will lead to a direct measure of the effect of nuclear motion on the NEXAFS spectra as any change in the temperature will change the nuclear motion. **Chapter Seven** will discuss the NEXAFS spectra of liquid *n*-alkanes from *n*-C_6H_{14} to *n*-$C_{16}H_{34}$ as a function of their chain length. The effect of phase change on the spectra will also be discussed in this chapter. Using the MD-DFT approach, the effect of chain length on the spectra is studied for the same *n*-alkanes computationally. Insights and conclusions drawn from these investigations will be discussed in **Chapter Eight.**

1.6 References

1. Hähner, G., Near edge X-ray absorption fine structure spectroscopy as a tool to probe electronic and structural properties of thin organic films and liquids. *Chemical Society Reviews* **2006,** *35* (12), 1244-1255.

2. Hitchcock, A. P., Dynes, James J., Johansson, Goran, Wang, Jian, Botton, Gianluigi, Comparison of NEXAFS microscopy and TEM-EELS for studies of soft matter. *Micron* **2008,** *39* (6), 741-748.

3. Stöhr, J., *NEXAFS Spectroscopy*. Springer, Springer Series in Surface Sciences,: Berlin; London, **1992**; Vol. 25, p 404.

4. Wu, J., Zhu, Xiaohui, West, Marcia M., Tyliszczak, Tolek, Shiu, Hung-Wei, Shapiro, David, Berejnov, Viatcheslav, Susac, Darija, Stumper, Juergen, Hitchcock, Adam P., High-Resolution Imaging of Polymer Electrolyte Membrane Fuel Cell Cathode Layers by Soft X-ray Spectro-Ptychography. *The Journal of Physical Chemistry C* **2018,** *122* (22), 11709-11719.

5. Urquhart, S. G., Martinson, Mercedes, Eger, Shaylin, Murcia, Victor, Ade, Harald, Collins, Brian A., Connecting Molecular Conformation to Aggregation in P3HT Using Near Edge X-ray Absorption Fine Structure Spectroscopy. *The Journal of Physical Chemistry C* **2017,** *121* (39), 21720-21728.

6. Rightor, E. G., Urquhart, S. G., Hitchcock, A. P., Ade, H., Smith, A. P., Mitchell, G. E., Priester, R. D., Aneja, A., Appel, G., Wilkes, G., Lidy, W. E., Identification and Quantitation of Urea Precipitates in Flexible Polyurethane Foam Formulations by X-ray Spectromicroscopy. *Macromolecules* **2002,** *35* (15), 5873-5882.

7. Zhu, X., Hitchcock, Adam P., Le Nagard, Lucas, Bazylinski, Dennis A., Morillo, Viviana, Abreu, Fernanda, Leão, Pedro, Lins, Ulysses, X-ray Absorption Spectroscopy and Magnetism of Synthetic Greigite and Greigite Magnetosomes in Magnetotactic Bacteria. *Geomicrobiology Journal* **2018,** *35* (3), 215-226.

8. Fu, J., Urquhart, Stephen G., Linear Dichroism in the X-ray Absorption Spectra of Linear n-Alkanes. *The Journal of Physical Chemistry A* **2005,** *109* (51), 11724-11732.

9. Masnadi, M., Urquhart, S.G., Effect of Substrate Temperature on the Epitaxial Growth of Oriented n-Alkane Thin Films on Graphite. *Langmuir* **2012,** *28* (34), 12493-12501.

10. H. A. Durr, T. E., H. Elmers, S. Eisebitt, M. Farle, W. Kuch, F. Matthes, M. Martins, H. Mertins, P. M. Oppeneer, L. Plucinski, C. M. Schneider, H. Wende, W. Wurth, H. Zabel, A Closer Look Into Magnetism: Opportunities With Synchrotron Radiation. *IEEE Transactions on Magnetics* **2009,** *45* (1), 15-57.

11. Rehr, J. J., Albers, R. C., Theoretical approaches to x-ray absorption fine structure. *Reviews of Modern Physics* **2000,** *72* (3), 621-654.

12. Fracchia M. , G. P., Vertova A. , Rondinini S. , Minguzzi A. , Time-Resolved X-ray Absorption Spectroscopy in (Photo)Electrochemistry. *Surfaces* **2018,** *1* (1), 138-150.

13. Urquhart, S. G. Delocalization and Functional Group Fingerprinting in the Core Excitation Spectroscopy of Molecules and Polymers, PhD. Thesis. McMaster University, **1997**.

14. Walsh, R. Polarization: Linear and circular polarizations - 2019. https://www.japanistry.com/polarization/ (accessed February 11, 2020).

15. Chen, J. G., NEXAFS investigations of transition metal oxides, nitrides, carbides, sulfides and other interstitial compounds. *Surface Science Reports* **1997,** *30* (1), 1-152.

16. Prange, A., Modrow, Hartwig, X-ray absorption spectroscopy and its application in biological, agricultural and environmental research. *Reviews in Environmental Science and Biotechnology* **2002,** *1* (4), 259-276.

17. Urquhart, S. G., Ade, H., Trends in the Carbonyl Core (C 1S, O 1S) → π*C=O Transition in the Near-Edge X-ray Absorption Fine Structure Spectra of Organic Molecules. *The Journal of Physical Chemistry B* **2002,** *106* (34), 8531-8538.

18. Ade, H.; Stoll, H., Near-Edge X-Ray Absorption Fine-Structure Microscopy of Organic and Magnetic Materials. *Nature Materials* **2009,** *8* (4), 281-290.

19. Hilgevoord, J., The uncertainty principle for energy and time. *American Journal of Physics* **1996,** *64* (12), 1451-1456.

20. Levine, I. N., *Quantum Chemistry*. 7th ed.; Pearson Advanced Chemistry Series: University of New York, **2014**.

21. F. Sette, J. S., A. P. Hitchcock, Determination of intramolecular bond lengths in gas phase molecules from K shell shape resonances. *The Journal of Chemical Physics* **1984,** *81* (11), 4906-4914.

22. Fu, J., Urquhart, Stephen G., Effect of Chain Length and Substrate Temperature on the Growth and Morphology of n-Alkane Thin Films. *Langmuir* **2007,** *23* (5), 2615-2622.

23. Klues, M., Hermann, K., Witte, G., Analysis of the near-edge X-ray-absorption fine-structure of anthracene: A combined theoretical and experimental study. *Journal of Chemical Physics* **2014,** *140* (1).

24. Verhoeven, J. W., Glossary of terms used in photochemistry (IUPAC Recommendations 1996). **1996,** *68* (12), 2223.

25. Ma, Y., Chen, C. T., Meigs, G., Randall, K., Sette, F., High-resolution K-shell photoabsorption measurements of simple molecules. *Physical Review A* **1991,** *44* (3), 1848-1858.

26. Theodosiou, C. E.; Inokuti, M.; Manson, S. T., Quantum defect values for positive atomic ions. *Atomic Data and Nuclear Data Tables* **1986,** *35* (3), 473-486.

27. Remmers, G., Domke, M., Kaindl, G., Vibrationally resolved carbon core excitations in alkane molecules. *Physical Review A* **1993,** *47* (4), 3085-3091.

28. Charney, E., Electric linear dichroism and birefringence of biological polyelectrolytes. *Quarterly Reviews of Biophysics* **1988,** *25* (1), 1-60.

29. Rodger, A., Linear Dichroism. In *Method in Enzymology*, Riordan, J. F.; Vallee, B. L., Eds. Academic Press, Inc.: San Diego, **1993**; Vol. 226, pp 232-258.

30. Sedlmair, J., Gleber, Sophie-Charlotte, Peth, Christian, Mann, Klaus, Niemeyer, Jürgen, Thieme, Jürgen, Characterization of refractory organic substances by NEXAFS using a compact X-ray source. *Journal of Soils and Sediments* **2012,** *12* (1), 24-34.

31. Schuster, S.; Fuser, M.; Asyuda, A.; Cyganik, P.; Terfort, A.; Zharnikov, M., Photoisomerization of azobenzene-substituted alkanethiolates on Au(111) substrates in the context of work function variation: the effect of structure and packing density. *Physical Chemistry Chemical Physics* **2019,** *21* (18), 9098-9105.

32. Völkner, J.; Klues, M.; Witte, G., Assignment of NEXAFS Resonances in Alkanethiols and Their Implication on the Determination of Molecular Orientation of Aliphatic SAMs. *The Journal of Physical Chemistry C* **2018,** *122* (29), 16810-16820.

33. Endo, O.; Horikoshi, T.; Katsumata, N.; Otani, K.; Fujishima, T.; Goto, H.; Minami, K.; Akaike, K.; Ozaki, H.; Sumii, R.; Amemiya, K.; Nakamura, M.; Kosugi, N., Incommensurate Crystalline phase of n-Alkane Monolayers on Graphite (0001). *J. Phys. Chem. C* **2011,** *115* (13), 5720-5725.

34. Dannenberger, O.; Weiss, K.; Himmel, H. J.; Jager, B.; Buck, M.; Woll, C., An orientation analysis of differently endgroup-functionalised alkanethiols adsorbed on Au substrates. *Thin Solid Films* **1997,** *307* (1-2), 183-191.

35. Hähner, G.; Kinzler, M.; Wöll, C.; Grunze, M.; K. Scheller, M.; Cederbaum, L. S., Near edge x-ray-absorption fine-structure determination of alkyl-chain orientation: Breakdown of the ``building-block'' scheme. *Physical Review Letters* **1991,** *67* (7), 851-854.

36. Rabe, J. P.; Swalen, J. D.; Outka, D. A.; Stöhr, J., Near-edge X-ray absorption fine structure studies of oriented molecular chains in polyethylene and Langmuir-Blodgett monolayers on Si(111). *Thin Solid Films* **1988,** *159* (1), 275-283.

37. Gartner, M.; Sauter, E.; Nascimbeni, G.; Petritz, A.; Wiesner, A.; Kind, M.; Abu-Husein, T.; Bolte, M.; Stadlober, B.; Zojer, E.; Terfort, A.; Zharnikov, M., Understanding the Properties of Tailor-Made Self-Assembled Monolayers with Embedded Dipole Moments for Interface Engineering. *J. Phys. Chem. C* **2018,** *122* (50), 28757-28774.

38. Heimel, G.; Romaner, L.; Zojer, E.; Bredas, J. L., The interface energetics of self-assembled monolayers on metals. *Acc. Chem. Res.* **2008,** *41* (6), 721-729.

39. Wang, Y.; Canchaya, J. G. S.; Dong, W.; Alcami, M.; Busnengo, H. F.; Martin, F., Chain-Length and Temperature Dependence of Self-Assembled Monolayers of Alkylthiolates on Au(111) and Ag(111) Surfaces. *J. Phys. Chem. A* **2014,** *118* (23), 4138-4146.

40. Fenter, P.; Eberhardt, A.; Liang, K. S.; Eisenberger, P., Epitaxy and chainlength dependent strain in self-assembled monolayers. *Journal of Chemical Physics* **1997,** *106* (4), 1600-1608.

41. Perera, S. D., Wang, Jian, Urquhart, Stephen G., Linear dichroism in the NEXAFS spectra of n-alkane crystalline polymorphs. *Journal of Electron Spectroscopy and Related Phenomena* **2019,** *232*, 5-10.

42. Endo, O.; Ozaki, H.; Sumii, R.; Amemiya, K.; Nakamura, M.; Kosugi, N., Orientation of n-alkane in thin films on graphite (0001) studied using C K-NEXAFS. *Journal of Electron Spectroscopy and Related Phenomena* **2011,** *184* (3), 257-260.

43. Schöll, A.; Fink, R.; Umbach, E.; Mitchell, G.; Urquhart, S.; Ade, H., *Towards a detailed understanding of the NEXAFS spectra of bulk polyethylene copolymers and related alkanes*. 2003; Vol. 370, p 834-841.

44. Urquhart S. G.; Gillies R., Rydberg−Valence Mixing in the Carbon 1s Near-Edge X-ray Absorption Fine Structure Spectra of Gaseous Alkanes. *The Journal of Physical Chemistry A* **2005,** *109* (10), 2151-2159.

45. Ueda, K., Okunishi, M., Chiba, H., Shimizu, Y., Ohmori, K., Sato, Y., Shigemasa, E., Kosugi, N., Rydberg—valence mixing in the C 1s excited states of CH4 probed by electron spectroscopy. *Chemical Physics Letters* **1995,** *236* (3), 311-317.

46. Hitchcock, A. P.; Newbury, D. C.; Ishii, I.; Stöhr, J.; Horsley, J. A.; Redwing, R. D.; Johnson, A. L.; Sette, F., Carbon K-shell excitation of gaseous and condensed cyclic hydrocarbons: C3H6, C4H8, C5H8, C5H10, C6H10, C6H12, and C8H8. *The Journal of Chemical Physics* **1986,** *85* (9), 4849-4862.

47. Bagus, P. S., Weiss, K., Schertel, A., Wöll, Ch, Braun, W., Hellwig, C., Jung, C., Identification of transitions into Rydberg states in the X-ray absorption spectra of condensed long-chain alkanes. *Chemical Physics Letters* **1996,** *248* (3), 129-135.

48. Weiss K.; Bagus P. S.; Wöll Ch., Rydberg Transitions in X-ray Absorption Spectroscopy of Alkanes: The Importance of Matrix Effects. *J. Chem. Phys.* **1999,** *111* (15), 6834-6845.

49. Schöll, A., Fink, R., Umbach, E., Mitchell, G. E., Urquhart, S. G., Ade, H., Towards a Detailed Understanding of the NEXAFS Spectra of Bulk Polyethylene Copolymers and Related Alkanes. *Chem. Phys. Lett.* **2003,** *370* (5), 834-841.

50. Stöhr, J.; Outka, D.; Baberschke, K.; Arvanitis, D.; Horsley, J., Identification of C—H Resonances in the K-Shell Excitation Spectra of Gas-Phase, Chemisorbed, and Polymeric Hydrocarbons. *Physical Review B* **1987,** *36* (5), 2976.

51. Robin, M. B., *Higher Excited States of Polyatomic Molecules*. **1974**.

52. Urquhart S. G.; Gillies R., Matrix effects in the carbon 1s near edge x-ray absorption fine structure spectra of condensed alkanes. *The Journal of Chemical Physics* **2006,** *124* (23), 234704.

53. Swaraj, S., Ade, Harald, Differences in NEXAFS of Odd/Even Long Chain n-Alkane Crystals. *J. Electron. Spectrosc. Relat. Phenom.* **2013,** *191*, 60-64.

54. Schwartz, C. P., Uejio, Janel S., Saykally, Richard J., Prendergast, David, On the importance of nuclear quantum motions in near edge x-ray absorption fine structure spectroscopy of molecules. *J. Chem. Phys.* **2009,** *130* (18), 184109.

55. Chakravarty, C., Path integral simulations of atomic and molecular systems. *International Reviews in Physical Chemistry* **1997,** *16* (4), 421-444.

56. Nilsson, A., Pettersson, Lars G. M., The Structural Origin of Anomalous Properties of Liquid Water. *Nature Communications* **2015,** *6*, 8998.

57. Leetmaa, M., Ljungberg, M. P., Lyubartsev, A., Nilsson, A., Pettersson, L. G. M., Theoretical approximations to X-ray absorption spectroscopy of liquid water and ice. *Journal of Electron Spectroscopy and Related Phenomena* **2010,** *177* (2), 135-157.

58. Craig P. Schwartz, R. J. S., David Prendergast, An analysis of the NEXAFS spectra of a molecular crystal: α-glycine. *The Journal of Chemical Physics* **2010,** *133* (4), 044507.

59. Marx, D.; Parrinello, M., Ab initio path integral molecular dynamics: Basic ideas. *The Journal of Chemical Physics* **1996,** *104* (11), 4077-4082.

60. Triguero, L., Pettersson, L. G. M., Ågren, H., Calculations of Near-Edge X-Ray-Absorption Spectra of Gas-Phase And Chemisorbed Molecules by Means of Density-Functional and Transition-Potential Theory. *Phys. Rev. B.* **1998,** *58* (12), 8097-8110.

61. Y. Zou, T. A., G. Appel, A. L. D. Kilcoyne, H. Ade, , Solid State Effects in the NEXAFS Spectra of Alkane-Based van der Waals Crystals: Breakdown of Molecular Model. *Chem. Phys. Lett.* **2006,** *430*, 287-292.

62. Perera, S. D., Shokatian, Sadegh, Wang, Jian, Urquhart, Stephen G., Temperature Dependence in the NEXAFS Spectra of n-Alkanes. *The Journal of Physical Chemistry A* **2018,** *122* (49), 9512-9517.

63. Endo, O., Nakamura, Masashi, Amemiya, Kenta, Phase Transition of n-C36H74 Monolayer on Pt(111) Covered with Monolayer Graphene Studied by C K-NEXAFS. *The Journal of Physical Chemistry C* **2013,** *117* (42), 21856-21863.

64. Osamu Endo, T. H., Nobuyuki Katsumata, Keita Otani, Takumi Fujishima, Hiromichi Goto, Kazuhiro Minami, Kouki Akaike, Hiroyuki Ozaki, Ryouhei Sumii, Kenta Amemiya, Masashi Nakamura, Nobuhiro Kosugi, Incommensurate Crystalline phase of n-Alkane Monolayers on Graphite (0001). *The Journal of Physical Chemistry C* **2011,** *115* (13), 5720-5725.

65. Basson, I., Reynhardt, Eduard C., Identification of a Defect Chain Motion in n-Alkanes by Means of Nuclear Magnetic Resonance Spin-Lattice Relaxation Time Measurements. *J. Chem. Phys.* **1990,** *93* (5), 3604-3609.

66. Byrd, J. N., Bartlett, Rodney J., Montgomery, John A., At What Chain Length Do Unbranched Alkanes Prefer Folded Conformations? *The Journal of Physical Chemistry A* **2014,** *118* (9), 1706-1712.

67. Lüttschwager, N. O. B., Wassermann, Tobias N., Mata, Ricardo A., Suhm, Martin A., The Last Globally Stable Extended Alkane. *Angewandte Chemie International Edition* **2013,** *52* (1), 463-466.

68. Uejio, J. S., Schwartz, Craig P., Saykally, Richard J., Prendergast, David, Effects of vibrational motion on core-level spectra of prototype organic molecules. *Chemical Physics Letters* **2008,** *467* (1), 195-199.

69. Endo, O., Nakamura, Masashi, Amemiya, Kenta, Ozaki, Hiroyuki, Compression-Induced Conformation and Orientation Changes in an n-Alkane Monolayer on a Au(111) Surface. *Langmuir* **2017,** *33* (16), 3934-3940.

70. Johnstone, J., Peacock, Carol, J. Roberts, Kevin, Application of polarised NEXAFS spectroscopy to the structural characterisation of condensed molecular surfaces and interfaces. *Journal of Crystal Growth* **1999,** *198-199*, 275-281.

71. Hastie, G. P., Johnstone, Joy, Roberts, Kevin J., Fischer, Dan, Examination of the structure and melting behaviour of thin film n-alkanes using ultra-soft polarised near-edge X-ray absorption spectroscopy. *Journal of the Chemical Society, Faraday Transactions* **1996,** *92* (5), 783-789.

Chapter 2 – Instrumentation and Experimental Measurements

2.1 Synchrotron Radiation

Synchrotron radiation is a very bright, broadband, coherent, polarized source of light extending from far infrared to hard X-ray regions. This type of radiation is emitted when charged particles at a velocity close to the speed of light are accelerated radially.

In a synchrotron facility, an electron gun produces electrons with the energy of several tens of MeV. Using a Linear Accelerator (LINAC), these electrons are accelerated to several hundreds of MeV. These electrons are then injected into the booster ring, which increases their energy to the range of GeV. After this point, electrons are transferred to the storage ring. The injection process can be done in a 'top-up' or periodic injection approach. In the top-up approach, the beam current is kept in a narrow range close to the maximum current with small injections that occur every few minutes. In periodic injection, the beam current is replenished through an injection that occurs with a frequency of every 4 to 12 hours.[1] Figure 2.1 shows the scheme of a typical synchrotron facility.

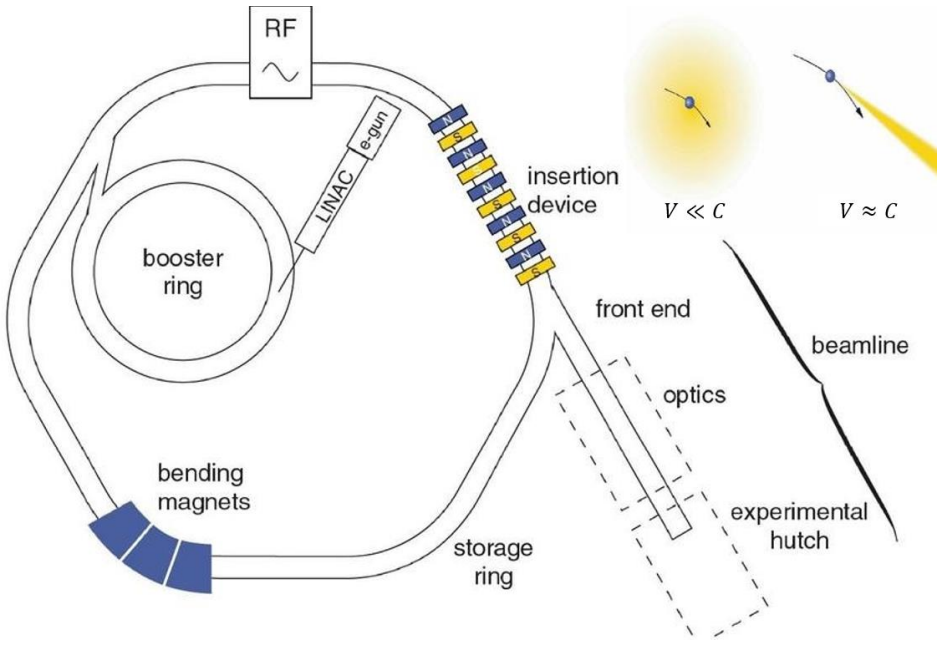

Figure 2.1 - Schematic of a synchrotron facility. Figure is reprinted with permission[2]

Bending magnets (BM) in the storage ring force the electrons to follow a circular path. This radial acceleration leads to the emission of the synchrotron radiation, which reduces the energy of the electrons in their storage ring. The lost energy/speed of electrons is regained through the use of a radio frequency (RF) cavity that is placed on the storage ring.

During the 1950s and early 1960, the first-generation synchrotron radiation facilities were developed as side projects at high energy particle accelerator facilities used for nuclear physics research; so-called 'parasitic' use.[3-4] Second-generation sources were the first sources dedicated specifically to synchrotron studies. The dedicated sources led to an increase in the quality of the beam, which in turn led to an increase in research conducted in various fields using synchrotron radiation. The third generation of synchrotron facilities was characterized by advancements in the storage ring design, and in particular, being specifically designed for the use of Insertion Devices (ID).[4-5] Even though the third generation still has the potential for improvement, several new approaches including Free Electron Lasers (FEL), and diffraction-limited light sources are being developed and are described as fourth-generation synchrotron facilities.[4]

X-ray radiation sources are characterized by their spectral brightness, which can be obtained using the following equation.

$$Spectral\ Brightness = \frac{(Photons/second)}{(source\ area)\times(bandwidth)\times(solid\ angle\ of\ emission)} \qquad \textit{Equation 2.1}$$

The photon flux has units of photons per second. The source area is the synchrotron electron beam size with the unit of mm^2. The solid angle of emission is also known as the source divergence. This angle is obtained from the beam divergence as it propagates and has units of $mrad^2$. The bandwidth represents the photon energy range of the metric, and is obtained using the following equation:

$$\Delta\lambda/\lambda = \Delta h\nu/h\nu \qquad \textit{Equation 2.2}$$

Figure 2.2 shows an example schematic of a synchrotron storage ring with some of the major components of the ring included. The energy of the electron beam will gradually decrease as the electrons pass through BM's and other IDs. The RF cavity

provides an energy boost that compensates for these energy losses and allows the beam to maintain a fixed orbit in the storage ring.[3] BM's and ID's are described in more detail below.

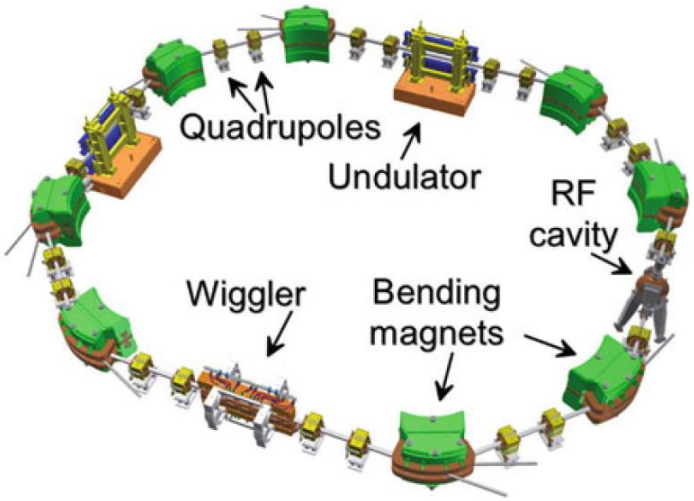

Figure 2.2 - Schematic of the storage ring with the main components. Figure is reprinted with permission[4]

2.1.1 Properties of Bending Magnets (BM) and Insertion Devices (ID)

X-ray sources, including conventional and synchrotron, receive electrical energy and convert it to X-rays and heat. Note that heat is an undesirable by-product. In the X-ray tube, as the electrical current flows through the tube from the cathode to the anode, the high energy electron beam creates core holes in the anode, which will be refilled by the valence electrons and emit X-rays that are characteristic of the anode. The generated X-rays are not tunable, have a relatively low flux, and are not collimated as they are emitted in all directions. Therefore, the X-ray tubes are not suitable for NEXAFS spectroscopy studies. BM's and ID's are the sources of X-ray radiation in a synchrotron ring. Figure 2.3 shows a scheme of various generations of X-ray radiation, including synchrotron radiation.

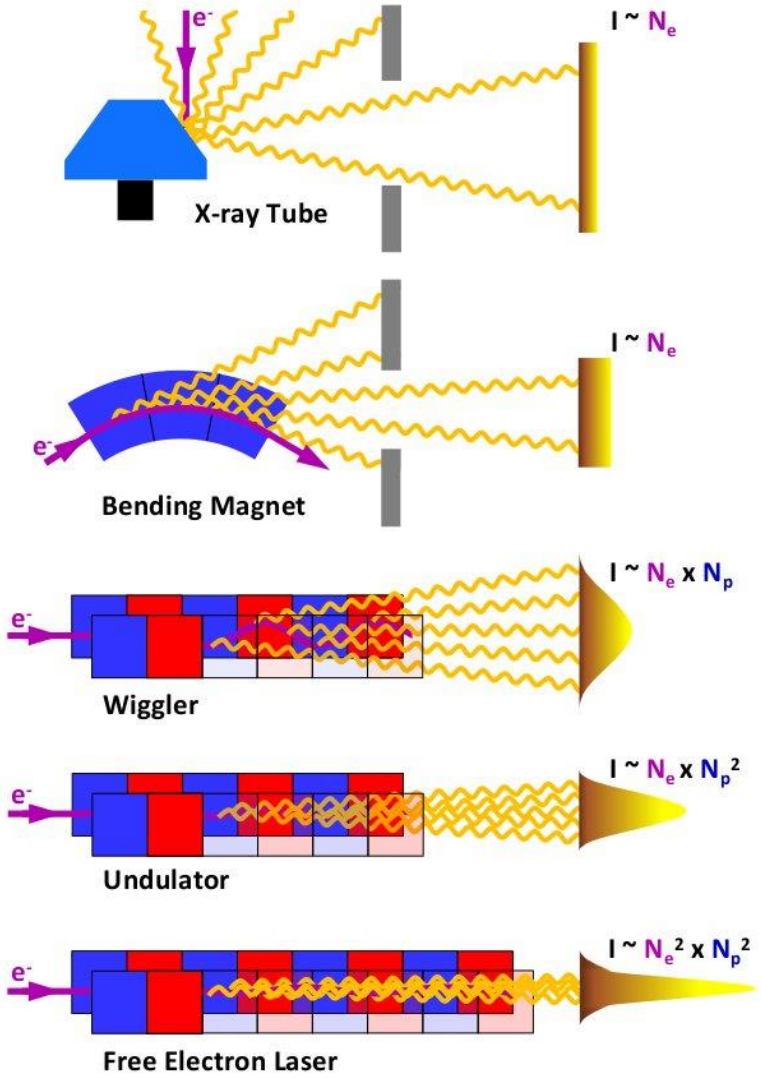

Figure 2.3 - Properties of X-ray generation using various devices. Figure is reprinted with permission[6]

The intensity of a synchrotron beam has a direct relation with the number of electrons (N_e) passing through the source (BM, ID, etc.) as well as the number of magnet poles (N_p) in the case of wiggler or undulator. As shown in Figure 2.3, a BM is a single dipole magnet that causes a singularly curved electron trajectory and produces a cone of radiation that is emitted tangentially. Both linear and circular polarized light (See section 2.1.2) with a broad energy distribution can be generated using a BM.[4]

Wigglers are a way of increasing the intensity of the synchrotron radiation by arranging a series of dipole magnets next to each other. The dipoles are arranged with alternating polarity, so the electrons move with small wiggles where radiation is emitted.

Comparing BMs with the wigglers, the radiation cone is much narrower in the wigglers. This creates a polarized wave with an enhanced intensity by a factor of the number of poles (N_p) in comparison with the BM.[4, 7]

Similar to the wigglers, undulators consist of a periodic arrangement of dipole magnets and generate an alternating magnetic field that deflects the beam sinusoidally. The radiation passing through the undulators is characterized by very narrow and discrete harmonics. The narrow harmonics will lead to the generation of a very narrow beam cone compared to the wigglers. This is the result of using small magnetic field and short magnetic periods in the undulators.

The smaller magnetic field and short magnetic periods lead to a small angular divergence of the beam. As a consequence, the undulator intensity scales as $N_e \times N_p^2$ which is increased by a factor of N_p in comparison with the wigglers ($N_e \times N_p$). The energy of the narrow X-ray beam harmonics produced by an undulator could be varied by varying the gap between the rows of magnets.

2.1.2 X-ray Polarization

EMR has an electric and a magnetic field which are orthogonal to each other and perpendicular to the direction of propagation, as presented in Figure 2.4. As discussed in §1.2.3, NEXAFS can reveal information about the orientation of molecules through LD, which is the anisotropic absorption of linearly polarized EMR. In the discussion of X-ray polarization, the orientation of the electric field vector (***E***) is used to describe the polarization. Therefore, the linear vertical and horizontal polarizations are used to define the orientation of the ***E*** vector (Figures 2-5, a and b). Following the same trend, circular left and right polarizations are defined when the ***E*** vector is rotating around the propagation axis (Z-axis in Figure 2.5) counterclockwise and clockwise, respectively (Figure 2.5, c and d). The elliptical polarization will produce two perpendicular waves of unequal amplitudes which differ in phase by 90°.[8-10] Figure 2.4 presents a schematic of the EMR with the electric and magnetic field vectors.[11]

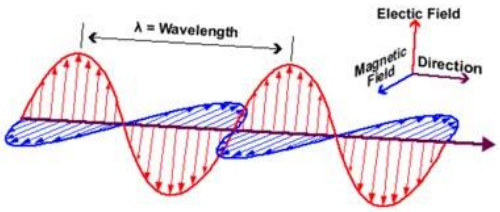

Figure 22.4 - Schematic of the EMR.[11]

Figure 2.5 presents a schematic of various types of linear and circular polarization of the EMR.

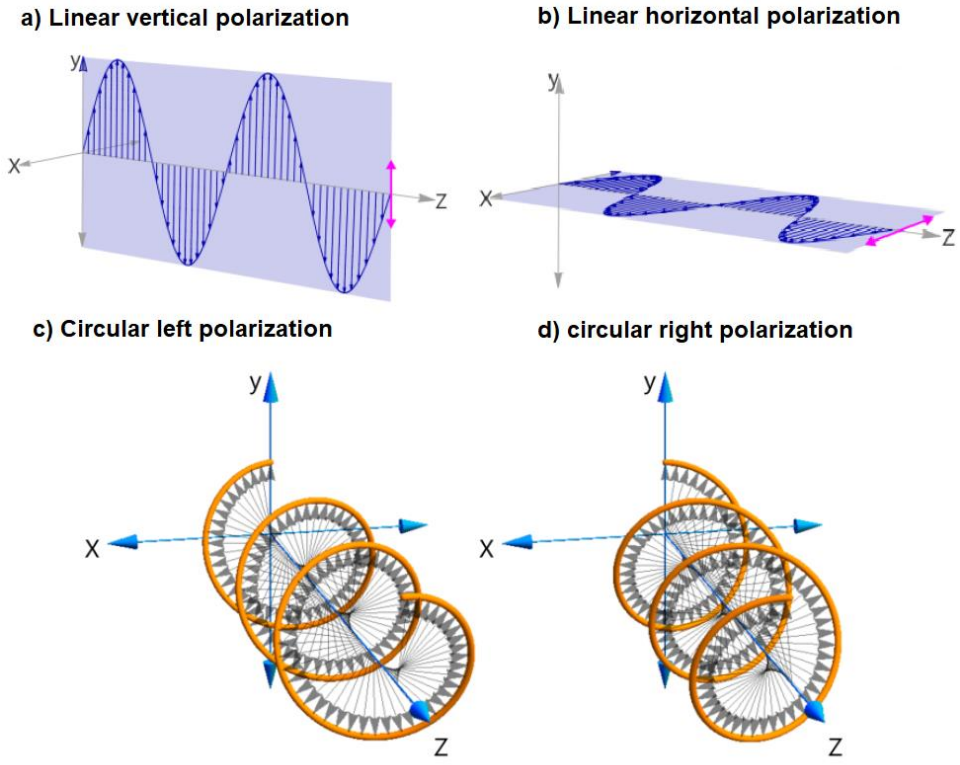

Figure 2.5 - Schematic of (a), (b) linear polarization, and (c), (d) circular polarization of the light. Figure is reprinted with permission.[12]

The X-rays produced by BM are mostly (between 85% to 90%) linearly polarized in the plane of the ring and circularly polarized above and below the plane.[8-10] Undulators are categorized as either linear undulators, which will produce linearly polarized light or Elliptically Polarized Undulators (EPU) which can produce a variety of polarization (Figure 2.6), from linear horizontal (0°) to linear vertical (90°) as well as both right and left circular polarizations.[4, 7]

A schematic diagram of an EPU and the polarization produced is shown in Figure 2.6. An EPU contains four quadrants of periodic magnets rather than the two rows in a linear undulator. By shifting the movable magnet rows with respect to the other row, it is possible to force different undulating trajectories to the electrons, and this leads to linear or circular polarization of the emitted synchrotron radiation.[4, 7, 13]

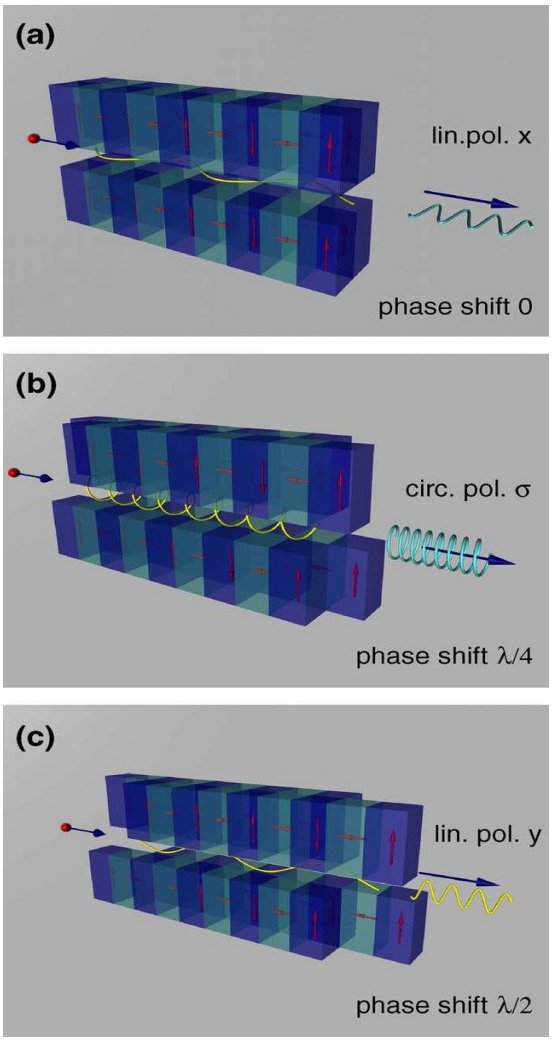

Figure 2.6 - Schematic diagram of an EPU. Figure is reprinted with permission[13]

In an FEL, long undulator sections are used on a beam with small emittance, low energy spread, and large critical current. This produces coherent, ultra-brilliant, tunable laser pulses with Angstrom ($10^{-10}\ m$) wavelength and simultaneously femtosecond ($10^{-15}\ s$) pulse durations in the X-ray regime. This will allow to resolve the structure and dynamics of matter on the atomic scale.[6] In a diffraction-limited storage ring, the average

spectral brightness and the coherent fraction are optimized by decreasing the magnet gaps drastically[14] and using improved vacuum technologies for pumping vacuum systems of a few centimeter diameter and several hundred meters long. [15]

2.2 Measuring NEXAFS Spectra

2.2.1 Excitation and Relaxation Processes

The absorption of X-rays by an atom or molecule can lead to the excitation or ionization of a core electron. This core hole will then be filled during the relaxation process by another electron, either from the valence levels or a shallower core level. This process results either in the ejection of an Auger electron or the emission of a fluorescent photon. The total decay is defined as the total of radiative and non-radiative decay and is proportional to the absorption cross-section. The energy of the Auger electron or the fluorescent photon depends on the conservation of energy and the atomic number. Figure 2.7 presents the schematic diagram of these photoabsorption and relaxation processes.[16]

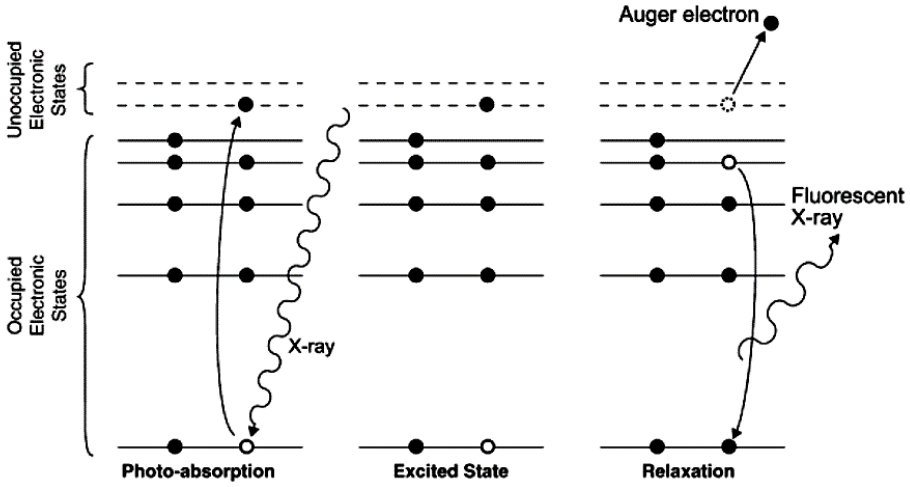

Figure 2.7 - Schematic of the photoabsorption and relaxation process occurring in NEXAFS experiments. Figure is reprinted with permission[16]

2.2.2 Detection Techniques

Measuring the Auger or fluorescence decay channel signal would lead to the measurement of the NEXAFS spectrum. The probability of a decay channel depends on the atomic number (Z), where Auger decay is dominant at low Z. Figure 2.8 presents the

common detection techniques used in NEXAFS spectroscopy. These detection modes are explained in the following sections.

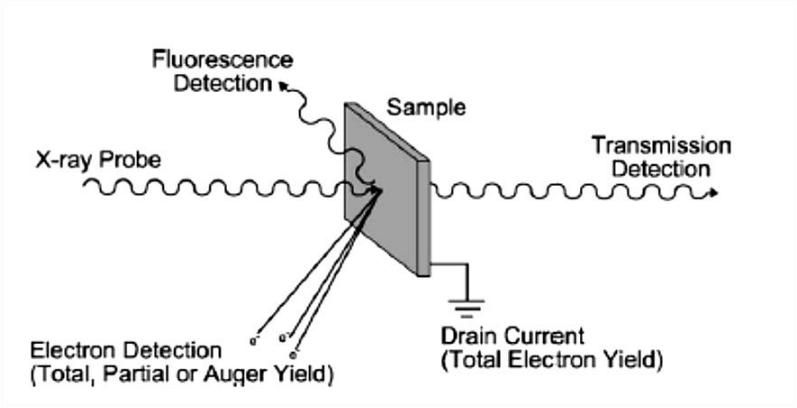

Figure 2.8 - Schematic of various detection techniques used in NEXAFS spectroscopy. Figure is reprinted with permission[16]

2.2.2.1 **Transmission Detection**

In this method, a thin sample is placed in the beam. Transmission can be recorded by placing a detector behind the sample in the beam path. The incident flux (I_0) can be obtained using the detector behind an empty sample holder. The I_o spectrum is used to remove any structure in the incident flux that arises from the source properties, mirror reflectivity, and window absorption. The X-ray transmission spectrum is then obtained by calculating the optical density using the following equation.

$$OD = -ln\frac{I}{I_0} = \mu(E) \times \rho \times d \qquad \textit{Equation 2.3}$$

In this equation, μ ($cm^2.g^{-1}$) is the mass absorption coefficient at energy E, ρ ($g.cm^{-3}$) is the density of the sample, and d (cm) is the thickness of the sample. Note that in the experimental condition, OD is simply calculated using $(-\ln\frac{I}{I_0})$ by obtaining *I* and I_0.[10] The mass absorption coefficient (μ) is related to the absorption cross-section (σ_x) as explained in chapter 1.1.

Figure 2.9 presents the schematic diagram of the transmission detector used in the STXM end station at the CLS. This detector is placed behind the sample, and the synchrotron beam hits the detector after passing through the sample.

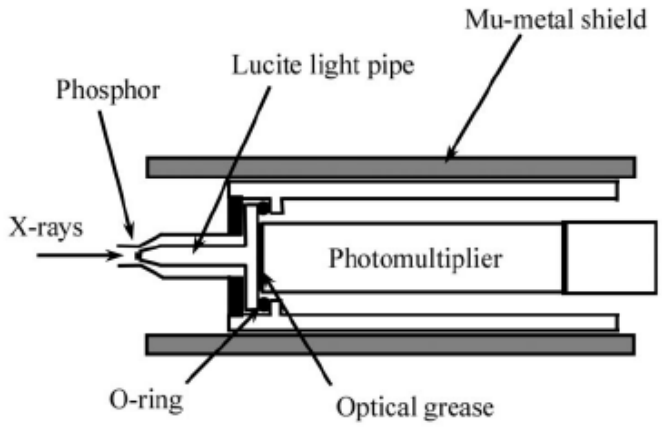

Figure 2.9 - Schematic diagram of the transmission detector used in the STXM end station. Figure is reproduced with permission of the International Union Crystallography[17]

In this detector, a phosphor is used to convert the X-ray signal to the visible light. The visible photons are then counted by the photomultiplier (PMT).

All NEXAFS spectra reported in this thesis are obtained using transmission detection, and the spectra are converted to the optical density using Beer's law (Equation 2.3) The background which is the photoelectron cross-section from the valence electrons is deducted, and all the spectra are normalized to the Henke cross-sections[18] for the carbon atom[19] using the aXis2000[20] program.

2.2.2.2 **Electron Yield Detection**

As shown in Figure 2.7, the absorption of the X-ray beam will lead to the excitation or ionization of core electrons. During the relaxation process, an electron is transferred from the valence orbital or another core orbital (e.g., a 2p electron in silicon) to fill the core-hole with an energy release. This energy is either released radiatively, by the emission of a fluorescent photon, or non-radiatively, through Auger electron emission. Electrons emitted by photoionization and Auger decay are known as the primary electrons. These primary photoionized electrons can inelastically scatter in the sample to create a wide distribution of secondary electrons also known as the inelastic tail. The secondary electrons will have a lower kinetic energy and appear as a low energy broad band.[10]

The current of primary and secondary photoelectrons and Auger electrons is proportional to the X-ray absorption cross-section. Using an electron analyzer, it is possible to select an energy window and only detect the Auger electrons. This approach is known as the Auger Electron Yield (AEY) detection technique.[7, 10] Using the Partial Electron Yield (PEY) detection, it is possible to filter these electrons and only detect electrons with the kinetic energy higher than the defined energy threshold. The PEY detection is usually performed with a negative grid potential (E_p) before the electron detector which will filter the electrons with an energy lower than the defined threshold.[7, 10] This method can improve surface sensitivity.

The third type of electron yield detection is known as the Total Electron Yield (TEY) detection, which detects all the electrons emitted from the sample, including the primary and secondary electrons. The TEY measurement could be done in two ways. The first one is by using an electron detector to measure all the electrons emitted from the sample surface and the second method is done using a high sensitivity ammeter to measure the sample drain current generated from all the electrons that emerge from the surface of sample.[5, 10, 16]

In the TEY detection mode, the sample drain current (I) will be normalized with respect to the incident photon flux (I_0). The incident photon flux is obtained by measuring the drain current of an empty sandwich. The normalization equation for TEY is given below.[7, 10]

$$TEY = \frac{I}{I_0}$$ *Equation 2.4[10]*

2.2.2.3 **Fluorescence Yield Detection (FY)**

Fluorescence detection mode is a bulk-sensitive technique that detects the photon emission from fluorescence decay in the sample. As presented in Figure 2.7, the fluorescence decay will happen when a valence electron is transferred to fill the core-hole, and the conserved energy of this process is released as a fluorescence photon. The FY is the radiative fraction of the total decay. FY is a bulk sensitive technique because X-rays interact less strongly with the matter than electrons. This means the inelastic

scattering process is much smaller for photons, which leads to longer penetration and escape depth. As a consequence, photons can escape from deeper within the sample compared to the electrons.[10] However, this technique is restricted to species with a low concentration of the core excited element on account of self-absorption processes.

Bulk-sensitivity of the FY detection method makes it a good option for liquid samples since it is harder to control the thickness of the liquid samples. However, FY doesn't work for highly concentrated samples due to self-absorption.

An example of the application of FY for studying liquid samples would be the study conducted by Hitchcock *et al*.[21], who used low energy X-ray fluorescence detection to study arsenic immobilization by a Fe(II)-oxidizing freshwater bacteria. Also, FY measurement for the carbon 1s edge in the STXM endstation at the CLS is particularly difficult due to low detector quantum yield at the carbon edge, limited solid angle, low emission at low Z, and the interference from the light coming from the laser interferometer.[10]

2.2.3 **Beamline Used to Measure NEXAFS Spectra**

NEXAFS spectra were recorded at the Soft X-ray Spectromicroscopy (SM) beamline (10ID1)[22] at the CLS, located at the University of Saskatchewan in Saskatoon, Saskatchewan, Canada. All the measurements were done using the ambient STXM end station using transmission detection modes.[22]

The SM beamline uses an Apple II EPU, which can deliver both circular (left and right) and linear (horizontal, vertical, and inclined) polarizations by changing the relative positions of its periodic magnets. Figure 2.10 shows a schematic layout of the SM beamline[22], as well as an actual photo from the SM beamline.

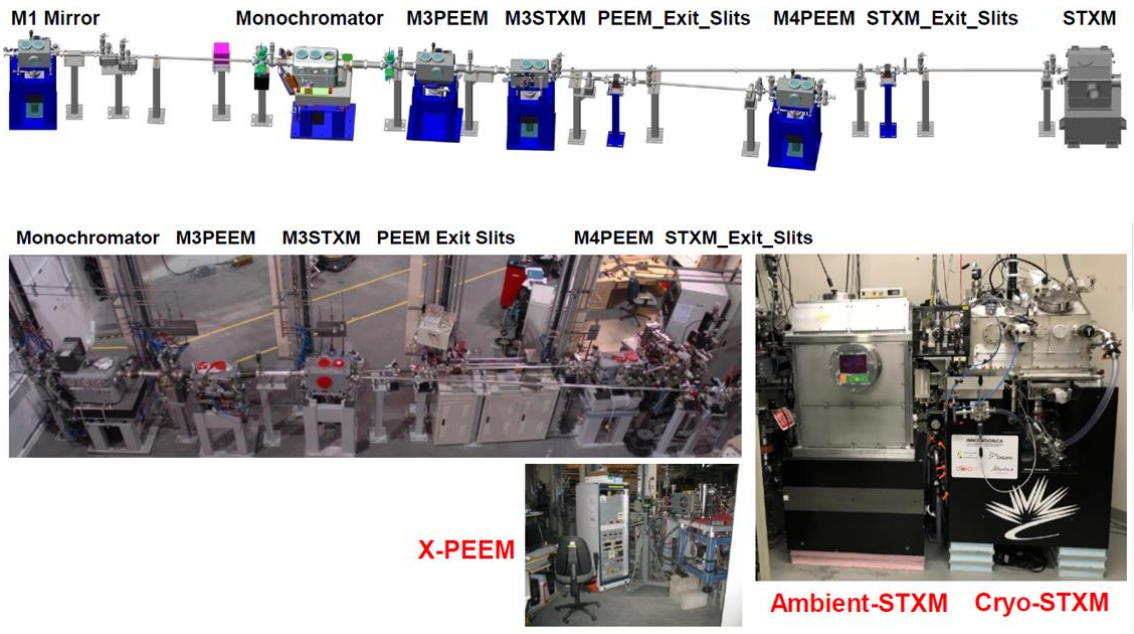

Figure 2.10 - Schematic layout and an actual photo of the SM beamline located at the CLS. Figure is reprinted with permission[22]

The X-rays produced by the EPU will be reflected by the M1 mirror and will be focused on the pre-mirror of the Plane Grating Monochromator (PGM). Using the three different gratings in the PGM, an energy range of 100 eV to 2500 eV is achievable. The grating selection is changed based on the required X-ray energies for the experiment (e.g., Carbon 1s, Oxygen 1s, Nitrogen 1s, etc.).[22] All the measurements in this study are performed using the low energy grating (250 $lines/mm$) which offers the energy range of 130 – 400 eV.

The monochromatic X-ray beam is then reflected using the M3 set of mirrors to either the X-ray Photoemission Electron Microscope branch (X-PEEM) or the STXM branch. All the measurements in this research are done using the STXM end station which is explained in detail in the following section.[22]

2.2.4 **STXM End Station**

X-ray spectromicroscopy is the technique that offers both high energy resolution XAS as well as high spatial resolution X-ray imaging. Figure 2.11 shows a schematic of the ambient STXM end station in the SM beamline at CLS.[23]

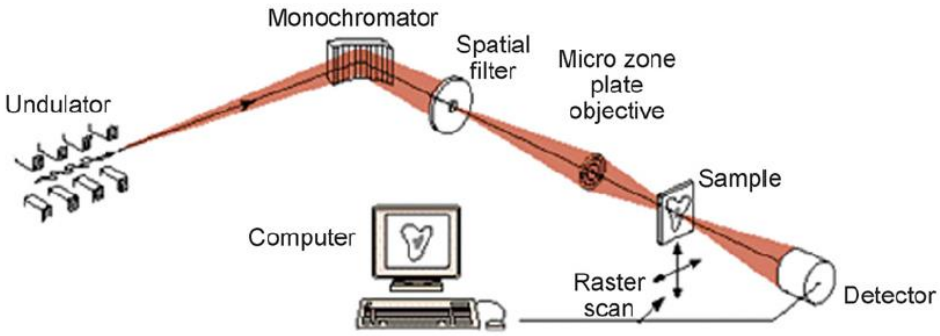

Figure 2.11 - Schematic diagram of the instrumental setup of a zone-plate-based STXM. Figure is reprinted with permission.[24]

Monochromatic light passes through the Fresnel Zone Plate (ZP), which produces a small X-ray spot by diffractive focusing. ZPs are circular variable line-spacing diffractive focusing devices made of alternated transparent and opaque rings. The OSA is the next component that is located between the ZP and the sample so that only the first-order diffracted beam hits the sample, and higher-order diffraction is blocked. Undiffracted light is blocked by the central stop of the ZP. Figure 2.12 shows a schematic of the ZP and OSA and how they focus the first-order light on the sample.

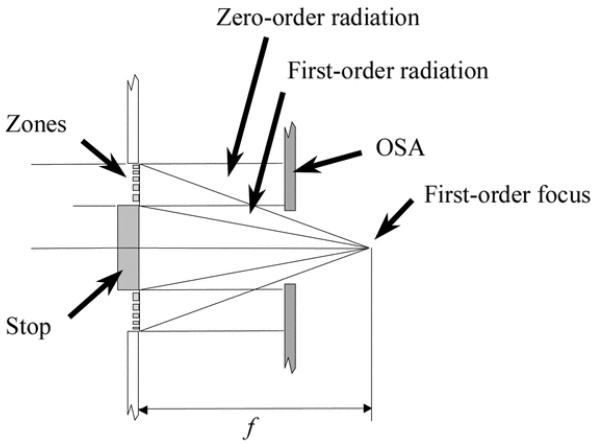

Figure 2.12 - Scheme of the focusing components in the STXM end station. Figure is reproduced with permission of the International Union Crystallography.[17]

Some fraction of the higher-order light can still reach the detector which can distort the NEXAFS spectra of highly absorbing species.[25]

To be able to obtain high energy resolution spectra (as well as high spatial resolution images), all the components of the end station must be aligned with each other. Optimized exit slit settings will lead to a higher spatial resolution, and the dispersive exit slit, in particular, will affect the energy resolution. A laser interferometer is employed that gives the precise position of these components with respect to the sample.

2.2.5 Data Acquisition in STXM

With the sample in the chamber, transmission imaging is used to locate an area of interest which is thin enough so the beam can pass through and be measured in transmission and thick enough to produce spectra with a good signal to noise ratio. When an image of the area of interest is obtained, it is possible to obtain the high-energy resolution NEXAFS spectrum of the sample area by measuring the transmission of that area as a function of the X-ray energy. Major methods of obtaining the spectra are point scan, line scan, and image sequence scan. These methods are explained in the following sections.

2.2.5.1 Point Scan

A point scan can be one of the fastest approaches to acquiring a NEXAFS spectrum. In this method, one or more spots (x, y) of the sample are selected, and by varying the X-ray energy, the transmission spectrum of each of these spots are obtained. This gives a 1D dataset of transmission as a function of X-ray energy. The I_0 spectrum could be obtained by simply selecting an empty area. It is also possible to obtain the I_0 spectrum from a measurement without the sample in the chamber. The point scan will not be a good option if the sample is heterogeneous since a single spectrum is insensitive to the spatial variation of the sample. Since liquid samples are homogeneous and sensitive to beam damage, most of the data acquisition of this research are made using point scans with a defocused X-ray beam.

2.2.5.2 Line Scan

The line scan is similar to the point scan with the difference that rather than a few spots, a line on the sample is scanned as a function of the X-ray energy. This gives a 2-

dimensional dataset of transmission (position, photon energy). Similar to the point scan, it is possible to obtain the I_0 from an empty area along with the line scan or an extra measurement without the sample in the beam. Figure 2.13 shows an example of a transmission spectrum obtained from a line scan on a sample of liquid *n*-$C_{15}H_{32}$. The line scan area is shown by the thin orange line. This line-scan includes an area containing a small liquid drop (darker region) and an empty area (lighter region), providing the I and Io.

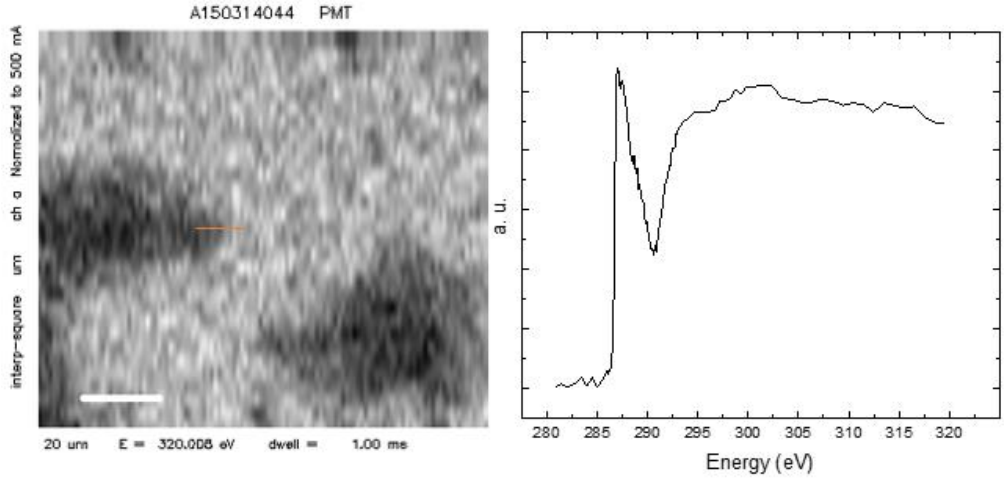

Figure 2.13 - STXM image obtained at 320 eV for liquid n-$C_{15}H_{32}$ sample(left) and the carbon 1s NEXAFS spectrum obtained from the line scan(right).

Since the samples in the liquid cells were mostly uniform and did not frequently provide an open area for I_0 normalization, this type of scan was not used for measurements reported in this thesis.

2.2.5.3 **Image Sequence**

In this type of data acquisition, a series of images are acquired over a range of X-ray energies. This gives a 3-D dataset of transmission as a function of position along two axes (x, y) and the X-ray energy. By integrating the transmitted signals from different areas of these image sequences as the function of X-ray energy, it is possible to generate a NEXAFS spectrum.[22, 26-28] Figure 2.14 shows an image sequence scan of a sample of liquid *n*-$C_{16}H_{34}$.

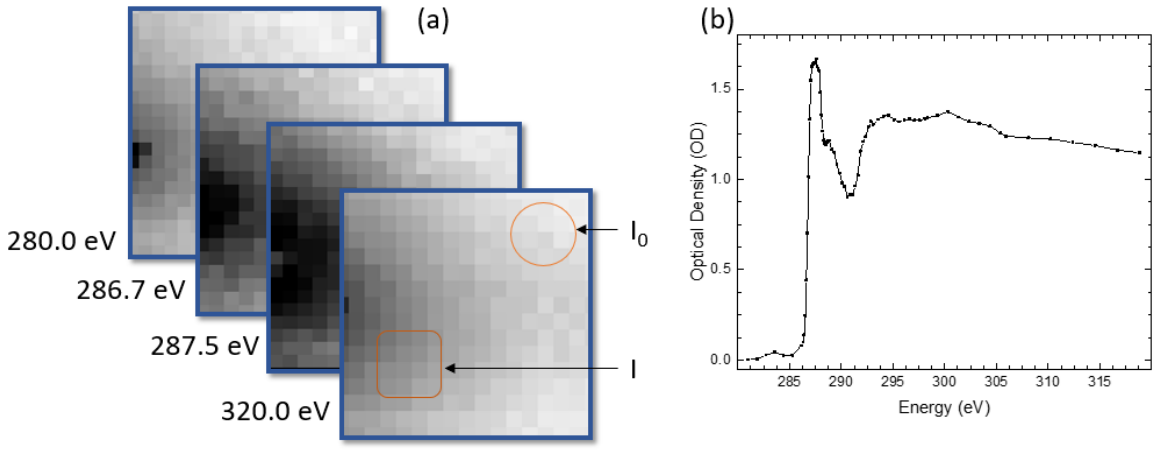

Figure 2.14 - (a) Image sequence of n-$C_{16}H_{34}$ obtained over a range of X-ray energies, and (b) Carbon 1s NEXAFS spectrum obtained from the image sequence

With an image sequence dataset, it is possible to select an area containing the sample (I) and an empty spot (Io) from the same data. This process is shown in Figure 2.14, where the circle shows the selected empty spot (Io), and the square represents the area with the sample (I). As both the *I* and I_0 spectra contain the absorption of the windows, the optical density spectrum collected in this mode does not include the absorption of these windows.

2.2.6 Radiation Sensitivity of Liquid *N*-alkanes

Most organic molecules show some degree of sensitivity to radiation damage. Therefore, for a meaningful measurement, it is critical to know the threshold for radiation damage and to work within it. Radiation damage can take several forms, such as mass loss and chemical modification, which includes the formation of carbon-carbon double bonds in the case of *n*-alkanes.[29] During the carbon 1s NEXAFS spectroscopy, mass loss is observed as an intensity drop in the post-edge region of the spectrum, and chemical modification is observed through a change in fine structure. For hydrocarbons such as *n*-alkanes, radiation damage is seen through a new peak at 285 eV from carbon $1s \rightarrow \pi^*$ transitions, from the loss of hydrogen and the formation of carbon-carbon double bonds.[29]

Each scanning mode (i.e., point, line, and image sequence scans) can have a different exposure time and different radiation damage impact on the sample.[24] As liquid

phase molecules are not fixed in space, the radiation damage should be lower compared to the solid phase, as molecules can diffuse through the focus spot. Since all the samples in this study are saturated liquid *n*-alkanes, the formation of π^* peak is a good indication of radiation damage in the sample. For each measurement in this study, the beam focus, dwell time, and energy point spacing were optimized to minimize radiation damage. A fresh sample region was examined in each measurement in order to minimize the impact of radiation damage on the spectra.

2.2.7 Energy Scale Calibration and Normalization of Spectra

The energy scale must be reliably calibrated to be able to compare spectra obtained in different experiments. All the spectra obtained in this study are calibrated to the values from the carbon 1s spectrum of CO_2 of Ma *et al.*[30] Calibrations were performed without the sample in the beam but with CO_2 gas introduced into the STXM chamber. The carbon 1s transmission spectrum was then obtained for this CO_2 gas, and selected transitions in this spectrum were calibrated to the values from Ma *et al*.[30] study. These transitions are the carbon $1s \rightarrow 3s$ $(v = 0)$ and carbon $1s \rightarrow 3p$ $(v = 0)$ transitions that appear at 292.74 eV and 294.96 eV, respectively.[30]

2.2.8 Substrates for the NEXAFS Measurements

Depending on the physical phase of the sample, different substrates and sample holders are required. Since all experimental measurements performed in this thesis project are in the liquid phase, the especial experimental design for these samples is discussed below.

- **Samples in the liquid phase**

Liquid samples can be measured using a static liquid cell or flow-through liquid cell. The static cells are made by trapping a fixed amount of liquid between two transparent windows, and flow-through cells are made in a way that liquid is passing through the cell during the experiment. Since the liquid in the static cell is not changing, beam damage is higher, in comparison with the flow-through cells. Goncz *et al*.[31] and

Neuhäusler *et al*.[32] have used static liquid cells to obtain the NEXAFS spectra of liquid samples in the STXM.[28, 31-33] Figure 2.15 shows the schematic of a static liquid cell.

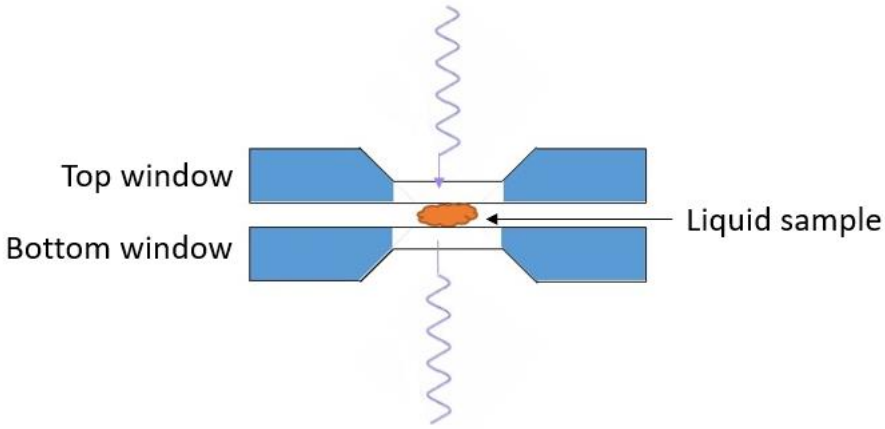

Figure 2.15 - Schematic of static liquid cell

In this cell, the liquid is trapped between two Si_3N_4 windows and mounted on a sample holder to be used in the STXM chamber. This liquid cell is sealed, so the liquid does not evaporate. Static cells are cheaper to make and easier to handle for the spectroscopy measurements.

A major challenge with liquid cells is controlling the thickness of the liquid. Using conditions such as sample temperature, environment airflow, speed of making the cell, and trial and error, it is possible to obtain an ideal film thickness roughly. Another major challenge in making the static liquid cell is the risk of contamination from the glue. Almost all types of glue have carbon-based chemicals and could cause contamination in the sample if they get in contact with the liquid sample or inside the windows. Epoxy-based glue could help reduce the risk of carbon contamination. However, even this type of glue is not carbon-free and needs to be used with extra care. The extra amount of the liquid inside the cell could either break the windows or exit the sandwich by dissolving the glue. This would also increase the risk of contamination in the sample.

Figure 2.16 shows an example of a flow-through liquid cell used by M. Nagasaka *et al.* to measure the soft X-ray absorption of water.[33] In this type of cell, a pump is used to transfer the liquid sample from an external container into the cell. The thickness of the

liquid cell is controlled using the flow rate of the liquid. Flow-through liquid cells are more difficult to make and are much more expensive. Also, if transmission is the selected method of the detection, for the organic molecules at the carbon 1s edge, the cell must have a sample thickness of less than 100 nm. This introduces a capillary effect that could change the orientation of molecules because of the interactions with the surface.[33] The obtained spectra, in this case, will no longer be representative of the bulk properties since surface interactions influence the orientation of molecules. The thickness of the cell is not an issue for FY detection mode since transmission through the cell is no longer required. The main advantage of the flow-through cells is the possibility of studying various samples using the same cell. Also, as the liquid flows through the cell, the beam hits a fresh portion of the sample, depending on the flow speed. This will minimize the beam damage caused by irradiation of the same spot.

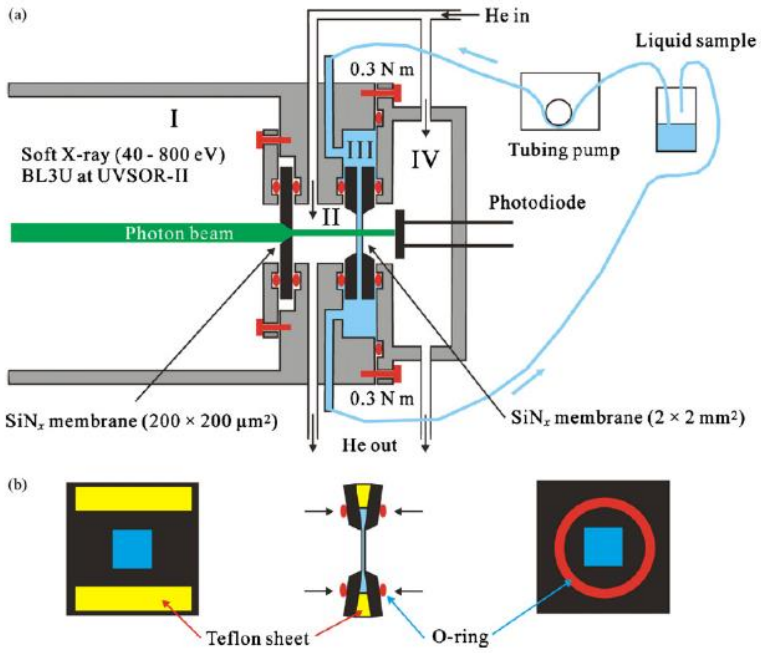

Figure 2.16 - Flow-through liquid cell used to study Oxygen 1s NEXAFS of water by Nagasaka et al. Figure is reprinted with permission[33]

As the static cells are cheaper and easier to make, all the measurements in this study are performed using the static cells. The cell preparation procedure is explained in the following sections, depending on the detection mode used.

2.3 Sample Candidates

The liquid *n*-alkanes used in this research project were *n*-hexane (*n*-C_6H_{14}, 99%), *n*-dodecane (*n*-$C_{12}H_{26}$, 99%), *n*-tetradecane (*n*-$C_{14}H_{30}$, 99%), *n*-pentadecane (*n*-$C_{15}H_{32}$, 99%), and *n*-hexadecane (*n*-$C_{16}H_{34}$, 99%). These samples were purchased from Sigma-Aldrich Canada Co. and used without further purification. These samples were selected to obtain the spectra for the shortest and the longest chain liquids and a several *n*-alkanes in between these.

2.4 Detection Methods for the Liquid Samples

To obtain the carbon 1s NEXAFS spectra of liquid *n*-alkanes with transmission detection, the sample needs to be thin enough (less than 100 nm), so the beam can go through and reach the detector and yet thick enough to obtain a reasonable optical density. Since it is difficult to control the thickness of the liquid cell, alternative approaches to recording the NEXAFS spectra were examined. Both TEY and FY can lead to similar spectra as transmission detection. In the TEY method, the drain current is measured, so there is no need for the beam to pass through the sample. The FY detector also is not placed behind the sample and has a 45^o angle with the sample (with respect to the incident beam), which means the beam does not need to pass through the sample (Figure 2.8). This reduces the need for making a thin sample for transmission. Therefore, a logical approach would be to try and obtain the NEXAFS spectra of the liquids by FY as an initial step. However, each of these approaches requires additional optimization to be able to measure the spectra of the liquid phase. These optimizations are explained in the following sections.

2.4.1 TEY Measurements

The TEY measurements explored in this thesis are different from the sample/vacuum interface of the typical TEY measurements, where a surface is exposed to X-rays, and the sample current measured. In the proposed experiments, the liquid sample is confined beneath a transparent window, and the TEY signal measured through a thin conductive electrode on the window. In this thesis, the sample/conductive layer on a window interface was prepared by modifying the design of the sample holder; this

design is presented in Figure 2.17. These sample holders were manufactured using the positive photo-fabrication process and chemical etching technique on a Printed Circuit Board (PCB). This procedure is explained in the following section. The top window in this design is coated with a thin layer of gold (~50 *nm*), which is in contact with the copper wire on the sample holder. This gold layer will transfer the electrons that are escaped from the liquid to the copper wires and the connections. This will lead to the direct measurement of the current of photoelectrons created in the liquid.

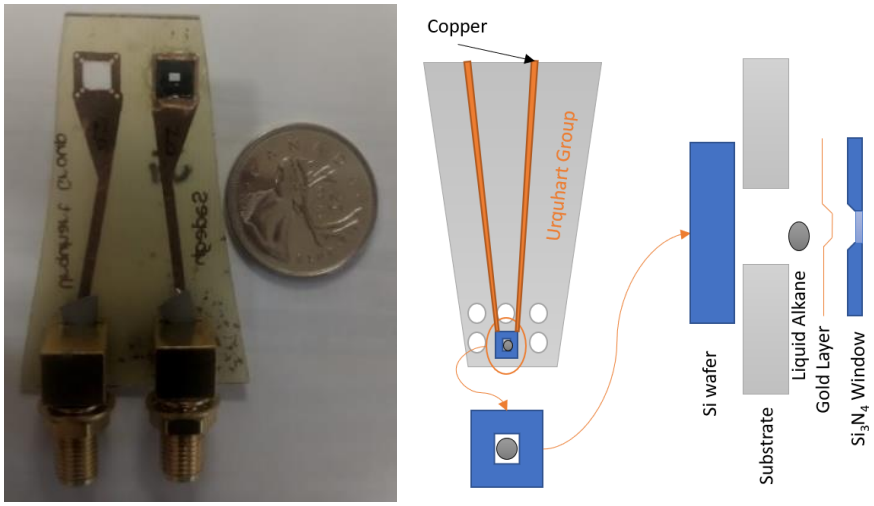

Figure 2.17 - Sample holder for the TEY measurements

2.4.1.1 TEY Sample Holder Design

In this process, copper wires between the connections and the sample windows were designed using the PCB designer program and printed on a heat-stabilized transparent paper using a laser printer. The TEY sample holders were designed by etching this design onto a pre-sensitized copper board using iron (III) chloride. Two 4-pin connectors were added to the sample holder to be able to measure the electron yield in the STXM chamber.

2.4.1.2 Liquid Sandwich for TEY

As in conventional TEY, photons come through the thin electrode, only electrons generated within 5 *nm* of the electrode are expected to be detected. Therefore, the thickness of the sample is not as important as the transmission detection methods. To

prepare the liquid sandwich, a silicon wafer was used as a base behind the plastic sample holder (see Figure 2.17). The liquid was added into the hole (sample window) on the sample holder, and a gold coated Si_3N_4 window was used as the top part of the liquid sandwich. The schematic of this process is presented in Figure 2.17. The gold layer was coated on the window using the physical vapor deposition. The gold layer was electrically connected to the copper wires on the plastic sample holder and connected to a high sensitivity ammeter. Although, the TEY approach was explored for the liquid *n*-alkane samples, the experimental measurements did not lead to reliable spectra. Therefore, these measurements are not presented in this thesis.

2.4.2 FY Measurements

As presented in section §2.2.2.3, fluorescence detection is a bulk sensitive method. Figure 2.11 presents the arrangement of the fluorescence detector in the STXM chamber at CLS. In the beamline, by carefully positioning the Fluorescence detector relative to the Order Sorting Aperture (OSA), it is possible to eliminate most of the background signals from both the laser interferometer and the X-rays scattered/emitted from the OSA. It is possible to discriminate fluorescence from different edges by using a proportional detector with adequate energy resolution.[21, 34] In this work, we used an Amptek™ X123 Silicon Drift Detector (SDD), which works based on the Energy Dispersive Spectroscopy approach to detect the elemental composition of the studied system based on the energy of the electrons that are ejected. [21, 34] Figure 2.18 shows the sample holder that was used for the FY measurements.

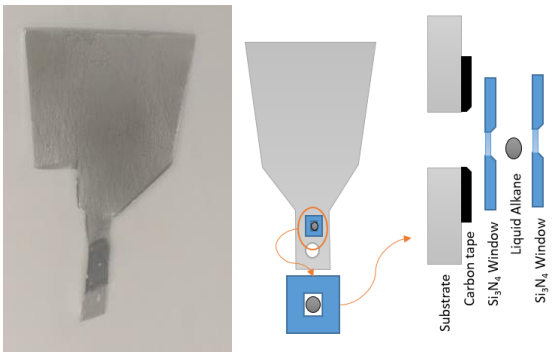

Figure 2.18 - Sample holder for the FY measurements

In this method, thin areas of the liquid sample were located using the transmission detector, and the spectroscopy was done using the fluorescent detector. Similar to the TEY approach, the FY approach was explored for the liquid *n*-alkane samples, but the results are not presented in this thesis as in all the measured spectra, the peak from the laser interferometer had an overlap with the carbon edge and it was not possible to obtain the carbon 1s NEXAFS spectra for the liquid samples.

2.4.3 Transmission Mode Measurements

Because of the volatility of liquid *n*-alkanes, the liquid must be trapped in a sealed cell. Various low-stress silicon nitride (Si_3N_4) windows (Norcada Inc.) have been examined to obtain the optimized sample thickness for the X-ray spectroscopy measurements. The schematic and the real photo of the liquid sample for transmission measurement is presented in Figure 2.19

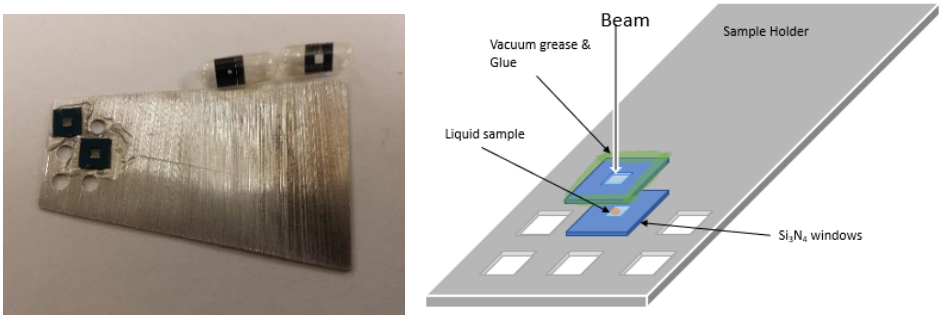

Figure 2.19 - A schematic(right) and a real photo of the sample (left) for the transmission measurements

Figure 2.20 shows the calculated optical density of a 100 nm of *n*-$C_{12}H_{26}$ trapped between two 100 nm low-stress Si_3N_4 windows. This is only the atomic cross-section and not the near-edge component. As can be observed, even with only 100 nm of the liquid, the optical density drops by about 30%. So, variations in the thickness must be controlled to keep consistency in the high level.

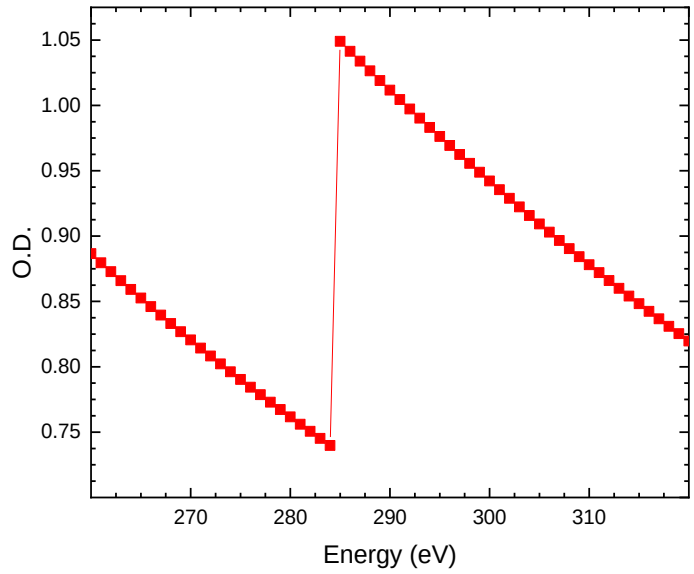

Figure 2.20 - Calculated optical density of 100 nm of n-$C_{12}H_{26}$ trapped between two 100 nm Si_3N_4 windows.

There are a few challenges with this simple design.

- **The thickness of the cell**: It is difficult to have a consistent sample thickness as the volatility of the liquid and the speed of cell assembly affect the outcome. If the thickness is too low, the optical density will be low, and the signal to noise ratio will decrease (noise will increase). A thick sample will have more distortion as well as more noise in the spectra.
- **Movement of the top window during the preparation process:** As the two windows are not fixed, the top window can move during the sealing process. Because of the surface tension between the liquid and both windows, this movement can break one or both windows and lead to the liquid evaporating before the experiment even starts. This movement could also lead to contamination as the sample can get in contact with the carbon tape and glue on the sample holder.
- **The requirement of glue and vacuum grease:**The liquid is very volatile. If too much liquid is added to the cell, the cell can break the window or start to leak from the sides. As the liquids are light *n*-alkanes, they can easily dissolve the vacuum

grease and glue used to secure the windows, which can lead to contamination of the liquid sample.

To have more control over the thickness of the samples and overcome other issues in the simple transmission design, new sample holders were prepared using 3d printers. The schematic and a real photo of these sample holders are presented in Figure 2.21. Liquid samples were prepared in a cell consisting of two 50 nm thick low-stress silicon nitride (Si_3N_4) windows (Norcada Inc.). One of the windows in the pair had a thin spacer on the frame (50 nm silicon + 50 nm gold), to control window separation.

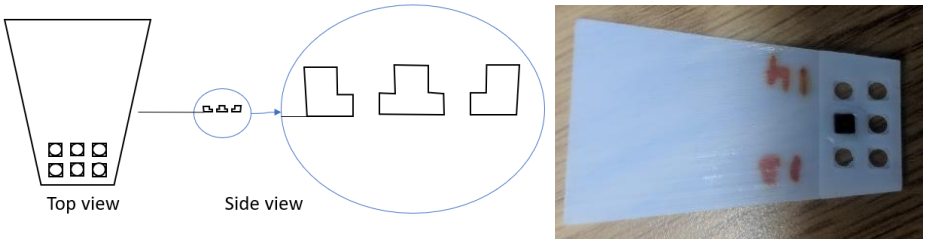

Figure 2.21 - 3D printed sample holders for the transmission measurements

In this method, the need for glue is removed by having a space that both windows will fit tightly into. The bottom window (which has the spacer) is placed in one of the holes, and a small drop of liquid is added on top of this window. Since it is not possible to control the exact amount of the liquid in the cell, this droplet is allowed to evaporate partially until it only covers the window part of the bottom frame. The top window will be added then, making sure that liquid stays only within the windows part of the top and bottom frames. This way, the liquid will not leak from the cell (because of the spacers, which will make a seal). As both windows will fit in the hole, the movements of the top window will not occur.

The summary of pros and cons of each of these detection techniques are presented in the following table.

Table 2.1. Pros and cons of various detection techniques in the STXM chamber

Technique	Pros	Cons
TEY	• Surface sensitive/No thickness effects	• Liquids are not conductive
FY	• Bulk sensitive/no thickness effect	• Low signal in the carbon edge • Self-absorption
Transmission	• Minimized exposure time/less radiation damage • Possibility of image + spectra measurements in a microscope	• Poor control of thickness

2.5 Sample Characterization by Optical Microscopy (OM)

The initial characterization of the liquid cells (color interference and the existence of liquid after sealing) was done using a Nikon Eclipse ME600 reflection microscope with a Q-Imaging Charged Coupled Device (CCD) camera that was connected to the optical microscope. These measurements were done to make sure that some liquid is present in the sample holder, and it does not look too thick.

2.6 References

1. Silzer R. M., B. R., Bergstrom J., Dallin L., Shen X., and Vogt J. M. In *Injection System for the Canadian Light Source*, Proceedings of EPAC, Lucerne, Switzerland, Lucerne, Switzerland, **2004**.

2. Willmott, P., *An Introduction to Synchrotron Radiation Techniques and Applications Introduction*. John Wiley & Sons: **2019**; p 483.

3. Shenoy, G., Basic Characteristics of Synchrotron Radiation. *Structural Chemistry* **2003,** *14* (1), 3-14.

4. Mobilio S., B. F., Meneghini C., *Synchrotron Radiation: Basics, Methods and Applications*. Springer-Verlag Berlin Heidelberg: New Delhi, India, **2015**.

5. Hähner, G., Near edge X-ray absorption fine structure spectroscopy as a tool to probe electronic and structural properties of thin organic films and liquids. *Chemical Society Reviews* **2006,** *35* (12), 1244-1255.

6. Von, V. Coherent X-ray diffraction studies of mesoscopic materials, PhD. Thesis. University of Hamburg, Hamburg, **2015**.

7. Attwood D., S. A., *X-Rays and Extreme Ultraviolet Radiation Principles and Applications*. **2017**.

8. Margaritondo, G., *Elements of synchrotron light for biology, chemistry, & medical research*. Oxford University Press Inc.: New York, **2002**.

9. Margaritondo, G., *Introduction to Synchrotron Radiation*. Oxford University Press: New York, **1988**.

10. Stöhr, J., *NEXAFS Spectroscopy*. Springer, Springer Series in Surface Sciences,: Berlin; London, **1992**; Vol. 25, p 404.

11. Walsh, R. Polarization: Linear and circular polarizations - 2019. https://www.japanistry.com/polarization/ (accessed February 11, 2020).

12. Yadavalli, N. S. Advances in Experimental Methods to Probe Surface Relief Grating Formation Mechanism in Photosensitive Materials, PhD. Thesis. University of Potsdam, Potsdam, Germany, **2014**.

13. H. A. Durr, T. E., H. Elmers, S. Eisebitt, M. Farle, W. Kuch, F. Matthes, M. Martins, H. Mertins, P. M. Oppeneer, L. Plucinski, C. M. Schneider, H. Wende, W. Wurth, H. Zabel, A Closer Look Into Magnetism: Opportunities With Synchrotron Radiation. *IEEE Transactions on Magnetics* **2009,** *45* (1), 15-57.

14. Johansson, M., Anderberg, Bengt, Lindgren, Lars-Johan,, Magnet design for a low-emittance storage ring. *Journal of Synchrotron Radiation* **2014,** *21* (5), 884-903.

15. Eriksson, M., van der Veen, J. Friso, Quitmann, Christoph, Diffraction-limited storage rings - a window to the science of tomorrow. *Journal of Synchrotron Radiation* **2014,** *21* (5), 837-842.

16. Watts, B., Thomsen, L., Dastoor, P. C., Methods in carbon K-edge NEXAFS: Experiment and analysis. *Journal of Electron Spectroscopy and Related Phenomena* **2006,** *151* (2), 105-120.

17. Kilcoyne, A. L. D., Tyliszczak, T., Steele, W. F., Fakra, S., Hitchcock, P., Franck, K., Anderson, E., Harteneck, B., Rightor, E. G., Mitchell, G. E., Hitchcock, A. P., Yang, L., Warwick, T., Ade, H.,, Interferometer-controlled scanning transmission X-ray microscopes at the Advanced Light Source. *Journal of Synchrotron Radiation* **2003,** *10* (2), 125-136.

18. Henke, B. L., Gullikson, E. M., Davis, J. C., X-Ray Interactions: Photoabsorption, Scattering, Transmission, and Reflection at E = 50-30,000 eV, Z = 1-92. *Atomic Data and Nuclear Data Tables* **1993,** *54* (2), 181-342.

19. Hitchcock, A. P., Mancini, D. C., Bibliography and database of inner shell excitation spectra of gas phase atoms and molecules. *Journal of Electron Spectroscopy and Related Phenomena* **1994,** *67* (1), vii.

20. Hitchcock, A. P. *aXis 2000*, Hamilton, ON, **2017**.

21. Hitchcock, A. P., Obst, M., Wang, J., Lu, Y. S., Tyliszczak, T., Advances in the Detection of As in Environmental Samples Using Low Energy X-ray Fluorescence in a Scanning Transmission X-ray Microscope: Arsenic Immobilization by an Fe(II)-Oxidizing Freshwater Bacteria. *Environmental Science & Technology* **2012,** *46* (5), 2821-2829.

22. Kaznatcheev, K. V., Karunakaran, Ch, Lanke, U. D., Urquhart, S. G., Obst, M., Hitchcock, A. P., Soft X-ray Spectromicroscopy Beamline at the CLS: Commissioning Results. *Nucl. Instrum. Methods Phys. Res., Sect. A* **2007,** *582* (1), 96-99.

23. Hitchcock, A. P., Toney, Michael F.,, Spectromicroscopy and coherent diffraction imaging: focus on energy materials applications. *Journal of Synchrotron Radiation* **2014,** *21* (5), 1019-1030.

24. Hitchcock, A. P., Dynes, James J., Johansson, Göran, Wang, Jian, Botton, Gianluigi, Comparison of NEXAFS microscopy and TEM-EELS for studies of soft matter. *Micron* **2008,** *39* (6), 741-748.

25. Warwick, T., Ade, Harald, Kilcoyne, David, Kritscher, Michael, Tylisczcak, Tolek, Fakra, Sirine, Hitchcock, Adam, Hitchcock, Peter, Padmore, Howard, A new bend-magnet beamline for scanning transmission X-ray microscopy at the Advanced Light Source. *Journal of Synchrotron Radiation* **2002,** *9* (4), 254-257.

26. Otero, E. Soft X-ray Spectroscopy of Organic and Organometallic Molecules and Polymers, PhD. Thesis. University of Saskatchewan, **2008**.

27. Perera, S. D. Systematic Investigation of Intermolecular Interactions in NEXAFS Spectroscopy, PhD. Thesis. University of Saskatchewan, **2018**.

28. Jacobsen, W., Flynn, Zimba, Soft X-ray spectroscopy from image sequences with sub-100 nm spatial resolution. *Journal of Microscopy* **2000,** *197* (2), 173-184.

29. Coffey, T., Urquhart, S. G., Ade, H., Characterization of the Effects of Soft X-Ray Irradiation on Polymers. *Journal of Electron Spectroscopy and Related Phenomena* **2002,** *122* (1), 65-78.

30. Ma, Y., Chen, C. T., Meigs, G., Randall, K., Sette, F., High-resolution K-shell photoabsorption measurements of simple molecules. *Physical Review A* **1991,** *44* (3), 1848-1858.

31. Goncz, K. K., Batson, P., Ciarlo, D., Loo Jr, B. W., Rothman, S. S., An environmental sample chamber for X-ray microscopy. *Journal of Microscopy* **1992,** *168* (1), 101-110.

32. Neuhausler, U., Jacobsen, Chris, Schulze, Darrell, Stott, Diane, Abend, Sven,, A specimen chamber for soft X-ray spectromicroscopy on aqueous and liquid samples. *Journal of Synchrotron Radiation* **2000,** *7* (2), 110-112.

33. Nagasaka, M., Hatsui, Takaki, Horigome, Toshio, Hamamura, Yutaka, Kosugi, Nobuhiro, Development of a liquid flow cell to measure soft X-ray absorption in transmission mode: A test for liquid water. *Journal of Electron Spectroscopy and Related Phenomena* **2010,** *177* (2), 130-134.

34. Zhou, J., Wang, Jian, Cutler, Jeffrey, Hu, Enyuan, Yang, Xiao-Qing, Imaging the surface morphology, chemistry and conductivity of LiNi1/3Fe1/3Mn4/3O4 crystalline facets using scanning transmission X-ray microscopy. *Physical Chemistry Chemical Physics* **2016,** *18* (33), 22789-22793.

Chapter 3 – Computational Methodology

The main objectives of this thesis are to understand the effect of structural differences (e.g., chain length) and the role of disorder (e.g., geometry defects, thermally populated vibrations) on the NEXAFS spectra of *n*-alkanes. Using computational modeling and experimental measurements, the effect of chain length, phase change, geometry defects, and thermally populated vibrations on the NEXAFS spectra of *n*-alkanes are measured. A methodology is explored to calculate the degree of Rydberg-valence mixing in molecules using DFT calculations. Also, using Molecular Dynamics - Density Functional Theory (MD-DFT) simulations, initial steps are taken toward understanding the effect of disorder on the NEXAFS spectra of liquid *n*-alkanes. As the DFT is the main approach to all the computational studies in this thesis project, this chapter will describe the quantum chemistry background behind these DFT studies.

3.1 Background

Classical mechanics accurately describes the motion and position of objects if the study is restricted to large objects and non-relativistic speeds. This approach will not be useful in the case of microscopic objects such as electrons and nuclei. QM describes the properties of microscopic objects in terms of their wave character. Using QM, various observables such as position, momentum, and energy can be obtained.

In 1926 Erwin Schrödinger formulated the time-dependent Schrödinger's Equation (SE) to describe the behaviour of microscopic particles.[1]

$$-\frac{\hbar}{i}\frac{\partial\Psi(x,t)}{\partial t} = -\frac{\hbar^2}{2m}\frac{\partial^2\Psi(x,t)}{\partial x^2} + V(x,t)\Psi(x,t) \qquad \textit{Equation 3.1}$$

In this equation, the term $-\frac{\hbar^2}{2m}\frac{d^2}{dx^2} + V(x)$ is an alternative form of Newton's equations of motion and is known as the Hamiltonian operator for the system. The Hamiltonian operator can be expressed in the form of the kinetic and potential energy operators, as follows:

$$\hat{H} = \hat{T} + \hat{V} = -\frac{\hbar^2}{2m}\frac{d^2}{dx^2} + V(x) \qquad \textit{Equation 3.2}$$

In this equation, $\hat{\mathrm{T}}$ and $\hat{\mathrm{V}}$ are the kinetic and the potential energy operators for the system, respectively, and $\hat{H}$ is the Hamiltonian. As it is often impractical (or unnecessary for closed systems with no time-varying potentials) to use the time-dependent form of the Schrödinger equation, the time-independent SE is often used. The one-dimensional time-independent SE is written as follows:

$$-\frac{\hbar^2}{2m}\frac{d^2\psi(x)}{dx^2} + V(x)\psi(x) = E\psi(x) \qquad \textit{Equation 3.3}$$

Using the Laplacian operator, ∇^2, it is possible to express this equation in the form of the three-dimensional, time-independent SE as follows:

$$-\frac{\hbar^2}{2m}\vec{\nabla}^2\psi + V\psi = E\psi \qquad \textit{Equation 3.4}$$

The Laplacian operator can be expressed in cartesian coordinates, as follows:

$$\nabla^2 = \frac{\partial^2}{\partial x^2} + \frac{\partial^2}{\partial y^2} + \frac{\partial^2}{\partial z^2} \qquad \textit{Equation 3.5}$$

There are four common ways to calculate molecular structure. The first one, Molecular Mechanics (MM), is a classical approach which leads to the structure while the other three approaches will lead to the geometry and electronic structure of molecules.[2-3]

- **MM** uses the classical mechanics approaches to solve the molecular structure and does not use the Hamiltonian operator or wavefunction.[3]
- **Semiempirical methods** use a simplified Hamiltonian with parameters based on experimental results (or results calculated at a higher level) in place of more complex calculations.
- ***ab initio* (first principle)** is a MO-based approach that uses the correct Hamiltonian without including any experimental parameters other than the fundamental physical constants.[2] The **Hartree-Fock (HF)** method is a common *ab initio* technique used to calculate molecular properties.[2]

- **DFT** calculates the molecular electron density (ρ), and uses this density to calculate the molecular energy. In this approach, the properties of the many-body system are calculated using functionals.[2-3]

3.1.1 The Many-Body Problem

The many-body problem deals with the complex systems with more than one quantum particle, such as more than one electron in an atom. In such systems, the calculation needs to address electron-electron and/or nuclear-nuclear interactions. If we neglect spin-orbit interactions and assume the nuclei to be point masses, then the Hamiltonian operator of a hypothetical molecule can be expressed as:[2]

$$\hat{H} = -\frac{\hbar^2}{2m_e}\sum_i \nabla_i^2 - \frac{\hbar^2}{2}\sum_\alpha \frac{\nabla_\alpha^2}{m_\alpha} + \sum_\alpha \sum_{\beta>\alpha} \frac{Z_\alpha Z_\beta e^2}{4\pi\varepsilon_0 r_{\alpha\beta}} + \sum_\alpha \sum_i \frac{Z_\alpha e^2}{4\pi\varepsilon_0 r_{i\alpha}} + \sum_j \sum_{i>j} \frac{e^2}{4\pi\varepsilon_0 r_{ij}} \quad \textit{Equation 3.6}$$

In this equation, *i* and *j* are the indices of electrons, and α and β are the indices of nuclei. Z_α and Z_β are the atomic numbers of atoms with indices of α and β. Also, $r_{ij}, r_{i\alpha}$ and $R_{\alpha\beta}$ represent electron-electron, electron-nuclei, and nuclei-nuclei distances, respectively. In this Hamiltonian operator, the first two terms are the kinetic energy operators for electrons and nuclei, respectively, and the latter three terms are potential energy operators for nuclear-nuclear, electron-nuclear, and electron-electron coulombic interactions. So, the Hamiltonian can be presented as follows:

$$\hat{H} = \hat{T} + \hat{T}_n + \hat{V}_{nn} + \hat{V}_{ne} + \hat{U}_{ee} \quad \textit{Equation 3.7}$$

where the $\hat{T}$ and $\hat{T}_n$ are the kinetic energy operators of the electrons and nuclei of the system respectively and $\hat{\mathrm{V}}_{\mathrm{nn}}$, $\hat{\mathrm{V}}_{\mathrm{ne}}$ and, $\hat{\mathrm{U}}_{\mathrm{ee}}$ are the nuclei-nuclei repulsion, nuclei-electron coulombic attraction, and electron-electron repulsion potential energy operators, respectively. These terms are as follows:

$$\hat{T} = -\frac{\hbar^2}{2m_e}\sum_i \nabla_i^2 \quad \textit{Equation 3.8}$$

$$\hat{T}_n = -\frac{\hbar^2}{2}\sum_\alpha \frac{\nabla_\alpha^2}{m_\alpha} \quad \textit{Equation 3.9}$$

$$\hat{V}_{nn} = \sum_\alpha \sum_{\beta>\alpha} \frac{Z_\alpha Z_\beta e^2}{4\pi\varepsilon_0 r_{\alpha\beta}} \quad \textit{Equation 3.10}$$

$$\hat{V}_{ne} = \sum_\alpha \sum_i \frac{Z_\alpha e^2}{4\pi\varepsilon_0 r_{i\alpha}} \quad \textit{Equation 3.11}$$

$$\widehat{U}_{ee} = \sum_j \sum_{i>j} \frac{e^2}{4\pi\varepsilon_0 r_{ij}}$$ *Equation 3.12*

The exact solution to the SE is only known for very simple systems (hydrogenic atoms and H_2^+, within the BO approximation) since it is impossible to analytically solve the SE for more complicated systems.[2-3] Therefore, various approximations are required to simplify the equation down to a level that can be solved computationally. The BO approximation is used to treat the nuclear motion as a parameter.[2] The Linear Combination of Atomic Orbitals (LCAO) approximation along with the variational theorem in an SCF approach, are used to approximate a solution to the SE. These approximations are explained in the following sections.

3.1.2 The Born-Oppenheimer (BO) Approximation

Because nuclei are much heavier than electrons, electrons can move much faster than nuclei. As an approximation, nuclear motion can be considered to be negligible on the timescale of electronic motion. Hence, it is possible to treat nuclei as fixed particles while solving for the wavefunction of electrons. This allows us to separate the electronic and nuclei terms of the Hamiltonian operator, and exclude the term representing the kinetic energy of nuclei from the equation. Also, instead of total energy as the eigenvalue of the SE, the electronic energy will be obtained.

$$\left(\widehat{H}_{electron} + V_{electron}\right)\psi_{electron} = U\psi_{electron}$$ *Equation 3.13*

As the kinetic and potential terms for nuclei are removed, the pure electronic Hamiltonian is:

$$\widehat{H}_{electron} = -\frac{\hbar^2}{2m_e}\sum_i \nabla_i^2 + \sum_\alpha \sum_i \frac{Z_\alpha e^2}{4\pi\varepsilon_0 r_{i\alpha}} + \sum_j \sum_{i>j} \frac{e^2}{4\pi\varepsilon_0 r_{ij}}$$ *Equation 3.14*

Within the BO approximation, nuclear coordinates can be considered as parameters, and the electron properties are calculated for each value of the nuclear coordinate parameter.[2-3]

For a diatomic molecule, the SE for nuclear motion is presented as follows:

$$\left[-\frac{\hbar^2}{2m_\alpha}\nabla_\alpha^2 - \frac{\hbar^2}{2m_\beta}\nabla_\beta^2 + U(\vec{r})\right]\psi_N = E\psi_N$$ *Equation 3.15*

In this equation α and β are the nuclei, and ψ_N is the nuclear motion wavefunction. This nuclear motion wavefunction can be separated into terms based on the translational motion of the entire molecule (e.g., the motion of the centre of mass) and the motion of the nuclei relative to each other (e.g., internal motion).[2-3]

$$\psi_N = \psi_{N,tr}\psi_{N,int} \quad \textit{and} \quad E = E_{tr} + E_{int} \qquad \textit{Equation 3.16}$$

In this equation, ψ_N is the nuclear motion wavefunction, $\psi_{N,tr}$ is the translational motion of the entire molecule, $\psi_{N,int}$ is the internal motion (motion of the nuclei relative to each other) and E_{tr} and E_{int} are the energies corresponding to these motions. Also, E is the total molecular energy and can be presented as follows:

$$E \approx E_{tr} + E_{rot} + E_{vib} + E_{elec} \qquad \textit{Equation 3.17}$$

These topics will not be further discussed since they are outside the scope of this thesis.

3.1.3 Variational Theorem

The variational method is an approximation used in QM to estimate the energy of the system. According to the variational theory, the calculated energy for any normalized trial wavefunction is always an upper bound of the system's exact ground state energy.

$$\int \phi^* \hat{H} \phi \, d\tau \geq E_1 \qquad \phi \; normalized \qquad \textit{Equation 3.18}^2$$

In this equation, ϕ is known as the trial variation function, $\hat{H}$ is the time-independent Hamiltonian operator and E_1 is the exact ground state energy. This equation will change to the following for the trial functions that are not normalized:

$$\frac{\int \phi^* \hat{H} \phi d\tau}{\int \phi^* \phi d\tau} \geq E_1 \qquad \textit{Equation 3.19}^2$$

In this theorem, trial variation functions are examined to minimize the variational integral ($\int \phi^* \hat{\mathrm{H}} \phi \, \mathrm{d}\tau$) as a function of the variables of the system and obtain energy close to the E_1. It turns out that the variational energy approaches E_1 much faster than the trial variation function approaches the exact wavefunction (ψ_1). This means that although a good trial wavefunction will lead to a good approximation of the E_1, it is possible to get a good approximation of the E_1 using a poor trial wavefunction.[2]

3.2 Molecular Orbital Theory

Molecular Orbital (MO) theory has been the dominant electronic structure theory in chemistry and many of the computational studies. In this theory, each electron in the system is described by a wavefunction (ψ), and, an MO, which is the solution to the SE, is defined as the area around the molecule with the highest possibility of finding the electron ($|\psi|^2$).[2, 4]

The analytical solution to the SE equation is only possible for systems as simple as H_2^+ by using the BO approximation. For more complicated systems, additional approximations are needed to simplify the equation. The LCAO-MO method treats molecular orbitals as orbitals constructed by the quantum superposition of AOs, each weighted by a coefficient, a_{ij}. A linear combination of AOs will lead to an approximate wavefunction for the MO.

$$\psi_i = \sum_{v=1}^{k} c_{vi}\phi_v \qquad \textit{Equation 3.20}^2$$

In this equation, ψ_i is the wavefunction of a given MO, and, ϕ_v and c_{vi} represent the atomic orbital and their atomic coefficients, respectively.

3.3 Hartree-Fock (HF) Method

HF is one of the approaches that will help to find an approximate solution to the SE. Using the variational theory and by approximating interelectronic repulsion in the solution to the Hamiltonian, it is possible to use a product of one-electron wavefunctions to describe the many-electron wavefunction.

$$\Psi = \psi_{a,\alpha}(1)\psi_{a,\beta}(2)\ldots\psi_{z,\beta}(N) \qquad \textit{Equation 3.21}^4$$

The wavefunction is anti-symmetric on account of the Pauli exclusion principle. The antisymmetric requirement expresses that two electrons with the same spin (m_s) have zero probability of being found in the same position (same x, y, and z), and therefore will be forced to keep apart from each other. The wavefunction must be antisymmetric under exchange of any two particles. Therefore, this anti-symmetric many electron wavefunction can be written as the following determinant:

$$\Psi = \frac{1}{\sqrt{N!}} det\left|\psi_{a,\alpha}(1)\psi_{a,\beta}(2) \ldots \psi_{z,\beta}(N)\right| \quad \textit{Equation 3.22}^{4}$$

The HF equation for the lowest energy wavefunction can be written as follows:

$$f_1\psi_{a,\sigma}(1) = \varepsilon_1\psi_{a,\sigma}(1) \quad \textit{Equation 3.23}$$

In this equation, α or β are the spins of the electrons and σ is either α or β. The "1" subscripti following the Fock operator (and later the Hamiltonian) indicates the one-electron nature of the operator. The Fock operator (f_1) is expressed as follows:

$$f_1 = h_1 + \sum_j \left\{2J_j(1) - K_j(1)\right\} \quad \textit{Equation 3.24}^{4}$$

In this equation, h_1 is the one-electron core Hamiltonian ($h_1 = -\frac{\hbar^2}{2m_e}\nabla_1^2 - \sum_n \frac{Z_n e^2}{4\pi\varepsilon_0 r_{ni}}$). Also, J and K are the Coulomb operator and exchange operator, respectively. These two terms are expressed as follows:

$$J_j(1)f_1 = f_1 \int \left|\psi_j(2)\right|^2 \frac{1}{r_{12}} dv_2 \quad \textit{Equation 3.25}^{2}$$

$$K_j(1)f_1 = \psi_j(1) \int \frac{\psi_j^*(2)f_2}{r_{12}} dv_2 \quad \textit{Equation 3.26}^{2}$$

Several approximations, such as LCAO, are required to find an accurate wavefunction for systems that are more complicated than the hydrogenic atom. The next step is to solve one electron's wavefunction in the static potential of the other electrons. The solved wavefunction is used in the equation, and this process is then repeated until the changes in the calculated energy of each cycle is lower than a defined threshold. This process, also known as Self-Consistent Field (SCF) process, will lead to a set of MOs with their energy and is the most time-consuming part of the calculations. The properties of the system will be calculated using the energy-optimized system after the SCF is converged.[2, 4]

3.4 Density Functional Theory (DFT)

The wavefunction of a many-body system contains more information than necessary, and this often complicates calculations by adding unnecessary parameters. DFT uses the electron density of the system to calculate the desired molecular

properties.[2, 5] This method describes the many-body interacting system through its density and not the wavefunction of each electron. Figure 3.1 presents a schematic of the many-body problem from the point of classical computational approach compared with the DFT approach.

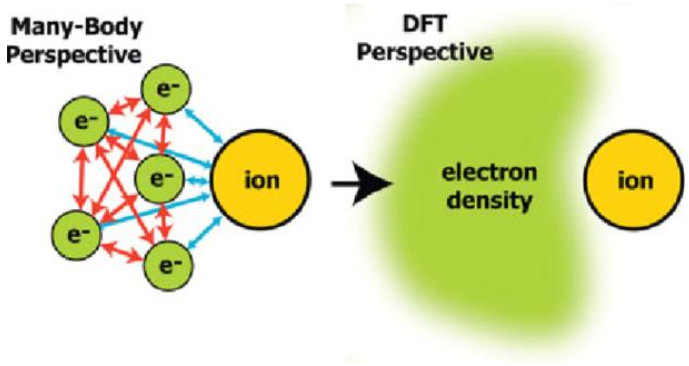

Figure 3.1 - The DFT approach, in comparison with the common many-body approach. Figure is reprinted with permission.[6]

An N-body system has a 3N degree of freedom. The main advantage of using the DFT approach is the fact that it reduces the degrees of freedom to only 3 (x, y, z) by defining an overall density grid for the system. The functional notation is used because DFT uses functionals ($F[f]$), which are functions of functions, to solve for properties. There are a few theorems that describe molecular properties based on the electronic density. Some of these theorems are explained in the following section.

3.4.1 Hohenberg-Kohn Theorem

The Hohenberg-Kohn theorem expresses the ground-state electronic energy (E_0) as a functional of the ground state density (ρ_0).[2]

$$E_0 = E_0[\rho_0] \qquad \textit{Equation 3.27}^2$$

In this theorem, the interaction between electron i and the nuclei is called the **external potential** ($v(r_i)$), expressed as:

$$v(r_i) = -\sum_\alpha \frac{Z_\alpha}{r_{i\alpha}} \qquad \textit{Equation 3.28}^2$$

Generally, the external potential is a function of the coordinates (x_i, y_i, z_i) of electron i as well as the nuclear coordinates, but within the BO approximation, it can be

expressed as a function of electron coordinates. Pure electronic Hamiltonian can be written as follows:

$$\widehat{H}_{electron} = -\frac{1}{2}\sum_{i=1}^{n}\nabla_i^2 + \sum_{i=1}^{n} v(r_i) + \sum_j \sum_{i>j} \frac{1}{r_{ij}} \qquad \textit{Equation 3.29}^2$$

where *i* and *j* are electrons and $\mathrm{v(r_i)}$ is the external potential. r_{ij} is the distance between electrons *i* and *j*. Based on this theorem, the following relation exists:

$$E_0 = E_v[\rho_0] = \int \rho_0(r)v(r)dr + \bar{T}[\rho_o] + \bar{V}_{ee}[\rho_o] = \int \rho_0(r)v(r)dr + F[\rho_o] \qquad \textit{quation 3.30}^2$$

In this equation, ρ_0 is the true ground-state electron density, $\bar{T}[\rho_o]$ is the average kinetic energy term, $\bar{V}_{ee}[\rho_o]$ is the electron-electron repulsion and $\int \rho_0(r)v(r)dr = \bar{V}_{\mathrm{N}e}[\rho_o]$ is the electron-nuclear interaction. Value of $\bar{V}_{\mathrm{N}e}[\rho_o]$ is obtained using the integral, but the other two values are unknown ($F[\rho_o] = \bar{T}[\rho_o] + \bar{V}_{ee}[\rho_o]$). Therefore, this method does not provide a practical way to calculate the ground state energy from the ground state density.[2]

3.4.2 Hohenberg-Kohn Variational Theorem

The Hohenberg-Kohn variational theorem states that the ground state electron probability density ($\rho_0(r)$) determines the external potential.[2] The energy of the ground state and excited states can be obtained from the ground state electron density. Hohenberg and Kohn proved that for every trial density function (ρ_{tr}) that satisfies $\rho_{tr}(r) \geq 0$ and $\int \rho_{tr}(r)dr = n$, where n is the total number of electrons in the system, for all *r* values, the following relation exists:

$$E_0 \leq E_v[\rho_{tr}(r)] \qquad \textit{Equation 3.31}$$

Where E_v is the energy functional in the main Hohenberg-Kohn theorem. (Equation 3.29).

Using this theorem, Equation 3.29 changes to the following equation, which represents the Hohenberg-Kohn variational theorem.

$$\bar{T}[\rho_{tr}] + \bar{V}_{ee}[\rho_{tr}] + \int \rho_{tr}v(r)dr \geq E_v[\rho_o] \qquad \textit{Equation 3.32}$$

In this equation, both $\overline{\mathrm{T}}$ and $\overline{\mathrm{V}}_{\mathrm{ee}}$ functionals are the same as the previous theorem, and only functions are changed from ρ_0 to ρ_{tr} which is the trial electron density. Similar to the variational theorem, the calculated ground state energy using the Hohenberg-Kohen theorem, is always in the upper bound of the true ground state energy.[2]

3.4.3 **Kohn-Sham (KS) Method**

Based on the Hohenberg-Kohn theorem, it is possible to calculate all of the ground state molecular properties from the ground state density without having to find the wavefunction first.[2, 4] The main issue is that in the Hohenberg-Kohn theorem, the sum of average kinetic energy and average electron-electron repulsion ($F[\rho_o] = \bar{T}[\rho_o] + \bar{V}_{ee}[\rho_o]$) is unknown and not practical to calculate. Kohn and Sham considered a many-electron system as a system of *n* non-interacting electrons that each experience the same external potential-energy function ($v_s(r_i)$). The ground state probability density ($\rho_s(r)$) is assumed to be equal to the ground-state electron density ($\rho_0(r)$) of the molecule that is being studied. Considering the symmetry requirements, the antisymmetrized product of the lowest-energy KS spin-orbitals (u_i^{KS}) of the non-interacting system, can be written as:

$$\psi_{s,0} = |u_1^{KS} u_2^{KS} \dots u_n^{KS}| \qquad \textit{Equation 3.33}$$

This is also known as the Slater determinant. In this determinant, $u_1^{KS} = \theta_i^{KS}(r_i)\sigma_i$ with σ_i and $\theta_i^{KS}(r_i)$ corresponding to the spin part and the spatial part of each spin-orbital. Therefore, the following relation exists:

$$\hat{h}_i^{KS}\theta_i^{KS} = \varepsilon_i^{KS}\theta_i^{KS} \qquad \textit{Equation 3.34}$$

In this equation, $\hat{h}_i^{KS}$ is the one-electron KS Hamiltonian and, ε_i^{KS} is the KS orbital energy. Since in this representation, the electrons are not interacting with each other but with the average potential-energy function ($v_s(r_i)$). Therefore, the Hamiltonian can be expressed as:

$$\hat{H}_s = \sum_{i=1}^{n}\left[-\frac{1}{2}\nabla_i^2 + v_s(r_i)\right] \equiv \sum_{i=1}^{n}\hat{h}_i^{KS} \qquad \textit{Equation 3.35}$$

In this equation, $v_s(r_i)$) is the external potential energy. The one-electron KS Hamiltonian ($\hat{h}_i^{KS}$) can be expressed as follows:[2, 7]

$$\hat{h}_i^{KS} = -\frac{1}{2}\nabla_i^2 + v_s(r_i) = -\frac{1}{2}\nabla_i^2 - \frac{Z_\alpha}{|r_i - r_\alpha|} + \int \frac{\rho_s(r)}{|r_i - r|} dr + V_{xc} \quad \textit{Equation 3.36}$$

In this equation, *i* and α are indices of electron and nuclei, Z_α is the atomic number of the atom with the index of α, r_i and r_α are the positions of the electron and nuclei, $\rho_s(r)$ is the ground state probability density of the non-interacting system, and, $\mathrm{V_{xc}} = \frac{\delta E_{xc}}{\delta \rho}$ is known as the exchange-correlation potential. The Exchange-Correlation energy is obtained using the following equation based on the Hohenberg-Kohn theorem.

$$E_v[\rho] = \int \rho(r) v(r) dr + \bar{T}_s[\rho] + \frac{1}{2}\iint \frac{\rho(r_i)\rho(r_j)}{r_{ij}} dr_i dr_j + \Delta\bar{T}[\rho] + \Delta\bar{V}_{ee}[\rho] \quad \textit{Equation 3.37}$$

In this equation, $\int \rho(\mathrm{r})\mathrm{v}(\mathrm{r})\mathrm{dr}$ is the electron-nuclear interaction, $\overline{\mathrm{T}}_\mathrm{s}[\rho]$ is the average ground state kinetic energy of the non-interacting system, $\frac{1}{2}\iint \frac{\rho(\mathrm{r_i})\rho(\mathrm{r_j})}{\mathrm{r_{ij}}} \mathrm{dr_i dr_j}$ is the electron-electron interaction, $\Delta\overline{\mathrm{T}}[\rho]$ is the average ground state kinetic energy of the reference system and $\Delta\overline{\mathrm{V}}_{\mathrm{ee}}[\rho]$ is the electron-electron repulsion. The first three terms ($\int \rho(\mathrm{r})\mathrm{v}(\mathrm{r})\mathrm{dr}$, $\overline{\mathrm{T}}_\mathrm{s}[\rho]$, and, $\frac{1}{2}\iint \frac{\rho(\mathrm{r_i})\rho(\mathrm{r_j})}{\mathrm{r_{ij}}} \mathrm{dr_i dr_j}$) are easy to calculate from the density of the ground state. The last two terms ($\Delta\overline{\mathrm{T}}[\rho]$ and $\Delta\overline{\mathrm{V}}_{\mathrm{ee}}[\rho]$) are unknown and defined as the Exchange-Correlation energy functional as follows:

$$E_{xc}[\rho] \equiv \Delta\bar{T}[\rho] + \Delta\bar{V}_{ee}[\rho] \quad \textit{Equation 3.38}$$

The exchange-correlation functional is not easy to evaluate and needs to be calculated using various approximations in a self-consistent manner. The key to a good DFT calculation using the KS method is to get a good approximation to E_{xc}.Comparing results of this computational model with the experimental results of the same molecule is a good indication of the accuracy of the approximated exchange-correlation functional.[2, 7]

3.4.4 **Exchange-Correlation Functional**

The exchange-correlation functional is made up of the exchange and the correlation part. The equation of the exchange functional in DFT is similar to the exchange term in the HF theory. The difference is that the HF orbitals are replaced by the KS

orbitals. Also, the HF equation (Equation 3.39) sums over orbitals, while the DFT exchange equation sums over the electrons.

$$E_{HF} = 2\sum_{i=1}^{n/2} H_{ii}^{core} + \sum_{i=1}^{n/2}\sum_{j=1}^{n/2}\left(2J_{ij} - K_{ij}\right) + V_{NN} \qquad \textit{Equation 3.39}$$

Where J_{ij} and K_{ij} are the Coulomb operator and exchange operator, respectively (Equations 3.25 and 3.26). The DFT exchange functional equation is as follows.

$$E_x = -\frac{1}{4}\sum_{i=1}^{n}\sum_{j=1}^{n}\left\langle \theta_i^{KS}(1)\theta_j^{KS}(2)\left|\frac{1}{r_{12}}\right|\theta_j^{KS}(1)\theta_i^{KS}(2)\right\rangle \qquad \textit{Equation 3.40}$$

As the KS orbitals are expressed in a similar way to the HF orbitals, the DFT exchange energy is close to the HF exchange energy.[2, 4] The correlation part can be obtained through models such as Local-Density Approximation (LDA).[2, 4]

3.4.5 Kohn-Sham DFT Calculation Method

DFT calculations using the KS method start with an initial guess of the density (ρ) obtained by superposing the calculated electron densities of the individual atoms, given a molecular geometry. From the initial guess for $\rho(r)$, an initial estimate of the $v_{xc}(r)$ is found and used in the KS equation to find an initial estimate of the KS orbitals (θ_i^{KS}). The KS orbitals are usually expressed in terms of a set of basis functions (χ_r).

$$\theta_i^{KS} = \sum_{r=1}^{b} c_{ri}\chi_r \qquad \textit{Equation 3.41}$$

Contracted Gaussian orbitals, Slater Type Orbitals (STO) or other functions can be used as basis functions (χ_r) in the KS DFT calculation.[7]

The calculated KS orbitals are used to calculate the improved electron density and improved exchange-correlation potential ($v_{xc}(r)$) based on these orbitals. Auxiliary basis sets (in the form of contracted Gaussian-type functions) are used in most of the LCAO approaches to expand the exchange-correlation functional. This leads to the expanded form of the exchange-correlation functional as follows:

$$v_{xc} = \sum_{a}^{N} c_a G_a(r) \qquad \textit{Equation 3.42}^{8}$$

In this equation, $G_a(r)$ and c_a are Gaussian type functions and their coefficients, respectively. Using this expansion, it is possible to calculate the DFT potential integrals

over the auxiliary basis functions. At each SCF (or KS) iteration, the auxiliary basis set is fitted to the numerical form of the exchange-correlation functional.[8]

3.4.6 Exchange-Correlation Functional

LDA and GGA

LDA and Local Spin Density Approximation (LSDA) are two of the simplest approaches to solve the exchange-correlation functional as they only consider the small changes of density.[2] The LDA approximation was proposed by Hohenberg and Kohn and states that if the density varies extremely slowly with the position, then $E_{xc}[\rho]$ can be calculated using the following equation:[2]

$$E_{xc}^{LDA}[\rho] = \int \rho(r)\varepsilon_{xc}(\rho)dr \qquad \textit{Equation 3.43}^{2}$$

In this equation ε_{xc} is the exchange-correlation energy of an electron having a local electron density of ρ in a ***Jellium,*** which is a hypothetical electrically neutral system consist of the homogenous electron gas.[2, 4]

$$v_{xc}^{LDA} = \frac{\delta E_{xc}^{LDA}}{\delta\rho} = \varepsilon_{xc}\big(\rho(r)\big) + \rho(r)\frac{\partial\varepsilon_{xc}(\rho)}{\partial\rho} \qquad \textit{Equation 3.44}^{2}$$

In this equation, $\mathrm{v_{xc}^{LDA}}$ and $\mathrm{\delta E_{xc}^{LDA}}$ are the exchange-correlation potential and energy of the given system, $\mathrm{\varepsilon_{xc}}$ is the exchange-correlation energy of a Jellium, and ρ is the density of the system. The components of this exchange-correlation energy ($\varepsilon_{xc}(\rho)$) can be written separately as follows:

$$\varepsilon_{xc}(\rho) = \varepsilon_{x}(\rho) + \varepsilon_{c}(\rho) \qquad \textit{Equation 3.45}^{2}$$

In this equation, $\mathrm{\varepsilon_x(\rho)}$ is the exchange energy and $\mathrm{\varepsilon_c(\rho)}$ is the correlation energy. The correlation ($\varepsilon_c(\rho) = \varepsilon_c^{VWN}(\rho)$) is a complicated but known function of the local density, and the exchange part can be written as a function of the density (ρ) as follows:

$$\varepsilon_{x}(\rho) = -\frac{3}{4}\left(\frac{3}{\pi}\right)^{1/3}(\rho(r))^{1/3} \qquad \textit{Equation 3.46}^{2}$$

As can be observed, within this approximation, the exchange-correlation part depends mostly on the local density of electrons and does not account for the density variations across the system. Therefore, this approximation is good for systems with a

mostly homogeneous electron density.[3, 9] Complicated molecules such as *n*-alkanes do not have a homogeneous electron density across their structure, which means that the LDA would not be a good approach for these types of molecules. [2]

The LSDA is the better alternative of the LDA approximation in the case of open-shell molecules and molecular geometries near dissociation.[2, 4] In this approximation, each of the paired electrons (with the opposite spin) have their spatial orbitals known as $\theta_{i\alpha}^{KS}$ and $\theta_{i\beta}^{KS}$ orbitals for each spin. In the KS method, as the E_{xc} is approximated, it is beneficial to define different spatial orbitals for the electrons with the opposite spins to improve the calculated properties of the molecules. The approach is also known as the spin density functional theory and treats each of the electrons differently. The LSDA functional works well for calculating vibrational frequencies, molecular equilibrium geometries, dipole moments and the transition metals.[2, 4]

The Generalized Gradient Approximation (GGA), also known as the gradient-corrected approximation, and other approximations are introduced to take the effect of electron density as a function of position into consideration.[2, 4] The following equation is the representation of the GGA method.

$$E_{xc}^{GGA}\left[\rho^{\alpha},\rho^{\beta}\right]=\int \mathfrak{f}\left(\rho^{\alpha}(r),\rho^{\beta}(r),\nabla\rho^{\alpha}(r),\nabla\rho^{\beta}(r)\right)dr \qquad \textit{Equation 3.47}^{2}$$

In this equation, α and β are the electron spins, ρ is the density, and $\mathfrak{f}$ is the function used to define the spin densities and their gradients. In this approximation, the exchange and correlation parts are usually written separately and developed by the theoreticians independently.[2, 4]

$$E_{xc}^{GGA}=E_{x}^{GGA}+E_{c}^{GGA} \qquad \textit{Equation 3.48}^{2}$$

Where $\mathrm{E_x^{GGA}}$ and $\mathrm{E_c^{GGA}}$ are the exchange and correlation energy using the GGA. This process is usually done by introducing empirical parameters obtained from fitting known HF exchange energies of several atoms.[4] Another approach is the numerical approach without using any empirical numbers. In this approach, the exchange and correlation functional can be calculated independently. Generally, any exchange functional can be combined with any correlation functional to perform a calculation. A

widely used example of the numerical calculation without the empirical parameter is the Pedrew-Burke-Ernzerhof (PBE)[10] approach, which is used to calculate the exchange and correlation functional in most of the DFT calculations on solids. This approach is used for most of the calculations presented in this project.[2, 4, 10-11]

3.5 NEXAFS Spectra Simulations

3.5.1 Core-Hole Relaxation

The creation of a core hole has a significant effect on the electronic structure of the system, and therefore must be considered when simulating NEXAFS spectra. Therefore, calculating the core-hole relaxation is an expensive process because all the electrons undergo a relaxation process after the excitation step. The sudden approximation helps to simplify the core-excitation process by considering the excited electron as active and the rest of the electrons as passive. This approximation states that the excitation process of the active electron is much faster than the relaxation time of the passive electrons.[12-13] Therefore, it will be possible to write the initial and final wavefunctions for the active and passive parts, separately.[12]

The excitation process in computational studies involves the removal of the active electron from the core orbitals and (possibly) the addition of this electron to the outermost orbitals. The simplest computational approximation for the effect of the core hole is the Equivalent Ionic Core Virtual Orbital Model (EICVOM). In this model, also known as the “Z+1” model, an atom with the atomic number of “Z” is replaced by the “Z+1” atom and the electronic configuration of the molecule is changed from neutral to the cation form to keep the number of the electrons the same. This “Z+1” atom as a core potential is similar to that of the “Z” atom with a core (1s) hole. An example of this approach is changing the carbon atom to the nitrogen atom and placing a +1 charge on the molecule. The increased +1 charge on the core excited atom will remove the extra electron that comes the change to the nitrogen atom.[12, 14-15] The following figure presents a schematic of the EICVOM model.

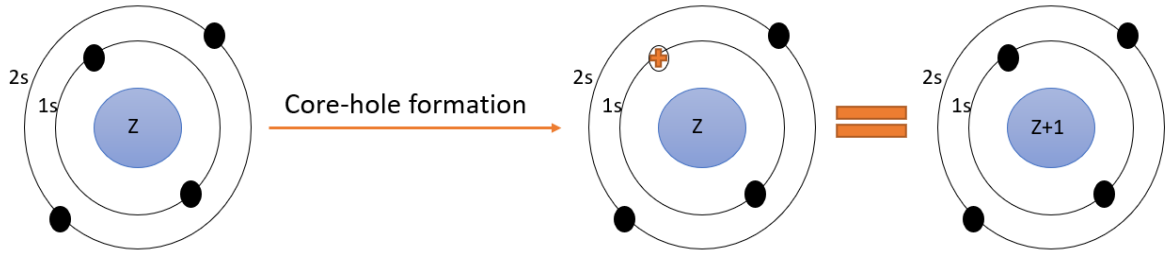

Figure 3.2 - Schematic representation of the EICVOM (Z+1) approximation

The Improved Virtual Orbital (IVO) method[16] is a more advanced method to explicitly account for the core hole, based on the modification of the Hartree-Fock operator. In this method, the static exchange Fock operator is used instead of the usual Fock operator, to account for the removal of the i^{th} electron from the usual Fock operator. The static exchange operator is then used to calculate the energy and wavefunctions of the unoccupied orbitals of the system in the presence of the core-hole. The intensity of NEXAFS transitions can, then, be calculated from the IVO energy and wavefunctions without the need to perform an extensive state-by-state calculations of each core excited state.[16]

H. Oji *et al.*[17] used the IVO approach to take the core-hole effect into account for the MO energy calculations. These authors observed a different relaxation effect for each of the unoccupied π MOs in benzene as well as a shift to the lower energy of these MOs in the excited state compared to the ground state. The energy (relative to the IP) and intensity of transitions of the carbon 1s NEXAFS spectra are obtained from the MO energies as well as the TDM. A deviation between the calculated DOUS (density of unoccupied states) and the NEXAFS spectra is observed, which is attributed to the core excitation effect, which affects the MO energies directly. This shows the importance of the calculation of core-hole relaxation on the final MO energy calculations in the excited state.[17]

The IVO approach leads to more accurate results compared to the Z+1 approach since it better accounts for the core-hole effect. However, in an actual NEXAFS transition, the electron in the excited orbital will interact with the passive part of the system. This shielding interaction will also affect the relaxation process. Since this effect is much

smaller than the core-hole effect, it is neglected in both IVO and Z+1 methods. The energy change of the whole system is the sum of the relaxation of the passive electrons in the full ionized system and the relaxation of the molecular ion core in the presence of the active electron.[16-19]

3.5.2 Core-Hole Relaxation in DFT

Full Core-Hole (FCH), and Half-Core Hole (HCH) are widely used approaches to approximate the core hole in DFT simulations of the NEXAFS spectra of molecules.[2, 4, 19-20] The FCH approach is the process of removing a full electron from the core level completely. In this approach, the system is variationally relaxed after the full electron is removed. All the transition states are then calculated based on the relaxed system. In the HCH approach, instead of one electron, only half an electron is removed from the core, and the system will be relaxed. Although 0.5 occupancy is physically meaningless, this approach has proven to correctly calculate the excitation energy and reproduce the most similarity to the experimental spectra.[2, 4, 19-20]

The Shielding effect of the active electron on the system is ignored in both FCH and HCH approaches, as discussed. This effect is an order of magnitude smaller than the relaxation of the molecular ion, but it should be considered in calculating the final energies. The effect of the active electron on the energy of the molecular ion system is calculated using a technique known as the delta Kohn-Sham (ΔKS) energy calculation, which will be explained in section 3.5.4.

3.5.3 Slater Transition State and Transition Potential DFT

The Slater transition-state method,[19, 21-22] is the process of state-by-state calculation by exciting half an electron from the core orbital into each of the valence orbitals without considering the relaxation effect after each excitation. Generating a complete NEXAFS spectra using this approach is often impractical or very expensive. The TP-DFT[19, 23] approach is described by Triguero *et al.*[23] as an approximation to the Slater transition state method.[23] In this approach all the excited state energies as well as transition intensities are calculated at once for the core excited system, while the density of the system is kept frozen.[4, 19, 23]

3.5.4 ΔKS Energy Approximation

Although using the TP-DFT method, the core-hole relaxation effect is considered in the calculations, the shielding effect of the active electron is ignored. This effect is an order of magnitude smaller than the relaxation effect.[19] By using the ΔKS energy approximation, it is possible to add this effect to the calculations. In this method, the energy difference between the ground state and the fully relaxed first excited state is calculated. This can be repeated on a state by state basis for all transitions in the NEXAFS spectrum. This is time-consuming, as a state by state calculation is required in order to determine the ΔKS energies for an entire NEXAFS spectrum. However, a composite approach is sometimes used, in which the energy of the lowest transition in the TP-DFT calculation is then modified to account for the shielding effect of the active electron. In this approach, the ΔKS core → LUMO transition can be used to 'calibrate' this transition energy from the TP-DFT calculation, thus calibrating the TP-DFT energy scale to the ΔKS energy scale. The following equation presents the energy correction using this method.[19]

$$\Delta E = E(C1s^{-1}; LUMO^{+1}) - E(ground\ state) \qquad \textit{Equation 3.49}$$

From a practical point of view, a full electron will be excited from the core level. The system will be relaxed. Then, an electron will be placed into the LUMO, and the system will be relaxed further. The energy difference between this excited state and the ground state is equal to energy to create the core excited state, where both the core hole and active electron are considered.[19] This energy correction is used in all the TP-DFT spectra calculations (with the exception of MD-DFT calculations) in this research. The process of preparing computational models is explained in the following section.

Using the same approach, the IP of an atom can be determined using the ΔKS method, from the energy difference between the calculated ground state energy and energy of the core ionized molecule, calculated with a full core hole. Term values will be calculated for the lowest energy transition, using the formula $\Delta E_{exc} = \in_f^T - \in_{1s}^T$, where $\in_f^T$ is the valence orbital energy, $\in_{1s}^T$ is the 1s IP from the ΔKS calculation, and ΔE_{exc} is the transition energy from the TP-DFT calculations.[19]

3.6 MD-DFT Calculations

3.6.1 Molecular Dynamics Simulations

Molecular Dynamics (MD) simulations are used to study the dynamic properties of a given system that are observable within the timescale of the simulation. Using MD simulations, it is possible to use the potential energy of a given system and mimic the behaviour of atoms in the system.[24] In this approach, classical Newton's law of motion is used to predict the behaviour of the atoms in the system, while interacting with each other.[24] The following equations of motion are solved iteratively for each atom:

$$F_i = m_i a_i = m_i \frac{d^2 r_i}{dt^2} \qquad \textit{Equation 3.50}$$

In this equation, F_i is the force on a given atom (i), m_i is the mass of the atom, and $a_i = \frac{d^2 r_i}{dt^2}$ is the atom's acceleration, which is the second derivative of the coordinates of the atom over a period of time. The force on each atom is the negative of the derivative of the potential energy with respect to the position of the atom.

$$F_i = -\frac{\partial V}{\partial r_i} \qquad \textit{Equation 3.51}$$

Knowing the potential energy, it is possible to calculate the velocities for each atom and apply them to the starting coordinates of the atom. This step will be repeated for the new coordinates in defined intervals. The trajectory corresponding to the changes in the system over time will be generated at the end of the simulation. The following diagram presents the steps in a classical MD simulation.

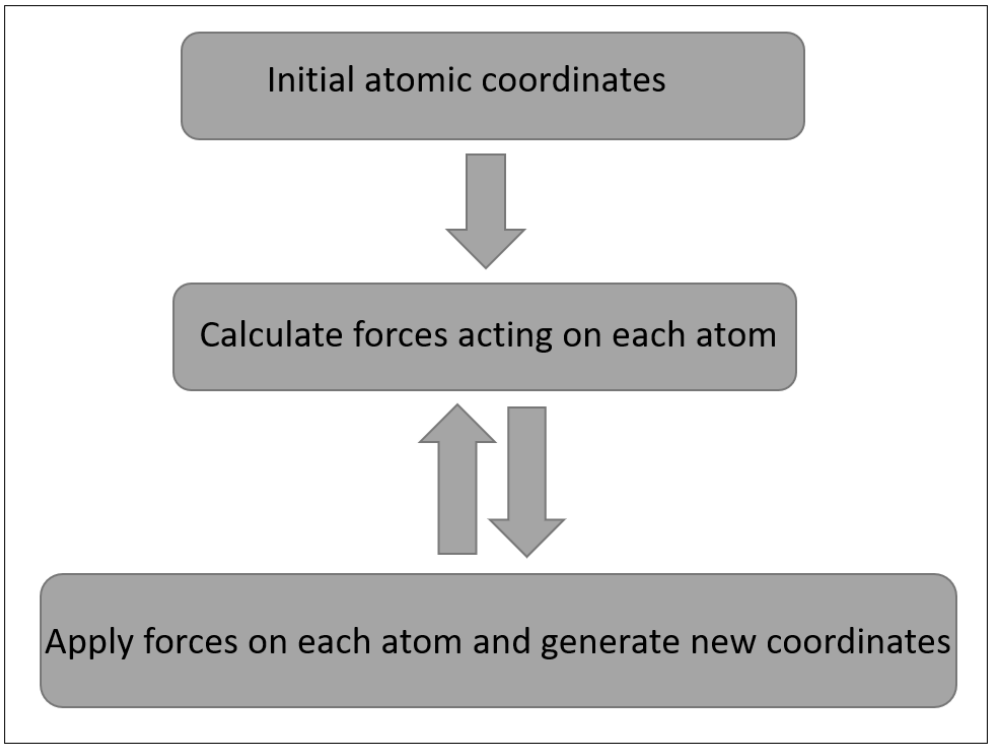

Figure 3.3 - Schematic of the MD simulation steps.

The accuracy of the simulation is directly related to the functions that are used to define the potential energy of the system. These functions are expressed in term of bonded and non-bonded terms as presented in the following figure.[24]

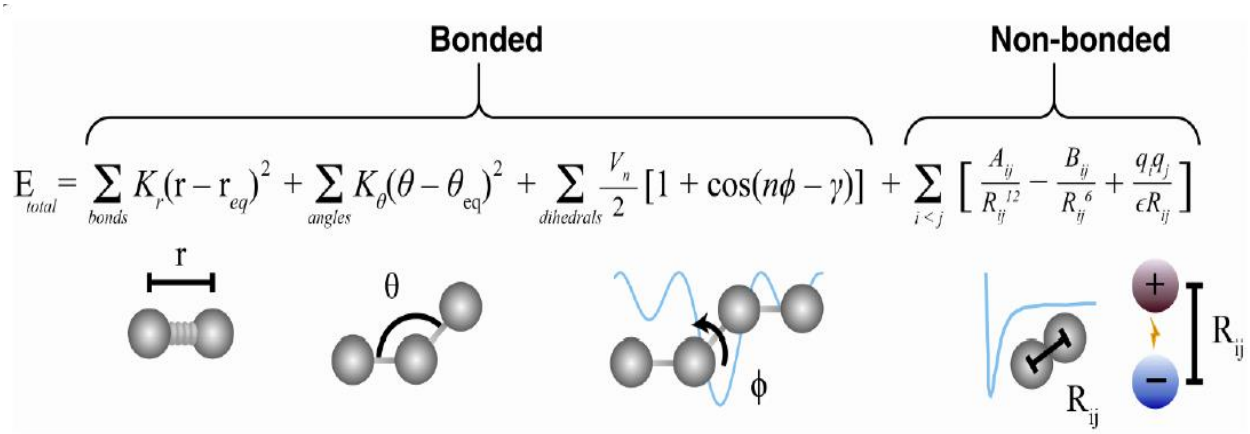

Figure 3.4 - The equation used to calculate the atomic forces in a given system. Types of interactions are also presented under each term in the equation. Figure is reprinted with permission.[24]

In this equation, r, θ, and, ϕ are the bond length, bond angle, and dihedral angle, respectively. k with various subscription represents the force constant in each equation. γ and V_n are also the initial dihedral angle and the force constant, respectively. The non-bonded term represents the interactions between particles that are separated by more than three covalent bond lengths on either the same molecule or different molecules. These interactions are also known as electrostatic interactions and are usually described by Coulomb's law and the Lennard-Jones (LJ) potential.[25] The following term in the non-bonded expression is used to describe the Van der Waals interactions using the LJ equation as follows:

$$V_{LJ} = \sum_{i<j} 4\epsilon_{ij}\left[(\frac{\sigma}{R_{ij}})^{12} - (\frac{\sigma}{R_{ij}})^{6}\right] = \sum_{i<j} \frac{A_{ij}}{R_{ij}^{12}} - \frac{B_{ij}}{R_{ij}^{6}} \qquad \textit{Equation 3.52}^{24}$$

In this equation, ϵ_{ij} is the attraction force (between any two given particles), σ is the Van der Waals radius, r is the atomic distance between particles i and j, $A = 4\epsilon\sigma^{12}$ and $B = 4\epsilon\sigma^{6}$. The Coulomb's interactions are calculated using the following equation:

$$V_{Coulomb} = \sum_{i<j} \frac{q_i q_j}{\epsilon R_{ij}} \qquad \textit{Equation 3.53}^{24}$$

In this equation, q represents partial charge for each particle and $\epsilon = 8.854 \times 10^{-12}$ C^2/Nm^2 is the vacuum permittivity. A set of parameters, including the bond angles, bond lengths, dihedral angles, partial charges, and LJ parameters, are used as the forcefield parameters to describe a given system. The forcefield parameters can be obtained from the experimental measurements as well as *ab initio* calculations.[24] CHARMM36 Force Field (C36 FF)[26] was the selected forcefield to reproduce all the parameters in the *n*-alkane model since it was originally developed for high precision MD-NMR measurements. [26]

Although MD simulations can provide detailed information for a given system, it suffers certain limitations such as computational cost. Depending on the size of the system, the simulations could get very expensive. Hence, most of the simulations for large systems are executed in the timescale of picoseconds and nanoseconds. All the MD simulations in this study have been performed using Gromacs 2019 program.[27-28]

3.6.2 Simulation Ensembles

A collection of replicates of a given system with a set of fixed thermodynamic variables is known as an ensemble. The ensemble is known as the canonical ensemble if all of the systems in the ensemble are in thermal contact with each other so they can exchange energy with each other. This ensemble is also known as NVT, which means constant temperature, volume, and the number of molecules. This system can exchange energy with a thermal source at a constant temperature. Therefore, in such an ensemble, the system is in thermal equilibrium with the heat source. Various types of thermostats could be defined to keep the temperature constant in the NVT ensemble. A microcanonical ensemble is defined with the condition of constant energy across the collection of systems. This type of ensemble is also defined as NVE. NPT is the other popular ensemble that represents a system with a constant number of particles, pressure, and temperature. In the NPT ensemble, in addition to a thermostat, a barostat is needed to keep the pressure constant.[4] All the MD calculations in this thesis are carried out in the canonical ensemble (NVT) with constant volume and temperature.

3.6.3 Periodic Boundary Conditions (PBC)

Ideally, to be able to simulate the bulk properties, the number of particles in the system should be close to infinity ($N \to \infty$). Practically only a finite number of particles can be used to design a system. This introduces the problem of the surface effects or the surface to bulk ratio. Hence, the periodic boundary condition is defined to overcome this problem. Based on the PBC concept, it is imagined that the simulation unit cell is replicated in various directions to form an infinite lattice.[29] The 2d representation of the periodic boundary condition is presented in the following figure.

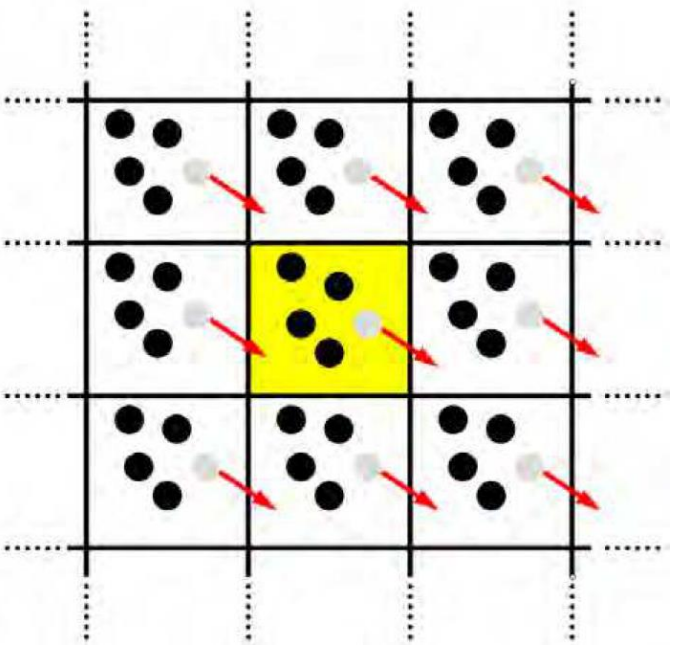

Figure 3.5 - Periodic boundary condition used in MD simulations. Figure is reprinted with permission.[29]

As it can be observed, in this system, when a particle exits from the main simulation box, one of its periodic replicas from a neighboring box will move in to replace it. All the MD simulations performed for this thesis were done using cubic boxes with the PBC in all directions.

3.7 Computational Models

In this project, the DFT method using a few different approaches to calculate the $E_{xc}$are employed to obtain the computational carbon 1s NEXAFS spectra of linear and branched alkanes. For all the calculations, the geometry optimization is performed before calculating the spectra. Also, the spectra calculation for various gauche defects and thermally excited states is performed. All the calculations are automated using python.

The computational studies in this thesis, including geometry optimization, spectra calculations, and MD simulations are performed using the support provided by WestGrid (www.westgrid.ca; Grex) and Compute Canada Calcul Canada (www.computecanada.ca; Cedar and Graham), and University of Saskatchewan HPC resources (Plato).

3.7.1 deMon2k Software

The deMon2k program uses the Kohn-Sham formulation and the Linear Combination of Gaussian Type Orbitals (LCGTO) method to calculate the properties of the given system. The Kohn-Sham SCF (E_{SCF}) is defined using the LCGTO for the KS orbitals and the electronic density of the system. Using the auxiliary function density in deMon2k, the time-consuming step of the Coulomb repulsion energy calculation is avoided. The program uses a minimal auxiliary basis function that only contains the 1s orbital and is known as A1. The more complicated auxiliary basis functions are generated from this basis. Each of the generated auxiliary basis functions is labeled as either **Gen-A*n*** with *n* = 1,2,3,4, or **Gen-A*n**** with n = 2,3,4 that contains *s*, *p, d*, *f*, *g* Hermite Gaussian functions. [8, 30-32] Since the auxiliary basis functions are used to fit the electron density, they are grouped in ***s***, ***spd***, and ***spdfg*** sets, which the last one is only used in case of the **Gen-A*n**** auxiliary basis sets. The total number of auxiliary function sets (N) in deMon2k is calculated using the following equation:

$$N = \int \left(\frac{ln(\beta_{max}/\beta_{min})}{ln(6-n)} + 0.5\right) \qquad \textit{Equation 3.54}$$

In this equation, β_{max} and β_{min} are the largest and smallest primitive Gaussian exponents of the specified orbital basis set, respectively. The *n* value defines the number of functions that are used to describe each group of the orbitals (***s***, ***spd***, and ***spdfg***).[8, 30-32] Note that these auxiliary basis sets are different from the basis sets that are used to describe the KS orbitals; these auxiliary basis sets are used to determine $v_{xc}(r)$. The improved $v_{xc}(r)$ is then used to improve the KS orbitals, and so on. This iteration continues until the changes in the density, and the KS orbitals are smaller than a defined tolerance value. These iterations continue until self-consistency within the exchange-correlation potential ($v_{xc}(r)$) and the KS orbitals (θ_i^{KS}) has been reached. This method is known as an SCF calculation. The ground state energy and other molecular properties are then calculated from this converged potential.[2-3, 7]

3.7.2 Geometry Optimizations

Geometry optimization of the molecules was performed with the program Gaussian 16[33] with a B3LYP DFT functional[34-37] and a 6-31+G(d, p) basis set.

3.7.3 Spectra Calculations

Carbon 1s NEXAFS simulations were obtained from DFT calculations using the deMon2K code (version 4.3.4)[32] with the PBE exchange-correlation functional.[10] All the NEXAFS spectra calculations with deMon2k are performed using the XAS code accompanying the program.[32, 38] Spectroscopic simulations were obtained using the half-core-hole (HCH) transition-potential density functional theory (TP-DFT) method.[23] The Effective Core Potential (ECP) basis sets are used to help with defining the atom with the core hole. ECP basis sets only have the valence orbitals and a defined effective potential for the core electrons in the atom.[32] Triple-zeta basis set was used for all the hydrogen atoms in the system. The diffuse IGLO-III basis set[39] was used on the core excited carbon atom, augmented by the XAS-I basis set, which contains hundreds of large diffuse basis functions (s, p, d) to increase the flexibility of the orbital basis sets and the accuracy of the calculated spectra.[32, 40-42] Separate spectra calculations were performed for each of the carbons in the structure by defining the core-hole on the carbon and ECP for the rest of the carbons in the structure. The contributions from individual carbon atoms were added to give an overall molecular spectrum.

The following figure presents an example of the sum spectra obtained from the individual contributions of each of the carbons in the structure.

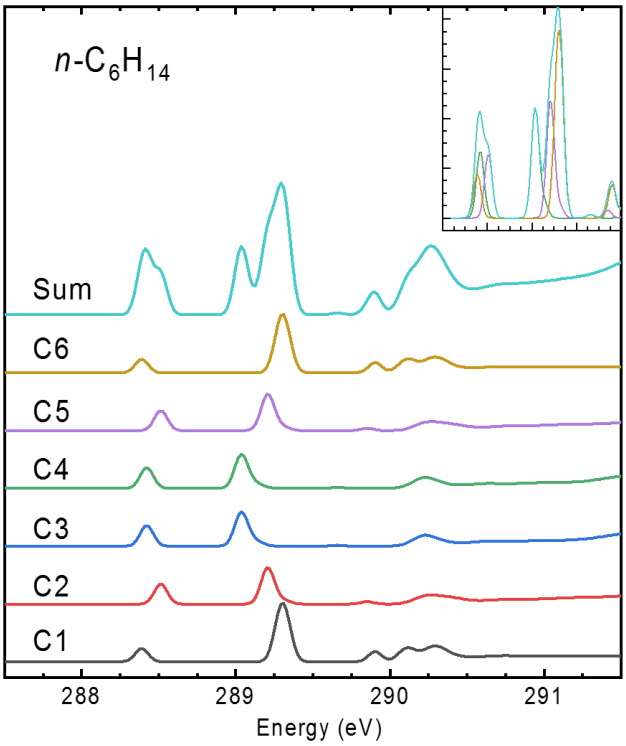

Figure 3.6 – Carbon 1s NEXAFS spectrum of n-hexane, obtained from the contribution of individual spectra of all the carbons in the structure.

The energies of spectra were corrected by changing the energy of the $1s \rightarrow LUMO$ transition to corrected energy using the ΔKS calculations (Equation 3.49).

3.7.4 Simulation of the Orthorhombic Structure

An orthorhombic unit cell ($Pca2_1$, a=4.93 Å, b=7.40 Å, c=16.82 Å, CCC inclination angle=48.8° in the ab plane) was chosen as the starting point of the simulation of *n*-pentane. In this arrangement, one molecule is at the centre and four molecules are placed in the corners of the unit cell (Figure 4.1). This is a made-up structure, as *n*-pentane is used as a model for longer n-alkanes that crystalize in an orthorhombic crystal structure, and structures containing various numbers of molecules were simulated using a Python program. These results are presented in Chapter 4.

3.7.5 Chain Length

The carbon 1s NEXAFS spectra of isolated linear *n*-alkanes, from ethane to *n*-tetracontane (*n*-$C_{40}H_{82}$), were simulated with the TP-DFT method. The effect of chain

length on the spectra was studied using these results. These results are presented in Chapter 5 – Effect of Chain Length on the NEXAFS Spectra of *n*-alkanes.

3.7.6 **Rydberg-Valence Mixing**

Rydberg-valence mixing is observed in the carbon 1s NEXAFS spectra of alkanes, when the energy and symmetry of the Rydberg and σ^*_{C-H} valence orbitals are matched. The energy difference of the singlet and triplet excited states can be used to understand the degree of Rydberg-valence mixing. According to the Pauli exclusion principle, an electron in a triplet excited state will have less repulsion with the other valence electrons relative to an electron in a singlet excited state; therefore, the forbidden triplet transition would appear at lower energy than the singlet transition in a NEXAFS spectrum. Also, an electron that is excited to a valence orbital will have stronger Coulombic interaction with the other valence electrons in comparison with an electron that is excited to the Rydberg orbitals. This is because the valence orbitals are smaller than the Rydberg orbitals. So, the electron that is excited to the valence orbitals will be closer to the other electrons in comparison with the electrons that are excited to the Rydberg orbitals. Therefore, a larger energy difference between the singlet and triplet excited states will indicate a larger valence character. As an approximate guide, a $\Delta E_{(S-T)}$ of less than 0.05 eV implies Rydberg character, and if it is greater than 0.05 eV, some valence character exists.[43]

deMon2k defines spin up and spin down electrons in the form of α and β. The singlet excited state can be created by exciting an electron while its spin is preserved. This means exciting an electron from a core α MO into a valence α MO. The triplet excited state is, therefore, created by changing the spin sign during the excitation process. This means the electron is excited from a core β MO into a valence α MO. A triplet state can be described using three combinations of space and spin wavefunctions (only spin shown here):

$$\Psi(s=1, m_s=1) = |\alpha(1)\alpha(2)| \qquad \textit{Equation 3.55}^2$$

$$\Psi(s=1, m_s=0) = \frac{1}{\sqrt{2}}(|\alpha(1)\beta(2)| + |\beta(1)\alpha(2)|) \qquad \textit{Equation 3.56}^2$$

$$\Psi(s=1, m_s=-1) = |\beta(1)\beta(2)| \qquad \textit{Equation 3.57}^2$$

And singlet is defined as follows:

$$\Psi(s=0, m_s=0) = \frac{1}{\sqrt{2}}(|\alpha(1)\beta(2)| - |\beta(1)\alpha(2)|) \qquad \textit{Equation 3.58}^{2}$$

The singlet excited state energy in deMon2k is not the true singlet excited energy as its wavefunction is a product of two electron wavefunctions as follows:

$$\psi(\textit{singlet, calculated, incorrect wavefunction}) = \alpha(1)\beta(2) \qquad \textit{Equation 3.59}$$

This wavefunction is incorrect because this wavefunction assumes distinguishability of electrons. The energy calculated using this wavefunction is an equal mix of the true singlet and triplet. Therefore, it is possible to write the following equation to obtain the correct singlet energy:

$$E_s(True) = 2E_s(calculated) - E_T \qquad \textit{Equation 3.60}$$

In this equation, E_s(True) is the true singlet energy (corresponding to the MO in Equation 3.56), E_s(calculated) is the energy obtained from the deMon2k calculations of the singlet excited state, and E_T is the calculated value for the energy of the triplet excited state. Having true singlet and triplet energy, it is possible to calculate the difference between the energy of the singlet and triplet excited states as follows:

$$\Delta E_{(S-T)} = E_S(True) - E_T \qquad \textit{Equation 3.61}$$

Using deMon2k, the energy of the molecule in its ground state, singlet excited state, and triplet excited state were calculated, and the $\Delta E_{(S-T)}$ was obtained for molecules such as 2,2-dimethylpropane, and linear short-chain alkanes. The contribution of Rydberg and Valence's character was studied using these results (Chapter 6 – Temperature Dependence NEXAFS Spectra of *n*-alkanes).

3.7.7 **Angle Dependent Spectra**

The deMon2k program has a built-in library that is used to calculate the angle integrated spectra by default. In this library, it is possible to change the default settings to calculate the angle-resolved spectra in each direction (x, y, z). Using a single X-ray file that is obtained from the calculation, it is possible to calculate all three angle-resolved spectra (Chapter 5 – Effect of Chain Length on the NEXAFS Spectra of *n*-alkanes).

3.7.8 Effect of Nuclear Motion and Disorder on the NEXAFS Spectra

The effect of disorder on the NEXAFS spectra is studied by obtaining the NEXAFS spectra for the structures with gauche defects. The starting step to study the effect of nuclear motion on the NEXAFS spectra was to study the effect of thermally populated vibrations on the NEXAFS spectra of given molecules. Using the MD simulations, various models are defined to study the effect of nuclear motion and disorder (in the form of chain length, temperature dependence, and geometry defects) on the NEXAFS spectra in a more systematic approach.

3.7.8.1 Gauche Defects:

Using python scripting, the dihedral angles involving the carbon atoms in the structure (C-C-C-C, H-C-C-H, C-C-C-H) were changed incrementally to reproduce the bond rotations of various degrees. To ease the scripting, the Z-matrix coordinates of the molecule were generated using the Avogadro[44] program. The distribution of gauche defect for each bond was taken from the MD simulations performed by L. L. Thomas *et al.*[45] for *n*-alkanes of various chain lengths in the liquid phase and gas phase. The overall spectra were obtained from the sum of weighted individual spectra. The effect of the gauche defect on the NEXAFS spectra was then studied as a function of the angle of the rotation as well as the position of the rotation. These results are presented in Chapter 6 – Temperature Dependence NEXAFS Spectra of *n*-alkanes.

3.7.8.2 Thermally Populated Vibrations

Thermally populated vibrations are among the contributors to the nuclear motion, which in turn affects the intensity and energy of transitions in the NEXAFS spectra. Therefore, studying the effect of thermally populated vibrations on the NEXAFS spectra of *n*-alkanes could help understand this effect better.

The optimized geometry and vibrational modes of the molecule (*n*-$C_{10}H_{22}$) in the ground state were calculated using ωB97X-D DFT calculations at the 6-31+G(d, p) level, performed with the program Gaussian 16 program.[33] Gaussian generates an output file containing the atomic displacements for each vibrational normal mode. Assuming that

the geometry displacements represent the turning points for each frequency, vibrationally distorted structures were generated for each turning point on the principle that for each vibrational mode, the molecule's geometry will spend most of its time in these turning points.

The NEXAFS spectra of this study were calculated using deMon2k, with the same setup that is explained in section 3.7.2, for the distorted structure at each turning point, for all the vibrational states. Averaging the spectra obtained from these two turning point geometries are a good measure of the spectra of the molecule in each vibrational state. The Boltzmann distribution equation is used to obtain the population of molecules in various states. This equation is as follows[4]:

$$\frac{n_i}{N} = \frac{e^{-\beta\varepsilon_i}}{\sum_i e^{-\beta\varepsilon_i}} \qquad \textit{Equation 3.62}^4$$

In this equation, n_i is the number of molecules in a given state, N is the total number of molecules, ε_i is the calculated vibrational energy, and β is the most probable population of the states in the system. β can be calculated using the following equation.

$$\beta = \frac{1}{kT} \qquad \textit{Equation 3.63}^4$$

In this equation, T is the temperature, and k is the Boltzmann's constant. The Boltzmann distribution function can be written as follows:

$$p_i = \frac{e^{-\beta\varepsilon_i}}{q} \qquad \textit{Equation 3.64}^4$$

In this equation, $p_i = \frac{n_i}{N}$ is the fraction of molecules in state i, and q is the molecular partition function. The molecular partition function for a harmonic oscillator can be expressed as follow:

$$q = \frac{1}{1-e^{-\beta\varepsilon_i}} \qquad \textit{Equation 3.65}^4$$

The fraction of molecules in each state for a harmonic oscillator is obtained from the following equation:

$$p_i = \frac{e^{-\beta\varepsilon}}{q} = \left(1 - e^{-\beta\varepsilon_i}\right)e^{-\beta\varepsilon_i} \qquad \textit{Equation 3.66}^4$$

The ratio of the molecules in each vibrational state in this study was calculated using the Equation 3.64 at standard room temperature (298 K). Note that this model only considers the population of molecules in each vibrationally populated state at a certain temperature and does not account for the zero-point motion.

All of the steps, including geometry optimization, the spectra calculation for the two turning points of the distorted geometry at each vibrational state, and the normalized weighted final spectra calculation using the partition functions at room temperature, are automated using Python programming language and can be used for various molecules. These results are presented in Chapter 6 – Temperature Dependence NEXAFS Spectra of *N*-alkanes.

3.7.9 Molecular Dynamics Simulations – DFT Calculation Models

The goal of this part of the study was to use MD-DFT simulations to study the effect of structural variations on the calculated NEXAFS spectra of *n*-alkanes. Using MD-DFT, it is possible to obtain the spectra of the molecule at various temperatures. A change in the temperature will affect the nuclear motion and the final NEXAFS spectra of the molecule. Since the movements of molecules are considered using MD simulations, the final spectra are more similar to the experimental spectra of the given molecule.

For this approach, geometry optimized *n*-alkane structures were equilibrated in MD using the steepest descent minimization algorithm. The equilibrated systems were placed under an NVT ensemble with the leapfrog integrator algorithm for 100 *picoseconds*. A snapshot of the structure was saved at each picosecond ending up with 102 snapshots for each system. During the simulation, the periodic boundary condition was defined in all directions. These snapshots were saved in the form of cartesian coordinates and used to calculate the NEXAFS spectra with deMon2k without further optimization.

For this research, the largest models have less than 5000 atoms and considered to be small systems. Also, the changes in the energy (such as kinetic and potential energies) were not measured, and only snapshots were extracted as the simulation progressed. These results are presented in Chapter 6 – Temperature Dependence

NEXAFS Spectra of *N*-alkanes and Chapter 7 – NEXAFS Spectroscopy of Liquid *N*-alkanes.

3.7.9.1 Effect of Chain Length on the NEXAFS Spectra Using MD-DFT Calculations

The effect of chain length on the spectra was calculated using the MD-DFT approach by using the snapshots obtained in the MD simulations for the NEXAFS spectra calculations. This is mainly to obtain an average spectrum of all the snapshots. In this approach, two models were prepared. In the first model, only isolated molecules from *n*-C_6H_{14} to *n*-$C_{20}H_{42}$ were studied. Each of the individual spectra was normalized based on the number of carbons in the structure. The final spectrum was obtained by averaging all the individual spectra. The Standard Deviation (SD) was calculated for the final spectrum obtained from each snapshot in comparison with the average spectrum. The calculated sum SD spectra were then added to and subtracted from the average spectra to form the final spectra with the SD. These results are presented in Chapter 7 – NEXAFS Spectroscopy of Liquid *N*-alkanes.

3.7.9.2 Temperature Dependence NEXAFS Spectra of *N*-alkanes Using MD-DFT Calculations

Using MD simulations, it will be possible to calculate the geometry changes of molecules at various temperatures. The average NEXAFS spectra of the molecule can be calculated using these geometries for given temperatures. The spectra of various *n*-alkanes from *n*-C_6H_{14} to *n*-$C_{20}H_{42}$ were calculated through MD simulations performed at various temperatures to study the effect of changes in the temperature on the NEXAFS spectra. The overall process was similar to the previous section with the difference of variations in the temperature during the NVT step. A change in temperature will change the ratio of molecules in each thermally accessible configuration, and this will change the final spectra. The normalization and SD calculations were carried out using the same steps that were explained in the previous section. These results are presented in Chapter 6 – Temperature Dependence NEXAFS Spectra of *N*-alkanes.

3.8 References

1. Schrödinger, E., An Undulatory Theory of the Mechanics of Atoms and Molecules. *Physical Review* **1926,** *28* (6), 1049-1070.

2. Levine, I. N., *Quantum Chemistry*. 7th ed.; Pearson Advanced Chemistry Series: University of New York, **2014**.

3. McQuarrie, D. A., Simon, John D., *Physical chemistry : a molecular approach*. University Science Books: Sausalito, Calif, 1997.

4. Atkins, P., Paula, Julio D.,, *Atkins' Physical Chemistry*. 8th ed.; Oxford University Press: 2014.

5. Yin, Z. Microscopic Mechanisms of Magnetism and Superconductivity Studied from First Principle Calculations. University of California, California, **2009**.

6. Bechstedt, F., *Density Functional Theory. In: Many-Body Approach to Electronic Excitations*. Springer, Berlin, Heidelberg: **2015**; Vol. 181.

7. Kohn, W.; Sham, L. J., Self-Consistent Equations Including Exchange and Correlation Effects. *Physical Review* **1965,** *140* (4A), A1133-A1138.

8. Towler, M. D.; Zupan, A.; Causà, M., Density functional theory in periodic systems using local Gaussian basis sets. *Computer Physics Communications* **1996,** *98* (1), 181-205.

9. Hohenberg, P.; Kohn, W., Inhomogeneous Electron Gas. *Physical Review* **1964,** *136* (3B), B864-B871.

10. Perdew, J. P.; Burke, K.; Ernzerhof, M., Generalized Gradient Approximation Made Simple. *Physical Review Letters* **1996,** *77* (18), 3865-3868.

11. A.M. Koster, G. G., A. Alvarez-Ibarra, P. Calaminici, M.E. Casida, J. Carmona-Espindola, V.D. Dominguez, R. Flores-Moreno, G.U. Gamboa, A. Goursot, T. Heine, A. Ipatov, A. de la Lande, F. Janetzko, J.M. del Campo, D. Mejia-Rodriguez, J. U. Reveles, J. Vasquez-Perez, A. Vela, B. Zuniga-Gutierrez, and D.R. Salahub *deMon2k*, 6; The deMon developers: Mexico City, 2018.

12. Stöhr, J., *NEXAFS Spectroscopy*. Springer, Springer Series in Surface Sciences,: Berlin; London, **1992**; Vol. 25, p 404.

13. Attwood D., S. A., *X-Rays and Extreme Ultraviolet Radiation Principles and Applications*. **2017**.

14. Urquhart, S. G. Delocalization and Functional Group Fingerprinting in the Core Excitation Spectroscopy of Molecules and Polymers, PhD. Thesis. McMaster University, **1997**.

15. Schwarz, W. H. E., Continuous change from valence to Rydberg type states. An example of XUV spectroscopy. *Chemical Physics* **1975,** *9* (1), 157-164.

16. Hunt, s. J.; Goddard, W. A., Excited States of H2O using improved virtual orbitals. *Chemical Physics Letters* **1969,** *3* (6), 414-418.

17. Oji, H.; Mitsumoto, R.; Ito, E.; Ishii, H.; Ouchi, Y.; Seki, K.; Yokoyama, T.; Ohta, T.; Kosugi, N., Core hole effect in NEXAFS spectroscopy of polycyclic aromatic hydrocarbons: Benzene, chrysene, perylene, and coronene. *The Journal of Chemical Physics* **1998,** *109* (23), 10409-10418.

18. Kosugi, N., Strategies to vectorize conventional SCF-Cl algorithms. *Theoretica chimica acta* **1987,** *72* (2), 149-173.

19. Leetmaa, M., Ljungberg, M. P., Lyubartsev, A., Nilsson, A., Pettersson, L. G. M., Theoretical approximations to X-ray absorption spectroscopy of liquid water and ice. *Journal of Electron Spectroscopy and Related Phenomena* **2010,** *177* (2), 135-157.

20. Prendergast, D.; Galli, G., X-Ray Absorption Spectra of Water from First Principles Calculations. *Physical Review Letters* **2006,** *96* (21), 215502.

21. Slater, J. C., Statistical Exchange-Correlation in the Self-Consistent Field. In *Advances in Quantum Chemistry*, Löwdin, P.-O., Ed. Academic Press: 1972; Vol. 6, pp 1-92.

22. Slater, J. C.; Johnson, K. H., Self-Consistent-Field Xα Cluster Method for Polyatomic Molecules and Solids. *Physical Review B* **1972,** *5* (3), 844-853.

23. Triguero, L., Pettersson, L. G. M., Ågren, H., Calculations of Near-Edge X-Ray-Absorption Spectra of Gas-Phase And Chemisorbed Molecules by Means of Density-Functional and Transition-Potential Theory. *Phys. Rev. B.* **1998,** *58* (12), 8097-8110.

24. Durrant, J. D.; McCammon, J. A., Molecular dynamics simulations and drug discovery. *BMC Biology* **2011,** *9* (1), 71.

25. Lennard-Jones, J. E., On the Forces between Atoms and Ions. *Proceedings of the Royal Society of London. Series A, Containing Papers of a Mathematical and Physical Character* **1925,** *109* (752), 584-597.

26. J. Huang, A. D. M. J., CHARMM36 all-atom additive protein force field: Validation based on comparison to NMR data. *Journal of Computational Chemistry* **2013,** *34* (25), 2135-2145.

27. Páll, S.; Abraham, M. J.; Kutzner, C.; Hess, B.; Lindahl, E. In *Tackling Exascale Software Challenges in Molecular Dynamics Simulations with GROMACS*, Solving Software Challenges for Exascale, Cham, 2015//; Markidis, S.; Laure, E., Eds. Springer International Publishing: Cham, 2015; pp 3-27.

28. Abraham, M. J.; Murtola, T.; Schulz, R.; Páll, S.; Smith, J. C.; Hess, B.; Lindahl, E., GROMACS: High performance molecular simulations through multi-level parallelism from laptops to supercomputers. *SoftwareX* **2015,** *1-2*, 19-25.

29. Steinhauser, M. O., Introduction to Molecular Dynamics Simulations: Applications in Hard and Soft Condensed Matter Physics. In *Molecular Dynamics - Studies of Synthetic and Biological Macromolecules*, Southern Illinois University Carbondale, 2012.

30. Calaminici P., J. F., Köster A. M., Mejia-Olvera R., Zuniga-Gutierrez B., Density functional theory optimized basis sets for gradient corrected functionals: 3d transition metal systems. *The Journal of Chemical Physics* **2007,** *126* (4), 044108.

31. Calaminici, P.; Flores–Moreno, R.; Köster, A. M., A Density Functional Study of Structures and Vibrations of Ta3O and Ta3O−. **2005,** *1* (4), 164.

32. Koster A.M. , G. G., Calaminici P., Casida M. E., Dominguez V. D., Flores-Moreno R., Gamboa G. U., Goursot A., Heine T., Ipatov A., Janetzko F., del Campo J. M., Reveles J. U., Vela A., Zuniga-Gutierrez B., Salahub D. R. *deMon2k*, Cinvestav, Mexico City 2011.

33. Frisch, M. J.; Trucks, G. W.; Schlegel, H. B.; Scuseria, G. E.; Robb, M. A.; Cheeseman, J. R.; Scalmani, G.; Barone, V.; Petersson, G. A.; Nakatsuji, H.; Li, X.; Caricato, M.; Marenich, A. V.; Bloino, J.; Janesko, B. G.; Gomperts, R.; Mennucci, B.; Hratchian, H. P.; Ortiz, J. V.; Izmaylov, A. F.; Sonnenberg, J. L.; Williams; Ding, F.; Lipparini, F.; Egidi, F.; Goings, J.; Peng, B.; Petrone, A.; Henderson, T.; Ranasinghe, D.; Zakrzewski, V. G.; Gao, J.; Rega, N.; Zheng, G.; Liang, W.; Hada, M.; Ehara, M.; Toyota, K.; Fukuda, R.; Hasegawa, J.; Ishida, M.; Nakajima, T.; Honda, Y.; Kitao, O.; Nakai, H.; Vreven, T.; Throssell, K.; Montgomery Jr., J. A.; Peralta, J. E.; Ogliaro, F.; Bearpark, M. J.; Heyd, J. J.; Brothers, E. N.; Kudin, K. N.; Staroverov, V. N.; Keith, T. A.; Kobayashi, R.; Normand, J.; Raghavachari, K.; Rendell, A. P.; Burant, J. C.; Iyengar, S. S.; Tomasi, J.; Cossi, M.; Millam, J. M.; Klene, M.; Adamo, C.; Cammi, R.; Ochterski, J. W.; Martin, R. L.; Morokuma, K.; Farkas, O.; Foresman, J. B.; Fox, D. J. *Gaussian 16 Rev. B.01*, Wallingford, CT, 2016.

34. Becke, A. D., Density-functional thermochemistry. III. The role of exact exchange. *The Journal of Chemical Physics* **1993,** *98* (7), 5648-5652.

35. Lee, C.; Yang, W.; Parr, R. G., Development of the Colle-Salvetti correlation-energy formula into a functional of the electron density. *Physical Review B* **1988,** *37* (2), 785-789.

36. Vosko, S. H.; Wilk, L.; Nusair, M., Accurate spin-dependent electron liquid correlation energies for local spin density calculations: a critical analysis. *Canadian Journal of Physics* **1980,** *58* (8), 1200-1211.

37. Stephens, P. J.; Devlin, F. J.; Chabalowski, C. F.; Frisch, M. J., Ab Initio Calculation of Vibrational Absorption and Circular Dichroism Spectra Using Density Functional Force Fields. *The Journal of Physical Chemistry* **1994,** *98* (45), 11623-11627.

38. Geudtner, G.; Calaminici, P.; Carmona-Espíndola, J.; del Campo, J. M.; Domínguez-Soria, V. D.; Moreno, R. F.; Gamboa, G. U.; Goursot, A.; Köster, A. M.; Reveles, J. U.; Mineva, T.; Vásquez-Pérez, J. M.; Vela, A.; Zúñinga-Gutierrez, B.; Salahub, D. R., deMon2k. *Wiley Interdisciplinary Reviews: Computational Molecular Science* **2011,** *2* (4), 548-555.

39. Huzinaga, S., Gaussian-Type Functions for Polyatomic Systems. I. *The Journal of Chemical Physics* **1965,** *42* (4), 1293-1302.

40. Godbout, N.; Salahub, D. R.; Andzelm, J.; Wimmer, E., Optimization of Gaussian-type basis sets for local spin density functional calculations. Part I. Boron through neon, optimization technique and validation. *Canadian Journal of Chemistry* **1992,** *70* (2), 560-571.

41. Ågren, H.; Carravetta, V.; Vahtras, O.; Pettersson, L. G. M., Direct, atomic orbital, static exchange calculations of photoabsorption spectra of large molecules and clusters. *Chemical Physics Letters* **1994,** *222* (1), 75-81.

42. Ågren, H.; Carravetta, V.; Vahtras, O.; Pettersson, M. L. G., Direct SCF direct static-exchange calculations of electronic spectra. *Theoretical Chemistry Accounts* **1997,** *97* (1), 14-40.

43. Urquhart S. G.; Gillies R., Rydberg−Valence Mixing in the Carbon 1s Near-Edge X-ray Absorption Fine Structure Spectra of Gaseous Alkanes. *The Journal of Physical Chemistry A* **2005,** *109* (10), 2151-2159.

44. Cornell T., H. G. Avogadro. https://avogadro.cc.

45. Thomas, L. L.; Christakis, T. J.; Jorgensen, W. L., Conformation of Alkanes in the Gas Phase and Pure Liquids. *The Journal of Physical Chemistry B* **2006,** *110* (42), 21198-21204.

Chapter 4 – Computational Studies of the NEXAFS Spectra of Condensed *N*-alkanes

4.1 Description

The carbon 1s NEXAFS spectra of *n*-alkanes are complicated despite the molecules' structural simplicity. Understanding the spectra of these simple structures will help understand the spectra of more complicated structures. As discussed in Chapter 1 – Introduction, the NEXAFS spectra of *n*-alkanes are not well understood, and in particular, the C-H band in condensed n-alkanes is considered to have either pure Rydberg character or a mixture of Rydberg and valence character.[1-5] Modeling the solid phase spectra of alkanes is challenging due to the numerous variations of the spectra for reasons such as variation in density, with melting, etc.

In this chapter, the criteria for a successful DFT cluster model will be discussed. Computational modeling could help understand these phenomena and the nature of core excited states of *n*-alkanes, in general. However, as Rydberg orbitals have a large radius, a 'cluster' model used for calculations should have a radius larger than the Rydberg orbitals, so that Rydberg orbitals on a calculated atom at the centre of the cluster do not extend into the vacuum around the cluster model.[4] An alternative to the cluster model calculation is use of PBC (§3.6.3) which will not have a vacuum or surface state effect. The selection of the basis set is also an important step in this approach as the basis set should be large enough to reproduce the Rydberg transitions in the experimental gas phase spectrum and yet small enough to be contained within the edges of the cluster model. Generally, several diffuse functions are used in the basis sets in order to have a good representation of the NEXAFS spectra of the molecule. These diffuse functions are usually very large and would therefore need a large cluster to be able to contain them. This could lead to a significant increase in the computational cost. Trimming some of the diffuse functions from the basis set would help to contain the remaining basis functions within the cluster radius. However, a trimmed basis set should also be able to reproduce the gas phase spectra. Using a large cluster and a trimmed basis set, it might be possible

to reproduce the experimental shift to the higher energy for the spectra of the cluster model in comparison with the spectra of the isolated molecule model.

4.2 Computational Approach

studies on the computational NEXAFS spectroscopy of *n*-alkanes have examined isolated molecules, small clusters, and isolated molecules embedded in small clusters of inert atoms (e.g., neon atoms) to discuss the spectra of the condensed phase.[1, 4, 6] These approaches either do not consider intermolecular interactions[1] or have used small molecules to make conclusions about the condensed phase.[6]

Linear *n*-alkanes have the all-trans geometry as their lowest energy geometry in the solid phase, with the molecules arranged parallel to each other.[7] The crystal structure of these molecules depends on the chain length and the number of carbons in the chain (odd/even numbers).[8] For *n*-alkanes with an even number of carbon atoms, triclinic is the dominant structure for the chains shorter than 26 carbon ($n \leq 26$) and both monoclinic and orthorhombic polymorphs exist for the chains longer than 26 carbon ($n>26$).[9-13] For *n*-alkanes with an odd number of carbon atoms, the orthorhombic structure is the dominant structure at room temperature.[11, 14] The short molecule *n*-pentane (*n*-C_5H_{12}) was selected for this study as there was a good trade-off between the complexity of the molecule and the computational cost toward the condensed phase spectra calculation. It is hoped that the calculation of CH_3 and CH_2 groups in *n*-pentane will be a good representative of the spectra of the CH_3 and CH_2 in longer chain molecules. Although *n*-pentane does not form the orthorhombic structure in its solid phase, this crystal structure was nevertheless selected since it can be used as a means to study the behavior of longer chain polymers such as polyethylene that have the orthorhombic crystal structure.[15] Using python scripting, the high-quality geometry optimized structure of the *n*-pentane molecule was rotated and translated into the predefined positions (Figure 4.1) to generate orthorhombic clusters (a=4.93 Å, b=7.40 Å, c=16.82 Å, CCC inclination angle=48.8° in the ab plane) of *n*-pentane with various sizes.

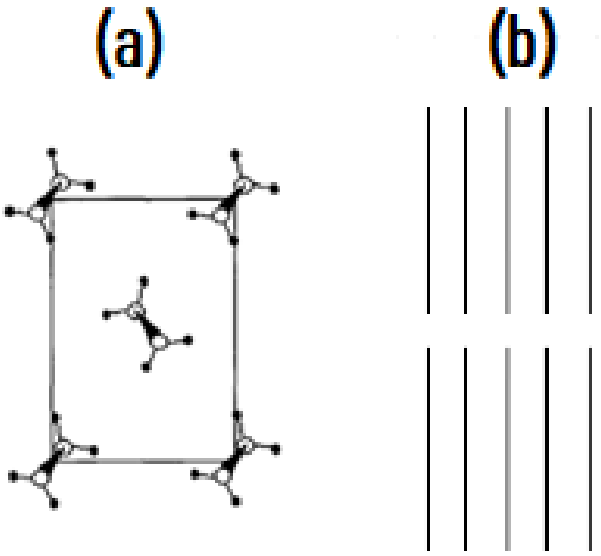

Figure 4.1-Orthorhombic structure of n-pentane used to develop the model. (a) the top view, (b) the side view

Note that in such clusters, the carbon 1s NEXAFS spectra calculations will only be performed for the molecule in the centre of the cluster since it has the largest distance from the edges of the cluster. The final size of the cluster must be larger than the size of the optical orbital to avoid the interaction of the orbital with the vacuum. As shown in Urquhart and Gillies study,[4] a cluster of insufficient size (too small) will lead to a mixed cluster/vacuum environment for the Rydberg orbitals and will not properly model the NEXAFS spectra of the condensed phase. The authors[4] discussed that the small size of the cluster used by Weiss *et al.*[5] and Schöll *et al.*[6] to model solid alkanes does not fully reproduce the solid state spectra as the Rydberg orbitals extend into the vacuum. However, an increase in the size of the cluster will increase the computational cost significantly. In this study, various cluster sizes were generated based on the number of molecules required around the central molecule to create a spherical cluster with a certain radius. The cluster size varied from 5 molecules to 193 molecules (cluster diameter of ~30 Å) to study the changes on the spectra as the size of the cluster increased. Computational settings were adjusted to reproduce the Rydberg transitions in the gas phase spectra for the isolated molecule and to have the Rydberg orbitals contained within

the cluster model for solid phase. These computational settings include basis sets and auxiliary basis sets. These changes are discussed in detail in the following sections.

4.2.1 NEXAFS Spectra Calculations for the Isolated Molecules

All the carbon 1s NEXAFS simulations were performed using half core-hole TPDFT approach in deMon2k (version 4.3.4)[16] with the PBE exchange correlation functional.[17] Effective core potential basis sets were used for all the carbons except the core excited one. Triple -zeta basis set was used on all the hydrogens in the system. Core excited carbons were defined using the IGLO-III basis set augmented by the XAS-I basis set.[18] Simulated spectra for each calculation was generated by using a static 0.2 eV wide Gaussian line shape, using the XAS code accompanying deMon2k. The final spectra were obtained by summing the spectrum of each of the individual carbon atoms in the structure.

4.2.1.1 Basis Set

To validate the method for calculating the spectrum of a cluster model, the same approach must be able to reproduce a spectrum of the molecule in the gas phase using an isolated molecule instead of a cluster. This includes the overall shape of the spectra as well as the relative energy of transitions with respect to each other. This comparison will increase the confidence in the calculated spectra of the condensed phase. The following figure presents a comparison between the calculated spectrum of propane with the experimental spectrum obtained by Urquhart *et al.*[3]

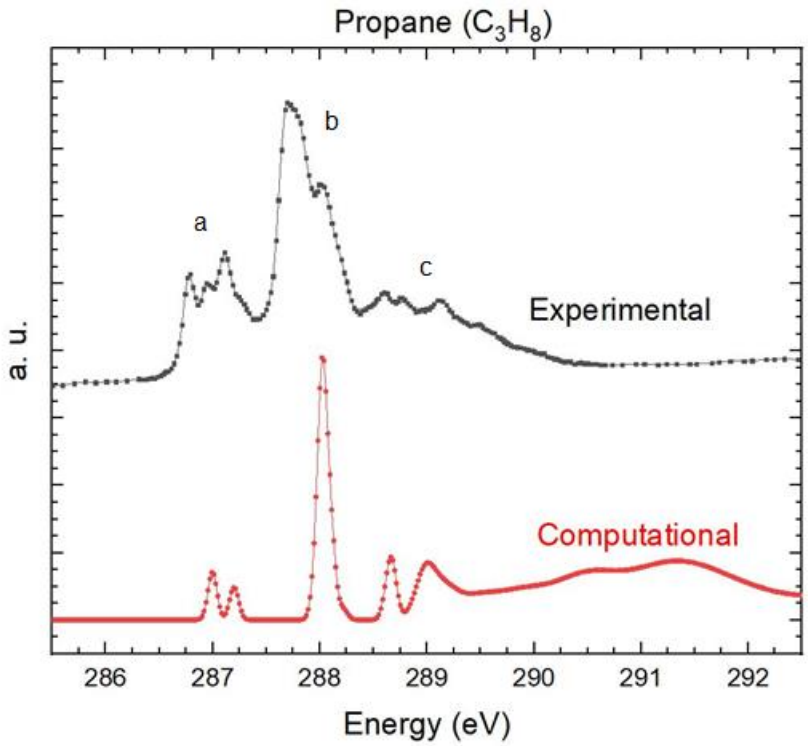

Figure 4.2 - Calculated carbon 1s NEXAFS spectrum of propane in comparison with the high-resolution experimental spectrum of propane. The experimental spectrum is reproduced from Urquhart et al.[3] with permission.

The computational spectrum in this figure is obtained after testing calculations with various basis sets. The IGLO-III[19] basis set, along with the XAS augmentation basis sets, has showed to successfully reproduce the NEXAFS spectra of *n*-alkanes with enough details.[19-20] The spectra calculation using various basis set has also led to IGLO-III[19] as the selected basis set that reproduces the spectra with the highest similarity to the experimental spectra. TZVP[21] was selected as the basis set for all the hydrogens in the structure, and an ECP basis set[22] was used for all the other carbons in the structure. The peak assignments in Figure 4.2 are similar to those of Ueda *et al.*[23] and Remmers *et al*.[24] This means that the peaks labeled as “a” are considered to be coming from the 1s → 3s transition (the lowers peak) and its vibronic transitions. The peaks representing 1s → 3p and 1s → 3d transitions along with their vibronic transitions are also labeled as “b” and “c”, respectively. In the case of the 3s peak in the computational spectrum, the doublet is observed because of separate contributions from the terminal CH_3 and the internal CH_2 groups.

These results show that using the IGLO-III basis set, along with the XAS augmentation basis sets, the calculated spectra of the isolated molecule will reproduce some of the spectral details that are observed in the experimental spectra of the gas phase propane, successfully. Therefore, this basis set could be a good option to calculate the spectra of condensed *n*-alkanes since it provides enough details in the spectra for the Rydberg transitions and it's not computationally expensive for small molecules.

4.2.1.2 **Auxiliary Basis Functions**

Auxiliary basis functions are used to calculate the exchange-correlation potential and reduce the time-consuming step of the Coulomb repulsion energy calculations. Using deMon2k, the carbon 1s NEXAFS spectrum of the isolated molecule of *n*-pentane was studied with various auxiliary basis functions. Figure 4.3 presents the effect of auxiliary basis function on the NEXAFS spectra of *n*-pentane.

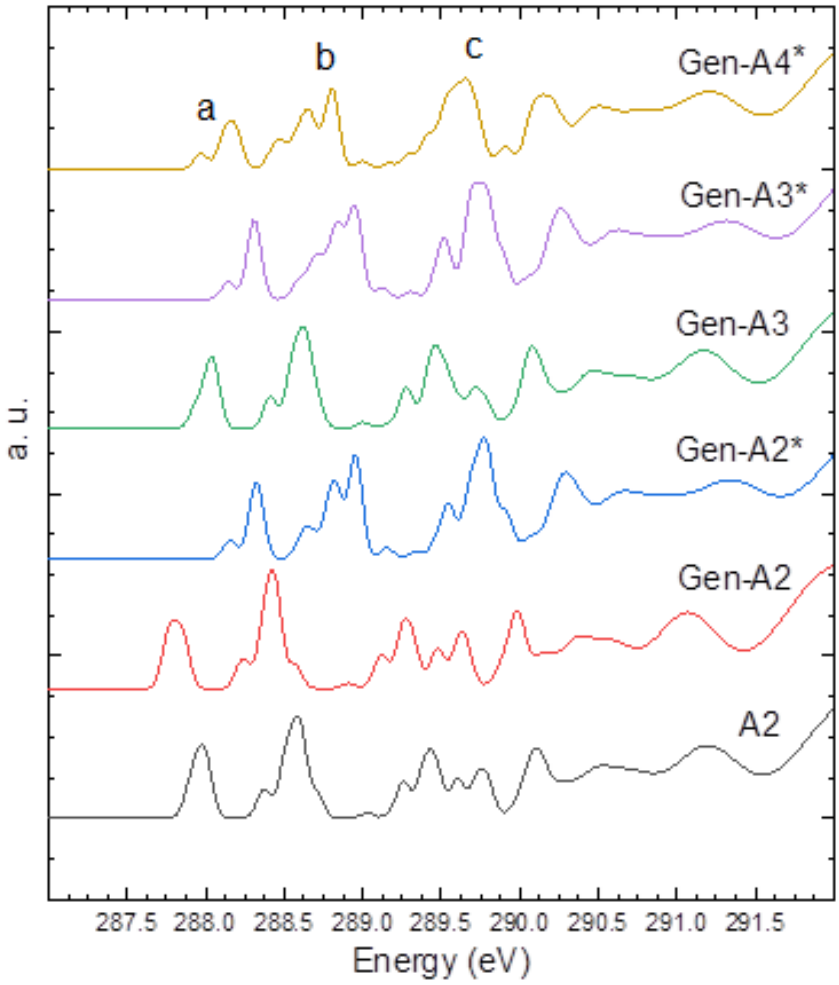

Figure 4.3 - Effect of auxiliary basis functions on the carbon 1s NEXAFS spectra of isolated n-pentane

In this figure, similar to Figure 4.2, a, b, and c labels are used for the 1s → 3s, 1s → 3p, and 1s → 3d transitions respectively. A1 is the minimal auxiliary basis function that only contains the 1s orbital and A2 contains 1s, 2s, and 2p orbitals. The more complicated basis sets of Gen-A*n* (*n*=1, 2, 3, 4, containing ***s*** and ***spd*** orbital groups) and Gen-A*n**(*n*=2, 3, 4, containing ***s***, ***spd***, and, ***spdfg*** orbital groups) are generated from the minimal basis set using the largest and smallest primitive Gaussian exponents of the specified orbital basis set that is defined on the atom (Explained in detail in Chapter 3). In this regard, Gen-A1 auxiliary basis function will only have one layer of each of the ***s*** and ***spd*** orbital groups that is fitted to the components of the selected basis set (IGLO-III). As presented

in Figure 4.3, A2 auxiliary basis function does not reproduce the splitting of the terminal CH_3 and internal CH_2 groups in the 3s peak. This is due to the simplicity of this basis set which doesn't have enough functions to define the orbitals. Comparing Gen-A2 with Gen-A3, it can be observed that the addition of the third layer of electrons (n=3, 3 layers of ***s*** and ***spd*** orbital groups) will not change the spectra significantly. The same observation can be made for the Gen-A2* and the Gen-A3* basis sets. However, the addition of the ***spdfg*** orbital groups will add more spectroscopic detail to the calculated spectra. This includes the low energy shoulder peak for the 3s peak as well as the splitting in the 3p and 3d peaks. Although using the smaller auxiliary basis sets could help reducing the computational cost, however, Gen-A4* is the best option among all the auxiliary basis functions since it produces a spectrum that is more similar to the experimental spectra of *n*-alkanes.

4.2.2 NEXAFS Spectra Calculations for the Cluster on *N*-alkanes

The calculation of the isolated molecule model is a representative of the molecule in the gas phase, and the cluster model calculation is intended to represent the condensed phase. So, to follow the experimental trend (Figure 1.22)[4], the calculated NEXAFS spectra of the cluster model should appear in higher energy than the calculated NEXAFS spectra of the isolated molecule model. Quenching of the Rydberg character, as well as the Rydberg-valence mixing, is expected to be observed in the calculated NEXAFS spectra of the cluster model, relative to the calculated NEXAFS spectra of the isolated molecule.

The program Spartan'14[25] was used as a graphical editor to define the molecular structure of *n*-pentane (*n*-C_5H_{12}). Geometry optimization was performed using the program Gaussian 16[26] with the M06-2X DFT approach[27] and the 6-31+G(d, p) basis set. Using python codes, this high-quality geometry was translated to the origin (0, 0, 0) and aligned to align the molecule's backbone along the **z** axis. As presented in Figure 4.1(a), molecule's CCC plane will have two different rotations in the xy plane; these are perpendicular to each other with the initial inclination angle of 48.8 for the central molecule

in the ab plane. Therefore, a rotation matrix with the rotation angle of 90° is used to generate both rotations of the molecules. The rotation matrix is as follows:

$$R_z(\gamma) = \begin{vmatrix} cos\,\gamma & sin\,\gamma & 0 \\ -sin\,\gamma & cos\,\gamma & 0 \\ 0 & 0 & 1 \end{vmatrix} \qquad \textit{Equation 4.1}$$

Note that only rotation along **z** axis is presented as central molecule is aligned along the **z** axis before generating the two rotations. Using a simple translational matrix, these two rotations of molecule are copied into the pre-defined positions in the crystal structure to generate the final orthorhombic structure (Figure 4.5).

4.2.2.1 Radius of the Basis Functions vs the Cluster Size

The basis functions are normalized Gaussian Type Orbital (GTO), centered on an atom (A) with the orbital exponent of α. These are defined as follows:[28]

$$\phi_A(r) = Nr^{n-1}e^{-\alpha r^2}Y_l^m(\theta,\psi) \qquad \text{Equation 4.2}^{28}$$

In this equation, $r^{n-1}e^{-\alpha r^2}$ and $Y_l^m(\theta,\psi)$ are the radial component and angular components of the orbital, respectively. *N* is a normalization constant.

In case of the 1s orbital centred in the origin the GTO wavefunction can be written as follows:

$$\Phi^{GTO} = \left(\frac{2\alpha}{\pi}\right)^{3/4} e^{-\alpha r^2}Y_l^m(\theta,\psi) \qquad \textit{Equation 4.3}^{28}$$

For the 2p and 3d orbitals, the radial component of the orbital's equation is $\left(\frac{2\alpha}{\pi}\right)^{3/4} re^{-\alpha r^2}$ and $\left(\frac{2\alpha}{\pi}\right)^{3/4} r^2e^{-\alpha r^2}$, respectively. It is possible to calculate the basis set radial expectations for each of these GTO wavefunctions. The following equation, presents the radial expectation for a simple s type GTO wavefunction:

$$\langle r^2\rangle = \int_0^\infty \left(\frac{2\alpha}{\pi}\right)^{3/4} e^{-\alpha r^2} r^2 \left(\frac{2\alpha}{\pi}\right)^{3/4} e^{-\alpha r^2} dr \qquad \textit{Equation 4.4}$$

The IGLO-III basis set is a split basis set with multiple components for the 1s and 2p orbitals. In case of the split basis sets, the final wavefunction is written as the sum of each component in the basis set using the following equation:

$$\Phi_{orb}(r) = \sum_1^n d_{orb}\Phi_{orb}^{GF} \qquad \textit{Equation 4.5}$$

In this equation, *orb* is the type of basis function, *d* is the coefficient of each wavefunction, and Φ is the gaussian function generated based on the orbital exponents (α) of the basis function. As an example, the radial expectation of the 2s orbital in the IGLO-III basis set (with only one component) can be expressed as follows:

$$\langle r^2 \rangle = \int_0^\infty \left(\frac{2\alpha}{\pi}\right)^{3/4} d.r.e^{-\alpha r^2} r^2 \left(\frac{2\alpha}{\pi}\right)^{3/4} d.r.e^{-\alpha r^2} dr \qquad \textit{Equation 4.6}^{28}$$

In this equation, *d* and α are the basis function coefficient and exponent, respectively. The radial expectation ($\langle r^2 \rangle$) value has been calculated for all the components of the IGLO-III basis set. The square root of these radial expectations, which give a good indication of the radiuses, are presented in the following table.

Table 4.1 - Radial expectation and radius of the orbitals in the IGLO-III basis set

n	l	Orbital coefficient	Orbital exponent (α) ($\frac{1}{Å}$)	$\sqrt{\langle r^2 \rangle}$ (Å)
1	0	0.0002264183	30936.8439986026	0.027
	0	0.0017844680	4586.3508013145	
	0	0.0094901567	1029.0392888705	
	0	0.0396605150	284.9798820419	
	0	0.1313402600	90.1553176935	
2	0	1.0	31.0996760179	0.088
3	0	1.0	11.4981470036	0.325
4	0	1.0	4.5022024369	1.054

5	0	1.0	1.2509732821	4.592
6	0	1.0	0.4667433652	14.452
7	0	1.0	0.1794999694	43.153
2	1	0.0040969752	77.0827224279	0.036
	1	0.0040969752	17.9589415795	
3	1	1.0	17.9589415794	0.152
4	1	1.0	5.5573736504	0.673
5	1	1.0	2.0316661422	2.335
6	1	1.0	0.8063506147	7.124
7	1	1.0	0.3303604989	20.418
3	2	1.0	2.6456163840	1.414
4	2	1.0	0.6614040960	7.172

As it can be observed, the 6s, 7s, 6p, 7p, and 4d orbitals in this basis set are much larger than the rest of the basis functions and need to be trimmed if larger than the extent of the cluster. Removing these large components is one of the steps that could be taken. However, the trimmed basis set must still be able to reproduce a good spectrum of the isolated molecule, before examining for the cluster model. The following figure presents the carbon 1s NEXAFS spectra of isolated *n*-pentane using the trimmed IGLO-III basis set in comparison with the spectra calculated using the normal IGLO-III basis set. All the other parameters are kept the same during this spectra calculation.

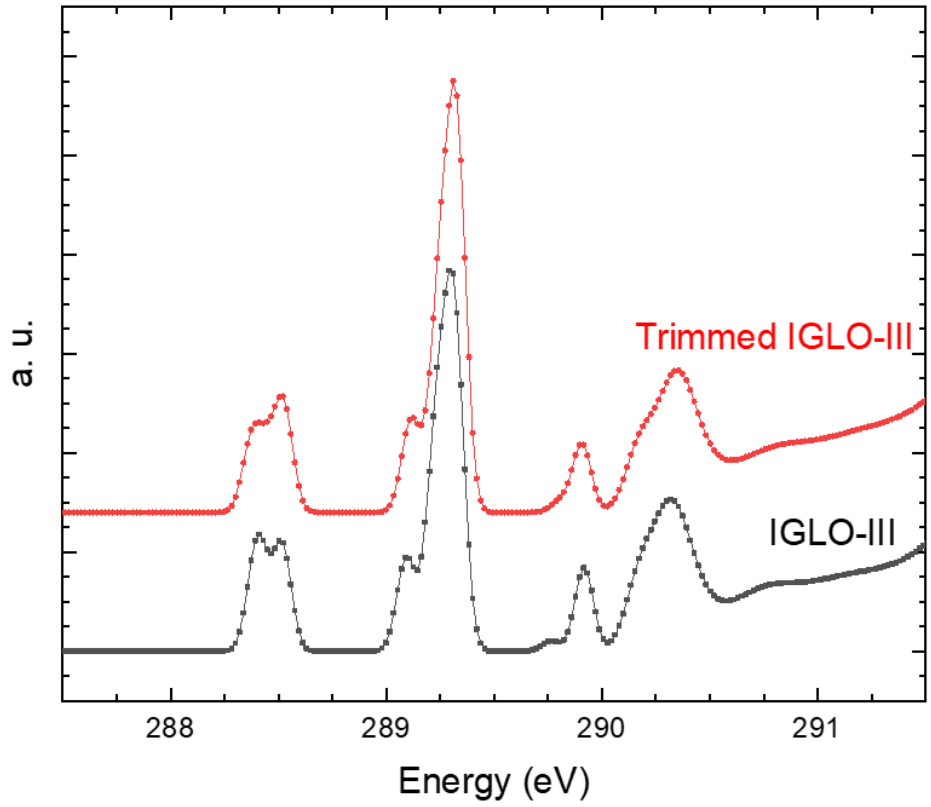

Figure 4.4 - Carbon 1s NEXAFS spectra of isolated n-pentane obtained using the regular (Bottom) and trimmed (Top) IGLO-III basis sets

As can be observed, trimming the basis set seems to only have a minor effect on the low energy shoulder of the 1s → 3s transition. Therefore, it should be fine to use the trimmed basis set in the spectra calculation of the cluster of *n*-pentane molecules. Based on the size of the orbitals ($\sqrt{\langle r^2 \rangle}$) in the trimmed IGLO-III basis set, clusters with the radiuses from ~5 Å to ~30 Å were examined. As the number of molecules in the cluster increases, the computational cost will increase significantly. Following figure presents the largest generated cluster containing 193 molecules of *n*-pentane with the radius of 30 Å.

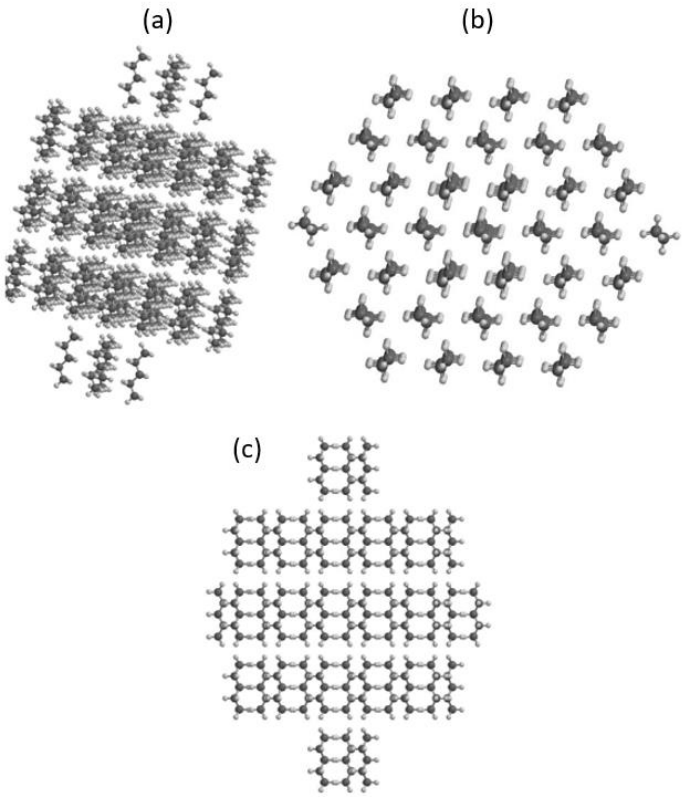

Figure 4.5 - Cluster of n-pentane containing 193 molecules from (a) side view, x-axis, (b) Top view, z-axis, and (c) side view, y-axis

The spectra of the *n*-pentane were obtained for various sizes of clusters. These results are presented in the following figure.

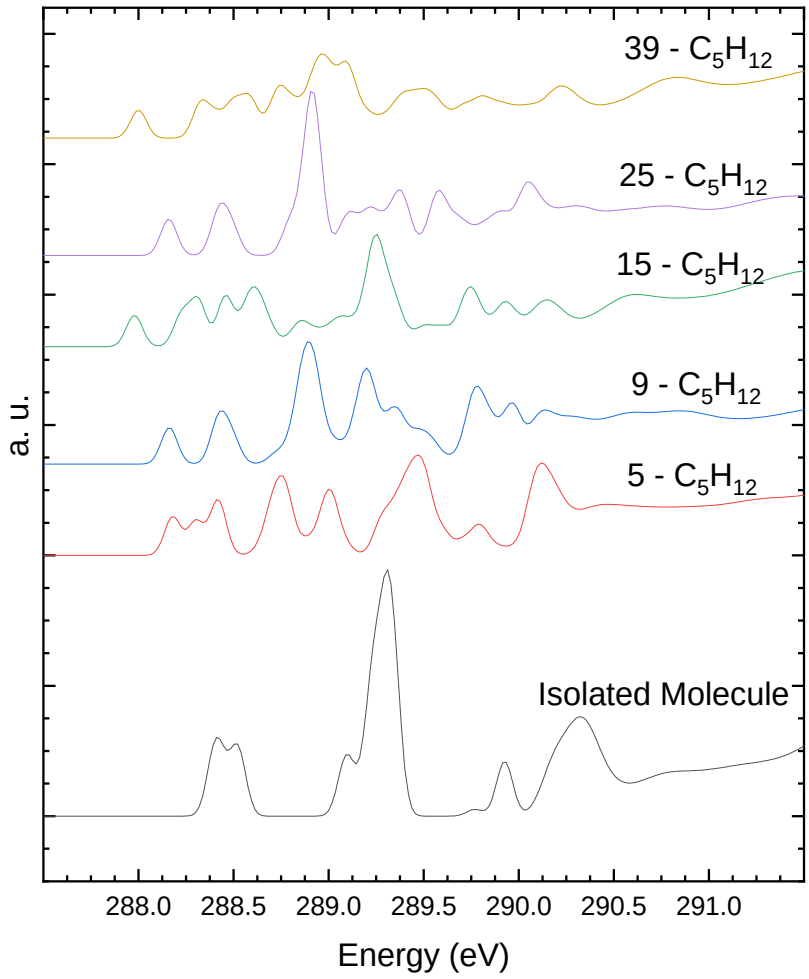

Figure 4.6 - Carbon 1s NEXAFS spectra of isolated n-pentane in comparison with clusters containing 5, 9, 15, 25, and 39 n-pentane molecules.

The NEXAFS spectra of the cluster with 51 molecules (51-cluster) is presented in figure 4.7. All of the spectra calculations for these clusters are performed using the trimmed IGLO-III basis set on the carbon with the core-hole augmented with the XAS-I augmentation basis functions. ECP and TZVP basis sets are used on all the other carbons and hydrogens in the system, respectively. As it can be observed from this figure, the spectra of the cluster show a degree of splitting with no clear pattern. The numbers in the spectra labels represent the number of molecules in each cluster, including the central molecule. This means that the 5-C_5H_{12} cluster contains 4 molecules surrounding the central molecule (total of 5). As can be observed, the spectra of the clusters containing 9

and 25 molecules show a sharp peak for the 1s → 3p transitions. This is simply due to the orientation of the molecules around the central molecule and the interaction of the Rydberg orbitals (of the central molecule) with the cluster/vacuum environment. Also, an increase in the size of the cluster (up to 39 molecules in this case), doesn't seem to have an impact on the energy of the transitions in the spectra. However, for the clusters with more than 51 molecules of *n*-pentane (radius of 12 Å), even with the trimmed basis sets, the computational cost is increased significantly and does not converge within the maximum possible defined time of the calculations (as the Compute Canada platform had a 7 day limitation on the time of calculation when these data were calculated). Therefore, the spectra of the largest cluster that could be calculated (within the defined time limitations) was used to perform the ΔKS energy correction and to compare with the energy corrected spectra of the isolated molecule. Since the computational cost to obtain a NEXAFS spectrum for clusters larger than 12 Å(radius) was too high, this project was not continued after the ΔKS energy correction study.

4.2.2.2 Calculations Using the ΔKS Energy correction

As discussed in the previous section, it was not possible to obtain simulated NEXAFS spectra of clusters larger than 51 molecules (radius of 12 Å) within the defined time restrictions of Compute Canada platform. The spectra obtained for the 51-cluster still appears at a lower energy compared to the spectra of the isolated *n*-pentane molecule (left plot in Figure 4.8). Therefore, the ΔKS Energy correction was considered as the next step to optimize the spectra of the largest possible cluster, under the hypothesis that the excited state shielding effect is necessary to reproduce experiment. The ΔKS Energy correction will help account for the shielding effect of the active electron by improving the total energies obtained in the TP-DFT calculations. This process usually shifts the NEXAFS spectra to the lower energy. In this process, a full electron will be excited from the core level and the system will be relaxed. This electron will, then, be placed in the LUMO and the system is allowed to relax again. The energy difference between the final excited state and the ground state of the molecule is applied to the first transition to account for the shielding energy caused by the active electron. This energy correction will shift the spectra to lower energy for both the isolated molecule and the cluster. Since the

calculation is performed for each carbon separately, the excited state energy could be different for each carbon, depending on its position in the carbon chain. Since the final spectrum is the sum of all the individual spectra (which have been shifted differently), the final energy corrected spectrum will be different than the original spectrum.

Figure 4.7 presents the carbon 1s NEXAFS spectrum of the isolated *n*-pentane compared with the spectrum of a spherical cluster of *n*-pentane (51 molecules). The cluster containing 51 molecules was selected in this work as it represents a spherical cluster with the radius of ~12 Å (equal to having six layers of molecules around the central molecule) which should be larger than the extent of the trimmed basis sets used to describe the carbon with the core hole.

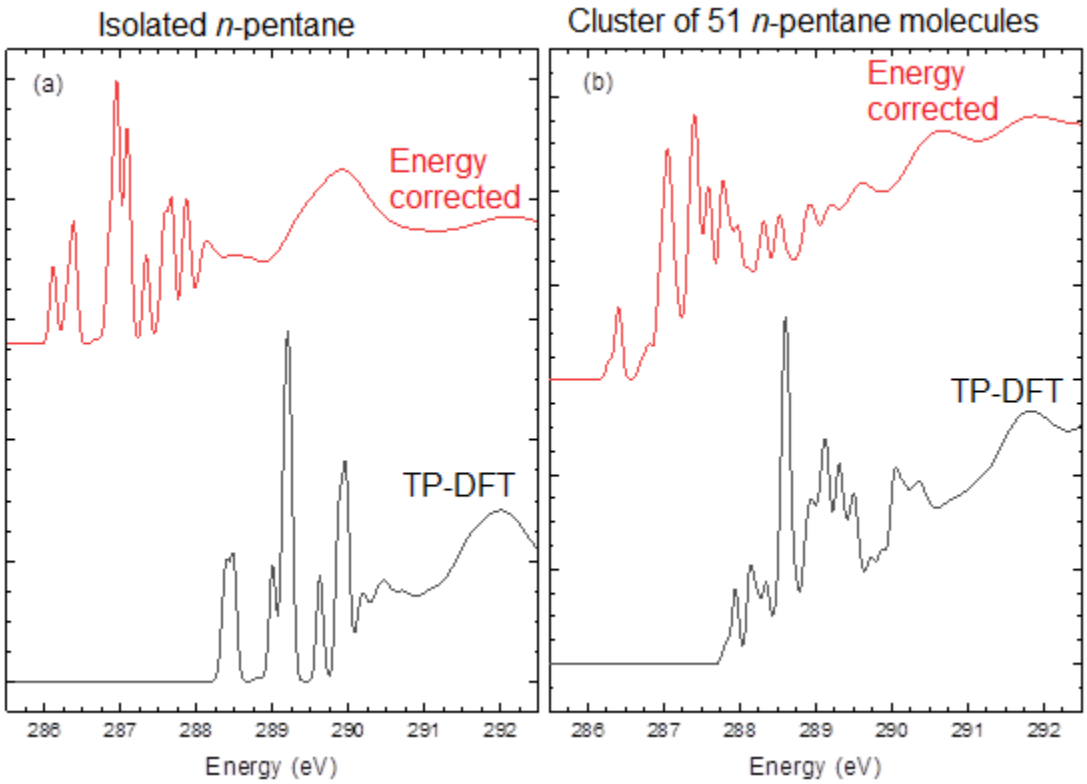

Figure 44.7 - ΔKS energy correction performed on the spectra of (a) the isolated pentane and (b) cluster containing 51 molecules of pentane

The ΔKS energy correction process will change the shape and energy of transitions in the spectra. This change is observed for both the isolated molecule and the cluster. If the radius of the basis functions is larger than the size of the cluster, parts of

the orbitals will be in the vacuum. In this case, the shielding effect will not be fully reproduced as the active electron that is placed into these orbitals will have less to no interaction with the passive electrons. This will lead to the appearance of low energy peaks with Rydberg character in the spectrum.

As it is shown in the following figure, the energy shift for the isolated molecule is more than the cluster, and after this energy correction, the spectrum of the isolated molecule appears in lower energy compared to the cluster.

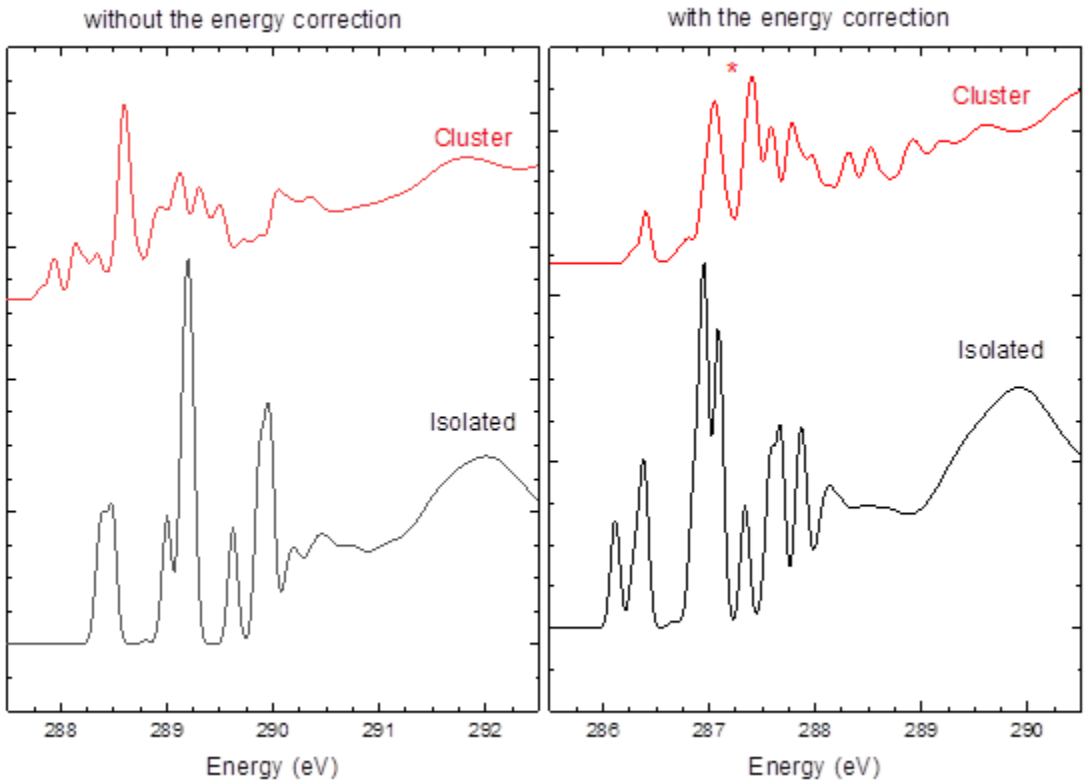

Figure 44.8 - Carbon 1s NEXAFS spectra of isolated pentane compared with the cluster containing 51 molecules with and without the ΔKS energy correction

The energy corrected spectra confirm the hypothesis of the shift to the higher energy for the NEXAFS spectra of the condensed phase in comparison with the gas phase *n*-alkanes. If we zoom in, on the area between 285.5-286.1 eV, we can see that in the spectrum of the cluster, a peak at 285.8 eV exists, which appears in lower energy compared to the peak of the transition of the isolated molecule. This peak is presented in Figure 4.9.

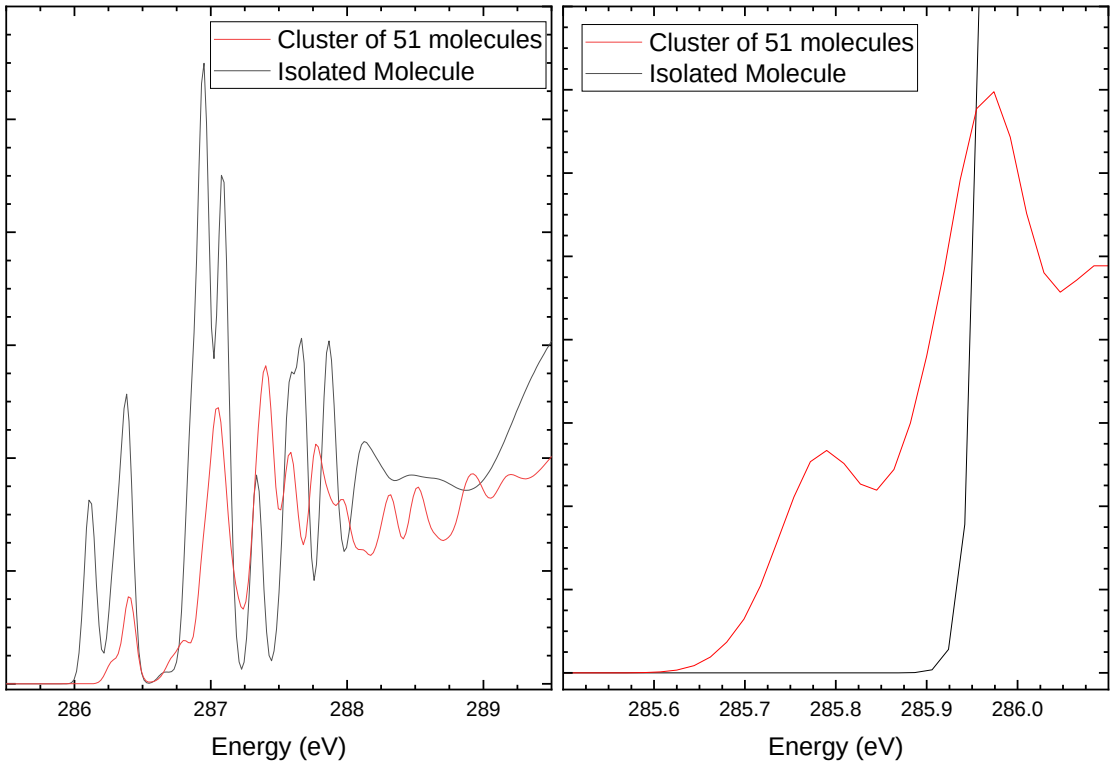

Figure 44.9 - First transition in the isolated molecule and the cluster of 51 pentanes after the ΔKS energy correction

The shift to the higher energy from the spectra of the isolated molecule to the cluster could be observed if this very weak (order of 10^{-50}) artefact is ignored. This artefact is simply the mathematical extension of the basis functions which will diminish as the radius is increased. The main reason behind this low energy peak could be because of the components of the auxiliary basis functions that might be larger than the radius of the cluster. Therefore, it is possible to observe the shift to the higher energy for the spectra of the cluster compared to the isolated molecule, if this low energy artefact is ignored.

4.3 Discussion and Conclusion

Experimental measurements have shown a shift to the higher energy for the condensed phase compared to the gas phase.[4, 29-31] This work was focused on replicating the experimental trend by defining the gas phase as the isolated molecule and the condensed phase as the cluster of molecules oriented to generate the orthorhombic

structure. The main hypothesis was that the size of the computational cluster needs to be larger than the spatial extent of the Rydberg orbitals, so the correct character of these orbitals can be calculated. The first parameter that was studied was the type of basis set, which is used on the carbon with the core hole. It was concluded that IGLO-III presents the best result for the isolated *n*-pentane since it will be possible to identify various transitions distinctly. However, calculating the size of the orbitals in the IGLO-III basis set, it was concluded that some of the very diffuse basis functions need to be trimmed from this basis set to be able to have the orbitals within the boundaries of a cluster of less than 30 Å. This is done mainly to keep the computational cost low while calculating a good spectrum of the cluster model. The trimmed IGLO-III basis set was used to calculate the spectra of the isolated molecule and the result was compared with the spectrum obtained using a regular IGLO-III basis set. As the final result were similar, the trimmed IGLO-III basis set was selected and used for the rest of the spectra calculations performed in this study.

Spectra calculation was performed using various auxiliary and augmentation basis sets and the best basis sets were selected based on the computational cost and the reproduced spectral details. These calculation were carried out on an isolated molecule using the deMon2k program.[32] The selected basis set (trimmed IGLO-III on the carbon with the core hole, ECP on all the other carbons, and TZVP on the hydrogen atoms), auxiliary basis set (Gen-A4* on the carbon with the core hole and Gen-A2 on all the other atoms), augmentations (XAS-I) and exchange-correlation functionals(PBE) were used for the rest of the measurements in this study to have a good consistency between the calculated spectra.

The carbon 1s NEXAFS spectra were studied as a function of the size of the cluster in comparison with the spectrum of the isolated molecule. As it can be observed in Figure 4.6, an increase in the size of the cluster doesn't change the position of the Rydberg peaks significantly. Clusters with up to 51 molecules of *n*-pentane were examined, and all the measured spectra showed a wrong shift to the lower energy for the spectra of the cluster compared with the isolated molecule. The ΔKS energy approximation was the next improvement on the method that was performed on the spectra of the isolated molecule

as well as the cluster. This energy correction shifts both spectra to the lower energy. However, the amount of energy shift for the isolated molecule is larger than the cluster. A comparison between the spectra of the isolated molecule and the cluster using this approach shows a slight shift to the higher energy for the cluster. Looking at the outputs of deMon2k for both models, as well as zooming on the first peaks in an overlap plot, it is observed that a small low energy peak appears at lower energy compared to the spectra of the isolated *n*-pentane. The main reason for this low energy peak is the mathematical equations that are used to express the orbitals. These equations will not simply converge to zero at a certain number, but instead, they diminish gradually as the size of the orbital increases to the infinity. This low energy feature can be neglected as it is on the scale of 10^{-50} compared with the main spectrum. Therefore, the experimental shift to the higher energy for the cluster (condensed phase) compared to the isolated molecule (gas phase) is successfully reproduced. However, due to the high computational cost of this approach, this study was not continued further. Alternative models were designed to study the effect of chain length, temperature changes, geometry defects, and vibrations on the NEXAFS spectra of *n*-alkanes. MD-DFT simulations approach was also used as an alternative approach to obtain the spectra of the molecules considering the nuclear motions. These approaches are explained in the next chapters in detail.

Another good approach to have the orbital contained in the cluster is to use PBC in the calculation. This option is explained in detail in Chapter 3. Unfortunately, deMon2k doesn't have the option of calculations using PBC. Programs that support calculations with PBC, such as GPAW[33], would offer a better approach for the comparison of isolated molecule vs. cluster. However, using the PBC, the unit cell needs to be large enough to avoid the interaction of two carbons with the core hole in the neighboring unit cells. This approach is explained in chapter 9 – future work, in more detail.

4.4 References

1. Bagus, P. S., Weiss, K., Schertel, A., Wöll, Ch, Braun, W., Hellwig, C., Jung, C., Identification of transitions into Rydberg states in the X-ray absorption spectra of condensed long-chain alkanes. *Chemical Physics Letters* **1996,** *248* (3), 129-135.

2. Robin, M. B., *Higher Excited States of Polyatomic Molecules*. **1974**.

3. Urquhart S. G.; Gillies R., Rydberg−Valence Mixing in the Carbon 1s Near-Edge X-ray Absorption Fine Structure Spectra of Gaseous Alkanes. *The Journal of Physical Chemistry A* **2005,** *109* (10), 2151-2159.

4. Urquhart S. G.; Gillies R., Matrix effects in the carbon 1s near edge x-ray absorption fine structure spectra of condensed alkanes. *The Journal of Chemical Physics* **2006,** *124* (23), 234704.

5. Weiss K.; Bagus P. S.; Wöll Ch., Rydberg Transitions in X-ray Absorption Spectroscopy of Alkanes: The Importance of Matrix Effects. *J. Chem. Phys.* **1999,** *111* (15), 6834-6845.

6. Schöll, A., Fink, R., Umbach, E., Mitchell, G. E., Urquhart, S. G., Ade, H., Towards a Detailed Understanding of the NEXAFS Spectra of Bulk Polyethylene Copolymers and Related Alkanes. *Chem. Phys. Lett.* **2003,** *370* (5), 834-841.

7. Nozaki, K.; Higashitani, N.; Yamamoto, T.; Hara, T., Solid–solid phase transitions in n-alkanes C23H48 and C25H52: X-ray power diffraction study on new layer stacking in phase V. *The Journal of Chemical Physics* **1995,** *103* (13), 5762-5766.

8. Plomp, M.; van Enckevort, W. J. P.; Hoof, P. J. C. M. v.; Streek, C. J. v. d., Morphology of and dislocation movement in n-C40H82 paraffin crystals grown from solution. *Journal of Crystal Growth* **2003,** *249* (3), 600-613.

9. Muller, A.; Lonsdale, K., The low-temperature form of C18H38. *Acta Crystallographica* **1948,** *1* (3), 129-131.

10. Shearer, H. M. M.; Vand, V., The crystal structure of the monoclinic form of n-hexatriacontant. *Acta Crystallographica* **1956,** *9* (4), 379-384.

11. Broadhurst, M. G., An Analysis of the Solid Phase Behavior of the Normal Paraffins. *Journal of Research of the National Bureau of Standards-A.Physics and Chemsitry* **1962,** *66A* (3).

12. Hastie, G. P.; Johnstone, J.; Roberts, K. J.; Fischer, D., Examination of the structure and melting behaviour of thin film n-alkanes using ultra-soft polarised near-edge X-ray absorption spectroscopy. *Journal of the Chemical Society, Faraday Transactions* **1996,** *92* (5), 783-789.

13. Perera, S. D., Wang, Jian, Urquhart, Stephen G., Linear dichroism in the NEXAFS spectra of n-alkane crystalline polymorphs. *Journal of Electron Spectroscopy and Related Phenomena* **2019,** *232*, 5-10.

14. Smith, A. E., The Crystal Structure of the Normal Paraffin Hydrocarbons. *The Journal of Chemical Physics* **1953,** *21* (12), 2229-2231.

15. Hu, H.; Dorset, D. L., Three-dimensional electron diffraction structure analysis of polyethylene. *Acta Crystallographica Section B* **1989,** *45* (3), 283-290.

16. Koster A.M. , G. G., Calaminici P., Casida M. E., Dominguez V. D., Flores-Moreno R., Gamboa G. U., Goursot A., Heine T., Ipatov A., Janetzko F., del Campo J. M., Reveles J. U., Vela A., Zuniga-Gutierrez B., Salahub D. R. *deMon2k*, Cinvestav, Mexico City 2011.

17. Perdew, J. P.; Burke, K.; Ernzerhof, M., Generalized Gradient Approximation Made Simple. *Physical Review Letters* **1996,** *77* (18), 3865-3868.

18. Huzinaga, S., *J. Chem. Phys.* **1965,** *42*, 1293.

19. Huzinaga, S., Gaussian-Type Functions for Polyatomic Systems. I. *The Journal of Chemical Physics* **1965,** *42* (4), 1293-1302.

20. Patterson, L. G. M., Private communication. 2013.

21. Calaminici P., J. K., Köster A. M. , Density functional calculations of molecular polarizabilities and hyperpolarizabilities. *The Journal of Chemical Physics* **1998,** *109* (18), 7756-7763.

22. Pettersson, L. G. M.; Wahlgren, U.; Gropen, O., Effective core potential parameters for first- and second-row atoms. *The Journal of Chemical Physics* **1987,** *86* (4), 2176-2184.

23. Ueda, K., Okunishi, M., Chiba, H., Shimizu, Y., Ohmori, K., Sato, Y., Shigemasa, E., Kosugi, N., Rydberg—valence mixing in the C 1s excited states of CH4 probed by electron spectroscopy. *Chemical Physics Letters* **1995,** *236* (3), 311-317.

24. Remmers, G., Domke, M., Kaindl, G., Vibrationally resolved carbon core excitations in alkane molecules. *Physical Review A* **1993,** *47* (4), 3085-3091.

25. Thomas, L. L.; Christakis, T. J.; Jorgensen, W. L., Conformation of Alkanes in the Gas Phase and Pure Liquids. *The Journal of Physical Chemistry B* **2006,** *110* (42), 21198-21204.

26. Frisch, M. J.; Trucks, G. W.; Schlegel, H. B.; Scuseria, G. E.; Robb, M. A.; Cheeseman, J. R.; Scalmani, G.; Barone, V.; Petersson, G. A.; Nakatsuji, H.; Li, X.; Caricato, M.; Marenich, A. V.; Bloino, J.; Janesko, B. G.; Gomperts, R.; Mennucci, B.; Hratchian, H. P.; Ortiz, J. V.; Izmaylov, A. F.; Sonnenberg, J. L.; Williams; Ding, F.;

Lipparini, F.; Egidi, F.; Goings, J.; Peng, B.; Petrone, A.; Henderson, T.; Ranasinghe, D.; Zakrzewski, V. G.; Gao, J.; Rega, N.; Zheng, G.; Liang, W.; Hada, M.; Ehara, M.; Toyota, K.; Fukuda, R.; Hasegawa, J.; Ishida, M.; Nakajima, T.; Honda, Y.; Kitao, O.; Nakai, H.; Vreven, T.; Throssell, K.; Montgomery Jr., J. A.; Peralta, J. E.; Ogliaro, F.; Bearpark, M. J.; Heyd, J. J.; Brothers, E. N.; Kudin, K. N.; Staroverov, V. N.; Keith, T. A.; Kobayashi, R.; Normand, J.; Raghavachari, K.; Rendell, A. P.; Burant, J. C.; Iyengar, S. S.; Tomasi, J.; Cossi, M.; Millam, J. M.; Klene, M.; Adamo, C.; Cammi, R.; Ochterski, J. W.; Martin, R. L.; Morokuma, K.; Farkas, O.; Foresman, J. B.; Fox, D. J. *Gaussian 16*, Wallingford, CT, 2016.

27. Zhao, Y.; Truhlar, D. G., The M06 suite of density functionals for main group thermochemistry, thermochemical kinetics, noncovalent interactions, excited states, and transition elements: two new functionals and systematic testing of four M06-class functionals and 12 other functionals. *Theoretical Chemistry Accounts* **2008,** *120* (1), 215-241.

28. Petersson, T.; Hellsing, B., A detailed derivation of Gaussian orbital-based matrix elements in electron structure calculations. *European Journal of Physics* **2009,** *31* (1), 37-46.

29. Shokatian, S.; Urquhart, S. G., Near Edge X-ray Absorption Fine Structure Spectra of Linear n-Alkanes: Variation with Chain Length. *Journal of Electron Spectroscopy and Related Phenomena* **2019,** *236*, 18-26.

30. Urquhart, S. G.; Hitchcock, A. P.; Smith, A. P.; Ade, H. W.; Lidy, W.; Rightor, E. G.; Mitchell, G. E., NEXAFS Spectromicroscopy of Polymers: Overview and Quantitative Analysis of Polyurethane Polymers. *Journal of Electron Spectroscopy and Related Phenomena* **1999,** *100* (1), 119-135.

31. Perera, S. D., Shokatian, Sadegh, Wang, Jian, Urquhart, Stephen G., Temperature Dependence in the NEXAFS Spectra of n-Alkanes. *The Journal of Physical Chemistry A* **2018,** *122* (49), 9512-9517.

32. Geudtner, G.; Calaminici, P.; Carmona-Espíndola, J.; del Campo, J. M.; Domínguez-Soria, V. D.; Moreno, R. F.; Gamboa, G. U.; Goursot, A.; Köster, A. M.; Reveles, J. U.; Mineva, T.; Vásquez-Pérez, J. M.; Vela, A.; Zúñinga-Gutierrez, B.; Salahub, D. R., deMon2k. *Wiley Interdisciplinary Reviews: Computational Molecular Science* **2011,** *2* (4), 548-555.

33. Mortensen, J. J.; Hansen, L. B.; Jacobsen, K. W., Real-space grid implementation of the projector augmented wave method. *Physical Review B* **2005,** *71* (3), 035109.

Chapter 5 – Effect of Chain Length on the NEXAFS Spectra of *N*-alkanes

5.1 Description

Chapter 5 investigates the effect of chain length in the carbon 1s NEXAFS spectra of linear *n*-alkanes using Transition Potential Density Functional Theory (TP-DFT) calculations. Species from propane (C_3H_8) to *n*-icosane (*n*-$C_{20}H_{42}$) and selected longer chains were examined. This study focuses on the prominent 'C-H band' (287 - 288 eV) in these NEXAFS spectra. TP-DFT calculations show that contributions from interior methylene groups (3 or more positions from the chain end) are similar, while contributions from the terminal methyl and the first methylene groups differ. The evolution of the angle-dependent and Rydberg-valence mixing with chain length are also examined. This paper is published in the Journal of Electron Spectroscopy and related phenomena (DOI: 10.1016/j.elspec.2019.08.001). The manuscript is reformatted from the original version for inclusion in the thesis.

5.2 Description of Candidate Contribution

The author of this thesis was the primary investigator of this research work, and he developed the research concept of this study, data analysis, the computational model development and execution of the simulations, interpretation of the results, and writing of the document. S. G. Urquhart provided guidance throughout the model development, process of data interpretation and analysis, and actively involved in the editing process of the document.

5.3 Relation of Contribution to the Research Objectives

The main objective of this thesis is to understand the effect of structural variation and structural disorder in *n*-alkanes on their NEXAFS spectra. This manuscript provides some insights on the effect of one of the structural differences (chain length) on the NEXAFS spectra. Studying angle-dependent and angle-resolved spectra provide more details on the effect of orientation of the molecule (or beam) on the spectra. Together,

with the Rydberg-valence mixing studies, it is possible to gain a better understanding of the complicated spectra of *n*-alkanes.

5.4 Near Edge X-ray Absorption Fine Structure Spectra of Linear *N*-alkanes: Variation with Chain Length

Sadegh Shokatian and Stephen Urquhart*

Department of Chemistry, University of Saskatchewan, Treaty Six Territory, Saskatoon, SK, Canada S7N 5C9

Abstract

The effect of chain length on the carbon 1s Near Edge X-ray Absorption Fine Structure (NEXAFS) spectra of linear *n*-alkanes has been examined with Transition Potential Density Functional Theory (TP-DFT) calculations. Species from propane (C_3H_8) to *n*-icosane (*n*-$C_{20}H_{42}$) and selected longer chains were examined. This study focuses on the prominent 'C-H band' (287 - 288 eV) in these NEXAFS spectra. TP-DFT calculations show that contributions from interior methylene groups (3 or more positions from the chain end) are similar, while contributions from the terminal methyl and the first methylene groups differ. The evolution of the angle-dependent and Rydberg-valence mixing with chain length are also examined.

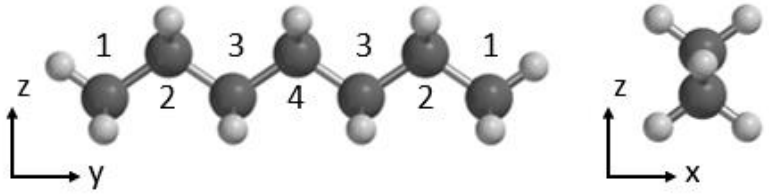

Scheme 5-1 - Orientation of the n-alkane backbone relative to the x, y, and z axes used in deMon2k calculations, and atomic site numbering used in this paper

5.4.1 Introduction

The carbon 1s Near Edge X-ray Absorption Fine Structure (NEXAFS) spectra of simple hydrocarbons (C_xH_y) have surprising complexity given their chemical simplicity. The NEXAFS spectra of condensed hydrocarbons are relevant for analytical studies,[1-2] as hydrocarbon chains are common components in modern materials and as side chains in the polymer P3HT[3] and as refractory carbon in soils with relevance to global carbon cycles.[4] Thin layer (monolayer and multilayer) alkanes deposited on various substrates have been the centre of attention in many surface studies, where the orientation of the deposited alkane,[5-11] the effect of functional group,[7, 12-14] alkane chain length,[15-16] and crystal structure[17-18] are shown to have a significant effect on the thin film properties. The analytical sensitivity of NEXAFS spectra to the chemistry and structure of hydrocarbons is frustrated by knowledge gaps, particularly as computational methods do an incomplete job in modeling the NEXAFS spectra of hydrocarbons such as alkanes.[19-20]

Saturated alkanes lack sharp low energy carbon 1s → π* transitions and are instead dominated by distinctive carbon 1s → σ* transitions that form the 'C-H' band (287-288 eV). In examining the NEXAFS spectra of alkanes, we see a large difference between their gas and condensed phase NEXAFS spectra, with subtler differences observed between different condensed forms.[19, 21-23] High-resolution gas phase spectra of small alkane molecules (e.g., methane, ethane, propane, etc.) show a series of sharp carbon 1s → Rydberg transitions, with rich vibronic character.[6, 24-26] The NEXAFS spectra of solid alkanes are relatively well explored, including linear and branched polyethylene,[20, 27] linear *n*-alkanes of various lengths,[6, 21-23, 28] and alkanes adsorbed on metal surfaces.[17, 29-30] NEXAFS spectra of ordered *n*-alkanes show a characteristic 'rabbit ear' splitting in the 'C-H' band at 287-288 eV. This 'C-H' band is broadened or obscured in disordered samples,[20-21] and becomes narrower in NEXAFS spectra recorded at cryogenic temperatures.[19]

A key difference between the gas and condensed phase spectra is the quenching of Rydberg orbitals in the condensed phase, the emergence of valence character, and a blue-shift and broadening of the 'C-H' band in the condensed phase spectra.[31] These

differences are evidenced by the differences between the gas and condensed phase spectra of the same species (2,2-dimethylpropane or neopentane)[31] and calculations that demonstrate Rydberg quenching[6, 31] and the emergence of valence character in the condensed phase.[31] This interpretation addresses a previous controversy in the literature, where some researchers argued that Rydberg character persists in the condensed phase.[32-33]

Significant Rydberg-valence mixing is observed when the energy and symmetry of the Rydberg and valence orbitals are matched.[34] For alkanes, Rydberg mixing with 'C-H' character valence orbitals have a direct correction with the number of hydrogen atoms directly bonded to the core excited carbon atom.[25, 34]

The role of chain length on Rydberg/valence mixing in the NEXAFS spectra of *n*-alkanes has not been well explored (exceptions, see ref. [21, 23]). In many studies, computational models used to simulate the NEXAFS spectra of long hydrocarbons use smaller molecule models (propane,[32] *n*-butane,[17-18, 20], etc.), or a single CH_2 group in the centre of a longer hydrocarbon to simulate the spectrum of a long chain.[6] The validity of these approximations has not been tested.

The effect of gauche defects and thermally populated vibrations on the NEXAFS spectra of *n*-alkanes was recently addressed.[19] As longer chains are considered, the number of gauche defects (e.g., rotations about individual $C-C$ bonds, distorting the *n*-alkane from its lowest energy all-trans geometry) is expected to increase. For example, Basson *et al.* [35] observed thermally populated gauche defects below the melting point of *n*-$C_{28}H_{58}$. These gauche defects and the thermal population of vibrational modes are expected to lead to new spectroscopic features below the 'C-H band'. These observations were used to explain differences in the temperature-dependent NEXAFS spectra of *n*-octacosane (*n*-$C_{28}H_{58}$), where the 'C-H band' in spectra recorded at cryogenic temperature is narrower, and spectra recorded at ambient temperatures have a lower-energy onset of the 'C-H band'.[19]

This work is focused on *n*-alkanes, the family of linear saturated hydrocarbons. The evolution of the carbon 1s NEXAFS spectra of linear *n*-alkanes with chain length is

explicitly explored with theoretical calculations. The carbon 1s NEXAFS spectra of linear *n*-alkanes from ethane to *n*-tetracontane (*n*-$C_{40}H_{82}$), and selected longer *n*-alkanes, are simulated with the transition potential density functional theory (TP-DFT) methods. Angle integrated and angle-resolved spectra are examined, and singlet-triplet energy differences are calculated for low energy transitions. Key differences with chain length are identified and rationalized.

5.4.2 **Computational**

Molecular Geometries: The program Spartan '14[36] was used as a graphical editor to define the molecular structure of *n*-alkanes from propane (C_3H_8) to *n*-tetracontane (*n*-$C_{40}H_{82}$), and selected small alkanes (methane, ethane, 2-methyl propane, and 2,2 dimethylpropane). High symmetry was maintained: D_{2h} for ethane, C_{2v} for odd-numbered *n*-alkanes (propane, *n*-pentane, etc.) and D_{2h} for even-numbered *n*-alkane (*n*-butane, *n*-hexane, etc.). Geometry optimization was performed using the program Gaussian 16[37] with the M06-2X DFT approach[38] and the 6-31+G(d, p) basis set. Geometries of the *n*-alkanes were reoriented to align the molecular backbone with the y-axis and to place the C-C-C plane within the yz plane (See **Scheme 1**).

Spectroscopic Simulations: Carbon 1s NEXAFS simulations were obtained from DFT calculations using the deMon2K code (version 4.3.4)[39] with the PBE exchange-correlational functional.[40] Spectroscopic simulations were obtained using the half-core-hole (HCH) transition-potential density functional theory (TP-DFT) method.[41] Effective core potentials were used for all carbon atoms except for the core excited atom, and a triple-zeta basis set was used for hydrogen atoms. The IGLO-III basis set[42] was used on the core-excited carbon atom, augmented by the XAS-I basis set.[43-44] Simulated spectra were generated from these calculations by using a 0.2 eV wide Gaussian line shape for each calculated core excitation transition, using the XAS code accompanying deMon2k. Contributions from individual carbon atoms were each calculated, and added to give an overall molecular spectrum. Angle averaged spectra, and angle-resolved spectra with the X-ray polarization directed along the x, y, and z-axes were also simulated.

Ionization Potential and Valence Orbital Calculations: Carbon 1s ionization potentials for *n*-hexane and *n*-heptane was calculated using the ∆(SCF) method; these species were chosen to examine transitions at interior methylene sites. In the ∆(SCF) method, the ionization potential is determined from the energy difference between the calculated ground state energy and energy of the core ionized molecule, calculated with a full core hole. Effective core potentials were used for all atoms except the atom with the core hole. Term values (TV) were determined for the lowest energy transition, using Equation 5.1:

$$TV = TE - IP \qquad \textit{Equation 5.1}$$

where TE is the transition energy, obtained from the TP-DFT calculations and IP is the ionization potential, obtained from the Δ(SCF) calculations.

Rydberg-Valence Mixing: The energy difference between the calculated singlet and triplet excited state, ΔE(S-T), is a useful proxy for the Rydberg character. In improved virtual orbital (IVO) calculations, a singlet-triplet energy difference of less than 0.05 eV indicates 'pure' Rydberg character;[6, 25] a similar threshold is used here. The energy of triplet excited states were calculated by changing the spin of the excited electron. A small modification is needed to calculate the energy of the singlet excited state, as the DFT method calculates the energy of a pseudo-singlet (PS) state, e.g. $|ab^{-}|$, and not that of the indistinguishable superposition, $\frac{1}{\sqrt{2}}(|ab^{-}| - |a^{-}b|)$. The true singlet state energy is obtained using Equation 5.2:

$$E(S) = 2E(PS) - E(T) \qquad \textit{Equation 5.2}$$

A calculation of the singlet-triplet energy difference was performed for the first two excited states for each carbon atom in the *n*-alkanes from methane (CH_4) to *n*-nonane (*n*-C_9H_{20}) as well as 2-methyl propane and 2,2-dimethylpropane.

5.4.3 Results and Discussions

Figure 5.1 presents the experimental gas-phase NEXAFS spectrum of propane (C_3H_8),[6] recorded in total ion yield, in comparison to the condensed phase spectrum of *n*-tetracontane (*n*-$C_{40}H_{82}$),[45] recorded in transmission in STXM microscope. The gas-phase

spectrum shows rich vibronic structure and chemical splitting in the carbon 1s → 3s and the carbon 1s → 3p bands, while the spectrum of *n*-tetracontane shows the distinct 'C-H' band. These are 'extremes' in a comparison between the gas and condensed phases.

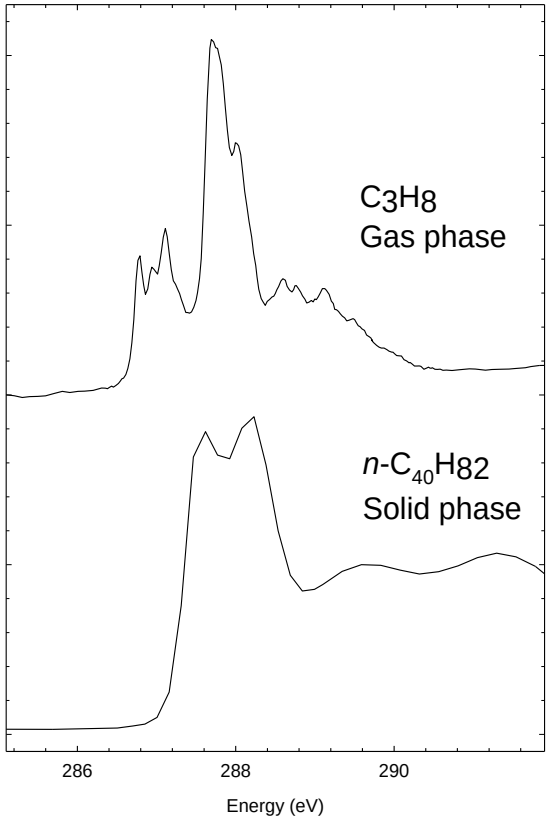

Figure 5.1 - Experimental carbon 1s NEXAFS spectrum of propane, recorded in total ion yield mode, and of n-tetracontane, n-$C_{40}H_{82}$, recorded in transmission.

Figure 5.2 presents the TP-DFT simulations of the carbon 1s NEXAFS spectra of linear *n*-alkanes from propane (C_3H_8) to *n*-octane (*n*-C_8H_{18}). **Figure 5.3** presents these simulations for linear *n*-alkanes from *n*-heptane (*n*-C_7H_{16}) to *n*-icosane (*n*-$C_{20}H_{42}$).

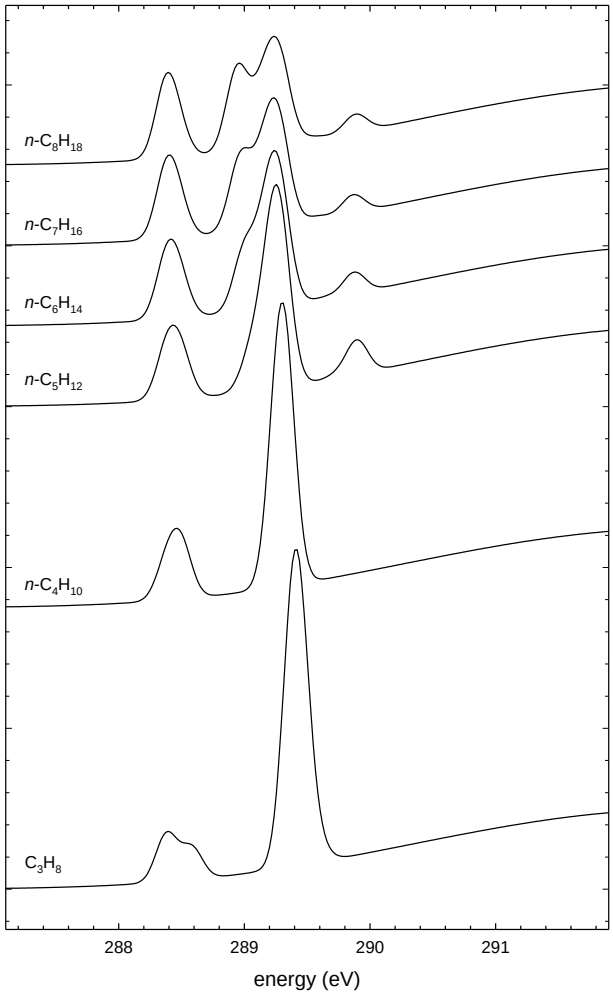

Figure 5.2 - Transition-potential density functional theory (TP-DFT) simulation of the Carbon 1s → C-H band in the NEXAFS spectra of linear n-alkanes, from propane (C_3H_8) to n-octane ($n\text{-}C_8H_{18}$).

In this figure, spectra are presented on an atomic-normalized basis, where each simulation is divided by the number of carbon atoms in that molecules (e.g., the simulation of propane, C_3H_8 is divided by 3).

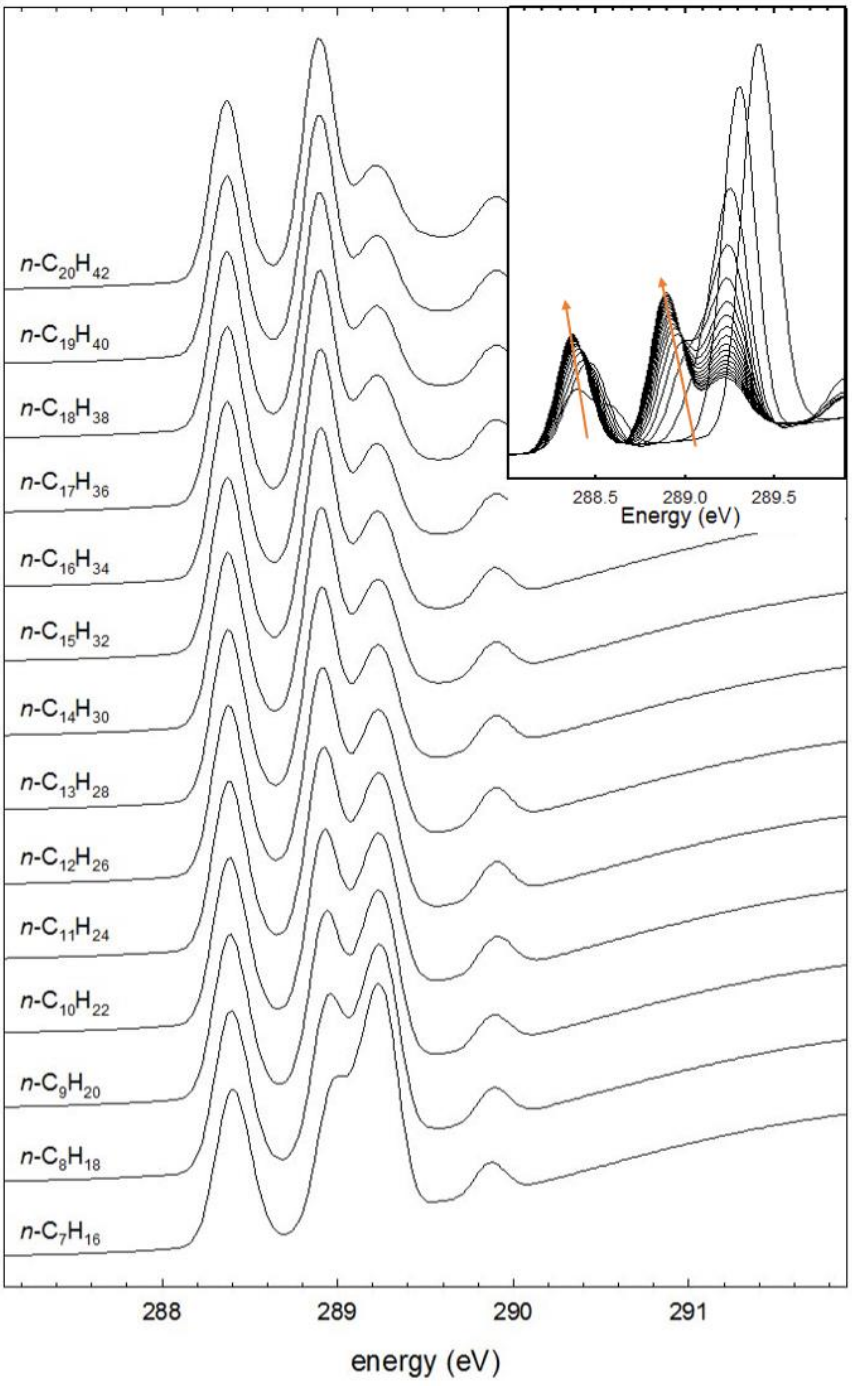

Figure 5.3 - Transition-potential density functional theory (TP-DFT) simulation of the Carbon 1s → C-H band in the NEXAFS spectra of linear n-alkanes, from n-heptane (n-C_7H_{16}) to n-icosane (n-$C_{20}H_{42}$).

Spectra in Figure 5.3 are normalized the same way as Figure 5.2.

Figure 5.4 presents these simulations for longer *n*-alkanes. To ease comparison, these simulations are normalized by the number of carbon atoms in each molecule.

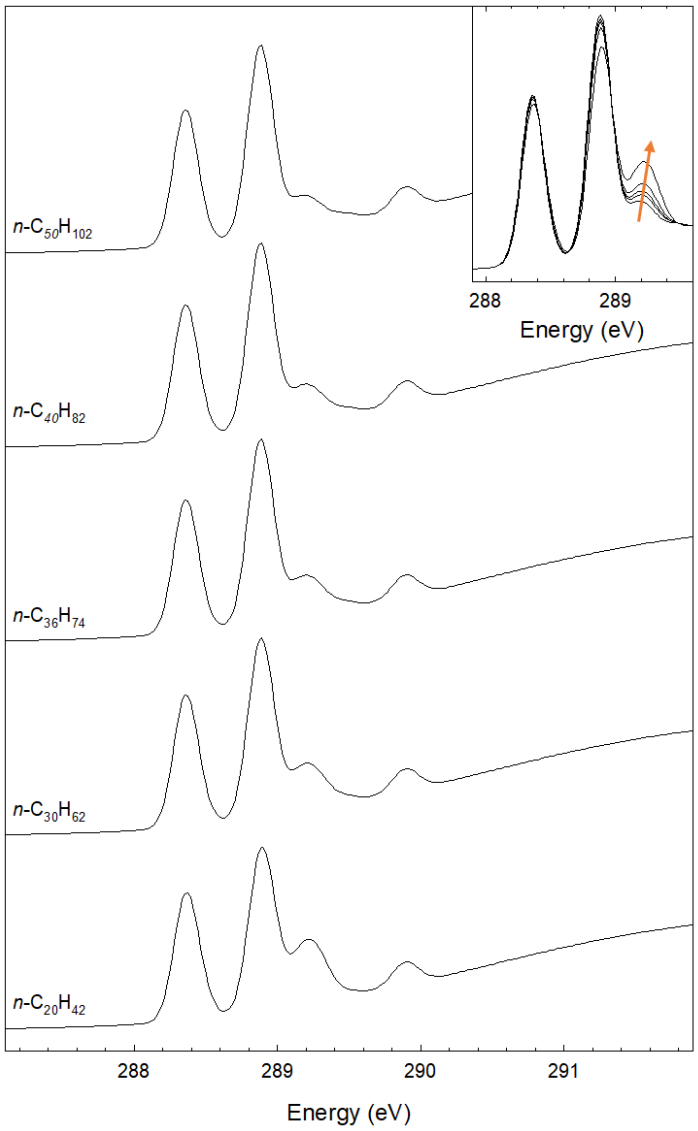

Figure 5.4 - Transition-potential density functional theory (TP-DFT) simulation of the Carbon $1s \rightarrow C-H$ *band in the NEXAFS spectra of linear n-alkanes n-icosane (n-$C_{20}H_{42}$), n-triacontane (n-$C_{30}H_{62}$), n-hexatriacontane (n-$C_{36}H_{74}$), n-tetracontane (n-$C_{40}H_{82}$) and n-pentacontane (n-$C_{50}H_{102}$).*

Table 5-1 presents the energies of characteristic transitions for different *n*-alkane chain positions.

Table 5.1 - Energies of characteristic transitions in TP-DFT calculations of linear n-alkanes by chain position

Molecule	C1$s \rightarrow 3s$ transition (eV)					C1$s \rightarrow 3p$ transition (eV)				
	CH_3(1)	CH_2(2)	CH_2(3)	CH_2(4)	CH_2(5+)	CH_3(1)	CH_2(2)	CH_2(3)	CH_2(4)	CH_2(5+)
Propane	288.38	288.58				289.39	289.49			
n-butane	288.38	288.50				289.29	289.32			
n-pentane	288.38	288.49	288.40			289.29	289.20	289.07		
n-hexane	288.37	288.49	288.39			289.28	289.18	289.01		
n-heptane	288.37	288.48	288.39	288.38		289.28	289.16	288.99	288.95	
n-octane	288.37	288.48	288.38	288.38		289.28	289.15	288.97	288.93	
n-nonane	288.37	288.48	288.38	288.38	288.38	289.28	289.15	288.96	288.92	288.91
n-decane	288.37	288.48	288.38	288.38	288.37	289.27	289.15	288.96	288.91	288.90
n-undecane	288.37	288.48	288.38	288.37	288.37	289.27	289.15	288.96	288.91	288.90
n-dodecane	288.37	288.48	288.37	288.37	288.37	289.27	289.15	288.96	288.91	288.89

The atomic contributions to the TP-DFT simulation of these species can be viewed in **figures S#** of the supplementary material, where # is the chain length. In the following discussion, the carbon atom sites are identified by their position relative to each end of the *n*-alkane chain: terminal methyl groups are the 1-position, the methylene group bonded to the methyl group is the 2-position, the next methylene groups further in are the 3-position, 4-position, etc. As an example, the atom positions in *n*-heptane would be identified as 1 2 3 4 3 2 1 (see **Scheme 1**).

Some clear patterns are observed in this data, which we will first discuss for shorter chain lengths where the differences are the most striking. The TP-DFT simulation of the carbon 1s NEXAFS spectrum of propane is similar to the IVO simulation found in the literature.[6] The experimental spectrum of propane is rich, with carbon 1s → 3s and carbon 1s → 3p transitions accompanied by a series of vibronic transitions.[6] These vibronic

effects are not accounted for in the IVO or TP-DFT simulations, which only simulate one-electron electronic transitions.[6] However, chemical shifts between the lower energy methyl (-CH_3) carbon 1s → 3s transition (288.38 eV) and the higher energy methylene (CH_2) carbon 1s → 3s transition (288.58 eV) are well reproduced by the IVO and TP-DFT methods.[6] The carbon 1s → 3p transition for propane (~289.4 eV) is narrow and intense, on account of the near degeneracy (~0.1 eV difference) of the carbon 1s → 3p transition from the CH_3 and CH_2 groups.

Schöll *et al.*[20] simulated the NEXAFS spectra of condensed *n*-alkanes using a model consisting of two molecules of *n*-butane oriented parallel or perpendicular to each other, at different intermolecular distances. The DFT simulated spectra of *n*-butane obtained within this research are similar to that presented in Schöll *et al.*[20] However, and as we demonstrate below, *n*-butane is a poor model for the NEXAFS spectra of extended *n*-alkane chains.

In this discussion and particularly for longer chains, we will use the labels '3s band' and '3p band' and simple transition assignments (carbon 1s → 3s transition and carbon 1s → 3p transition), based on the behavior of the spectra of short *n*-alkanes such as propane, where the Rydberg interpretation is unambiguous. For longer *n*-alkanes chain in the condensed phase, these assignments will be nuanced, as the Rydberg contribution will be attenuated by intermolecular interactions, as well as quenching by the size of the molecule by itself.

As longer chains are examined, the '3s band' shifts slightly to lower energy (see arrow in the inset to Figure 5.3) and the energy difference between the CH_3 and CH_2 carbon 1s → 3s contributions decreases (0.2 eV difference in propane; 0.12 eV difference for *n*-butane, decreasing to 0.11 eV for longer chains). The near degeneracy of 3s contributions for longer chains causes the relative intensity of the '3s band' to increase as this peak narrows. This narrowing, intensity increase, and energy shift can be seen in the inset to Figure 5.3. Unlike the 3s band, the 3p band does not increase in intensity with chain length, a molecular field splitting of the three 3p components appears to increase with chain length.

The origin of these trends in the energy of the carbon 1s → 3s transitions that make up the '3s band' with chain position can be seen in Table 5-1. The carbon 1s → 3s transition for the terminal methyl group (1-position) shifts slightly to lower energy as the chain length increases, ~10 meV from propane to *n*-undecane (*n*-$C_{11}H_{24}$). The carbon 1s → 3s transition from the first methylene (2-position; bonded to the terminal methylene) appears at ~110 meV higher in energy; this carbon atom site is present in *n*-butane (*n*-C_4H_{10}) and longer *n*-alkanes. Carbon 1s → 3s transitions for methylene groups that are two or more positions from the terminal methyl group (3-position, 4-position, etc.) appear at nearly the same energy as the carbon 1s → 3s transition of the terminal methyl group. These results are intriguing: the 'first methylene group from the end' (e.g., the 2-position) appears at a unique energy, higher than that of the inner methylene groups (3-position and higher) found on *n*-alkanes of length C5 or longer. The carbon 1s → 3s transition for the inner methylene groups (3+) and the terminal methyl group appear at nearly the same energy. Similar trends by chain position were observed for octadecanethiol by Völkner *et al*.;[8] this species is similar to our *n*-octadecane (*n*-$C_{18}H_{38}$) except for the thiol functionalization at one end of their molecule.

Calculations of ionization potentials and term values can provide additional information about the origin of the chain site dependence of the NEXAFS transition energies. **Table 5-2** presents calculated ionization potentials from ∆(SCF) calculations, term values, and excitation energies from TP-DFT calculations for the lowest energy carbon 1s → 3s transition in *n*-hexane and *n*-heptane.

These data show that the ionization potential of the methyl (-CH_3) and 2-position methylene (-CH_2) carbon atoms are identical, but that there is a 120 meV difference in the term value of this transition. This term value difference is unsurprising, given the chemical difference between the methyl and methylene groups. Valence orbital character is therefore responsible for the energy shift in the carbon 1s → 3s transition between the 2-position methylene group and the terminal methylene group.

In contrast, the ionization potential of the 3-position methylene group is 140 meV lower than that of the 2-position methylene group, with smaller shifts for the ionization

potential for methylene groups further to the centre of the molecule (4-position, etc.). As the term values make a shift of similar magnitude, the overall transition energies for the 3-, 4- position are similar to that of the terminal methylene and each other.

Table 5.2 - Calculated ionization potentials (from ΔSCF calculations), valence orbital energies, and transition energies (from TP-DFT calculations) for the lowest energy transition in n-hexane and n-heptane

	Carbon #	Ionization potential (eV)	Term Value (eV)	Transition energy (eV)
n-hexane	C1	-291.06	2.67	288.39
	C2	-291.06	2.55	288.51
	C3	-290.92	2.50	288.42
	C4	-290.92	2.50	288.42
	C5	-291.06	2.55	288.51
	C6	-291.06	2.67	288.39
n-heptane	C1	-291.05	2.66	288.39
	C2	-291.05	2.54	288.50
	C3	-290.90	2.48	288.42
	C4	-290.88	2.46	288.42
	C5	-290.90	2.48	288.42
	C6	-291.05	2.54	288.50
	C7	-291.05	2.66	288.39

The evolution of the ‘3p band’ with chain length is more complex. There is a large energy shift in the carbon 1s → 3p transition as the chain length increases from propane to *n*-butane, a further change to the shape of this peak for *n*-pentane, and the emergence of a new feature just below 290 eV for *n*-pentane.

In propane, the ‘3p band’ is narrow as the carbon 1s → 3p transitions that comprise this transition are nearly degenerate. This ‘3p band’ shifts to lower energy for *n*-butane. A low energy shoulder in the ‘3p band’ appears for *n*-pentane (at 289.1 eV; see ‘*’ in Figure 5.2); this shoulder increases in intensity as the chain length increases. Figures S5 (*n*-pentane), S6 (*n*-hexane), S7 (*n*-heptane), and beyond show this low energy shoulder arises from internal methylene groups (3-position or higher). Therefore, this transition only appears on *n*-alkanes of length C5 or higher. For longer chains, this ‘interior’ methylene peak grows in intensity, as the relative fraction of these atoms increases. The higher

energy band (~289.2 eV) decreases in intensity as the relative fraction of methyl, and 2-position methylene atoms decrease with increasing chain length.

These trends continue for longer *n*-alkanes. **Figure 5.4** presents TP-DFT simulations of the carbon 1s NEXAFS spectra of *n*-icosane (*n*-$C_{20}H_{42}$), *n*-triacontane (*n*-$C_{30}H_{62}$), *n*-hexatriacontane (*n*-$C_{36}H_{74}$), *n*-tetracontane (*n*-$C_{40}H_{82}$) and *n*-pentacontane (*n*-$C_{50}H_{102}$). The relative intensity of the methylene (2-position) contribution to the carbon 1s → 3p band at 289.2 eV decreases as the chain length increases, and the relative fraction of these atoms decreases. As the chain length increases, the relative energy of the '3s band' and the '3p band' stabilize, with an energy difference of ~0.5 eV. This is similar to the splitting in the 'C-H' band observed in *n*-octacosane (*n*-$C_{28}H_{58}$) recorded at cryogenic temperatures.[19]

The effect of gauche defects and molecular vibrations on the spectra of *n*-decane ($C_{10}H_{22}$) was studied previously.[19] In that study, both gauche defects and thermal population of vibrational levels were seen to broaden the C-H band, particularly at the low energy side of this band. As the sample temperature increases, the fraction of molecules in gauche defect states or thermally populated vibrational levels will increase and shift the onset of the C-H band to the lower energy.

When NEXAFS spectra of *n*-alkanes are recorded at cryogenic temperatures, the role of molecular motion (vibrations and defects) should be minimized, and a narrower 'C-H band' observed. In fact, the calculated 'C-H band' splitting between the 3s and 3p bands (~0.5 eV) for longer *n*-alkanes is similar to the 'C-H band' splitting observed in the NEXAFS spectrum of *n*-octacosane (*n*-$C_{28}H_{58}$) recorded at cryogenic temperatures.[19] This indicates that the long-standing inconsistency between theory and experiment for the 'C-H band' splitting arises from the enhanced width of the 'C-H band' at ambient temperature from thermally populated motion.

5.4.3.1 Polarization Dependence

Figure 5.5 presents the angle-dependent carbon 1s NEXAFS of *n*-alkanes from propane (*n*-C_3H_8) to *n*-icosane (*n*-$C_{20}H_{42}$) for the x, y, and z polarizations. The orientation

of the molecule in the x, y, z directions, as well as the carbon labels, are shown on top of Figure 5.5. These spectra are calculated for *n*-alkanes with a consistent alignment, where the *n*-alkane backbone is oriented along the y-axis, and the C-C-C plane oriented in the yz plane. The supplementary material (Figures S18 – S36) shows the polarization dependence on an atom by atom basis, for molecules propane (C_3H_8) to *n*-nonadecane (*n*-$C_{19}H_{40}$).

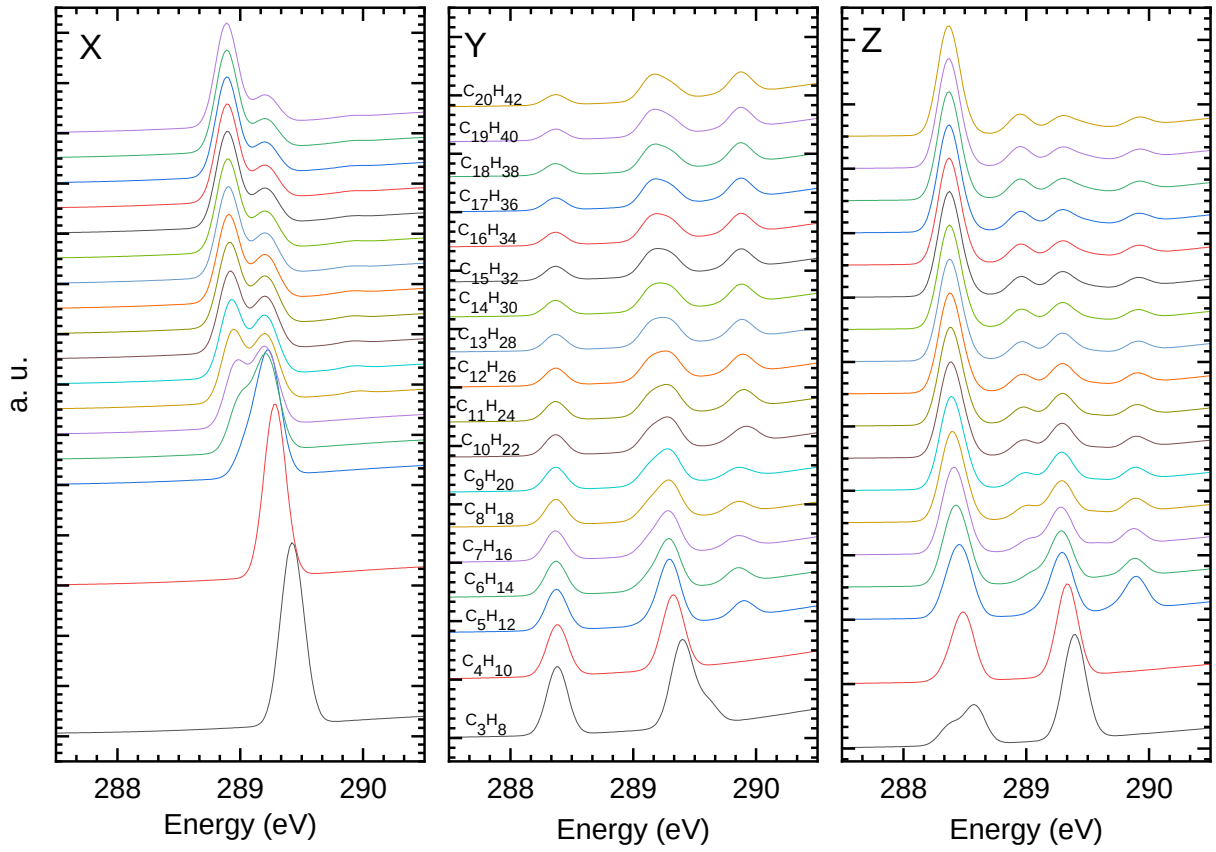

Figure 5.5 - Polarization-resolved transition-potential density functional theory (TP-DFT) simulations of the C-H band in the carbon 1s NEXAFS spectra of linear n-alkanes

These spectra are calculated for *n*-alkanes with a consistent alignment, where the *n*-alkane backbone is along the y-axis, and the C-C-C plane oriented in the yz plane. The three panes show the spectra with X-ray polarization directed along the x, y, and z-axes.

A comparison of Figure 5.5 to Figures 5-2 – 5-4 shows the polarization specific components of their NEXAFS spectra. For longer chains, the transition dipole moment for the low energy peak ('3s band' at 288.38 eV) is oriented along the z-axis, while the second peak ('3p band' at 289.3 eV) is oriented along the x-axis. The x and z directions are perpendicular to the backbone axis of the *n*-alkane chain (y-axis), so this effect demonstrates the linear dichroism expected for *n*-alkane chains.[6, 10-11] The angle dependence of the '3s band' oriented along z is consistent with its normal assignment as a carbon 1 s → $\sigma^*_{C\text{-}H}$ / $R_{\parallel}$ transition, as its transition dipole moment is parallel to the C-C-C plane (yz) but perpendicular to the *n*-alkane long axis (y-axis).[5] Likewise, the angle dependence for the second band ('3p band') is a predominantly along the x-direction, which is consistent with its observed linear dichroism and assignment as a carbon 1 s → $\sigma^*_{C\text{-}H}$ / $R_{\perp}$ transition, perpendicular to both the C-C-C plane (yz) and the *n*-alkane long axis (y axis).[5]

The y-polarized component is directed along the *n*-alkane backbone, with weak contributions to both the '3s' and '3p' bands. The atom-specific polarized spectra (supplementary material, Figures S18-S36), show that the lower energy carbon 1s → 3s contributions to the y-polarized spectrum arise from the terminal methyl groups. The relative intensity of these contributions decreases with the relative fraction of methyl groups, as the chain length increases.

In contrast, the carbon 1s → 3p band (at ~289.2 eV in the y-polarized spectra) has contributions from all *n*-alkane carbon atom sites. In the angle-dependent NEXAFS study by Fu and Urquhart[6], a weak backbone directed transition was observed at slightly higher energy than the two 'rabbit ear' C-H components.[6] This transition was also observed in monoclinic single crystals of n-alkanes.[21] The observation of this y-axis component in the TP-DFT calculations confirms the experimental observation of this backbone component at higher energy in the C-H band.

5.4.3.2 **Rydberg–Valence Mixing**

The degree of Rydberg–valence mixing with chain position and chain length was explored by calculating the singlet-triplet energy difference for the first two core-excited

states. Based on the Pauli exclusion principle, the excited electron in a triplet excited molecule has lower electron/electron repulsion than the excited electron in a singlet excited molecule. The calculated singlet-triplet energy difference is, therefore, a useful proxy for Rydberg character, as Rydberg excited states are more diffuse and will experience a lower electron/electron repulsion than a valence excited state. Therefore, a greater difference in the singlet-triplet excitation energies is expected if the orbital has a larger valence character.

Table 5-3 presents the difference between the singlet and triplet excited state energies, ($\Delta(S-T)$), for the first two transitions in methane, ethane, propane, 2-methylpropane, and 2,2-dimethylpropane; these correspond to the carbon 1s → 3s and the lowest energy carbon 1s → 3p transition.

Table 5.3 - Singlet triplet energy differences of the first two excited states for methane, ethane, propane, 2-methylpropane, and 2,2-dimethylpropane

	Carbon #	ΔE(S-T) (eV)[a]	
		First excited state Carbon 1s → 3s	Second excited state 1st carbon 1s → 3p
Methane	C1 (CH_4)	0.421	0.408
Ethane	C1 (CH_3)	0.376	0.363
Propane	C1 (CH_3)	0.366	0.344
	C2 (CH_2)	0.331	0.326
2-methylpropane	C1 (CH_3)	0.357	0.347
	C2 (CH)	0.253	0.027
2,2-dimethylpropane	C1 (CH_3)	0.343	0.343
	C2 (C)	0.001	<0.001

a. Singlet triplet energy differences are calculated with the corrected singlet state energy, per Equation 5.2

These molecules are chosen for comparison to similar singlet-triplet energy differences calculated using IVO calculations by Urquhart and Gillies.[34] The calculated singlet-triplet energy difference – and thus valence character – scales with the number of C-H bonds to the core excited carbon atom; highest for methane (4 C-H bonds to carbon), and decreasing in turn for methyl (3 C-H bonds), methylene (2 C-H bonds), methane (one C-H group) and smallest (near zero) for the quaternary carbon in 2,2-dimethylpropane.[34] The ($\Delta(S-T)$) values from TP-DFT calculations are somewhat higher than from the IVO

calculations, but follow the same trends. In particular, the ($\Delta(S-T)$) difference is near zero for the quaternary carbon in 2,2-dimethylpropane, consistent with the pure Rydberg character expected for core excitation transitions at this site.[34] These results confirm that TP-DFT calculations of this singlet-triplet energy difference are useful for examining the Rydberg character.

Figure 5.6 presents the ($\Delta(S-T)$) energy difference as a function of chain position for the first (top) and second (bottom) excited states of propane through *n*-octane.

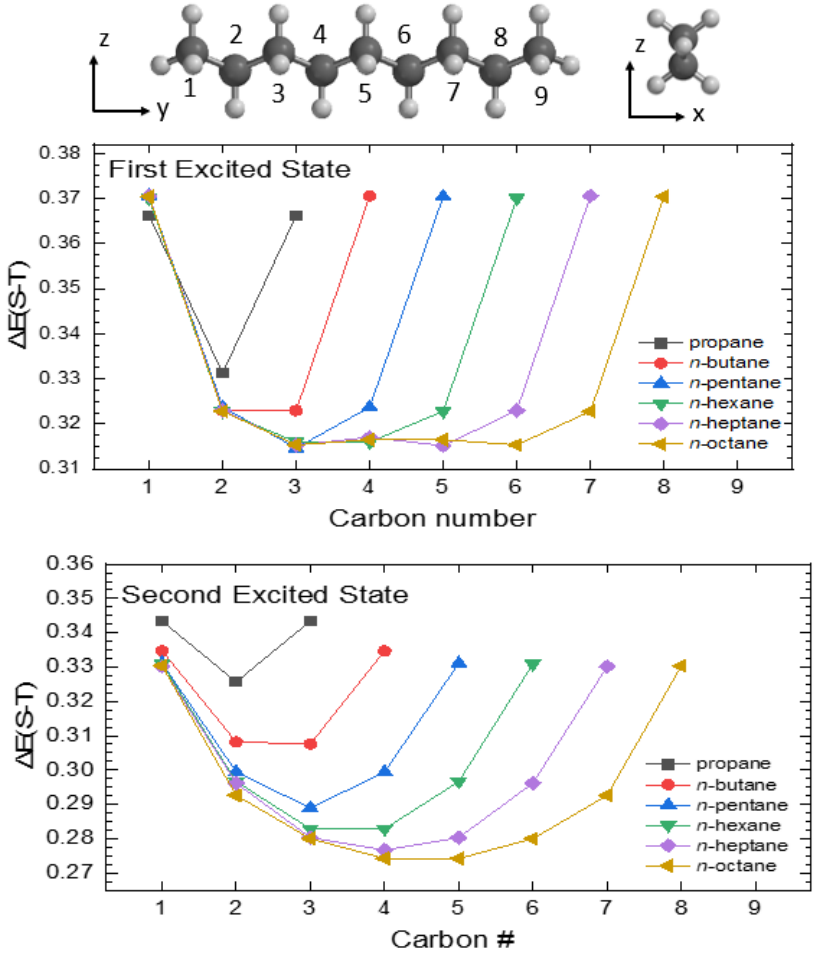

Figure 5.6 - The energy difference between the singlet and triplet excited states of propane, n-butane, n-pentane, n-hexane, n-heptane, and n-octane as a function of the position of the carbon in the structure

These data are summarized in **Table 5-4**. Except for propane, the $\Delta(S-T)$ energy differences are similar for all *n*-alkanes.

Table 5.4 - Singlet triplet energy differences of the first and second excited state for the n-alkanes from propane to n-octane

	Carbon #	ΔE(S-T) (eV)[a]	
		First excited state Carbon 1s → 3s	Second excited state 1st Carbon 1s → 3p
Propane	C1 (CH_3)	0.366	0.344
	C2 (CH_2)	0.331	0.326
n-Butane	C1 (CH_3)	0.371	0.335
	C2 (CH_2)	0.323	0.308
n-Pentane	C1 (CH_3)	0.371	0.331
	C2 (CH_2)	0.324	0.299
	C3 (CH_2)	0.315	0.289
n-Hexane	C1 (CH_3)	0.370	0.331
	C2 (CH_2)	0.323	0.297
	C3 (CH_2)	0.316	0.283
n-Heptane	C1 (CH_3)	0.371	0.330
	C2 (CH_2)	0.323	0.296
	C3 (CH_2)	0.315	0.280
	C4 (CH_2)	0.317	0.277
n-Octane	C1 (CH_3)	0.370	0.330
	C2 (CH_2)	0.323	0.293
	C3 (CH_2)	0.315	0.280
	C4 (CH_2)	0.317	0.274

a. Singlet triplet energy differences are calculated with the corrected singlet state energy, per Equation 5.2.

In Urquhart and Gillies, small shifts in the methyl $\Delta(S-T)$ energy difference were observed for different species (ethane, propane, 2-methyl propane, 2,2-dimethylpropane), as the group bonded to the terminal methyl group varied.[34] In this work, the terminal methyl group is bonded to a methylene group in all cases, and the Rydberg/valence character of the first excited state for the methyl group is constant. Likewise, excepting propane, the $\Delta(S-T)$ energy difference for the first methylene from the end (carbon 2) is similar, as are the interior carbon atoms (3 position and so forth) for *n*-pentane and longer. The results are similar for the second excited state, which is one of the three near-degenerate carbon 1s → 3p transitions. Propane remains an exception, and the values for *n*-butane are also somewhat higher. For longer chains, the $\Delta(S-T)$

energy difference for the methyl (carbon 1), first methylene from the end (carbon 2) and the interior methylene groups (carbon 3 and so forth) decrease very slightly with increased chain length. We note that these calculations were performed for isolated *n*-alkane chains, and thus do not reproduce full Rydberg quenching expected in the solid-state.[31] Nevertheless, a scaling of valence character with the number of C-H bonds to the core excited atom is confirmed.

5.4.4 **Conclusion**

This work presents the simulated NEXAFS spectra of linear *n*-alkanes from methane to *n*-tetracontane, *n*-$C_{40}H_{82}$, from TP-DFT calculations. These simulations show the chemical shifts between different chain sites (terminal methyl, first methylene, second methylene, etc.) and the similarity of transitions from methylene groups three or more positions from the chain end. This convergence leads to a distinct '3p band' feature (289.15 eV) that increases in intensity as the chain length increases. These results also show that simulations based on *n*-alkane chains shorter than five carbon atoms will note be effective at reproducing the spectra of longer *n*-alkanes.

In simulations of longer *n*-alkanes, the energy difference between the '3s band' and the '3p band' features matches that observed in the NEXAFS spectrum of *n*-octacosane (*n*-$C_{28}H_{58}$) recorded at cryogenic temperatures.[19] This demonstrates the effectiveness of these simulations, but also the importance of thermal population of vibrational modes (also known as nuclear motion effects) in determining the shape of molecular NEXAFS spectra recorded at ambient temperatures. This result is significant, as until now, there has been a very poor agreement between calculation and experiment.

Polarized X-ray absorption spectra of linear *n*-alkanes were examined as a function of chain length. Support for a 'backbone' oriented transition to the high side of the C-H band, shown experimentally by Fu and Urquhart[6], is supported by these calculations.

Finally, the degree of the Rydberg-valence character was examined as a function of chain length. The degree of Rydberg-valence mixing varies with the position on the

chain, with the most valence character for the terminal methyl group, and similar for internal methylene groups.

5.4.5 Acknowledgments

SGU is supported by the Natural Sciences and Engineering Research Council (NSERC Canada). This research was enabled in part by support provided by WestGrid (www.westgrid.ca; Grex) and Compute Canada Calcul Canada (www.computecanada.ca; Cedar and Graham), and University of Saskatchewan HPC resources (Plato). Experimental spectra were obtained using the Spherical Grating Monochromator of the Canadian Synchrotron Radiation Facility (CSRF) at the Synchrotron Radiation Centre (SRC) of the University of Wisconsin-Madison, and at the Spectromicroscopy beamline at the Canadian Light Source (CLS). We thank Sahan Perera for the carbon 1s NEXAFS spectrum of *n*-$C_{40}H_{82}$, recorded at the CLS. The SRC was supported by the National Science Foundation under award number DMR-0084402. The CSRF was supported by the National Science and Engineering Research Council (NSERC) Major Facilities Access Grant. The Canadian Light Source is supported by the Canada Foundation for Innovation, Natural Sciences and Engineering Research Council of Canada, the University of Saskatchewan, the Government of Saskatchewan, Western Economic Diversification Canada, the National Research Council Canada, and the Canadian Institutes of Health Research. We thank Lars Pettersson for his advice on calculating singlet and triplet excited states in deMon2k.

5.5 References

1. Stöhr, J., *NEXAFS Spectroscopy*. Springer-Verlag: New York, 1992; Vol. 25.

2. Lawrence, J. R.; Swerhone, G. D. W.; Dynes, J. J.; Korber, D. R.; Hitchcock, A. P., Soft X-ray spectromicroscopy for speciation, quantitation and nano-eco-toxicology of nanomaterials. *J. Microsc.* **2016,** *261* (2), 130-147.

3. Urquhart, S. G., Martinson, Mercedes, Eger, Shaylin, Murcia, Victor, Ade, Harald, Collins, Brian A., Connecting Molecular Conformation to Aggregation in P3HT Using Near Edge X-ray Absorption Fine Structure Spectroscopy. *The Journal of Physical Chemistry C* **2017,** *121* (39), 21720-21728.

4. Sedlmair, J., Gleber, Sophie-Charlotte, Peth, Christian, Mann, Klaus, Niemeyer, Jürgen, Thieme, Jürgen, Characterization of refractory organic substances by NEXAFS using a compact X-ray source. *Journal of Soils and Sediments* **2012,** *12* (1), 24-34.

5. Endo, O.; Ozaki, H.; Sumii, R.; Amemiya, K.; Nakamura, M.; Kosugi, N., Orientation of n-alkane in thin films on graphite (0001) studied using C K-NEXAFS. *Journal of Electron Spectroscopy and Related Phenomena* **2011,** *184* (3), 257-260.

6. Fu, J., Urquhart, Stephen G., Linear Dichroism in the X-ray Absorption Spectra of Linear n-Alkanes. *The Journal of Physical Chemistry A* **2005,** *109* (51), 11724-11732.

7. Dannenberger, O.; Weiss, K.; Himmel, H. J.; Jager, B.; Buck, M.; Woll, C., An orientation analysis of differently endgroup-functionalised alkanethiols adsorbed on Au substrates. *Thin Solid Films* **1997,** *307* (1-2), 183-191.

8. Völkner, J.; Klues, M.; Witte, G., Assignment of NEXAFS Resonances in Alkanethiols and Their Implication on the Determination of Molecular Orientation of Aliphatic SAMs. *The Journal of Physical Chemistry C* **2018,** *122* (29), 16810-16820.

9. Schuster, S.; Fuser, M.; Asyuda, A.; Cyganik, P.; Terfort, A.; Zharnikov, M., Photoisomerization of azobenzene-substituted alkanethiolates on Au(111) substrates in the context of work function variation: the effect of structure and packing density. *Physical Chemistry Chemical Physics* **2019,** *21* (18), 9098-9105.

10. Hähner, G.; Kinzler, M.; Wöll, C.; Grunze, M.; K. Scheller, M.; Cederbaum, L. S., Near edge x-ray-absorption fine-structure determination of alkyl-chain orientation: Breakdown of the ``building-block'' scheme. *Physical Review Letters* **1991,** *67* (7), 851-854.

11. Rabe, J. P.; Swalen, J. D.; Outka, D. A.; Stöhr, J., Near-edge X-ray absorption fine structure studies of oriented molecular chains in polyethylene and Langmuir-Blodgett monolayers on Si(111). *Thin Solid Films* **1988,** *159* (1), 275-283.

12. Heimel, G.; Romaner, L.; Zojer, E.; Bredas, J. L., The interface energetics of self-assembled monolayers on metals. *Acc. Chem. Res.* **2008,** *41* (6), 721-729.

13. Hahner, G.; Kinzler, M.; Thummler, C.; Woll, C.; Grunze, M., Structure of Self-Organizing Organic Films - A Near Edge X-Ray Absorption Fine-Structure Investigation of Thiol Layers Adsorbed nn Gold. *J. Vac. Sci. Technol. A-Vac. Surf. Films* **1992,** *10* (4), 2758-2763.

14. Gartner, M.; Sauter, E.; Nascimbeni, G.; Petritz, A.; Wiesner, A.; Kind, M.; Abu-Husein, T.; Bolte, M.; Stadlober, B.; Zojer, E.; Terfort, A.; Zharnikov, M., Understanding the Properties of Tailor-Made Self-Assembled Monolayers with Embedded Dipole Moments for Interface Engineering. *J. Phys. Chem. C* **2018,** *122* (50), 28757-28774.

15. Wang, Y.; Canchaya, J. G. S.; Dong, W.; Alcami, M.; Busnengo, H. F.; Martin, F., Chain-Length and Temperature Dependence of Self-Assembled Monolayers of Alkylthiolates on Au(111) and Ag(111) Surfaces. *J. Phys. Chem. A* **2014,** *118* (23), 4138-4146.

16. Fenter, P.; Eberhardt, A.; Liang, K. S.; Eisenberger, P., Epitaxy and chainlength dependent strain in self-assembled monolayers. *Journal of Chemical Physics* **1997,** *106* (4), 1600-1608.

17. Endo, O.; Nakamura, M.; Amemiya, K., Phase Transition of n-C36H74 Monolayer on Pt(111) Covered with Monolayer Graphene Studied by C K-NEXAFS. *J. Phys. Chem. C* **2013,** *117* (42), 21856-21863.

18. Endo, O.; Horikoshi, T.; Katsumata, N.; Otani, K.; Fujishima, T.; Goto, H.; Minami, K.; Akaike, K.; Ozaki, H.; Sumii, R.; Amemiya, K.; Nakamura, M.; Kosugi, N., Incommensurate Crystalline phase of n-Alkane Monolayers on Graphite (0001). *J. Phys. Chem. C* **2011,** *115* (13), 5720-5725.

19. Perera, S. D., Shokatian, Sadegh, Wang, Jian, Urquhart, Stephen G., Temperature Dependence in the NEXAFS Spectra of n-Alkanes. *The Journal of Physical Chemistry A* **2018,** *122* (49), 9512-9517.

20. Schöll, A.; Fink, R.; Umbach, E.; Mitchell, G.; Urquhart, S.; Ade, H., *Towards a detailed understanding of the NEXAFS spectra of bulk polyethylene copolymers and related alkanes*. 2003; Vol. 370, p 834-841.

21. Perera, S. D., Wang, Jian, Urquhart, Stephen G., Linear dichroism in the NEXAFS spectra of n-alkane crystalline polymorphs. *Journal of Electron Spectroscopy and Related Phenomena* **2019,** *232*, 5-10.

22. Zou, Y.; Araki, T.; Appel, G.; Kilcoyne, A. L. D.; Ade, H., Solid state effects in the NEXAFS spectra of alkane-based van der Waals crystals: Breakdown of molecular model. *Chemical Physics Letters* **2006,** *430* (4), 287-292.

23. Swaraj, S.; Ade, H., Differences in NEXAFS of odd/even long chain n-alkane crystals. *Journal of Electron Spectroscopy and Related Phenomena* **2013,** *191*, 60-64.

24. Remmers, G.; Domke, M.; Kaindl, G., Vibrationally resolved carbon core excitations in alkane molecules. *Physical Review A* **1993,** *47* (4), 3085-3091.

25. Ueda, K., Okunishi, M., Chiba, H., Shimizu, Y., Ohmori, K., Sato, Y., Shigemasa, E., Kosugi, N., Rydberg—valence mixing in the C 1s excited states of CH4 probed by electron spectroscopy. *Chemical Physics Letters* **1995,** *236* (3), 311-317.

26. Ma, Y., Chen, C. T., Meigs, G., Randall, K., Sette, F., High-resolution K-shell photoabsorption measurements of simple molecules. *Physical Review A* **1991,** *44* (3), 1848-1858.

27. Wang, Y.; Zou, Y.; Araki, T.; Lüning, J.; Kilcoyne, A. L. D.; Sokolov, J.; Ade, H.; Rafailovich, M., Probing the Chain and Crystal Lattice Orientation in Polyethylene Thin Films by Near Edge X-ray Absorption Fine Structure (NEXAFS) Spectroscopy. *Macromolecules* **2010,** *43* (19), 8153-8161.

28. Masnadi, M.; Urquhart, S. G., Effect of Substrate Temperature on the Epitaxial Growth of Oriented n-Alkane Thin Films on Graphite. *Langmuir* **2012,** *28* (34), 12493-12501.

29. Weiss, K.; Weckesser, J.; Wöll, C., An X-ray absorption study of saturated hydrocarbons physisorbed on metal surfaces. *J. Mol. Struct.* **1998,** *458* (1), 143-150.

30. Öström, H.; Triguero, L.; Weiss, K.; Ogasawara, H.; Garnier, M. G.; Nordlund, D.; Nyberg, M.; Pettersson, L. G. M.; Nilsson, A., Orbital rehybridization in n-octane adsorbed on Cu(110). *The Journal of Chemical Physics* **2003,** *118* (8), 3782-3789.

31. Urquhart, S. G.; Gillies, R., Matrix effects in the carbon 1s near edge x-ray absorption fine structure spectra of condensed alkanes. *The Journal of Chemical Physics* **2006,** *124* (23), 234704.

32. Bagus, P. S., Weiss, K., Schertel, A., Wöll, Ch, Braun, W., Hellwig, C., Jung, C., Identification of transitions into Rydberg states in the X-ray absorption spectra of condensed long-chain alkanes. *Chemical Physics Letters* **1996,** *248* (3), 129-135.

33. Weiss, K.; Bagus, P. S.; Wöll, C., Rydberg transitions in X-ray absorption spectroscopy of alkanes: The importance of matrix effects. *The Journal of Chemical Physics* **1999,** *111* (15), 6834-6845.

34. Urquhart S. G.; Gillies R., Rydberg−Valence Mixing in the Carbon 1s Near-Edge X-ray Absorption Fine Structure Spectra of Gaseous Alkanes. *The Journal of Physical Chemistry A* **2005,** *109* (10), 2151-2159.

35. Basson, I.; Reynhardt, E. C., Identification of a Defect Chain Motion in Normal-Alkanes by Means of Nuclear-Magnetic-Resonance Spin-Lattice Relaxation-Time Measurements. *Journal of Chemical Physics* **1990,** *93* (5), 3604-3609.

36. Thomas, L. L.; Christakis, T. J.; Jorgensen, W. L., Conformation of Alkanes in the Gas Phase and Pure Liquids. *The Journal of Physical Chemistry B* **2006,** *110* (42), 21198-21204.

37. Frisch, M. J.; Trucks, G. W.; Schlegel, H. B.; Scuseria, G. E.; Robb, M. A.; Cheeseman, J. R.; Scalmani, G.; Barone, V.; Petersson, G. A.; Nakatsuji, H.; Li, X.; Caricato, M.; Marenich, A. V.; Bloino, J.; Janesko, B. G.; Gomperts, R.; Mennucci, B.; Hratchian, H. P.; Ortiz, J. V.; Izmaylov, A. F.; Sonnenberg, J. L.; Williams; Ding, F.; Lipparini, F.; Egidi, F.; Goings, J.; Peng, B.; Petrone, A.; Henderson, T.; Ranasinghe, D.; Zakrzewski, V. G.; Gao, J.; Rega, N.; Zheng, G.; Liang, W.; Hada, M.; Ehara, M.; Toyota, K.; Fukuda, R.; Hasegawa, J.; Ishida, M.; Nakajima, T.; Honda, Y.; Kitao, O.; Nakai, H.; Vreven, T.; Throssell, K.; Montgomery Jr., J. A.; Peralta, J. E.; Ogliaro, F.; Bearpark, M. J.; Heyd, J. J.; Brothers, E. N.; Kudin, K. N.; Staroverov, V. N.; Keith, T. A.; Kobayashi, R.; Normand, J.; Raghavachari, K.; Rendell, A. P.; Burant, J. C.; Iyengar, S. S.; Tomasi, J.; Cossi, M.; Millam, J. M.; Klene, M.; Adamo, C.; Cammi, R.; Ochterski, J. W.; Martin, R. L.; Morokuma, K.; Farkas, O.; Foresman, J. B.; Fox, D. J. *Gaussian 16*, Wallingford, CT, 2016.

38. Zhao, Y.; Truhlar, D. G., The M06 suite of density functionals for main group thermochemistry, thermochemical kinetics, noncovalent interactions, excited states, and transition elements: two new functionals and systematic testing of four M06-class functionals and 12 other functionals. *Theoretical Chemistry Accounts* **2008,** *120* (1), 215-241.

39. Koster A.M. , G. G., Calaminici P., Casida M. E., Dominguez V. D., Flores-Moreno R., Gamboa G. U., Goursot A., Heine T., Ipatov A., Janetzko F., del Campo J. M., Reveles J. U., Vela A., Zuniga-Gutierrez B., Salahub D. R. *deMon2k*, Cinvestav, Mexico City 2011.

40. Perdew, J. P.; Burke, K.; Ernzerhof, M., Generalized Gradient Approximation Made Simple. *Physical Review Letters* **1996,** *77* (18), 3865-3868.

41. Triguero, L.; Pettersson, L. G. M.; Ågren, H., Calculations of near-edge x-ray-absorption spectra of gas-phase and chemisorbed molecules by means of density-functional and transition-potential theory. *Physical Review B* **1998,** *58* (12), 8097-8110.

42. Huzinaga, S., *J. Chem. Phys.* **1965,** *42*, 1293.

43. Ågren, H.; Carravetta, V.; Vahtras, O.; Pettersson, L. G. M., Direct, atomic orbital, static exchange calculations of photoabsorption spectra of large molecules and clusters. *Chemical Physics Letters* **1994,** *222* (1), 75-81.

44. Ågren, H.; Carravetta, V.; Vahtras, O.; Pettersson, M. L. G., Direct SCF direct static-exchange calculations of electronic spectra. *Theoretical Chemistry Accounts* **1997,** *97* (1), 14-40.

45. Perera, S. Effect of Intermolecular Interactions on the Carbon 1s Near Edge X-ray Absorption Fine Structure (NEXAFS) Spectroscopy of n-Alkanes. University of Saskatchewan, Saskatoon, SK, 2012.

Chapter 6 – Temperature Dependence in NEXAFS Spectra of *N*-alkanes

6.1 Description

Chapter 6 investigates the effect of changes in the temperature on the carbon 1s NEXAFS spectra of *n*-alkanes. The carbon 1s NEXAFS spectra of orthorhombic single crystals of *n*-octacosane (*n*-$C_{28}H_{58}$), recorded at room temperature (298 K) and cryogenic temperature (93 K), show distinct differences. The characteristic carbon C-H band in the NEXAFS spectrum of *n*-$C_{28}H_{58}$ is broader and has a lower energy onset in its room temperature spectrum compared to the cryogenic temperature spectrum. DFT simulations show that nuclear motion and molecular disorder contribute to the observed spectral broadness and are the origin of the low-energy onset of the C-H band in the room temperature spectrum. This manuscript is published in the Journal of Physical Chemistry A (DOI: 10.1021/acs.jcpa.8b10713). The manuscript is reformatted from the original version for inclusion in this thesis. The progress on this project since the publication of this paper is reported at the end of this chapter (§6.5).

6.2 Description of Candidate Contribution

The author of this thesis was the secondary investigator of this research work, and he developed all the computational models, including the gauche defects and thermally populated vibrational states models, interpretation of the computational results, and writing of the computational sections of the document. Sahan Perera was the primary investigator in this work, and he developed the research concept of the study, preparation of samples, experimental data acquisition, interpretation of the experimental results, and writing of the experimental sections of the document. J. Wang helped with the experimental set-up for the NEXAFS measurements of *n*-alkanes. S. G. Urquhart provided guidance throughout the experiments as well as the process of data analysis and was actively involved in the editing process of the document. This manuscript is also published in chapter 6 of Sahan Perera's thesis. The progress after the publication is provided at the end of this chapter. This research is carried out by the author of this thesis.

6.3 Relation of Contribution to the Research Objectives

This work investigates the origin of the spectral broadening in the carbon 1s NEXAFS spectra of short-chain *n*-alkanes, with a change in the temperature. This work supports the objective of understanding the contribution of the structural disorder (e.g., nuclear motion effect) on the NEXAFS spectra of *n*-alkanes. Using experimental measurements as well as computational modeling, it has been proven that an increase in the temperature will increase numbers of defects, the ratio of molecules in the thermally populated vibrational states, and motions of the molecules. These changes will contribute to the broadening of the spectra. The works in this chapter contribute to the second objective of this thesis, which is to understand the effect of structural disorder on the NEXAFS spectra of *n*-alkanes.

6.4 Temperature Dependence in the NEXAFS Spectra of *N*-Alkanes

*Sahan D. Perera,† Sadegh Shokatian,† Jian Wang,‡ Stephen G. Urquhart†**

† Department of Chemistry, University of Saskatchewan, Saskatoon, SK, Treaty Six Territory, Canada S7N 5C9 ‡ Canadian Light Source, University of Saskatchewan, Saskatoon, SK, Canada S7N 0X4

Abstract

The Near Edge X-ray Absorption Fine Structure (NEXAFS) spectra of orthorhombic single crystals of *n*-$C_{28}H_{58}$, recorded at room temperature (298 K) and cryogenic temperatures (93 K), show distinct differences. The characteristic carbon 1s → $\sigma^*_{C\text{-}H}$ band in the NEXAFS spectrum of o-rh *n*-$C_{28}H_{58}$ is broader and appears at a lower energy in the room temperature spectrum than in its NEXAFS spectrum recorded at cryogenic temperatures. Density functional theory simulations show that nuclear motion and molecular disorder contribute to the observed spectral broadness and are the origin of the low-energy onset of the C-H band in the room temperature spectrum.

Corresponding author: **e-mail:** stephen.urquhart@usask.ca

KEYWORDS

Nuclear motion, inhomogeneous broadening, temperature dependence, NEXAFS, alkanes

6.4.1 Introduction

The variation of molecular spectra (NMR, IR, etc.) with temperature can be used to probe molecular dynamics. This sensitivity to molecular dynamics and motion should also exist for molecular Near Edge X-ray Absorption Fine Structure (NEXAFS) spectroscopy. As an example, NEXAFS spectra of gas, liquid, supercooled liquid, and solid water show sensitivity to local hydrogen bonding, and changes in this bonding with temperature and phase.[1] However, experimental studies of the temperature variation of the NEXAFS spectra of molecules are limited.

This study examines the temperature dependence in the NEXAFS spectra of *n*-alkanes. *n*-alkanes, $CH_3(CH)_nCH_3$, are a family of simple organic molecules consisting of methyl (CH_3) and methylene (CH_2) moieties. Despite their relative simplicity, the NEXAFS spectra of *n*-alkanes show significant complexity, with characteristic differences with phase (gas versus condensed), chain length, degree of order, and with temperature.[2-10] Chemical analysis of these materials would be strengthened if fundamental understandings of their NEXAFS spectroscopy (including the role of order and dynamics) were improved, and if stronger structure/spectra relationships were established.

The carbon 1s NEXAFS spectra of simple gas-phase alkanes (methane, ethane, propane, etc.) are dominated by a series of narrow and well-resolved carbon 1s $\rightarrow$ Rydberg transitions, with rich vibronic structure.[2, 10-11] These gas-phase spectra are well modeled by calculations that consider the lowest energy geometry but neglect vibronic transitions,[2, 10] as core-excited potential energy surfaces are difficult to model. When neopentane was examined in the gas and condensed phases, characteristic Rydberg transitions observed in the gas phase spectra were shifted to higher energy and were broadened in the condensed phase spectra.[3] This effect was attributed to Rydberg quenching in the solid-state, and the emergence of valence (σ^*_{C-H}) character.[3] In the carbon 1s NEXAFS spectra of *n*-alkane solids such as paraffin and polyethylene, two low energy transitions of nearly equal strength (the “C-H band”, at 287.6 and 288.2 eV in paraffin) dominate the spectra.[7, 12] Schöll *et al.*[7] examined how this C-H band varied with elevated temperature and the degree of crystallinity in polyethylene copolymers. They

found that NEXAFS features were broader in the disordered polymer as well as in molten polyethylene. The origin of these changes was not well understood, but the following observation can be made: increased disorder leads to a broader “C-H” band.

Nuclear motion is predicted to play a role in the variation of NEXAFS spectra with temperature.[13-15] Pettersson and Nilsson have extensively studied the NEXAFS spectra of water (liquid, supercooled liquid, and solid phases) and have shown that its oxygen 1s NEXAFS spectrum is sensitive to the local hydrogen-bonded network, and its change with temperature and phase.[1, 16] The Pendergast group[13-14] has examined how ‘nuclear motion’ effects lead to spectral broadening in NEXAFS spectra of amino acids and related molecules. Their work compared DFT spectral simulations based on the lowest energy molecular geometry, to simulations that model the nuclear degrees of freedom by averaging ‘snapshots’ from molecular dynamics simulations. Their work predicted that zero-point motion and thermally excited vibrational modes contribute to the shape of NEXAFS spectra. In molecular solids such as glycine, these MD-DFT simulations predict that solid-phase vibrational modes are the origin of temperature-dependent broadening.[14-15]

Gauche defects (e.g., rotation about individual C-C bonds, distorting an *n*-alkane from the lowest energy, all-trans geometry) are another possible contributor to disorder in the NEXAFS spectra of *n*-alkanes, including single crystal *n*-alkanes. In the examination of the spin-lattice relaxation time ($T_{1\rho}$) for *n*-alkanes of various lengths, Basson *et al.*[17] observed a dynamic defect below the melting point for solid *n*-alkanes of length 28 (*n*-$C_{28}H_{58}$) or shorter. This dynamic process was identified as a thermally populated trans-*gauche* defect motion near the end of the *n*-alkane chains[17] (later classified as an end-*gauche* defects[18]). These defects were seen well below the characteristic pre-melting point solid/solid phase transition to the pseudohexagonal rotator phase,[19] in which an increased population of gauche defects near chain ends was also observed.[20] We, therefore, expect that some fraction of gauche defects will be present in solid *n*-alkanes, particularly for shorter *n*-alkane chains.

There is little experimental temperature dependent NEXAFS spectra of organic molecules and none that we are aware of at cryogenic temperatures. In this work, we examine the carbon 1s NEXAFS spectra of orthorhombic (o-rh) single crystals of *n*-$C_{28}H_{58}$ recorded at room temperature (298 K) and cryogenic temperature (93 K). Regular diamond or parallelogram-shaped *n*-$C_{28}H_{58}$ crystallites with straight edges and well-defined angles were identified by optical microscopy (OM). *n*-alkane crystals with acute interior angles of 68° ±1° are orthorhombic, while those with acute interior angles of 74° ±1° are monoclinic.[21-23] Only orthorhombic single crystals of *n*-$C_{28}H_{58}$ were examined in this work. These spectroscopic studies are accompanied by DFT simulations that model the effect of defects and vibrational modes on the NEXAFS spectra.

6.4.2 Experimental Section

Samples and Sample Preparation

Samples: *n*-octacosane (*n*-$C_{28}H_{58}$, 99%) was purchased from Alfa Aesar and used without purification. Isopropyl alcohol (99.9%) was ACS grade and purchased from Fisher Scientific.

Sample Preparation: Samples were prepared on 100 nm, 0.5 × 0.5 mm low-stress silicon nitride (Si_3N_4) windows (Norcada Inc.). Thin single crystals of *n*-octacosane (*n*-$C_{28}H_{58}$) were prepared by solution casting[5, 9] from an isopropyl alcohol solution with a mass/volume ratio of 1.0 mg/2.00 ml. The substrate temperature during solvent evaporation was optimized in order to isolate the orthorhombic structure over its monoclinic polymorph. Thin single crystals were obtained when the samples were cast at lower solvent evaporation temperature (~ 8 °C).

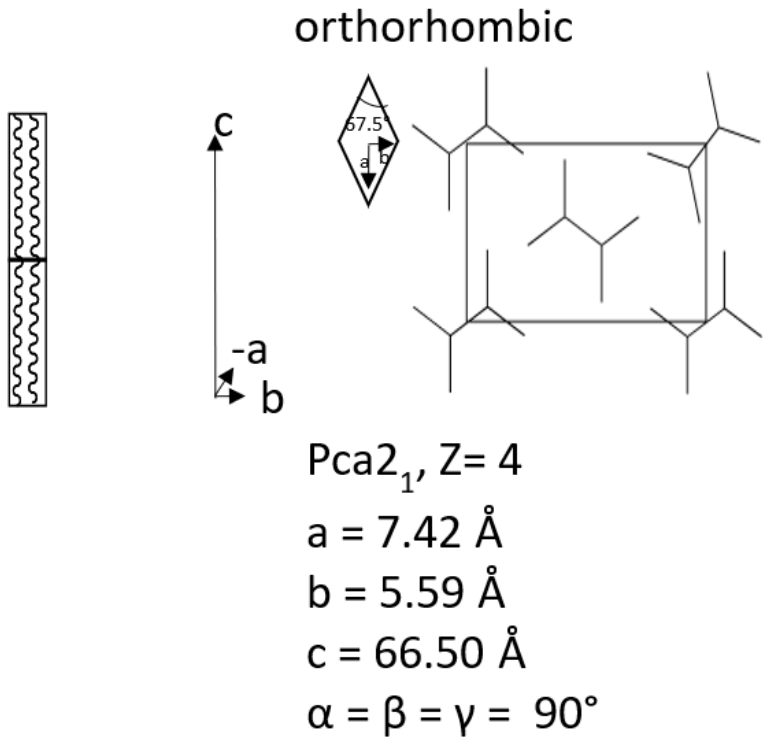

Figure 6.1 - Schematic diagram for chain length orientation, published unit cell parameters of orthorhombic structure of n-$C_{28}H_{58}$.[4-6]

The morphology of the *n*-$C_{28}H_{58}$ single crystals was characterized by optical microscopy (Nikon Eclipse ME600, with a Q-Imaging CCD camera). *n*-$C_{28}H_{58}$ crystals were found to be rectangular or diamond in shape in optical and X-ray microscopy examination. This indicates that the (*a, b*) unit cell axes of the crystals are oriented in the plane of the substrate (see Figure 6.1). Regular diamond or parallelogram-shaped *n*-alkane crystallites with straight edges and well-defined angles were identified by optical microscopy (OM). *n*-alkane crystals with acute interior angles of 68° ±1° are orthorhombic, with those with acute interior angles of 74° ±1° is monoclinic.[21-23] Only orthorhombic single crystals of *n*-$C_{28}H_{58}$ were examined in this work.

NEXAFS Spectroscopy

X-ray microscope images and variable temperature NEXAFS spectra were obtained at the Spectromicroscopy (SM) beamline[24] at the Canadian Light Source (CLS), using the cryogenic Scanning Transmission X-ray Microscope (c-STXM)[25] and the ambient STXM microscope (a-STXM).[24] STXM microscopy allows one to acquire the

transmission (I) spectra from individual single crystals, and to measure the incident flux (I_0) from areas adjacent to these crystals. NEXAFS spectra were acquired at cryogenic (93 K) and ambient temperatures (~ 298 K) with the c-STXM microscope.[26] All NEXAFS spectra were acquired using left circular X-ray polarization to eliminate potential linear dichroism from oriented crystals. Transmission spectra were converted to optical density with Beer's law ($OD = -\ln(I/I_0)$).

Data analysis was performed using aXis 2000[27], and spectra are presented using the Origin software package.[28] The data presentation focuses on the carbon 1s → σ^*_{C-H} band (287 − 288 eV), in order to highlight features that vary with nuclear motion contributions.

Experimental Artefacts and Energy Calibration

Care was taken to exclude experimental artifacts such as radiation damage and thickness effects. In order to avoid thickness effects associated with the small fraction of higher-order photons, only spectra from thinner crystals (OD < 1.5) were considered. The relatively high radiation sensitivity of *n*-alkane molecules.[29] limits the permissible dose that can be used for NEXAFS measurements. Experimental conditions (energy point spacing, dwell time, etc.) were optimized to minimize radiation exposure, and the STXM was defocused to 150 nm diameter during image sequence data acquisition. Fresh sample areas were used for each spectrum. Radiation damage was monitored by examining the NEXAFS spectra in the carbon 1s continuum (300 eV) to test for mass loss and at the energy of the carbon 1s → $\pi^*_{C=C}$ transition (285 eV) to test for the formation of C=C double bonds.[29-30] Radiation damage was found to be minimal in the experimental conditions used.

The energy scale of the ambient temperature NEXAFS spectrum was confirmed through *in situ* calibration to the Rydberg transitions (carbon 1s →3s (*v*=0) transition at 292.74 eV and carbon 1s → 3p (v=0) transition at 294.96 eV; after Ma *et al.*)[11] in the NEXAFS spectrum of CO_2, performed in the a-STXM. These data were used to calibrate the ambient temperature NEXAFS spectrum recorded in the c-STXM. The same shift was applied to calibrate the energy scale of the cryogenic measurements.

6.4.3 Computational Section

Density Functional Theory Calculations

n-decane (*n*-$C_{10}H_{22}$) was used as a computational model for this study. The lowest energy geometry (all-trans) of *n*-decane was determined by ωB97X-D DFT calculations at the 6-31+G(d, p) level, performed with the program Gaussian 16.[31] There were no imaginary frequencies in the vibrational analysis calculation. Several variations of the all-trans *n*-decane structure were examined in order to study the effect of disorder and nuclear motion effects. The effect of these gauche defects on the NEXAFS spectra are studied by rotating bond dihedrals in *n*-decane individually. The population of gauche defects at room temperature was obtained from the molecular dynamics simulation study of Thomas *et al*.[32] NEXAFS spectra were averaged according to the weights of these calculated gauche defect configurations. This method provides an estimate of the effect of gauche defects in *n*-decane, as an approximation for the effect of gauche defects in longer *n*-alkane crystals. These defects might be static, but Basson *et al*.[17] have noted that end-gauche defects can be thermally populated at room temperature in octacosane (*n*-$C_{28}H_{58}$).[17-18]

Many forms of motion that will contribute to 'nuclear motion effects' in an *n*-alkane solid, including zero-point motion and thermally populated vibrational modes. Zero-point motions should be expected to contribute at all temperatures, while the Boltzmann distribution of thermally populated vibrational modes will increase with sample temperature.

To examine the spectroscopic effect of the thermally populated modes, we have constructed a simple model based on the *n*-$C_{10}H_{22}$ molecule, which has 90 (3N-6) vibrational modes. We have constructed geometries for the turning points of all of these vibrational modes, on the principle that the molecule's geometry will spend most of its time at these turning points. DFT spectroscopic simulations were performed for these turning-point geometries and were averaged according to the expected Boltzmann population of these vibrational modes at 298 K. All vibrations are considered, as weighted by their Boltzmann population. This simple approach neglects the effects of zero-point

motion, as well as the population of vibrational modes above υ = 1, which will be significant for low-energy vibration modes.

Carbon 1s NEXAFS simulations of *n*-decane structures were obtained from DFT calculations[33-34] using the deMon2k package.[35-36] All NEXAFS simulations were performed using Transition Potential (TP-DFT) method with the half-core hole (HCH) approximation.[37] Spectral lines were simulated using 0.2 eV wide Gaussian line shapes. The molecular spectrum is generated by averaging the DFT simulation from each carbon atom. The IGLO-III basis set[38] was used for the core excited carbon atom, effective core potential (ECPs) for all other carbon atoms,[39] and the triple-zeta (TZVP) basis set for hydrogen atoms.[39] XAS-I augmentation orbitals were used on the core excited carbon atom.[37] The GEN-A4* auxiliary basis and the PBE GGA exchange-correlation functional were used.[40-41]

6.4.4 **Results**

In this section, the experimental spectra of the o-rh *n*-$C_{28}H_{58}$ at room temperature (298 K) compared with the experimental spectra of the o-rh *n*-$C_{28}H_{58}$ at cryogenic temperature (98 K) to examine the effect nuclear motion contribution to the NEXAFS spectroscopy. The experimental results were then interpreted by DFT simulations (*n*-decane) that model the effect of defects and vibrational modes on the NEXAFS spectra. The effects of nuclear motion contribution to the carbon 1s NEXAFS spectroscopy discussed in more detail below.

Figure 6.2 presents the variation in the C-H band of the carbon 1s NEXAFS spectra of o-rh *n*-$C_{28}H_{58}$ with temperature, comparing the room temperature (298 K) spectrum with that recorded at cryogenic temperatures (93 K). The shape of the C-H band is significantly broader at room temperature, and the C-H band has a lower energy onset (~200 meV lower) relative to that recorded at cryogenic temperatures. A broader C-H band is expected at the higher temperature, as nuclear motion will be more significant. However, the lower energy offset for the room temperature spectra was unexpected and requires further discussion. The observed spectroscopic trends (width and onset) were

also observed for *n*-$C_{40}H_{82}$ powders, recorded in TEY mode on the CLS SGM beamline (11 ID-1).[42]

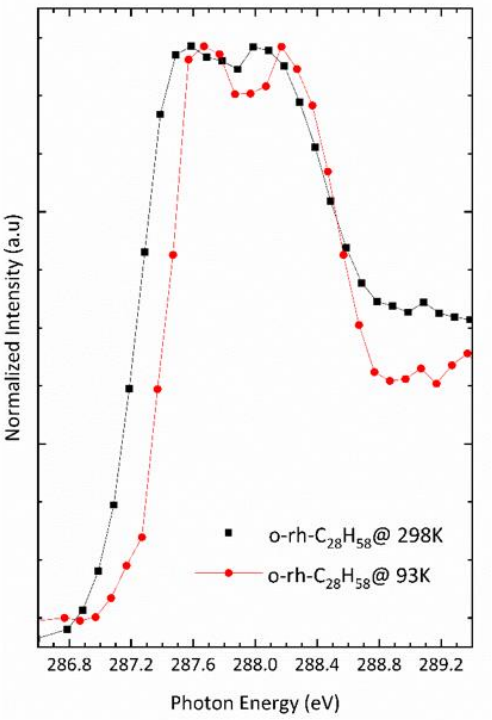

Figure 6.2 - Carbon 1s NEXAFS spectra of orthorhombic n-$C_{28}H_{58}$ at cryogenic (93 K) and ambient (298 K) temperatures, recorded with circular left polarization. Optical density spectra are rescaled for comparison.

Figure 6.3 compares the TP-DFT simulations of the carbon 1s NEXAFS spectra of *n*-$C_{10}H_{22}$ with an all-trans, minimum energy geometry, to simulations of gauche defects and thermally populated vibrational models. The shape of the TP-DFT simulation of the carbon 1s spectrum of *n*-$C_{10}H_{22}$ (in the all-trans geometry) differs from the experimental carbon 1s spectrum of *n*-$C_{28}H_{58}$ on account of chain length. The methyl-group and the first methylene in from the end of the chain contribute to the third band observed in Figure 6.3, at ~289.2 eV. For *n*-$C_{10}H_{22}$, this corresponds to 40% of the atomic sites in the *n*-alkane chain; therefore, this third band is exaggerated in this short *n*-alkane model. A full examination of the chain length dependence in the NEXAFS spectra of *n*-alkanes is in preparation.[43]

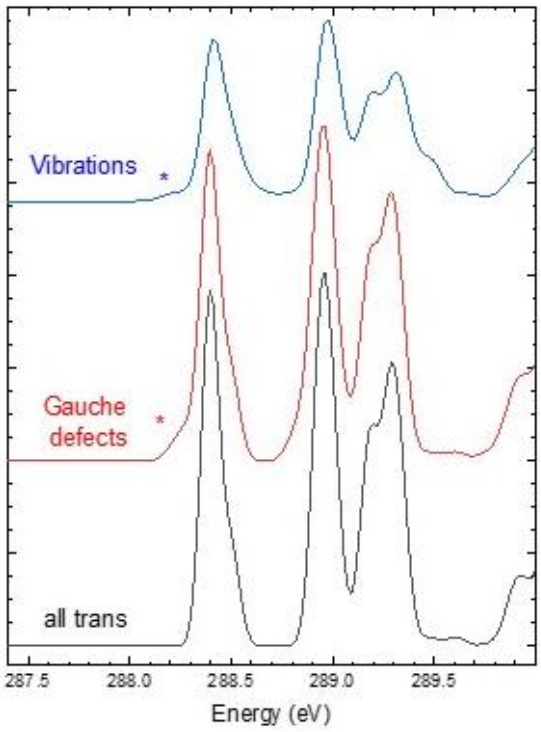

Figure 6.3 - TP-DFT simulations of the effect of thermally populated gauche defects and thermally populated vibrations (υ = 1) on the NEXAFS spectra of the isolated n-$C_{10}H_{22}$ molecule

The splitting between the first two peaks in the TP-DFT simulation (~0.6 eV) roughly matches the observed splitting in the experimental carbon 1s spectrum of *n*-$C_{28}H_{58}$ recorded at room temperature.

When gauche defects and populated vibrational modes are considered, new contributions are observed at lower energy; these are indicated by an asterisk in Figure 6.3. The TP-DFT simulations show that spectroscopic contributions from structural distortions (relative to the all-trans geometry) will appear at a lower energy in the NEXAFS spectrum. This trend is consistent with the lower energy onset of the C-H band observed in the room temperature NEXAFS spectrum of o-rh *n*-$C_{28}H_{58}$, where a greater difference from the static, all-trans structure is expected.

6.4.5 Discussion

Spectral broadening in the carbon 1s NEXAFS spectra of molecular solids is expected to have several origins. Beyond the intrinsic broadening from the core-hole

lifetime (~80 meV), vibronic contributions and nuclear motion are expected to contribute to the shape of the NEXAFS transitions.[13-14, 44] Vibronic contributions[2, 11] should be similar for spectra recorded at ambient and at cryogenic temperatures; as the additional energy required for vibronic excitation (e.g., Carbon 1s ($\upsilon = 0$) $\rightarrow$ $\sigma^*_{C\text{-}H}$ ($\upsilon = 1$) transition) comes from the absorbed photon. Vibronic contributions will appear at higher rather than lower energy. Vibronic contributions are, therefore, not responsible for the low-energy broadening observed in the room temperature NEXAFS spectrum of *n*-$C_{28}H_{58}$. However, nuclear motion effects, via population of vibrational modes and thermally populated molecular defects, are expected to differ with temperature.

The effect of the thermal population of vibrational modes and defects on the NEXAFS spectrum of *n*-alkanes was examined using TP-DFT simulations. This distortion from the lowest energy, all-trans geometry, results in a lower energy transition appearing at the low energy side of the C-H band. This is a reasonable observation; as geometries are distorted from the lowest energy geometry, the HOMO-LUMO gap will decrease, and with it, the energy of the core $\rightarrow$ LUMO transition will also decrease. A similar trend is observed for thermally populated gauche defects as well as vibrations.

We note that the TP-DFT simulations of thermally populated vibrations and defects do not completely reproduce the low energy onset observed in the room temperature NEXAFS spectrum. This is not completely unexpected, as our computational model is limited. We examined a shorter chain (10 carbon atoms long instead of 20) in order to be computationally more accessible (90 versus 252 normal modes). We have also only examined the turning points for the lowest energy thermally populated vibration ($\upsilon = 1$), and not higher quantum number vibrational states ($\upsilon > 1$), expected to be populated for low energy normal modes.

Our vibrational model is that of an isolated *n*-alkane molecule and not a solid structure. This model does not capture changes to vibrations due to intermolecular interactions in the condensed phase, or the low-energy shifts expected from dynamic stabilization.[45] A full approach to examine the temperature-dependent spectroscopy will require molecular dynamics simulations, which, with the appropriate size, will be able to

capture the effect of the solid-phase on nuclear motion contributions to the NEXAFS spectra, as well as thermally populated gauche defects. This requires considerable development and will be the subject of future work.

In this work, the carbon 1s NEXAFS spectrum of a condensed *n*-alkane (o-rh *n*-$C_{28}H_{58}$) recorded at cryogenic temperatures (93 K), is compared to its NEXAFS spectrum recorded at room temperature. Characteristic differences are observed with temperature. Specifically, the distinctive “C-H band” in the NEXAFS spectrum is narrower in the cryogenic spectrum, and the onset of this band appears at higher energy. DFT simulations show that distortions from the lowest energy all-trans geometry (thermally populated vibrational modes and gauche defects) result in new features appearing at a lower energy in the NEXAFS spectrum. Cryogenic temperatures restrict thermal motion in the sample, leading to a lower population of vibrational modes and thermally accessible defects. This results in a narrower C-H band in the spectrum recorded at cryogenic temperatures, as defects will result in NEXAFS transitions appearing at lower energy. At ambient temperatures, gauche defects will be more common, and nuclear motion effects will be enhanced.

6.4.6 Conclusion

This work reports remarkable differences in the NEXAFS spectra of an organic molecule with temperature and attributes these spectroscopic differences to molecular vibrations and defects populated at ambient temperatures, relative to that at cryogenic temperatures. Future work will include the acquisition of NEXAFS spectra at a broader range of temperatures and a more rigorous exploration of the temperature dependence of the observed nuclear motion effects.

6.5 Progress Since the Publication of the Paper

Molecular dynamics simulations provide information on the dynamic properties of the system and could be used to gain a better understanding of the electronic properties of the system if coupled with the DFT calculations. This way, the changes in the electronic properties of the system could be studied as a function of dynamic properties such as nuclear motions. Also, using the MD simulations, it is possible to model the system in

various temperatures and study the NEXAFS spectra of the system as a function of the temperature. Having these concepts in mind, new models designed to study the temperature dependence NEXAFS spectra of selected *n*-alkanes.

6.5.1 Temperature Dependence MD-DFT NEXAFS Spectra of *N*-Alkanes

In this approach, isolated *n*-alkanes from *n*-C_6H_{14} to *n*-$C_{12}H_{26}$ were generated, and geometry optimized using the same DFT calculations described in Chapter 3. These isolated molecules were then placed in a simulation box, and the system was allowed to go under equilibrium geometry optimization. The canonical ensemble (NVT) was studied for each system at 60 K, 150 K, and 298 K. Figure 6.4 presents the *n*-decane in the simulation box.

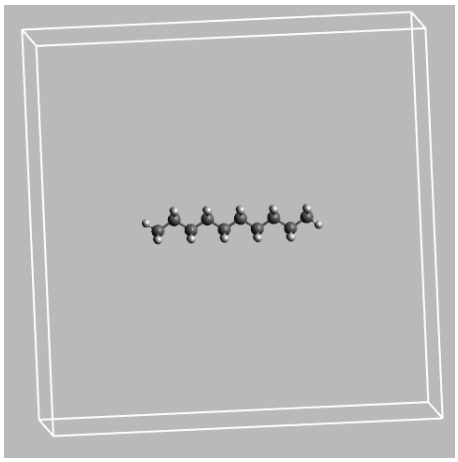

Figure 6.4 - The n-decane molecule in the simulation box

A hundred snapshots were extracted from the simulations for each of the molecules. Using deMon2k, the carbon 1s NEXAFS spectrum of each of the isolated molecules was calculated. The standard sum spectra and standard deviation were calculated for each molecule following the method explained in Chapter 3. Figure 6.5 presents the carbon 1s NEXAFS spectra of the *n*-hexane calculated using MD-DFT at 60 K, 150 K, and 298 K .

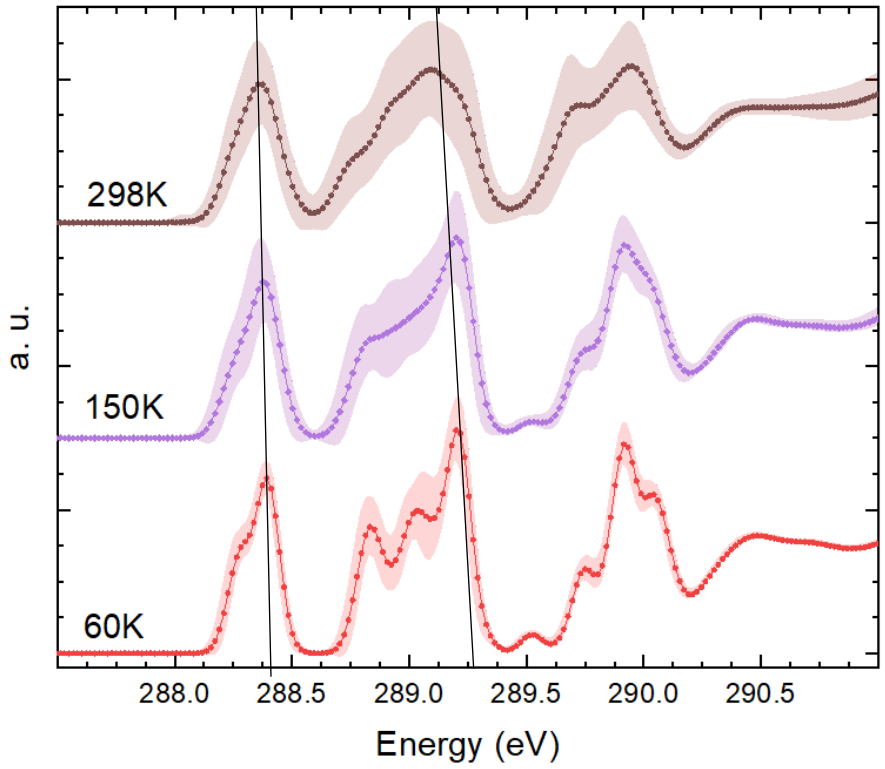

Figure 6.5 – Carbon 1s NEXAFS spectra of n-hexane in various temperatures obtained with the MD-DFT method

A few changes can be observed as the temperature increases. At 60 K, the carbon $1s \rightarrow 3s$ peak appears as a peak with a small shoulder showing the contributions of the lower energy methyl (-CH_3) groups and the higher energy methylene (-CH_2) groups toward the final peak. As the temperature increases to 150 K and 298 K, these two peaks will appear as a single peak due to the increased nuclear motion of the molecules at higher temperatures. This trend is repeated for the $1s \rightarrow 3p$ transition, where three distinct peaks are observed at 60 K; these disappear at higher temperatures. The $1s \rightarrow 3d$ peak shows the same trend. This change from distinct peaks to merged broader peaks for each transition with the increase in the temperature is one of the main reasons for the observed broadening in the spectra of *n*-alkanes. In both $1s \rightarrow 3s$ and $1s \rightarrow 3p$ peaks, a small shift (~0.12 eV) to the lower energy is observed as the temperature increases. This is attributed to the increased number of molecules in various thermally populated vibrations, as well as geometry defect molecules with the temperature increase. These shifts are illustrated with lines in Figure 6.5.

Figure 6.6 presents the MD-DFT simulated temperature dependence carbon 1s NEXAFS spectra of the *n*-alkanes from heptane to dodecane.

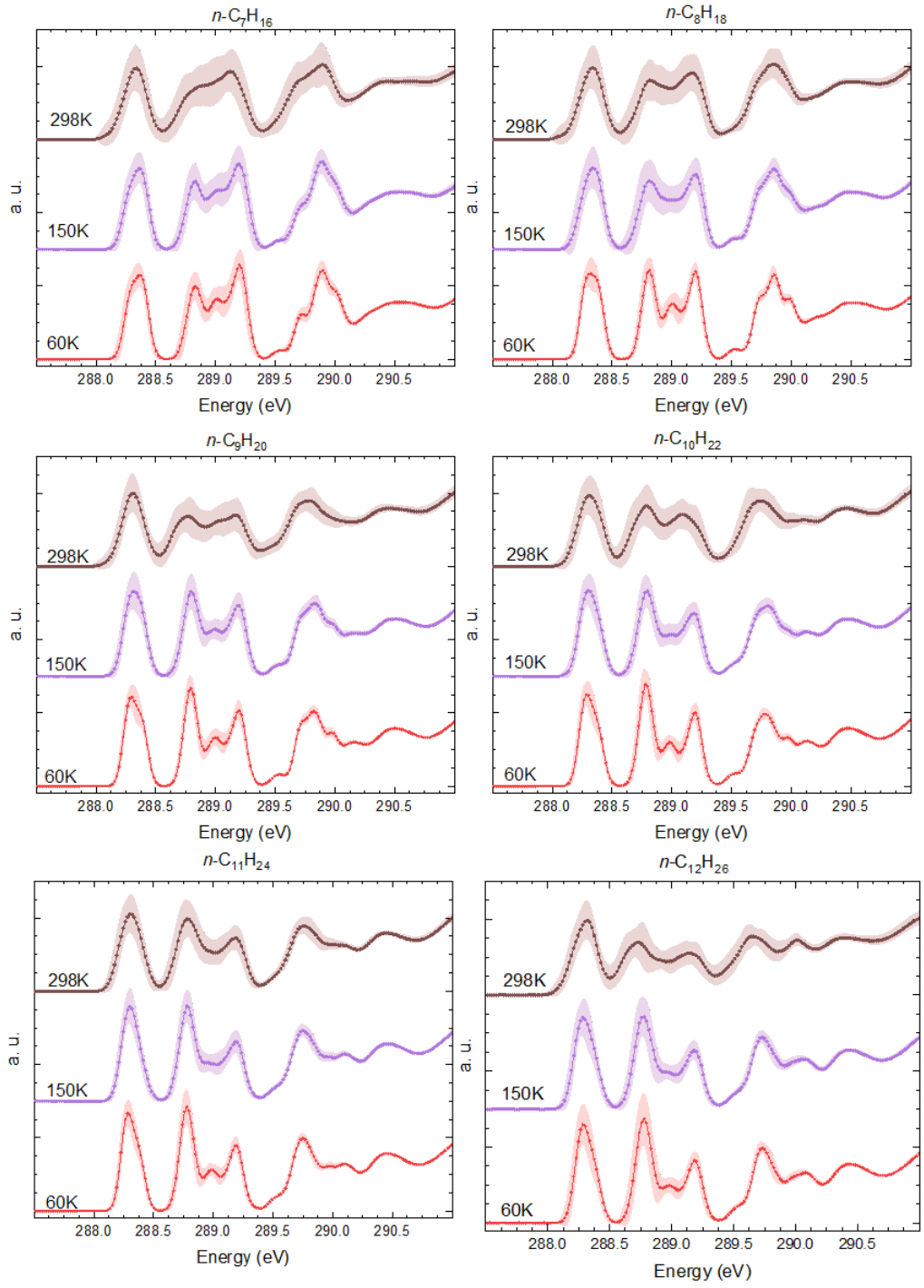

Figure 6.6 – Carbon 1s NEXAFS spectra of (a) heptane, (b) octane, (c) nonane, (d) decane, (e) undecane, and (f) dodecane in various temperatures obtained using the MD-DFT method

As it can be observed, the same trend of broadening and shift to the lower energy is observed for all these molecules with an increase in the temperature. The spectra obtained using this model should better represent the temperature dependence NEXAFS spectra of *n*-alkanes since it captures the dynamic motions of the molecules at each temperature using many of the molecular geometries (snapshots). This covers various changes in the configuration of the molecules, including gauche defects and thermally populated vibrations.

The MD-DFT approach captures some of the nuclear motion and, therefore, should have more similarities with the experimental spectra. Following figure presents the computational spectra of *n*-$C_{15}H_{32}$ obtained using TP-DFT and MD-DFT in comparison with the experimental spectra of the *n*-$C_{40}H_{82}$ obtained by Dr. Sahan Perera in our paper.[46]

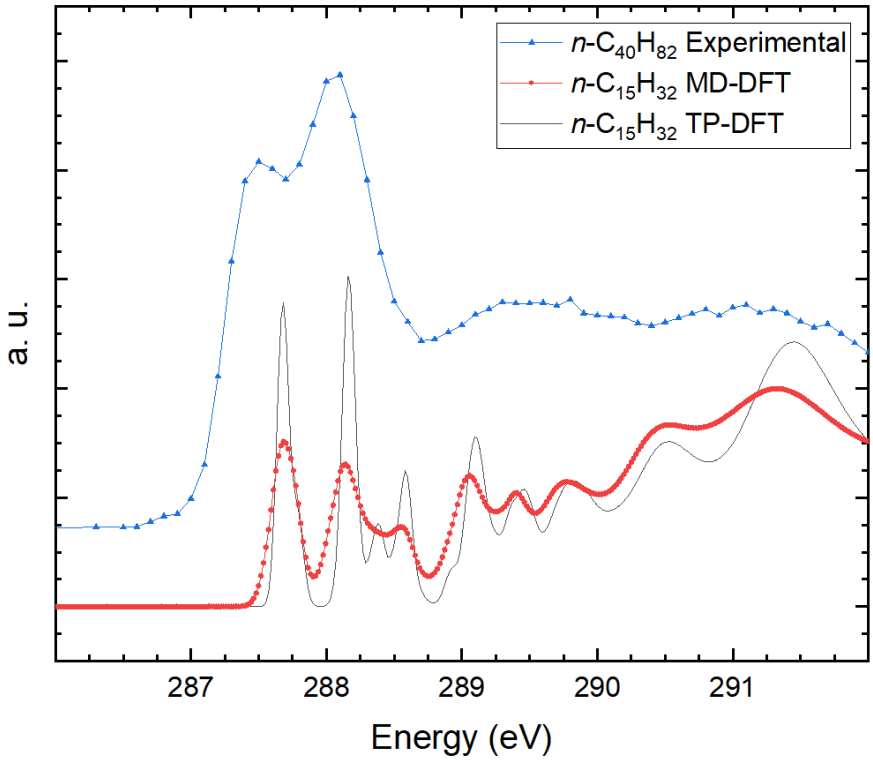

Figure 6.7 – Computational carbon 1s NEXAFS spectra of n-$C_{15}H_{32}$ in comparison with the experimental spectrum of n-$C_{40}H_{82}$.The computational spectra are shifted to the lower energy (0.6 eV)

In this figure, both the TP-DFT and MD-DFT spectra calculations are performed on an isolated *n*-$C_{15}H_{32}$ molecule. The computational spectra are manually shifted to the lower energy (by 0.6 eV) to show the comparison with the experimental spectra from point of the spectral shape and broadening. As it can be observed, the MD-DFT spectra has more similarity with the experimental spectra from point of the appearance of the doublet C-H band peak. This similarity is because MD-DFT calculation captures many geometry configurations in comparison with the single all-trans geometry of the TP-DFT calculations. It should be noted that in each study, the snapshots are obtained for isolated molecules and, therefore, the intermolecular interactions as well as the zero-point motion are not considered. Both of these effects could change the shape and energy of the features in the final spectra but are ignored since only trend of changes are studied in this thesis. To be able to simulate a spectrum similar to the experimental spectra, a proper way of addressing the intermolecular interaction, zero point motion and the R-V mixing is required which could be achieved by using the MD-DFT simulation for a cluster of *n*-alkane molecules. This is due to the increased computational cost if the solvent is introduced. This could be done by adding molecules (of the same kind of the studied molecule) in random orientations to the simulation box. The system could be equilibrated, and snapshots could be extracted after running a canonical ensemble for a few picoseconds. The spectra calculations for each simulation box could be performed in two ways. One way would be to only calculate the spectra of one of the molecules as part of the whole system. This means the spectra calculation model will have many molecules which means a high computational cost. The other approach would be to extract the geometry snapshots for every molecule in the system in the form of an isolated molecule. This approach would include many small calculations. Thanks to automation, this process could also be done automatically as the future work related to this project.

6.6 References

1. Fransson, T.; Harada, Y.; Kosugi, N.; Besley, N. A.; Winter, B.; Rehr, J. J.; Pettersson, L. G. M.; Nilsson, A., X-ray and Electron Spectroscopy of Water. *Chemical Reviews* **2016,** *116* (13), 7551-7569.

2. Urquhart S. G.; Gillies R., Rydberg−Valence Mixing in the Carbon 1s Near-Edge X-ray Absorption Fine Structure Spectra of Gaseous Alkanes. *The Journal of Physical Chemistry A* **2005,** *109* (10), 2151-2159.

3. Urquhart S. G.; Gillies R., Matrix effects in the carbon 1s near edge x-ray absorption fine structure spectra of condensed alkanes. *The Journal of Chemical Physics* **2006,** *124* (23), 234704.

4. Weiss, K.; Bagus, P.; Wöll, C., Rydberg Transitions in X-ray absorption Spectroscopy of alkanes: The Importance of Matrix Effects. *The Journal of Chemical Physics* **1999,** *111* (15), 6834-6845.

5. Zou, Y.; Araki, T.; Appel, G.; Kilcoyne, A. L. D.; Ade, H., Solid state effects in the NEXAFS spectra of alkane-based van der Waals crystals: Breakdown of molecular model. *Chemical Physics Letters* **2006,** *430* (4), 287-292.

6. Bagus, P.; Weiss, K.; Schertel, A.; Wöll, C.; Braun, W.; Hellwig, C.; Jung, C., Identification of Transitions into Rydberg States in the X-ray Absorption Spectra of Condensed Long-Chain Alkanes. *Chemical Physics Letters* **1996,** *248* (3-4), 129-135.

7. Schöll, A.; Fink, R.; Umbach, E.; Mitchell, G.; Urquhart, S.; Ade, H., Towards a Detailed Understanding of the NEXAFS Spectra of Bulk Polyethylene Copolymers and Related Alkanes. *Chemical Physics Letters* **2003,** *370* (5-6), 834-841.

8. Stöhr, J.; Outka, D.; Baberschke, K.; Arvanitis, D.; Horsley, J., Identification of C—H Resonances in the K-Shell Excitation Spectra of Gas-Phase, Chemisorbed, and Polymeric Hydrocarbons. *Physical Review B* **1987,** *36* (5), 2976.

9. Swaraj, S.; Ade, H., Differences in NEXAFS of odd/even long chain n-alkane crystals. *Journal of Electron Spectroscopy and Related Phenomena* **2013,** *191*, 60-64.

10. Ueda, K.; Okunishi, M.; Chiba, H.; Shimizu, Y.; Ohmori, K.; Sato, Y.; Shigemasa, E.; Kosugi, N., Rydberg—Valence Mixing in the C 1s Excited States of CH4 Probed by Electron Spectroscopy. *Chemical Physics Letters* **1995,** *236* (3), 311-317.

11. Ma, Y.; Chen, C.; Meigs, G.; Randall, K.; Sette, F., High-Resolution K-shell Photoabsorption Measurements of Simple Molecules. *Physical Review A* **1991,** *44* (3), 1848.

12. Fu, J., Urquhart, Stephen G., Linear Dichroism in the X-ray Absorption Spectra of Linear n-Alkanes. *The Journal of Physical Chemistry A* **2005,** *109* (51), 11724-11732.

13. Uejio, J. S.; Schwartz, C. P.; Saykally, R. J.; Prendergast, D., Effects of Vibrational Motion on Core-Level Spectra of Prototype Organic Molecules. *Chemical Physics Letters* **2008,** *467* (1-3), 195-199.

14. Schwartz, C. P.; Uejio, J. S.; Saykally, R. J.; Prendergast, D., On the Importance of Nuclear Quantum Motions in Near Edge X-ray Absorption Fine Structure Spectroscopy of Molecules. *The Journal of Chemical Physics* **2009,** *130* (18), 184109.

15. Schwartz, C. P.; Saykally, R. J.; Prendergast, D., An Analysis of the NEXAFS Spectra of a Molecular Crystal: α-Glycine. *The Journal of Chemical Physics* **2010,** *133* (4), 044507.

16. Sellberg, J. A.; Kaya, S.; Segtnan, V. H.; Chen, C.; Tyliszczak, T.; Ogasawara, H.; Nordlund, D.; Pettersson, L. G.; Nilsson, A., Comparison of X-Ray Absorption Spectra Between Water and Ice: New Ice Data with Low Pre-Edge Absorption Cross-Section. *The Journal of Chemical Physics* **2014,** *141* (3), 034507.

17. Basson, I.; Reynhardt, E. C., Identification of a defect chain motion in n-alkanes by means of nuclear magnetic resonance spin–lattice relaxation time measurements. *The Journal of Chemical Physics* **1990,** *93* (5), 3604-3609.

18. Basson, I.; Reynhardt, E., Identification of Defect Chain Motions in the Low Temperature Orthorhombic Phase of Binary Mixtures of n-Alkanes by Means of Nuclear Magnetic Resonance Spin-Lattice Relaxation Time Measurements. *The Journal of Chemical Physics* **1991,** *95* (2), 1215-1222.

19. Mukherjee, P. K., Phase Transitions Among the Rotator Phases of the Normal Alkanes: A Review. *Physics Reports* **2015,** *588*, 1-54.

20. Maroncelli, M.; Strauss, H.; Snyder, R., The Distribution of Conformational Disorder in the High-Temperature Phases of the Crystalline n-Alkanes. *The Journal of Chemical Physics* **1985,** *82* (6), 2811-2824.

21. Craig, S. R.; Hastie, G. P.; Roberts, K. J.; Sherwood, J. N., Investigation into the Structures of Some Normal Alkanes Within the Homologous Series C13H28 to C60H122 Using High-Resolution Synchrotron X-ray Powder Diffraction. *Journal of Materials Chemistry* **1994,** *4* (6), 977-981.

22. Plomp, M.; Van Enckevort, W.; Van Hoof, P.; Van De Streek, C., Morphology of and Dislocation Movement in n-C 40 H 82 Paraffin Crystals Grown From Solution. *Journal of Crystal Growth* **2003,** *249* (3), 600-613.

23. Teare, P., The Crystal Structure of Orthorhombic Hexatriacontane, C36H74. *Acta Crystallographica* **1959,** *12* (4), 294-300.

24. Kaznatcheev, K.; Karunakaran, C.; Lanke, U.; Urquhart, S.; Obst, M.; Hitchcock, A., Soft X-ray Spectromicroscopy Beamline at the CLS: Commissioning Results. *Nuclear*

Instruments and Methods in Physics Research Section A: Accelerators, Spectrometers, Detectors and Associated Equipment **2007,** *582* (1), 96-99.

25. Leontowich, A. F.; Berg, R.; Regier, C. N.; Taylor, D. M.; Wang, J.; Beauregard, D.; Geilhufe, J.; Swirsky, J.; Wu, J.; Karunakaran, C., Cryo Scanning Transmission X-ray Microscope Optimized for Spectrotomography. *Review of Scientific Instruments* **2018,** *89* (9), 093704.

26. Leontowich, A. F. G.; Berg, R.; Regier, C. N.; Taylor, D. M.; Wang, J.; Beauregard, D.; Geilfufe, J.; Swirsky, J.; Wu, J.; Karunakaran, C.; Hitchcock, A. P.; Urquhart, S. G., Cryo-STXM transmission X-ray microscope optimized for spectrotomography. *Under review by Rev. Sci. Instr.* **2018**.

27. *aXis; Software for Analysis of X-ray Microscopy Images and Spectra*, McMaster University: Ontario, Canada, 2000.

28. *Origin; Software For Data Analysis and Graphing*, Version 7.5; Origin Lab: Northampton State, USA, 1991.

29. Coffey, T.; Urquhart, S.; Ade, H., Characterization of the Effects of Soft X-ray Irradiation on Polymers. *Journal of Electron Spectroscopy and Related Phenomena* **2002,** *122* (1), 65-78.

30. Rightor, E.; Hitchcock, A.; Ade, H.; Leapman, R.; Urquhart, S.; Smith, A.; Mitchell, G.; Fischer, D.; Shin, H.; Warwick, T., Spectromicroscopy of Poly (ethylene terephthalate): Comparison of Spectra and Radiation Damage Rates in X-ray Absorption and Electron Energy Loss. *The Journal of Physical Chemistry B* **1997,** *101* (11), 1950-1960.

31. Frisch, M. J.; Trucks, G. W.; Schlegel, H. B.; Scuseria, G. E.; Robb, M. A.; Cheeseman, J. R.; Scalmani, G.; Barone, V.; Petersson, G. A.; Nakatsuji, H.; Li, X.; Caricato, M.; Marenich, A. V.; Bloino, J.; Janesko, B. G.; Gomperts, R.; Mennucci, B.; Hratchian, H. P.; Ortiz, J. V.; Izmaylov, A. F.; Sonnenberg, J. L.; Williams; Ding, F.; Lipparini, F.; Egidi, F.; Goings, J.; Peng, B.; Petrone, A.; Henderson, T.; Ranasinghe, D.; Zakrzewski, V. G.; Gao, J.; Rega, N.; Zheng, G.; Liang, W.; Hada, M.; Ehara, M.; Toyota, K.; Fukuda, R.; Hasegawa, J.; Ishida, M.; Nakajima, T.; Honda, Y.; Kitao, O.; Nakai, H.; Vreven, T.; Throssell, K.; Montgomery Jr., J. A.; Peralta, J. E.; Ogliaro, F.; Bearpark, M. J.; Heyd, J. J.; Brothers, E. N.; Kudin, K. N.; Staroverov, V. N.; Keith, T. A.; Kobayashi, R.; Normand, J.; Raghavachari, K.; Rendell, A. P.; Burant, J. C.; Iyengar, S. S.; Tomasi, J.; Cossi, M.; Millam, J. M.; Klene, M.; Adamo, C.; Cammi, R.; Ochterski, J. W.; Martin, R. L.; Morokuma, K.; Farkas, O.; Foresman, J. B.; Fox, D. J. *Gaussian 16 Rev. B.01*, Wallingford, CT, 2016.

32. Thomas, L. L.; Christakis, T. J.; Jorgensen, W. L., Conformation of Alkanes in the Gas Phase and Pure Liquids. *The Journal of Physical Chemistry B* **2006,** *110* (42), 21198-21204.

33. Kohn, W.; Sham, L. J., Self-Consistent Equations Including Exchange and Correlation Effects. *Physical Review* **1965,** *140* (4A), A1133.

34. Hohenberg, P.; Kohn, W., Inhomogeneous Electron Gas. *Physical Review* **1964,** *136* (3B), B864.

35. Geudtner, G.; Calaminici, P.; Carmona-Espíndola, J.; del Campo, J. M.; Domínguez-Soria, V. D.; Moreno, R. F.; Gamboa, G. U.; Goursot, A.; Köster, A. M.; Reveles, J. U., DeMon2k. *Wiley Interdisciplinary Reviews: Computational Molecular Science* **2012,** *2* (4), 548-555.

36. Koster, A.; Geudtner, G.; Calaminici, P.; Casida, M.; Dominguez, V.; Flores-Moreno, R.; Gamboa, G.; Goursot, A.; Heine, T.; Ipatov, A., DeMon2k, Version 3. *The deMon Developers, Cinvestav: Mexico City, Mexico* **2011**.

37. Triguero, L.; Pettersson, L.; Ågren, H., Calculations of Near-Edge X-ray-Absorption Spectra of Gas-Phase and Condense- Phase Molecules by Means of Density-Functional and Transition-Potential Theory. *Physical Review B* **1998,** *58* (12), 8097.

38. Kutzelnigg, W.; Fleischer, U.; Schindler, M., The IGLO-Method: ab-initio Calculation and Interpretation of NMR Chemical Shifts and Magnetic Susceptibilities. In *Deuterium and Shift Calculation*, Springer: 1990; pp 165-262.

39. Certain, P. R.; Moiseyev, N., Highly Excited Vibrational States by Adiabatic Vs Self-Consistent-Field Methods. *The Journal of Chemical Physics* **1987,** *86* (4), 2146-2151.

40. Calaminici, P.; Flores–Moreno, R.; Köster, A. M., A density Functional Study of Structures and Vibrations of Ta 3 O and Ta 3 O−. *Computing Letters* **2005,** *1* (4), 164-171.

41. Calaminici, P.; Janetzko, F.; Köster, A. M.; Mejia-Olvera, R.; Zuniga-Gutierrez, B., Density Functional Theory Optimized Basis Sets for Gradient Corrected Functionals: 3 d Transition Metal Systems. *The Journal of Chemical Physics* **2007,** *126* (4), 044108.

42. Regier, T.; Paulsen, J.; Wright, G.; Coulthard, I.; Tan, K.; Sham, T. K.; Blyth, R. I. R., Commissioning of the Spherical Grating Monochromator Soft X-ray Spectroscopy Beamline at the Canadian Light Source. *AIP Conference Proceedings* **2007,** *879* (1), 473-476.

43. Shokatian, S.; Urquhart, S. G., Near Edge X-ray Absorption Fine Structure Spectra of Linear n-Alkanes: Variation with Chain Length. *Journal of Electron Spectroscopy and Related Phenomena* **2019,** *236*, 18-26.

44. Patel, S. N.; Su, G. M.; Luo, C.; Wang, M.; Perez, L. A.; Fischer, D. A.; Prendergast, D.; Bazan, G. C.; Heeger, A. J.; Chabinyc, M. L.; Kramer, E. J., NEXAFS Spectroscopy Reveals the Molecular Orientation in Blade-Coated

Pyridal[2,1,3]thiadiazole-Containing Conjugated Polymer Thin Films. *Macromolecules* **2015,** *48* (18), 6606-6616.

45. Flesch, R.; Pavlychev, A.; Neville, J.; Blumberg, J.; Kuhlmann, M.; Tappe, W.; Senf, F.; Schwarzkopf, O.; Hitchcock, A.; Rühl, E., Dynamic Stabilization in 1 σ u→ 1 π g Excited Nitrogen Clusters. *Physical Review Letters* **2001,** *86* (17), 3767.

46. Perera, S. D., Shokatian, Sadegh, Wang, Jian, Urquhart, Stephen G., Temperature Dependence in the NEXAFS Spectra of n-Alkanes. *The Journal of Physical Chemistry A* **2018,** *122* (49), 9512-9517.

Chapter 7 – NEXAFS Spectroscopy of Liquid *N*-alkanes

7.1 Description

Chapter 7 investigates the carbon 1s NEXAFS spectra of liquid *n*-alkanes and the effect of chain length on their spectra. These spectra are studied for *n*-hexane (*n*-C_6H_{14}), *n*-dodecane (*n*-$C_{12}H_{26}$), *n*-tridecane (*n*-$C_{13}H_{28}$), *n*-tetradecane (*n*-$C_{14}H_{30}$), *n*-pentadecane (*n*-$C_{15}H_{32}$), and, *n*-hexadecane (*n*-$C_{16}H_{34}$) in the liquid phase. The spectra of *n*-hexadecane represent a mixture of solid and liquid phase because it's melting point is close to the room temperature (18 ℃). A trend of a shift to the lower energy is observed as the chain length increases. This is mainly attributed to the increased number of defects and thermally populated vibrational states as the chain length increases. This paper is published in the Chemical Physics Letters (DOI: 10.1016/j.cplett.2020.137564). The manuscript is reformatted from the original version for inclusion in the thesis. The supporting document that was published with this paper is presented at the end of this chapter(§7.4.7).

7.2 Description of Candidate Contribution

The author of this thesis was the primary investigator of this research work and developed the research concept of this study, sample preparations, experimental data acquisition, data analysis, the computational model development and execution of the simulations, interpretation of the results, and writing of the document. J. Wang helped with the experimental set-up for the spectra acquisition. S. G. Urquhart provided guidance throughout the experiments, process of data interpretation and analysis, and was actively involved in the editing process of the documents.

7.3 Relation of Contribution to the Research Objectives

Spectra of *n*-alkanes are well studied in the gas phase and the solid phase, but not explored in the liquid phase. As one of the main objectives of this thesis is to gain a better understanding of the role of disorder on the NEXAFS spectra of *n*-alkanes, this study

helps to build a general understanding of the liquid phase and the trend of energy changes in them.

7.4 Effect of Chain Length on the Near Edge X-ray Absorption Fine Structure Spectra of Liquid *n*-Alkanes

Sadegh Shokatian[1], Jian Wang[2], Stephen G. Urquhart[1*]

1. Department of Chemistry, University of Saskatchewan, Treaty Six Territory, Saskatoon, Saskatchewan, Canada, S7N 5C9

2. Canadian Light Source, University of Saskatchewan, Saskatoon, Saskatchewan, Canada, S7N 2V3

7.4.1 Abstract

The carbon 1s near edge X-ray absorption fine structure (NEXAFS) spectra of liquid phase *n*-alkanes have been measured for the first time. Clear trends are observed in the liquid phase spectra as a function of chain length. Specifically, the 'C-H band' in the NEXAFS spectra shifts to lower energy as the chain length increases. Characteristic differences between the gas, liquid, and solid-phase spectra are observed. Differences in the liquid phase *n*-alkane NEXAFS spectra are examined through molecular dynamics simulations coupled with density functional theory simulations of the NEXAFS spectra.

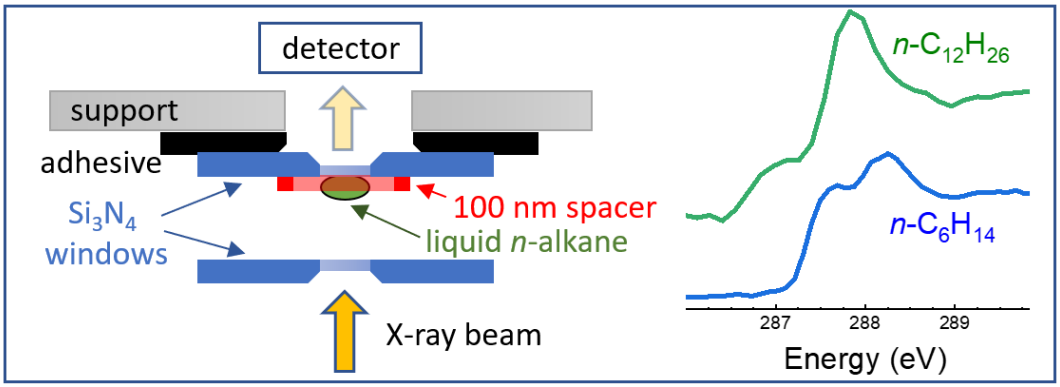

Scheme 7-1 - Carbon 1s NEXAFS spectroscopy of liquid n-alkanes

7.4.2 Introduction

The carbon 1s near edge X-ray absorption fine structure (NEXAFS) spectra of alkanes have been comprehensively examined in the gas phase (methane, ethane, propane, etc.)[1-7] and solid phase (paraffin to polyethylene),[1, 6-12] but not in the liquid phase. There are studies of the carbon 1s NEXAFS of molten polyethylene[8] and molten *n*-alkane thin films,[13] and Nagasaka *et al*. have examined the NEXAFS spectra of unsaturated benzene and pyridine species in the gas, liquid and solid phase.[14-17] However, to date, no systematic studies of alkane molecules in the *liquid* phase have been performed.

In this work, we predominantly focus on the NEXAFS spectra of linear *n*-alkanes because of their comparative simplicity relative to branched alkanes. Studies of simple species allow us to examine effects that will be obscured in larger molecules and may help us understand complex spectroscopic phenomena. We anticipate a series of differences between the gas, liquid, and solid-phase NEXAFS spectra of *n*-alkanes. The carbon 1s NEXAFS spectra of gas-phase alkanes are dominated by Rydberg transitions, accompanied by rich vibronic character.[3-4, 18] This Rydberg character is quenched in the solid phase as valence 'C-H' character becomes predominant. This Rydberg quenching was definitively shown through a comparison of the carbon 1s NEXAFS spectra of neopentane, recorded in the gas and solid phases.[7] The NEXAFS spectra of solid-phase *n*-alkanes show a characteristic low energy 'C-H band' at 287-288 eV. This 'C-H band' persists in *n*-alkanes from short paraffins to polyethylene.[1, 9, 19-20] We use the notation of Endo *et al*.[21] to assign the two components of the 'C-H band', where the first resonance is assigned as the carbon 1s → $\sigma^*_{C\text{-}H}/R_{\parallel}$ transition and the second resonance is assigned as the carbon 1s → $\sigma^*_{C\text{-}H}/R_{\perp}$ transition, where the parallel and perpendicular notation refers to the orientation of the transition dipole moment relative to the C-C-C plane of the *n*-alkane backbone.[21] The 'C-H band' splitting disappear when polyethylene samples were melted or become more disordered through the addition of crosslinks.[8] The 'C-H band' is therefore associated with the presence of crystalline order in the solid phase *n*-alkanes.[8] Recent temperature-dependent studies show that an increase in thermally activated nuclear motion with increased temperature leads to a lower energy onset of the

'C-H band' in the NEXAFS spectra of *n*-alkanes.[9] Such thermally activated motion and defects are expected to be more significant for shorter *n*-alkane chains, for experiments performed at higher sample temperatures where a higher concentration of defects is expected,[22-24] and for liquid phase *n*-alkanes where reptational motion and gauche defect structures are expected.

Overall, liquid *n*-alkanes are expected to share the *condensed phase* character of solid-phase *n*-alkanes, with significant Rydberg quenching and predominant valence character in the 'C-H band'. Liquids will also have a high degree of disorder due to reptational motion, which is one manifestation of the 'nuclear motion effects' [9, 25-28] that are expected to contribute to the NEXAFS spectra of molecules. Nuclear motion effects arise from spectroscopic sampling of the distribution of molecular geometries found in the electronic ground state, which includes zero-point motion, thermally populated vibrational modes (e.g., ν = 1, 2 …) and thermally populated conformations that have their own vibrational manifolds. The NEXAFS spectrum of a molecule will reflect the weighted contributions from all of these geometries.

Nuclear motion effect contributions to NEXAFS spectra have been examined by combining density functional theory (DFT) simulations with molecular dynamics (MD) simulations. These MD-DFT simulations differ from DFT simulations based on the single lowest energy geometry and predict a strong temperature dependence in the NEXAFS spectra.[9, 25-27] Nuclear motion effects lead to a broadening of NEXAFS transitions with increased temperature,[9, 25-27] and in particular the asymmetric broadening of the 'C-H band' to lower energy in the NEXAFS spectra of *n*-alkanes recorded at increased temperatures.[9] Nuclear motion effects are expected to be more significant in the liquid phase, as the manifold of molecular vibrations will be more complex in molecules that have reduced symmetry.

In this work, we have obtained the carbon 1s NEXAFS spectra of a series of liquid *n*-alkanes and examined the effect of chain length and phase change on their NEXAFS spectra. We hypothesize that increased randomness in the liquid phase will affect their

NEXAFS spectra. The observed trends are interpreted with the aid of MD-DFT simulations.

7.4.3 Methods

Samples and sample preparation. Liquid *n*-alkanes used in this study are *n*-hexane (*n*-C_6H_{14}, 99%), *n*-dodecane (*n*-$C_{12}H_{26}$, 99%), *n*-tetradecane (*n*-$C_{14}H_{30}$, 99%), *n*-pentadecane (*n*-$C_{15}H_{32}$, 99%), and *n*-hexadecane (*n*-$C_{16}H_{34}$, 99%). These samples were purchased from Sigma-Aldrich Canada Co. and used without further purification.

For X-ray spectroscopy and microscopy experiments, samples were prepared in a cell consisting of two 100 nm thick low-stress silicon nitride (Si_3N_4) windows (Norcada Inc.). One of the windows in the pair had a thin spacer on the frame (50 nm silicon + 50 nm gold, or 100 nm silicon) to control window separation. Molecules with lengths from 7 - 11 carbon atoms were not examined due to the difficulty in obtaining stable thin films.

To prepare samples for NEXAFS measurement, a small drop of each liquid was trapped between two silicon nitride windows to form a cell. These cells were placed inside a 3d printed sample holder, which alleviates the need of using glue to make a sealed cell. A Nikon Eclipse ME600 optical microscope with a Q-Imaging CCD camera was used to verify the presence of the trapped liquid *n*-alkane film, and to use the film's interference color as an indicator of film thickness.

NEXAFS Spectroscopy. NEXAFS spectra were recorded at the Soft X-ray Spectromicroscopy (SM) beamline (10ID-1) at the Canadian Light Source (CLS) using the ambient Scanning Transmission X-ray Microscope (STXM) end station.[29] The STXM allows liquid samples to be examined in a sealed liquid cell and allows for transmission measurements which would otherwise be impossible in a vacuum chamber used for total electron yield measurements.

X-ray images and NEXAFS spectra were recorded in transmission mode, with linear horizontal X-ray polarization. The low energy grating of the SM beamline was used for these measurements, with exit slits set to 50 microns (non-dispersive) and 20 microns (dispersive), which corresponds to a resolving power ($E/\Delta E$) of approximately 4000. The

energy scale of the beamline was calibrated by separately recording the carbon 1s NEXAFS spectrum of CO_2 (g), using the energies from Ma *et al*.[3] (carbon $1s \rightarrow 3s(v = 0)$ set to 292.72 eV; carbon $1s \rightarrow 3p\ (v = 0)$ set to 294.96 eV).

X-ray transmission images were used to select thin liquid areas for spectroscopy. NEXAFS spectra were acquired using point-scans (spectra acquired in transmission at a (x, y) single point, and normalized using a separately acquired Io spectrum) or in image-sequence mode.[30] The experimental mode chosen depended on the sample; image-sequences provide the best I_o normalization, but only if an open area exists within an STXM image.

As *n*-alkanes are very sensitive to radiation damage[31], the dose was kept as low as possible by optimizing the energy point scaling, slit settings, dwell time, and by defocusing the X-ray spot in the STXM to 500 nm diameter. The ~285 eV region of the NEXAFS spectra was examined as the onset of the carbon $1s \rightarrow \pi^*_{C=C}$ transition is a diagnostic for radiation damage. Radiation damage was found to be minimum in the experimental conditions used.[31-32]

The program aXis2000 was used for data processing.[33] Raw data were converted to optical density using the formula $-ln(I/I_o)$. Spectra were background-subtracted and normalized to the Henke cross-sections[34] for carbon.[35] Spectra of thick samples showed artefacts from residual higher-order contamination in the beamline and were disregarded; artefact-free spectra were averaged to obtain better statistics. Spectra are presented for publication using the Origin lab software package.[36] The data presentation focuses on the carbon 'C-H band' at 287-288 eV to highlight features that vary with chain length.

Computational Simulations. Transition potential DFT simulations of the NEXAFS spectra were performed with the half core hole approximation and the PBE GGA exchange-correlation functional[37-38] using the deMon2k code (version 4.3.4).[39] Diffuse IGLO-III[40] basis sets were used on the core excited carbon atom, a TZVP basis set on hydrogen atoms, and effective core potentials (ECP)[41] on all other carbon atoms. An augmented diffuse basis set (XAS-I) was used on the core excited atom to improve the quality of core-excited state calculations.[42] The GEN-A4* auxiliary basis set was used on

the core-excited carbon atom, and the GEN-A2* auxiliary basis set for all the other atoms.[43-44] The intensity of the spectral lines is obtained from the computed dipole transition matrix elements for excitations from the core (carbon 1s) orbitals, using the XAS simulation code that accompanies the demon2k code (0.1 eV Gaussian lineshapes were used for each transition).

DFT simulations of static structures were obtained previously[12] using geometries obtained from M06-2X DFT geometry optimization calculations[45] performed with 6-31+G(d, p) basis sets using the Gaussian 16 program.[46] Calculated carbon 1s NEXAFS spectra for *n*-C_6H_{14} to *n*-$C_{12}H_{26}$, *n*-$C_{15}H_{32}$ and *n*-$C_{20}H_{42}$ are reproduced from these published data.[12]

To get a better understanding about the NEXAFS spectra in the liquid phase, MD simulations were coupled with DFT calculations for *n*-alkanes *n*-C_6H_{14} to *n*-$C_{12}H_{26}$ as well as *n*-$C_{15}H_{32}$, *n*-$C_{20}H_{42}$, and, *n*-$C_{25}H_{52}$. MD simulations were carried out with the GROMACS[47] software, using the CHARMM36[48] forcefield. For these simulations, an isolated molecule was placed in the centre of a simulation box, and its geometry was optimized using the leap-frog[47] algorithm for integrating Newton's equation of motion. Canonical ensemble (NVT) simulations were carried out at room temperature for 100 ps. The Nośe-Hoover thermostat[49-50] and Parrinello-Rahman Barostat[51] were used to maintain a constant temperature and pressure during the simulation. The simulation was performed with the periodic boundary condition in all directions, and with the particle-mesh Ewald method.[52] One snapshot was extracted from each frame of the simulation, for a total of 102 frames. The molecular geometry from each snapshot was used to simulated the NEXAFS spectra using the DFT calculations with the deMon2k program, using the same basis sets as the DFT simulations performed on static molecules.[12] The average spectrum and standard deviation spectrum were calculated for the 102 NEXAFS snapshots, for each molecule examined.

7.4.4 **Results and Discussion**

Figure 7.1 presents the Carbon 1s NEXAFS spectra of a series of liquid phase *n*-alkane molecules, from a shorter species (*n*-C_6H_{14}) to a series of longer chains (*n*-$C_{12}H_{26}$ to *n*-$C_{16}H_{34}$). The presentation highlights the near edge region (285-292 eV).

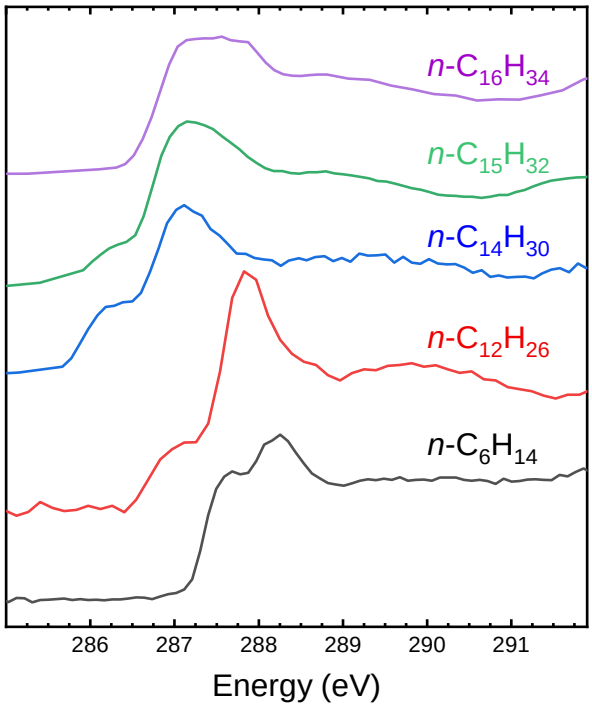

Figure 7.1 - Experimental carbon 1s NEXAFS spectra of liquid n-alkanes (n-C_6H_{14}, n-$C_{12}H_{26}$, n-$C_{14}H_{30}$, n-$C_{15}H_{32}$, and n-$C_{16}H_{34}$), recorded in transmission detection mode.

The energy of the 'C-H band' decreases as the chain length increases from *n*-C_6H_{14} to *n*-$C_{15}H_{32}$ but increases again for *n*-$C_{16}H_{34}$. A low energy shoulder (~287 eV) appears in *n*-$C_{12}H_{26}$ and longer *n*-alkanes, up to *n*-$C_{15}H_{32}$. This shoulder does not appear in the shortest (*n*-C_6H_{14}) or longest (*n*-$C_{16}H_{34}$) member of the series. The large length gap between *n*-C_6H_{14} and *n*-$C_{12}H_{26}$ might explain the differences between these spectra; as we discuss below, shorter *n*-alkanes may have more Rydberg character. As discussed in our previous work,[12] the low energy shoulder has carbon 1s → 3s/$\sigma^*_{C\text{-}H}$ character, while the strong band at 287.8 eV in *n*-$C_{12}H_{26}$ has carbon 1s → 3p/$\sigma^*_{C\text{-}H}$ character.

The difference between the NEXAFS spectra of *n*-$C_{15}H_{16}$ and *n*-$C_{16}H_{34}$ is less obvious, with the disappearance of the low energy 3s/$\sigma^*_{C\text{-}H}$ peak and the emergence of the 'doublet' in *n*-$C_{16}H_{34}$ that is characteristic of longer, solid-phase *n*-alkanes (287.2 – 288 eV). The spectrum of *n*-$C_{16}H_{34}$ is similar to the solid phase spectra of *n*-alkanes, in particular, its similarity to the 'C-H' band.[1, 10] This observation will be addressed in more detail below.

We will start by comparing the liquid and gas phase spectra. Figure 7.2 presents a comparison between the carbon 1s NEXAFS spectra of ethane (CH_3CH_3) and propane ($CH_3CH_2CH_3$), previously recorded in the gas phase using total ion yield[18] and the shortest liquid phase *n*-alkanes examined in this study, *n*-C_6H_{14} and *n*-$C_{12}H_{26}$. Clear differences between the gas and liquid phase are apparent. The gas-phase spectra have narrower line shapes, in particular, the sharp 3s and 3p Rydberg transitions that are accompanied by a vibronic series.[18] Spectroscopic features are broader and appear at higher energy in the liquid phase. This broadening is not due to a difference in instrumental energy resolution, as the gas phase spectra were recorded with a resolving power of ~2,600[18] while the liquid phase spectra were recorded with a resolving power of ~4000. A comparison of the carbon 1s NEXAFS spectra of neopentane recorded in the gas and condensed phases shows that there is a distinct shift to higher energy and a concomitant increase in peak broadening between the gas and condensed phases.[7] The observed energy shift and broadening were attributed to the quenching of the Rydberg character in the condensed phase, the emergence of valence character, and a decrease in the lifetime of the core excited states. When comparing the gas and condensed phase spectra in Figure 7.2, we can see that the narrow gas-phase Rydberg peaks become broader and shift to higher energy in the liquid phase spectra. This is consistent with the experimental observations for neopentane.[7] The observed spectroscopic differences between the gas and liquid phase spectra are therefore primarily associated with phase, and to a lesser extent, with chain length.

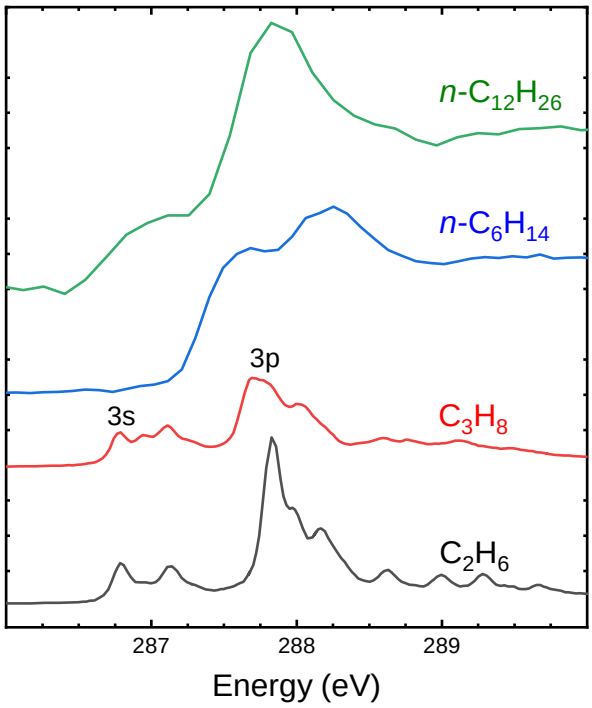

Figure 7.2 - Comparison of the carbon 1s NEXAFS spectra of ethane (C_2H_6) and propane (C_3H_8), recorded in the gas phase by total ion yield1 (bottom) to the carbon 1s NEXAFS spectra of n-C_6H_{14} and n-$C_{12}H_{26}$ (top), recorded in the liquid phase in transmission detection mode

The absence of the low energy 3s/σ^*_{C-H} shoulder in liquid phase *n*-C_6H_{14} is surprising. We are unaware of any published high-resolution gas phase NEXAFS spectra of alkanes larger than propane, although Hitchcock and Ishii examined alkane molecules up to *n*-hexane (*n*-C_6H_{14}) by inner shell electron energy loss spectroscopy (ISEELS) at moderate (0.6 eV fwhm) energy resolution.[53] These data show that the low energy carbon 1s → 3s/σ^*_{C-H} transition disappears and merges into the main (3p/σ^*_{C-H}) band as chain length increases from methane to *n*-hexane. In fact, the published gas-phase ISEELS spectrum of *n*-C_6H_{14}[53] is superficially similar to our liquid phase NEXAFS spectrum, except for a small energy shift where the liquid phase spectrum appears at higher energy than the gas phase spectrum (See Figure S1 in the supplementary material for this comparison). This energy shift between gas and liquid phase spectra is expected based on the gas/solid shifts observed for neopentane.[7]

The next logical comparison is between liquid and solid phase spectra. Figure 7.3 presents a comparison between the liquid phase carbon 1s NEXAFS spectra of *n*-$C_{15}H_{32}$ and *n*-$C_{16}H_{34}$ with the solid phase spectra of crystalline *n*-$C_{40}H_{82}$, from S. Perera *et al.*[10]. Features in the solid phase NEXAFS spectra of *n*-alkanes are narrower and more clearly defined than features in the liquid phase spectra.

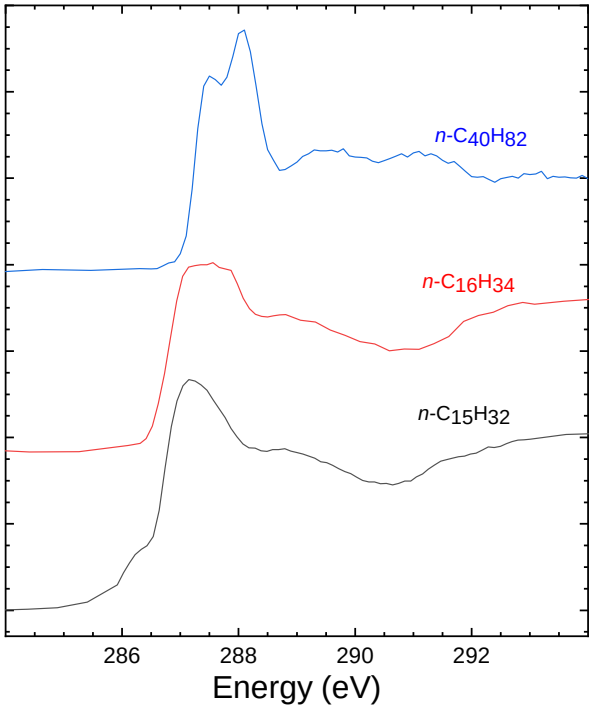

Figure 7.3 - Comparison of the carbon 1s NEXAFS spectra of n-$C_{15}H_{32}$ and n-$C_{16}H_{34}$, recorded in the liquid phase by transmission, with the NEXAFS spectrum of n-$C_{40}H_{82}$, recorded in the solid phase by transmission.

The solid phase spectra appear at slightly higher energy (0.9 eV). This spectral 'sharpness' in the solid phase is likely due to the crystalline nature of this sample, where conformational motion and defects are reduced relative to the liquid phase species. The observation of the 'C-H band' at lower energy for the liquid phase spectra is consistent with arguments made by Perera *et al.*[9] when interpreting the temperature dependence in the NEXAFS spectra of condensed *n*-alkanes: disorder asymmetrically broadens the 'C-H band' to lower energy. As liquids will be more disordered than solids, the observed trends in the NEXAFS spectra are consistent.

We turn to DFT calculations to interpret these liquid phase NEXAFS spectra, starting with calculations of static, lowest energy, all-trans molecular geometries. Our previous work[12] showed that the low energy region of the NEXAFS spectra is dominated by 3s/σ^*_{C-H} and 3p/σ^*_{C-H} bands, with characteristic energy shifts that depend on chain position. Figure S2 in the supplementary material presents the position by position contributions to the NEXAFS spectrum of *n*-hexane (*n*-C_6H_{12})[12], along with a brief description of the calculated spectra.

The chain length dependence of these spectra is shown in Figure 7.4, which presents a DFT simulation of the NEXAFS spectra of linear *n*-alkanes from *n*-hexane (*n*-C_6H_{14}) to *n*-dodecane (*n*-$C_{12}H_{26}$) as well as *n*-pentadecane (*n*-$C_{15}H_{32}$) and *n*-icosane (*n*-$C_{20}H_{42}$), reproduced from Shokatian and Urquhart.[12] A comparison of these DFT simulations of the chain length dependence (Figure 7.4) with experimental liquid phase spectra (Figure 7.1) shows the inadequacy of calculations performed on the single lowest energy all-trans geometry. In the gas and liquid phase, *n*-alkane molecules exist in a range of conformations, each broadened by nuclear motion effects, while solids are broadened by defect structures and nuclear motion effects.

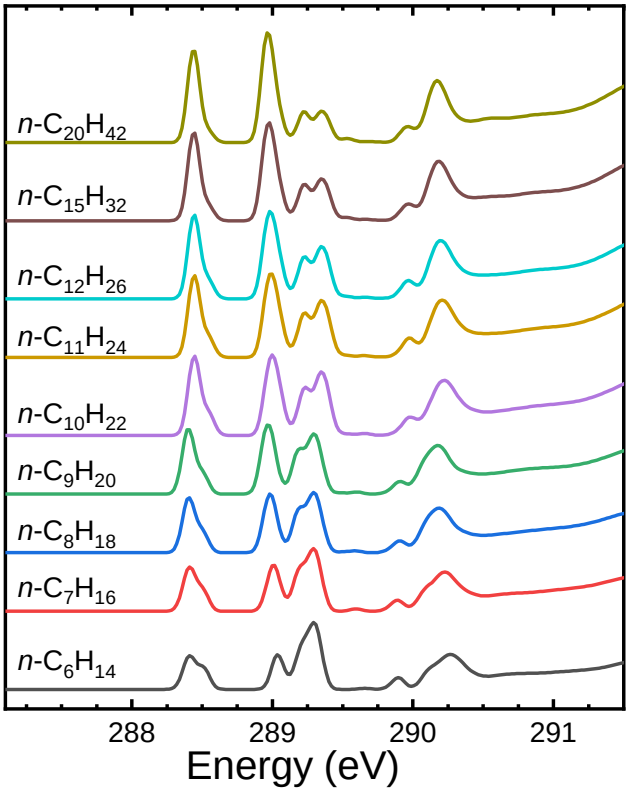

Figure 7.4 - DFT simulations of the carbon 1s NEXAFS spectra of linear n-alkanes in their lowest energy all-trans geometry, from n-hexane (n-C_6H_{14}) to n-dodecane (n-$C_{12}H_{26}$) as well as n-pentadecane(n-$C_{15}H_{32}$) and n-Icosane(n-$C_{20}H_{42}$).

Nuclear motion effects in NEXAFS spectroscopy can be simulated by MD simulations combined with DFT calculations. Figure 7.5 presents MD-DFT simulations of the carbon 1s NEXAFS spectra of *n*-alkanes from *n*-C_6H_{14} to *n*-$C_{12}H_{26}$, using MD simulations performed at 298 K. The spectral simulation is the average of DFT calculations performed for 102 MD snapshots, where the standard deviation is shown as the shaded region. The 3s/$\sigma^*_{C\text{-}H}$ and 3p/$\sigma^*_{C\text{-}H}$ bands shift to lower energy, and the relative magnitude of the standard deviation decreases slightly with increasing chain length. The 3s/$\sigma^*_{C\text{-}H}$ and 3p/$\sigma^*_{C\text{-}H}$ bands are broader in the MD-DFT simulations than in the DFT calculations of the single lowest energy geometry. This is on account of the range of geometries probed in the MD-DFT calculations. The MD-DFT simulations follow the experimental trend, specifically the shift of the 'C-H band' to lower energy as the chain length increases. This trend is attributed to increased disorder in the NEXAFS spectra of

the liquid phase *n*-alkanes, which we can conceptually relate to increased gauche defects and vibrational nuclear motion modes in these different geometries.[9]

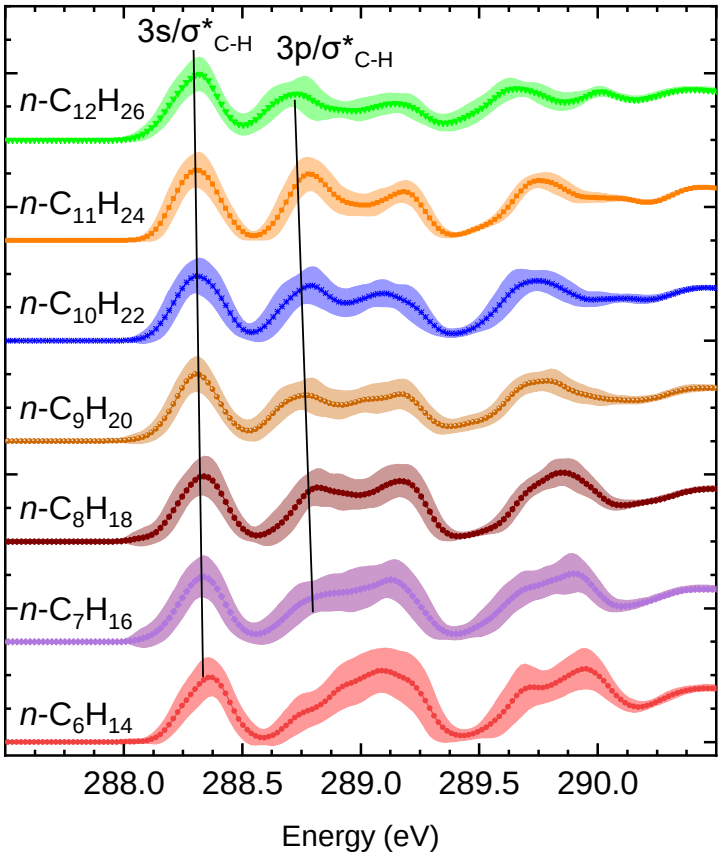

Figure 7.5 - MD-DFT simulations of the carbon 1s NEXAFS spectra of linear n-alkanes from n-hexane (n-C_6H_{14}) to n-dodecane (n-$C_{12}H_{26}$). MD simulations were performed at 298 K. TP-DFT spectral simulations from 102 MD snapshots were averaged (solid line). The standard deviation of this average is shown by the shaded region lines for the maximum of the 3s/σ^*_{C-H} and 3p/σ^*_{C-H} bands are provided as a guide for the eye.

With the exception of *n*-C_6H_{14}, the MD-DFT simulations closely model the experimental NEXAFS spectra, in particularly the broadness of the NEXAFS transitions. A possible interpretation for the mismatch between experiment and calculation for *n*-C_6H_{14} is the inability of the single-molecule MD-DFT simulations to properly account for Rydberg quenching. Rydberg character tends to be stronger in the gas phase NEXAFS spectra of smaller molecules. The electron density of a smaller molecule is less likely to overlap with and scatter the excited Rydberg electron. As a consequence, the Rydberg

character should be more significant in shorter *n*-alkane species, and Rydberg quenching will be more significant in the condensed phase NEXAFS spectra of these species.

Figure 7.6 presents the MD-DFT simulations for *n*-C_5H_{12}, *n*-$C_{10}H_{22}$, *n*-$C_{15}H_{32}$, *n*-$C_{20}H_{42}$, and *n*-$C_{25}H_{52}$, performed at 298 K. These molecules were selected to explore a wider range of chain lengths. The shift to the lower energy of the 3s/$\sigma^*_{C\text{-}H}$ and 3p/$\sigma^*_{C\text{-}H}$ transitions becomes static for chains longer than 20 carbon atoms. This trend is similar to that observed in the experimental spectra of liquid *n*-alkanes (Figure 7.1).

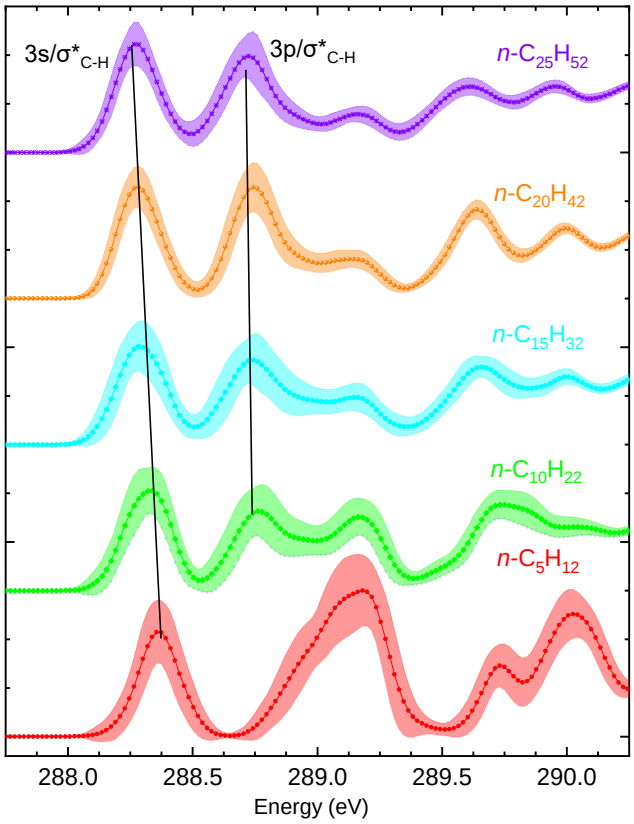

Figure 7.6 - MD-DFT spectra of n-pentane(n-C_5H_{12}), n-decane (n-$C_{10}H_{22}$), n-pentadecane(n-$C_{15}H_{32}$), n-icosane(n-$C_{20}H_{42}$) and n-pentacosane (n-$C_{25}H_{52}$). MD simulations were performed at 298 K. DFT spectral simulations from 102 MD snapshots were averaged (solid line). The standard deviation of this average is shown by the shaded region lines for the maximum of the 3s/σ^*_{C-H} and 3p/σ^*_{C-H} bands are provided as a guide for the eye.

These MD-DFT simulations are performed for a single molecule, and not a simulated liquid or solid. Therefore, intermolecular effects on the NEXAFS spectra (e.g., in particular, Rydberg quenching) and contributions from intermolecular interaction on the molecular geometries (such as excluded volume effects, geometry stabilization, and freezing) are not considered in this model. As the melting point of *n*-$C_{16}H_{34}$ is near ambient at 18°C, the coexistence of the liquid and solid phase or complete freezing into the solid phase is possible within the STXM microscope. This may be why the experimental NEXAFS spectrum of *n*-$C_{16}H_{34}$ is so similar to the NEXAFS spectra of solid *n*-alkanes. This intriguing observation will be subject of further investigation. Likewise, the difference between the experimental NEXAFS spectra of *n*-$C_{12}H_{26}$ and *n*-$C_{14}H_{30}$ lacks a simple explanation, although the differences observed fit into the broader trend. These observations will be comprehensively explored in future variable temperature NEXAFS studies, accompanied by expanded MD-DFT calculations that consider intermolecular interactions.

7.4.5 Summary and conclusions

The carbon 1s NEXAFS spectra of liquid *n*-alkanes are obtained for the first time. The effect of chain length on the NEXAFS spectra of liquid *n*-alkanes are examined experimentally and interpreted with the aid of MD-DFT simulations.

These results show that there is a large difference between NEXAFS spectra recorded in the gas and liquid phase, and a smaller difference between spectra recorded in the liquid and solid phase. The large difference between the gas and liquid phase spectra is attributed to Rydberg quenching[7] and the increase in the complexity of molecules as their chain length increases. The shift of the ‘C-H band’ to lower energy in the liquid phase NEXAFS spectra is attributed to increased disorder in the liquid phase, accompanied by nuclear motion effects within these disordered geometries. The small difference between the liquid and solid phases can be attributed to increased order in the solid phase.

MD-DFT calculations reproduce and explain the trends observed in the liquid phase spectra, in particular the shift of the ‘C-H band’ to lower energy as the chain length

increases. Consideration of nuclear motion effects is essential for interpreting the NEXAFS spectra of liquid phase molecules.

7.4.6 Acknowledgments

SGU is supported by the Nature Sciences and Engineering Research Council (Canada) and the Canadian Foundation for Innovation. This research was carried in Soft X-ray Spectromicroscopy (SM) beamline at the Canadian Light Source (CLS), which is supported by the Natural Sciences and Engineering Research Council of Canada, the National Research Council Canada, the Canadian Institutes of Health Research, the Province of Saskatchewan, Western Economic Diversification Canada, and the University of Saskatchewan. This research was enabled in part by support provided by WestGrid (www.westgrid.ca), Compute Canada Calcul Canada (www.computecanada.ca), University of Saskatchewan, and Terramera Inc (www.terramera.com) HPC resources.

7.4.7 Appendix A. Supplementary material

Supplementary data associated with this article can be found, in the online version, at https://doi.org/10.1016/j.cplett.2020.137564

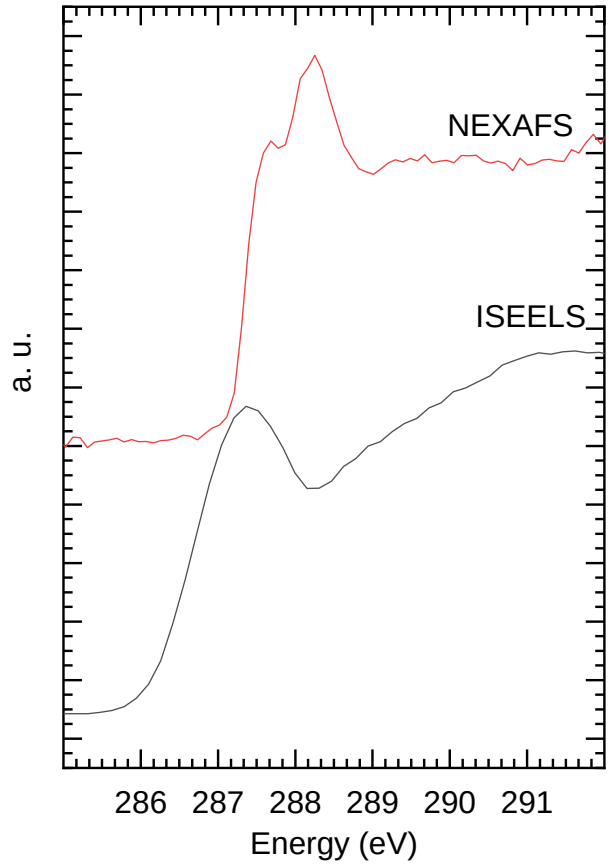

Figure S 7.1 – Comparison of the carbon 1s NEXAFS spectrum of liquid phase n-hexane (this work; top) to the published gas-phase Inner Shell Electron Energy Loss spectrum of n-hexane (from A. P. Hitchcock and I. Ishii, Journal of Electron Spectroscopy and Related Phenomena 42 (1), 11-26 (1987); bottom)

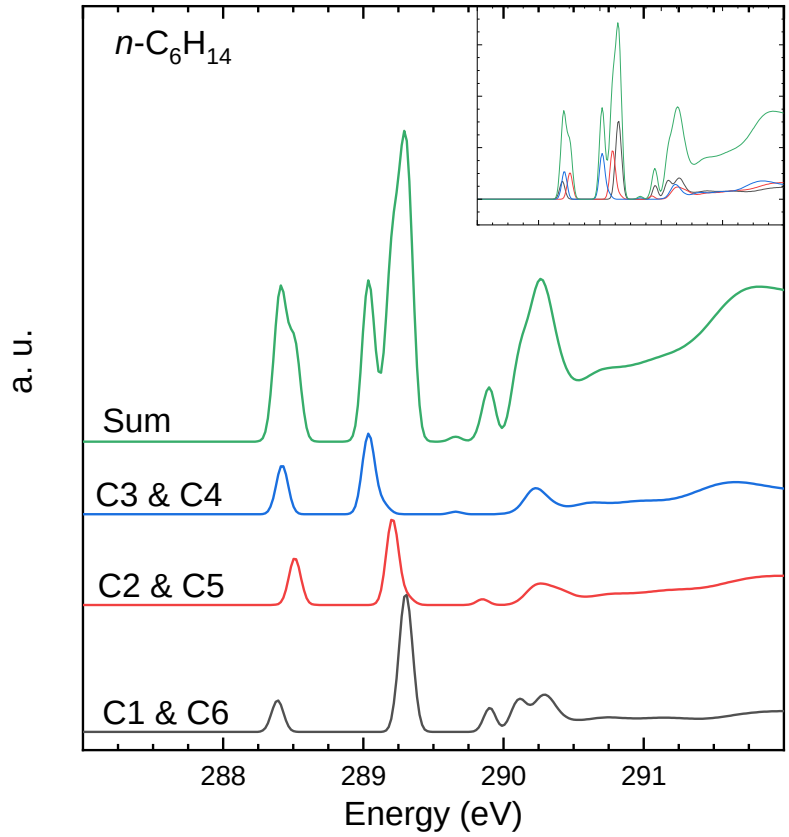

Figure S 7.2 - DFT simulations of the carbon 1s NEXAFS spectrum of n-hexane (n-C6H14), calculated for the lowest energy all-trans geometry (reproduced from S. Shokatian and S. Urquhart, Journal of Electron Spectroscopy and Related Phenomena 236, 18-26 (2019). The contribution of each carbon atom toward the total is shown. INSET: Over plot of the atom contributions toward the total carbon 1s NEXAFS spectrum of n-hexane

The carbon 1s → 3s/ σ^*_{C-H} transitions originating from the methyl (CH_3, atoms C1 and C6) and the internal methylene (CH_2, atoms C3 and C4) appear at lower energy (~288.4 eV), below the carbon 1s → 3s/σ^*_{C-H} transition for the methylene groups next to the terminal methyl groups (atoms C2 and C5; at ~288.5 eV). The carbon 1s → 3p/ σ^*_{C-H} transition is broadened (shown as separate lines in this figure) on account of the chemical splitting. The 3p/σ^*_{C-H} bands for the terminal methyl groups (CH_3, C1, and C6) appear at the highest energy, while the internal CH_2 groups (C3 and C4) appear at the lowest energy.

Table S 7.1 - Melting point of examined n-alkanes

Compound	Melting point (℃)
n-hexane (*n*-C_6H_{14})	-95.3
n-dodecane (*n*-$C_{12}H_{26}$)	-9.55
n-tridecane (*n*-$C_{13}H_{28}$)	-5.30
n-tetradecane (*n*-$C_{14}H_{30}$)	5.85
n-pentadecane (*n*-$C_{15}H_{32}$)	9.95
n-hexadecane (*n*-$C_{16}H_{34}$)	18.18

Haynes, W.M. (ed.) CRC Handbook of Chemistry and Physics. 91st ed. Boca Raton, FL: CRC Press Inc., 2010-2011, p. 3-282

7.5 References:

1. Fu, J., Urquhart, Stephen G., Linear Dichroism in the X-ray Absorption Spectra of Linear n-Alkanes. *The Journal of Physical Chemistry A* **2005,** *109* (51), 11724-11732.

2. Remmers, G.; Domke, M.; Kaindl, G., Vibrationally resolved carbon core excitations in alkane molecules. *Physical Review A* **1993,** *47* (4), 3085-3091.

3. Ma, Y., Chen, C. T., Meigs, G., Randall, K., Sette, F., High-resolution K-shell photoabsorption measurements of simple molecules. *Physical Review A* **1991,** *44* (3), 1848-1858.

4. Ueda, K., Okunishi, M., Chiba, H., Shimizu, Y., Ohmori, K., Sato, Y., Shigemasa, E., Kosugi, N., Rydberg—valence mixing in the C 1s excited states of CH4 probed by electron spectroscopy. *Chemical Physics Letters* **1995,** *236* (3), 311-317.

5. Schirmer, J.; Trofimov, A. B.; Randall, K. J.; Feldhaus, J.; Bradshaw, A. M.; Ma, Y.; Chen, C. T.; Sette, F., K-shell excitation of the water, ammonia, and methane molecules using high-resolution photoabsorption spectroscopy. *Physical Review A* **1993,** *47* (2), 1136-1147.

6. Bagus, P. S.; Weiss, K.; Schertel, A.; Wöll , C.; Braun, W.; Hellwig, C.; Jung, C., Identification of Transitions Into Rydberg States in the X-Ray Absorption Spectra of Condensed Long-Chain Alkanes. *Chemical Physics Letters* **1996,** *248* (3), 129-135.

7. Urquhart, S. G.; Gillies, R., Matrix effects in the carbon 1s near edge x-ray absorption fine structure spectra of condensed alkanes. *The Journal of Chemical Physics* **2006,** *124* (23), 234704.

8. Scholl, A.; Fink, R.; Umbach, E.; Mitchell, G. E.; Urquhart, S. G.; Ade, H., Towards a detailed understanding of the NEXAFS spectra of bulk polyethylene copolymers and related alkanes. *Chemical Physics Letters* **2003,** *370* (5), 834-841.

9. Perera, S. D.; Shokatian, S.; Wang, J.; Urquhart, S. G., Temperature Dependence in the NEXAFS Spectra of n-Alkanes. *The Journal of Physical Chemistry A* **2018**.

10. Perera, S. D., Wang, Jian, Urquhart, Stephen G., Linear dichroism in the NEXAFS spectra of n-alkane crystalline polymorphs. *Journal of Electron Spectroscopy and Related Phenomena* **2019,** *232*, 5-10.

11. Stöhr, J.; Outka, D. A.; Baberschke, K.; Arvanitis, D.; Horsley, J. A., Identification of C---H resonances in the K-shell excitation spectra of gas-phase, chemisorbed, and polymeric hydrocarbons. *Physical Review B* **1987,** *36* (5), 2976-2979.

12. Shokatian, S.; Urquhart, S., Near edge X-ray absorption fine structure spectra of linear n-alkanes: Variation with chain length. *Journal of Electron Spectroscopy and Related Phenomena* **2019,** *236*, 18-26.

13. Hastie, G. P., Johnstone, Joy, Roberts, Kevin J., Fischer, Dan, Examination of the structure and melting behaviour of thin film n-alkanes using ultra-soft polarised near-edge X-ray absorption spectroscopy. *Journal of the Chemical Society, Faraday Transactions* **1996,** *92* (5), 783-789.

14. Nagasaka, M.; Yuzawa, H.; Mochizuki, K.; Rühl, E.; Kosugi, N., Temperature-Dependent Structural Changes in Liquid Benzene. *The Journal of Physical Chemistry Letters* **2018,** *9* (19), 5827-5832.

15. Nagasaka, M.; Yuzawa, H.; Takada, N.; Aoyama, M.; Rühl, E.; Kosugi, N., Laminar flow in microfluidics investigated by spatially-resolved soft X-ray absorption and infrared spectroscopy. *The Journal of Chemical Physics* **2019,** *151* (11), 114201.

16. Nagasaka, M.; Yuzawa, H.; Horigome, T.; Kosugi, N., Reliable absorbance measurement of liquid samples in soft X-ray absorption spectroscopy in transmission mode. *Journal of Electron Spectroscopy and Related Phenomena* **2018,** *224*, 93-99.

17. Nagasaka, M.; Yuzawa, H.; Kosugi, N., Intermolecular Interactions of Pyridine in Liquid Phase and Aqueous Solution Studied by Soft X-ray Absorption Spectroscopy. In *Zeitschrift für Physikalische Chemie*, 2018; Vol. 232, p 705.

18. Urquhart S. G.; Gillies R., Rydberg−Valence Mixing in the Carbon 1s Near-Edge X-ray Absorption Fine Structure Spectra of Gaseous Alkanes. *The Journal of Physical Chemistry A* **2005,** *109* (10), 2151-2159.

19. Swaraj, S.; Ade, H., Differences in NEXAFS of odd/even long chain n-alkane crystals. *Journal of Electron Spectroscopy and Related Phenomena* **2013,** *191*, 60-64.

20. Zou, Y.; Araki, T.; Appel, G.; Kilcoyne, A. L. D.; Ade, H., Solid State Effects in the NEXAFS Spectra of Alkane-Based van der Waals Crystals: Breakdown of Molecular Model. *Chemical Physics Letters* **2006,** *430*, 287-292.

21. Endo, O.; Ozaki, H.; Sumii, R.; Amemiya, K.; Nakamura, M.; Kosugi, N., Orientation of n-alkane in thin films on graphite (0001) studied using C K-NEXAFS. *Journal of Electron Spectroscopy and Related Phenomena* **2011,** *184* (3), 257-260.

22. Basson, I.; Reynhardt, E. C., Identification of a Defect Chain Motion in Normal-Alkanes by Means of Nuclear-Magnetic-Resonance Spin-Lattice Relaxation-Time Measurements. *Journal of Chemical Physics* **1990,** *93* (5), 3604-3609.

23. Snyder, R. G.; Maroncelli, M.; Qi, S. P.; Strauss, H. L., Phase Transitions and Nonplanar Conformers in Crystalline n-Alkanes. *Science* **1981,** *214* (4517), 188.

24. Mukherjee, P. K., Phase transitions among the rotator phases of the normal alkanes: A review. *Physics Reports* **2015,** *588*, 1-54.

25. Schwartz, C. P.; Saykally, R. J.; Prendergast, D., An analysis of the NEXAFS spectra of a molecular crystal: α-glycine. *The Journal of Chemical Physics* **2010,** *133* (4), 044507.

26. Schwartz, C. P.; Uejio, J. S.; Saykally, R. J.; Prendergast, D., On the importance of nuclear quantum motions in near edge x-ray absorption fine structure spectroscopy of molecules. *The Journal of Chemical Physics* **2009,** *130* (18), 184109.

27. Uejio, J. S.; Schwartz, C. P.; Saykally, R. J.; Prendergast, D., Effects of vibrational motion on core-level spectra of prototype organic molecules. *Chemical Physics Letters* **2008,** *467* (1), 195-199.

28. Leetmaa, M.; Ljungberg, M. P.; Lyubartsev, A.; Nilsson, A.; Pettersson, L. G. M., Theoretical approximations to X-ray absorption spectroscopy of liquid water and ice. *Journal of Electron Spectroscopy and Related Phenomena* **2010,** *177* (2), 135-157.

29. Kaznatcheev, K. V.; Karunakaran, C.; Lanke, U. D.; Urquhart, S. G.; Obst, M.; Hitchcock, A. P., Soft X-ray spectromicroscopy beamline at the CLS: Commissioning results. *Nuclear Instruments and Methods in Physics Research Section A: Accelerators, Spectrometers, Detectors and Associated Equipment* **2007,** *582* (1), 96-99.

30. Jacobsen; Wirick; Flynn; Zimba, Soft X-ray spectroscopy from image sequences with sub-100 nm spatial resolution. *Journal of Microscopy* **2000,** *197* (2), 173-184.

31. Coffey, T.; Urquhart, S. G.; Ade, H., Characterization of the effects of soft X-ray irradiation on polymers. *Journal of Electron Spectroscopy and Related Phenomena* **2002,** *122* (1), 65-78.

32. Rightor, E. G.; Hitchcock, A. P.; Ade, H.; Leapman, R. D.; Urquhart, S. G.; Smith, A. P.; Mitchell, G.; Fischer, D.; Shin, H. J.; Warwick, T., Spectromicroscopy of Poly(ethylene terephthalate): Comparison of Spectra and Radiation Damage Rates in X-ray Absorption and Electron Energy Loss. *The Journal of Physical Chemistry B* **1997,** *101* (11), 1950-1960.

33. Hitchcock, A. P. *aXis2000*, Hamilton, ON, 2017.

34. Henke, B. L., Gullikson, E. M., Davis, J. C., X-Ray Interactions: Photoabsorption, Scattering, Transmission, and Reflection at E = 50-30,000 eV, Z = 1-92. *Atomic Data and Nuclear Data Tables* **1993,** *54* (2), 181-342.

35. Hitchcock, A. P., Mancini, D. C., Bibliography and database of inner shell excitation spectra of gas phase atoms and molecules. *Journal of Electron Spectroscopy and Related Phenomena* **1994,** *67* (1), vii.

36. *Origin 2019*, Northampton, MA, 2019.

37. Perdew, J. P.; Burke, K.; Ernzerhof, M., Generalized Gradient Approximation Made Simple. *Physical Review Letters* **1996,** *77* (18), 3865-3868.

38. Hammer, B.; Hansen, L. B.; Narskov, J. K., Improved adsorption energetics within density-functional theory using revised Perdew-Burke-Ernzerhof functionals. *Physical Review B* **1999,** *59* (11), 7413.

39. A.M. Koster, G. G., A. Alvarez-Ibarra, P. Calaminici, M.E. Casida, J. Carmona-Espindola, V.D. Dominguez, R. Flores-Moreno, G.U. Gamboa, A. Goursot, T. Heine, A. Ipatov, A. de la Lande, F. Janetzko, J.M. del Campo, D. Mejia-Rodriguez, J. U. Reveles, J. Vasquez-Perez, A. Vela, B. Zuniga-Gutierrez, and D.R. Salahub *deMon2k*, 4; The deMon developers: 2016.

40. Kutzelnigg, W.; Fleischer, U.; Schindler, M., The IGLO-Method: ab-initio Calculation and Interpretation of NMR Chemical Shifts and Magnetic Susceptibilities. In *Deuterium and Shift Calculation*, Springer: 1990; pp 165-262.

41. Pettersson, L. G. M.; Wahlgren, U.; Gropen, O., Effective core potential parameters for first • and second row atoms. *The Journal of Chemical Physics* **1987,** *86* (4), 2176-2184.

42. Triguero, L.; Pettersson, L. G. M.; Ågren, H., Calculations of near-edge x-ray-absorption spectra of gas-phase and chemisorbed molecules by means of density-functional and transition-potential theory. *Physical Review B* **1998,** *58* (12), 8097-8110.

43. Calaminici, P.; Janetzko, F.; Kaster, A. M.; Mejia-Olvera, R.; Zuniga-Gutierrez, B., Density functional theory optimized basis sets for gradient corrected functionals: 3 d transition metal systems. *The Journal of Chemical Physics* **2007,** *126* (4), 044108.

44. Calaminici, P.; Flores-Moreno, R.; Koester, A. M., A density functional study of structures and vibrations of Ta3O and Ta3O. *Computing Letters* **2005,** *1* (4), 164-171.

45. Zhao, Y.; Truhlar, D. G., The M06 suite of density functionals for main group thermochemistry, thermochemical kinetics, noncovalent interactions, excited states, and transition elements: two new functionals and systematic testing of four M06-class functionals and 12 other functionals. *Theoretical Chemistry Accounts* **2008,** *120* (1), 215-241.

46. Frisch, M. J.; Trucks, G. W.; Schlegel, H. B.; Scuseria, G. E.; Robb, M. A.; Cheeseman, J. R.; Scalmani, G.; Barone, V.; Petersson, G. A.; Nakatsuji, H.; Li, X.; Caricato, M.; Marenich, A. V.; Bloino, J.; Janesko, B. G.; Gomperts, R.; Mennucci, B.; Hratchian, H. P.; Ortiz, J. V.; Izmaylov, A. F.; Sonnenberg, J. L.; Williams; Ding, F.; Lipparini, F.; Egidi, F.; Goings, J.; Peng, B.; Petrone, A.; Henderson, T.; Ranasinghe, D.; Zakrzewski, V. G.; Gao, J.; Rega, N.; Zheng, G.; Liang, W.; Hada, M.; Ehara, M.; Toyota, K.; Fukuda, R.; Hasegawa, J.; Ishida, M.; Nakajima, T.; Honda, Y.; Kitao, O.; Nakai, H.; Vreven, T.; Throssell, K.; Montgomery Jr., J. A.; Peralta, J. E.; Ogliaro, F.; Bearpark, M. J.; Heyd, J. J.; Brothers, E. N.; Kudin, K. N.; Staroverov, V. N.; Keith, T. A.; Kobayashi, R.; Normand, J.; Raghavachari, K.; Rendell, A. P.; Burant, J. C.; Iyengar, S. S.; Tomasi, J.; Cossi, M.; Millam, J. M.; Klene, M.; Adamo, C.; Cammi, R.; Ochterski, J. W.; Martin,

R. L.; Morokuma, K.; Farkas, O.; Foresman, J. B.; Fox, D. J. *Gaussian 16 Rev. C.01*, Wallingford, CT, 2016.

47. Abraham, M. J.; Murtola, T.; Schulz, R.; Páll, S.; Smith, J. C.; Hess, B.; Lindahl, E., GROMACS: High performance molecular simulations through multi-level parallelism from laptops to supercomputers. *SoftwareX* **2015,** *1-2*, 19-25.

48. J. Huang, A. D. M. J., CHARMM36 all-atom additive protein force field: Validation based on comparison to NMR data. *Journal of Computational Chemistry* **2013,** *34* (25), 2135-2145.

49. Nosé, S., A unified formulation of the constant temperature molecular dynamics methods. *The Journal of Chemical Physics* **1984,** *81* (1), 511-519.

50. Hoover, W. G., Canonical dynamics: Equilibrium phase-space distributions. *Physical Review A* **1985,** *31* (3), 1695-1697.

51. Parrinello, M.; Rahman, A., Polymorphic transitions in single crystals: A new molecular dynamics method. *Journal of Applied Physics* **1981,** *52* (12), 7182-7190.

52. Darden, T.; York, D.; Pedersen, L., Particle mesh Ewald: An N·log(N) method for Ewald sums in large systems. *The Journal of Chemical Physics* **1993,** *98* (12), 10089-10092.

53. Hitchcock, A. P.; Ishii, I., Carbon K-shell excitation spectra of linear and branched alkanes. *Journal of Electron Spectroscopy and Related Phenomena* **1987,** *42* (1), 11-26.

Chapter 8 – Discussion and Conclusion

Structural variation and structural disorder are two of the effects that can change the shape and the energy of NEXAFS spectra. Both of these effects will lead to changes in the nuclear motion and the degree of Rydberg-valence mixing. Therefore, the goal of this research was to gain a better understanding of the effect of structural differences as well as the structural disorder on the NEXAFS spectra of *n*-alkanes. Studying the computational spectra of an orthorhombic model (**Chapter 4**) was the first step that was taken to shed some light on the objectives of this study. However, due to the computational cost, alternative models were designed to study these effects. These alternative models were designed to study the effect of chain length (**Chapter 5**), gauche defects (**Chapter 6** and **7**), temperature changes and thermally populated vibrations (**Chapter 6**), and dynamic motions (**Chapter 7**) on the NEXAFS spectra of *n*-alkanes. The chain length model was designed to study the effect of structural variations on the spectra. The rest of these alternative models are designed to address the effect of structural disorder on the spectra of n-alkanes.

8.1 Computational Studies of the NEXAFS Spectra of Condensed *N*-alkanes

As discussed above, for the first step, a computational model of an orthorhombic cluster of *n*-pentane was designed and used as the representative of the condensed phase in comparison with the isolated *n*-pentane as the representative of the gas phase spectra (**Chapter 4**). According to previously published experimental measurements on similar species, the carbon 1s NEXAFS spectra of the condensed phase should be broader than the spectra of the gas phase and appear at higher energy. A hypothesis for this study was that if the computational cluster is large enough to contain all the Rydberg orbitals within the boundaries of the cluster, the experimental shift should be observed for the TP-DFT computational spectra of the central molecule in the cluster in comparison with the isolated molecule. The *n*-pentane was selected as the simplest *n*-alkane that could potentially reproduce the spectra of the condensed phase. The orthorhombic structure was selected as the crystal structure to be studied due to the simplicity of

implementation as well as the importance of this structure for longer chain molecules such as polymers. Using python scripting and automation, various clusters with radiuses of 5 Å to 30 Å were generated. However, the TP-DFT spectra calculation was only successfully performed for the clusters with radius sizes up to 12 Å due to the time limitations of the computational platforms that were used (Compute Canada). As the expected shift to the higher energy was not observed for the largest cluster (12 Å radius), the next step was to obtain the size of the basis functions and trim the very diffuse functions. The hypothesis here was that the trimmed basis set could be used to calculate the spectra of the cluster, only if it leads to a reasonable spectrum for the isolated molecule. Five basis functions (6s, 7s, 6p, 7p, 4d) were trimmed to fit the basis set within the boundaries of the largest cluster that could generate the spectra within the maximum allowed time of calculation. Trimming the large basis functions didn't reproduce the experimental shift to the higher energy that is observed for the spectra of the condensed phase in comparison with the gas phase *n*-alkanes. The next improvement in this approach was the use of the ΔKS energy correction to compensate for the shielding effect of the active electron, which is not considered in the TP-DFT approach. Using the ΔKS energy correction, it was possible to reproduce the experimental energy trend for the spectrum of the cluster in comparison with the isolated molecule. However, a small peak (in the order of 10^{-51}) was observed in the spectrum of the cluster that appears in lower energy compared to the spectrum of the isolated molecule. The origin of this low energy artefact is the mathematical form of the basis functions, which will not simply cut-off at a certain radius and, instead, diminishes gradually as the radius of the basis function increases. This artefact can, therefore, be ignored, and the experimental trend of shift to the higher energy is observed for the spectrum of the cluster in comparison with the isolated molecule. However, due to the size of the cluster and the fact that the spectra calculation (TP-DFT) and the energy correction (ΔKS) needs to be repeated for all the carbons in the structure, the computational cost of this approach is high. Therefore, this project was not further explored due to the computational cost and the fact that the question could be addressed using simpler models with less computational cost.

8.2 Rydberg-Valence Mixing in the Computational NEXAFS Spectra of *N*-alkanes

A change in the structure or the physical phase of the system is discussed to have a significant effect on the character of the transitions below the IP.[1-5] Rydberg-valence mixing is observed to some degree in the spectra of *n*-alkanes in various physical phases. However, the degree of Rydberg-valence mixing could vary from low to high for the gas phase to the solid phase *n*-alkanes, respectively. Therefore, studying Rydberg-valence mixing could help understand the effect of structural disorder on the NEXAFS spectra of *n*-alkanes. Considering that a larger energy difference between the singlet and triplet states represents a larger valence character (as well as lower energy difference representing a more Rydberg character), the Rydberg-valence mixing could be obtained by calculating the difference between the energy of the triplet and the singlet states ($\Delta T - S$). In this study, the Rydberg-valence mixing is studied for the first and second excited states of a number of small leaner and branched alkanes using the TP-DFT approach. It was observed that similar to the previous studies in the literature,[4, 6] the valence character scales with the number of C-H bonds to the core excited carbon atom; highest for methane (4 C-H bonds to carbon), and decreasing in turn for methyl (3 C-H bonds), methylene (2 C-H bonds), methane (one C-H group) and smallest (near zero) for the quaternary carbon in 2,2-dimethylpropane. The spectra of the solid phase *n*-alkanes appear at higher energy compared to the gas phase. This could be due to the Rydberg-valence mixing considering that the gas phase shows more Rydberg character, and solid-phase shows more of higher energy valence character. Another contribution of this study to the literature is an established methodology to study the Rydberg-valence mixing of given molecules using the DFT approach. The DFT approach for this study has not been examined before this research.

8.3 NEXAFS Spectroscopy of Liquid *N*-alkanes

An important contribution of this research to the literature is the spectra measurement of liquid *n*-alkanes, which is not done before. In the liquid phase, NEXAFS spectra are expected to vary with the chain conformation. Molecules in the liquid phase will undergo constant reptational motions, and thus, their spectra will sample many

different molecular geometries. Also, various geometry distributions occur because of zero-point motion ($\nu = 0$), thermally populated vibrational modes ($\nu = 1, 2, \ldots$), and thermally populated molecular conformations with their vibrational manifolds. Therefore, the spectra of the liquid *n*-alkanes are obtained and studied in detail in comparison with the spectra of gas phase and solid phase *n*-alkanes. These studies are accompanied by the computational studies of the same *n*-alkanes using the MD-DFT approach.

The shift to the higher energy when the phase is changed from gas to liquid (as well as from liquid to solid) is observed. This is attributed to the decreased number of defects and also decreased conformational motion as the phase changes. It is also observed that the spectra of *n*-$C_{16}H_{34}$ have similarities to both liquid and solid phases, which could be due to the coexistence of the liquid and solid phase of the sample at room temperature. The effect of chain length on the NEXAFS spectra of liquid n-alkanes is studied after obtaining the experimental NEXAFS of selected liquid *n*-alkanes (*n*-C_6H_{14}, *n*-$C_{12}H_{26}$, *n*-$C_{13}H_{28}$, *n*-$C_{14}H_{30}$, *n*-$C_{15}H_{32}$, *n*-$C_{16}H_{34}$). A shift to the lower energy is observed as the chain length increases. This is attributed to the increased numbers of gauche defects and thermally populated vibrations, which shift the spectra to the lower energy. The spectra of *n*-$C_{15}H_{16}$ and *n*-$C_{16}H_{34}$ are similar to each other as the 3s/$\sigma^*_{C\text{-}H}$ disappears, and the doublet characteristic of solid *n*-alkanes starts to appear (287.2 - 288 eV). As the melting point of $C_{16}H_{34}$ is 18 ℃, the coexistence of liquid and solid phase is possible for this molecule. Spectra of solid *n*-alkanes are narrower and appear in higher energy compared with the spectra of liquid *n*-alkanes. This is due to the fact that in solid-phase molecules, crystalline and conformational motion is reduced compared to the liquid phase. The rabbit-ear feature of solid *n*-alkanes representing the $1s \rightarrow \sigma^*_{C-H}$ does not exist in the liquid phase mainly due to disorder. Comparing the results, the 3s/$\sigma^*_{C\text{-}H}$ and 3p/$\sigma^*_{C\text{-}H}$ bands are broader and shift to the lower energy in MD-DFT calculations compared with the TP-DFT calculations. The MD-DFT results will also follow the experimental trend of the shift to the lower energy as the chain length increases. However, there is a mismatch between the computational spectra of *n*-hexane with the experimental spectra. This is probably because the single-molecule MD-DFT does not properly account for Rydberg quenching. The Rydberg character is stronger in the gas phase (isolated molecule)

spectra of small molecules, and therefore, the spectra of the condensed phase for these molecules will have a more significant Rydberg quenching. Therefore, there will be a mismatch between the MD-DFT of these small molecules with the experimental spectra, if the Rydberg quenching is not properly modeled. For longer chains such as *n*-$C_{15}H_{32}$, the similarity of the computational room temperature spectra with the experimental spectra can easily be observed. However, a proper approach is needed to address the zero-point motion, intermolecular interactions, and the R-V mixing to be able to simulate a computational spectrum similar to the experimental spectra.

8.4 Effect of Chain Length on the NEXAFS Spectra of *N*-alkanes

Studying the effect of the chain length on the NEXAFS spectra is one of the effects that could help understand the effect of structural changes on the NEXAFS spectra of *n*-alkanes in the bigger picture. In this project, the effect of chain length on the NEXAFS spectra of *n*-alkanes is studied through both experimental measurements (explained in §8.3) as well as computational modeling. The experimental energy trend of shift to the lower energy as the chain length increases is also observed for models studying isolated *n*-alkanes using both TP-DFT and MD-DFT approaches. It is observed that with an increase in the chain length, the 3s band shifts slightly to lower energy, and the energy difference between the CH_3 and CH_2 carbon 1s→3s contribution decreases (Figure 5.3). Interestingly, the first methylene group from the end appears at higher energy compared to the terminal methyl group and all the other inner methylene groups. The inner methylene groups (3-position and inward) and the terminal methyl groups are appearing at almost the same energy. Völkner *et al*.[7] have observed the same energy trend for the octadecanethiol. Using the IP and TV calculations, it can be observed that the valence orbital character is responsible for this energy shift in the carbon 1s→3s transition between the methylene groups (2-position) and the terminal methyl groups. In the case of the 3p band, the increase in the chain length will not increase the intensity of the peak. However, the splitting of the three components of the 3p band will increase as the chain length increases. The inner methylene groups (3-position) will also have an interesting effect on the carbon 1s→3p transition by introducing a new peak that is not observed for the chains shorter than five carbons. The intensity of this low energy shoulder will increase

as the chain length increases. This proves that the models with shorter than five carbons are not a good representative of the condensed phase. The model used to represent the condensed phase should at least have five carbons in the chain to be able to capture all the possible peaks (including the one appearing for the chains longer than five carbons) in the spectra of the condensed phase *n*-alkanes. This also justifies the choice of *n*-pentane for the cluster model in Chapter 4. This could be one of the shortcomings with the previous models which have picked propane or *n*-butane as the model to represent the solid-state spectra of longer chain *n*-alkanes.

8.5 Effect of Structural Disorder on the Computational NEXAFS Spectra of *N*-alkanes

The effect of the structural disorder on the NEXAFS spectra of *n*-alkanes is the second objective of this study. This effect can be studied using various approaches focusing on structural defects, vibronic effect, and nuclear motion. The origin of the spectral broadening in the carbon 1s NEXAFS spectra of solids is expected to be nuclear motions and vibronic contributions. In fact, the computational spectra of *n*-alkanes obtained for the all-trans geometry using TP-DFT approach are similar to the experimental spectra obtained at -93 K that lacks lots of nuclear motion. This could be one of the main reasons why calculations will not reproduce the experimental spectra as the calculations do not consider nuclear motion. Vibronic contributions will appear at higher energy and not responsible for the low-energy broadening observed at room temperature. However, nuclear motion via thermally populated molecular defects, as well as vibrational modes, are expected to vary with the temperature. An increase in the chain length is also expected to increase both the thermally populated vibrations and the geometry defects in the structure. Computational results in comparison with the experimental results (conducted by Dr. Sahan Perera) have shown that the geometry defects will broaden the spectra, and the thermally populated vibrations will shift the spectra to the lower energy. As the geometry is distorted from the lowest energy geometry, the HOMO-LUMO gap will decrease, and this will decrease the core→LUMO transition energy. This effect is also observed for the *n*-alkanes in the liquid phase since the molecular motions and reptation will lead to deviation from the all-trans geometry. An

increase in the temperature will broaden and shift the spectra to the lower energy. This is attributed to the increased number of gauche defects and the population of molecules in the thermally populated vibrational states. The results of both TP-DFT and MD-DFT simulations also follow the experimental trend of broadening and shift to the lower energy as the chain length increases.

On the other hand, a change in the temperature will directly change the nuclear motion as well as the population of molecules with the distorted geometry (gauche, vibrational modes, etc.). Both of these changes will have a direct effect on the energy and shape of the NEXAFS spectra of these molecules. The temperature dependence NEXAFS spectroscopy calculation is performed by repeating the MD-DFT simulations in various temperatures and compared with the experimental trend obtained for the *n*-$C_{28}H_{56}$ at room and -93 K temperatures by Dr. Sahan Perera. The computational results show the same trend of broadening and shift to the lower energy as the temperature increases. This confirms that an increase in the temperature will increase the nuclear motion as well as the population of molecules with the distorted geometry and that will lead to the spectral broadening and shift to the lower energy.

8.6 Conclusions

The objectives of this study are to study the effect of structural variations as well as the role of disorder on the NEXAFS spectra of *n*-alkanes through experimental measurements and computational modeling. A methodology is developed to study the Rydberg and valence character of the first two excited states of the molecules using DFT.

8.6.1 Computational Studies of the NEXAFS Spectra of Condensed *N*-alkanes

The orthorhombic model of *n*-pentane with various sizes is generated, and the spectra measurements are performed for these models. For these calculations, it was necessary to account for the shielding effect if the electron in the excited orbital in order to reproduce the observed trend in the experimental spectra. It was also concluded that PBC is necessary for the spectra calculation of the cluster of molecules to contain the Rydberg orbitals within the cluster. This project was not continued due to the computational cost and the fact that the same goal could be achieved using cheaper

computational models. This study shows that if the Rydberg orbitals are properly modeled, the experimental shift to the higher energy will be observed for the NEXAFS spectra of the condensed phase model (cluster model) in comparison with the spectra of the gas phase model (isolated molecule).

8.6.2 Rydberg-Valence Mixing in the Computational NEXAFS Spectra of *N*-alkanes

In this study, a methodology is established to obtain the degree of Rydberg-valence mixing of various molecules, up to the second excited state using the DFT approach. This method is used to obtain the Rydberg-valence mixing of short alkanes. The Rydberg-valence mixing is concluded to be one of the contributors to the shift to the higher energy in the NEXAFS spectra of the solid *n*-alkanes in comparison to the gas phase molecules. So, the key contribution of this part of the study is the methodology establishment using the DFT approach as well as a reasoning for the spectral shift to the higher energy, when the phase is changed from gas to condensed.

8.6.3 NEXAFS Spectroscopy of Liquid *N*-alkanes

The spectra of liquid *n*-alkanes are obtained using the transmission detection in the STXM chamber at Canadian Light Source. The changes in the experimental spectra are studied as a function of chain length. The effect of physical phase change on the spectra is also studied for the changes from the gas phase to the liquid phase and also from the liquid phase to the solid phase. It is observed that a change from the gas to the liquid, and from the liquid to the solid phase would shift the spectra to the higher energy. This is attributed to the decrease degree of freedom of the molecules, hence, decreased nuclear motions, as the phase changes. This study provides an experimental measure of the effect of structural disorder on the NEXAFS spectra of *n*-alkanes. It has been observed that an increase in the disorder will shift the spectra to the lower energy. The disorder in this context can be referred to as the reptation of molecules as well as geometry defects caused by molecular motion (Gauche defect and thermally populated vibrations).

8.6.4 Effect of Chain Length on the NEXAFS Spectra of *N*-alkanes

The effect of chain length on the NEXAFS spectra is studied computationally and experimentally. The computational results follow the experimental trend of shift to lower energy as the chain length increases. It is also observed that the inner methylene groups from position 3 in the chain and inward (3-, 4-, 5-, and, etc.) will have a unique feature associated with them, which are observed at roughly the same energy. This means the studies that used alkanes shorter than five carbons will not fully represent the spectra of the solid phase *n*-alkanes. The same study (effect of chain length on the spectra) is carried out for a smaller subset of molecules using molecular dynamics simulation combined with the TP-DFT approach (MD-DFT). This approach provided spectra that are more similar to the liquid phase as it is averaging the spectra from lots of snapshots while the molecule is in equilibrium. These results follow the same trend as the experimental results. One of the takeaways of this study is that, similar to the experimental NEXAFS spectra, an increase in the chain length will shift the computational NEXAFS spectra to the lower energy. This contributes to the first objective of the study: the effect of structural changes on the NEXAFS spectra of *n*-alkanes. Another major takeaway of this study is that any model that is used to describe the behaviour of condensed *n*-alkanes must have at least five carbons to be able to simulate all the features in the solid phase spectra.

8.6.5 Effect of Structural Disorder on the NEXAFS Spectra of *N*-alkanes

Effect of gauche defects and thermally populated vibrations on the NEXAFS spectra are also explicitly studied for selected *n*-alkanes. These results confirm that both gauche defects and thermally populated vibrations play an important role in broadening and shifting the spectra to the lower energy. The computational results are expanded through studying the temperature dependence of the NEXAFS spectra for selected *n*-alkanes using TP-DFT as well as MD-DFT approaches. As the zero-point motions are contributing to the spectra in all the temperatures, their effect is ignored in this study. Both of these calculations are in good agreement with the experimental results and show the trend of narrowing and shifting to the higher energy as the temperature decreases. This is due to the decrease in the number of nuclear motions and thermally populated vibrations as the temperature decreases. Using the results of this study, it can be

concluded that an increase in the nuclear motion as well as structural disorder, in the form of defects and thermally populated vibrations, will shift the NEXAFS spectra to the lower energy. This conclusion is drawn using both experimental results (conducted by Dr. Sahan Perera) and computational results (TP-DFT and MD-DFT). An increase in the temperature will increase both nuclear motion and structural disorder, and this will lead to a shift to the lower energy.

8.7 References

1. Bagus, P. S., Weiss, K., Schertel, A., Wöll, Ch, Braun, W., Hellwig, C., Jung, C., Identification of transitions into Rydberg states in the X-ray absorption spectra of condensed long-chain alkanes. *Chemical Physics Letters* **1996,** *248* (3), 129-135.

2. Weiss K.; Bagus P. S.; Wöll Ch., Rydberg Transitions in X-ray Absorption Spectroscopy of Alkanes: The Importance of Matrix Effects. *J. Chem. Phys.* **1999,** *111* (15), 6834-6845.

3. Schöll, A., Fink, R., Umbach, E., Mitchell, G. E., Urquhart, S. G., Ade, H., Towards a Detailed Understanding of the NEXAFS Spectra of Bulk Polyethylene Copolymers and Related Alkanes. *Chem. Phys. Lett.* **2003,** *370* (5), 834-841.

4. Urquhart S. G.; Gillies R., Rydberg−Valence Mixing in the Carbon 1s Near-Edge X-ray Absorption Fine Structure Spectra of Gaseous Alkanes. *The Journal of Physical Chemistry A* **2005,** *109* (10), 2151-2159.

5. Urquhart S. G.; Gillies R., Matrix effects in the carbon 1s near edge x-ray absorption fine structure spectra of condensed alkanes. *The Journal of Chemical Physics* **2006,** *124* (23), 234704.

6. Stöhr, J., *NEXAFS Spectroscopy*. Springer, Springer Series in Surface Sciences,: Berlin; London, **1992**; Vol. 25, p 404.

7. Völkner, J.; Klues, M.; Witte, G., Assignment of NEXAFS Resonances in Alkanethiols and Their Implication on the Determination of Molecular Orientation of Aliphatic SAMs. *The Journal of Physical Chemistry C* **2018,** *122* (29), 16810-16820.

Chapter 9 – Future work

9.1 Experimental NEXAFS Spectroscopy of Liquid *n*-alkanes

9.1.1 Chain Length

As discussed, only a subset of all the liquid *n*-alkanes was studied in this thesis, and the *n*-alkanes with the chain length between 7 to 12 carbons were not studied. One study that could follow this thesis would be the study of the rest of these molecules to fill in the gap between the generated spectra. This will help understand the significant difference between the spectra of *n*-hexane(*n*-C_6H_{14}) with the spectra of *n*-dodecane (*n*-$C_{12}H_{26}$)

9.1.2 Temperature Dependence

The experimental NEXAFS spectroscopy in this thesis is performed at room temperature on various days. The effect of temperature variations on the NEXAFS spectra of liquid *n*-alkanes has not been studied yet. Based on the findings in this thesis, an increase in temperature will increase the nuclear motions and lead to the shift of the spectra to the lower energy. Therefore, studying the experimental NEXAFS spectra of liquid *n*-alkanes as a function of temperature could help fill in the knowledge gap about liquid *n*-alkanes.

For this study, the experimental measurement could be done using either a static or a flow-through liquid cell. The static cell design is similar to the design that is used for the measurements performed in this thesis, with the exception of having a Peltier mounted on the top part of the sample holder. The cold part of this Peltier is in contact with the sample holder, and the hot part is connected to two tubes to take the generated heat out. This is done using cold liquids such as liquid nitrogen. This setup is already designed and can be used in the STXM chamber at CLS. The following figure presents the STXM chamber with this system.

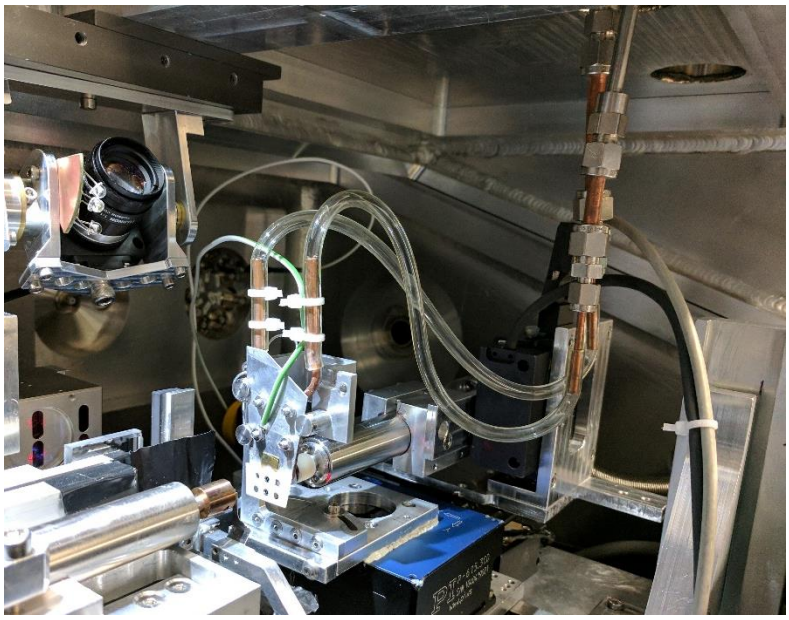

Figure 9.1 - Experimental design of the static cell to study NEXAFS spectra as a function of temperature.

The flow-through cell (Explained in Chapter 2), offers a more flexible option since it is possible to change the temperature of the liquid directly, by submerging part of the tube in the liquid nitrogen. Using either of these options, it would be possible to study the NEXAFS spectra of liquid *n*-alkanes for a variety of temperatures and to obtain a better understanding of the temperature dependence NEXAFS spectra.

9.2 Computational NEXAFS Spectroscopy of *N*-alkanes

9.2.1 PBC

Using deMon2k, the spectra of the orthorhombic structure will always show a wrong trend of shifting to the lower energy compared with the spectra of the isolated molecule. This is mainly due to the defined potential grid on all the atom, which will extend to the vacuum, especially for the outermost atoms. This issue could be resolved using PBC in the NEXAFS calculations. Since deMon2k does not support calculations with the PBC, an alternative opensource program named GPAW[1-3] can be used to simulate the spectra of isolated molecules as well as bulk systems. GPAW is a python code based on the Projector-Augmented Wave (PAW) method and the Atomic Simulation Environment (ASE) library.[1-3] Using GPAW, it is possible to define the wavefunctions as plane-waves

(PW), potential grids (finite difference approximation, FD), and the LCAO approximations. GPAW has the PBC as a default option for all calculations. Therefore, the size of the unit cell is used to study systems in the form of isolated molecules and crystals. The initial python codes are prepared to study the NEXAFS spectra of molecules using the ΔKS energy correction. A future step will include testing various basis sets and unit cell sizes for a given molecule to obtain the NEXAFS of the molecule in the form of the isolated molecule and the crystal.

9.2.2 MD-DFT Simulations – Solvation Box

All the MD-DFT simulations in this thesis are performed on the isolated molecule in the vacuum and therefore, have not considered effects such as intermolecular interactions and zero-point motion. Although using the PBC, the intermolecular interactions, to a limited degree, are considered in calculating the geometry variations, these interactions are not fully represented. A future step would be to solvate the isolated molecule in a solvation box of the same type of molecules. This will allow studying a system that is more similar to a real experimental system, and the outcome could better replicate the experimental results since it better models the R-V mixing as well as the intermolecular interactions. Using automation scripts (already developed), it is possible to create the solvated model and submit the rest of the calculations without many manual steps. However, this increase in the size of the model, will increase the computational cost significantly and need more time to optimize all the parameters.

9.3 References

1. Mortensen, J. J.; Hansen, L. B.; Jacobsen, K. W., Real-space grid implementation of the projector augmented wave method. *Physical Review B* **2005,** *71* (3), 035109.

2. Hjorth Larsen, A.; Jørgen Mortensen, J.; Blomqvist, J.; Castelli, I. E.; Christensen, R.; Dułak, M.; Friis, J.; Groves, M. N.; Hammer, B.; Hargus, C.; Hermes, E. D.; Jennings, P. C.; Bjerre Jensen, P.; Kermode, J.; Kitchin, J. R.; Leonhard Kolsbjerg, E.; Kubal, J.; Kaasbjerg, K.; Lysgaard, S.; Bergmann Maronsson, J.; Maxson, T.; Olsen, T.; Pastewka, L.; Peterson, A.; Rostgaard, C.; Schiøtz, J.; Schütt, O.; Strange, M.; Thygesen, K. S.; Vegge, T.; Vilhelmsen, L.; Walter, M.; Zeng, Z.; Jacobsen, K. W., The atomic simulation environment—a Python library for working with atoms. *Journal of Physics: Condensed Matter* **2017,** *29* (27), 273002.

3. Enkovaara, J.; Rostgaard, C.; Mortensen, J. J.; Chen, J.; Dułak, M.; Ferrighi, L.; Gavnholt, J.; Glinsvad, C.; Haikola, V.; Hansen, H. A.; Kristoffersen, H. H.; Kuisma, M.; Larsen, A. H.; Lehtovaara, L.; Ljungberg, M.; Lopez-Acevedo, O.; Moses, P. G.; Ojanen, J.; Olsen, T.; Petzold, V.; Romero, N. A.; Stausholm-Møller, J.; Strange, M.; Tritsaris, G. A.; Vanin, M.; Walter, M.; Hammer, B.; Häkkinen, H.; Madsen, G. K. H.; Nieminen, R. M.; Nørskov, J. K.; Puska, M.; Rantala, T. T.; Schiøtz, J.; Thygesen, K. S.; Jacobsen, K. W., Electronic structure calculations with GPAW: a real-space implementation of the projector augmented-wave method. *Journal of Physics: Condensed Matter* **2010,** *22* (25), 253202.

Appendix: deMon2k Input Files

- **TP-DFT calculations**

The following input is used to calculate the carbon 1s NEXAFS spectra of *n*-alkanes in this thesis, using the TP-DFT with the HCH approach.

```
PRINT MOS XRAY
AUGMENT
C1 (XAS-I)
BASIS (TZVP)
C1 (IGLO-III)
C (RECP4|SD)
AUXIS (GEN-A4*)
SCFTYPE UKS MAX=150 TOL=0.100E-05
VXCTYPE PBE
MOMODIFY 1 0
1 0.5
XRAY XAS
VISUALIZE MOLDEN FULL
```

This code will change the occupancy of the core in the α spin orbital to 0.5. To change the occupancy of the core in the β spin orbital, the “MOMODIFY” keyword needs to change. Changing the 0.5 to 0 in the third line from the last, will change the approach from the HCH to the FCH.

- **Ground state calculations**

```
PRINT MOS
AUGMENT
C1 (XAS-I)
BASIS (TZVP)
C1 (IGLO-III)
```

```
C (RECP4|SD)
AUXIS (GEN-A4*)
SCFTYPE UKS MAX=150 TOL=0.100E-05
VXCTYPE PBE
VISUALIZE MOLDEN FULL
```

- **Calculation of the singlet excited state**

```
CHARGE -1
PRINT MOS XRAY
AUGMENT
C1 (XAS-I)
BASIS (TZVP)
C1 (IGLO-III)
C (RECP4|SD)
AUXIS (GEN-A4*)
SCFTYPE UKS MAX=150 TOL=0.100E-05
VXCTYPE PBE
MOMODIFY 1 0
1 0.0
VISUALIZE MOLDEN FULL
```

In order to submit a calculation for the higher excited states, the keyword MOEXCHANGE needs to be used to exchange the MO that is being studied with the LUMO. This way, the transition will happen into the exchanged orbital. Following input file is an example for a calculation of the singlet second excited state of *n*-pentane.

```
CHARGE -1
PRINT MOS XRAY
AUGMENT
C1 (XAS-I)
BASIS (TZVP)
C1 (IGLO-III)
C (RECP4|SD)
```

```
AUXIS (GEN-A4*)
SCFTYPE UKS MAX=150 TOL=0.100E-05
VXCTYPE PBE
MOMODIFY 1 0
1 0.0
MOEXCHANGE 1
18 19
FIXMOS SCF=1
VISUALIZE MOLDEN FULL
```

- **Calculation of the triplet excited state**

```
CHARGE -1
PRINT MOS XRAY
AUGMENT
C1 (XAS-I)
BASIS (TZVP)
C1 (IGLO-III)
C (RECP4|SD)
AUXIS (GEN-A4*)
SCFTYPE UKS MAX=150 TOL=0.100E-05
VXCTYPE PBE
MOMODIFY 0 1
1 0.0
VISUALIZE MOLDEN FULL
```